

Forschungszentrum Karlsruhe
Technik und Umwelt

Wissenschaftliche Berichte
FZKA 5840

**Physics of Intense Light
Ion Beams, Production of
High Energy Density in
Matter, and Pulsed Power
Applications**
Annual Report 1995

H.-J. Bluhm (Editor)

Institut für Neutronenphysik und Reaktortechnik

November 1996

Forschungszentrum Karlsruhe

Technik und Umwelt

Wissenschaftliche Berichte

FZKA 5840

**Physics of Intense Light Ion Beams, Production of
High Energy Density in Matter, and Pulsed Power**

Applications

Annual Report 1995

H.-J. Bluhm (Editor)

Institut für Neutronenphysik und Reaktortechnik

Forschungszentrum Karlsruhe GmbH, Karlsruhe

1996

**Als Manuskript gedruckt
Für diesen Bericht behalten wir uns alle Rechte vor**

**Forschungszentrum Karlsruhe GmbH
Postfach 3640, 76021 Karlsruhe**

ISSN 0947-8620

Abstract:

This report presents the results obtained in 1995 within the FZK-program on "Physics of intense ion beams and pulsed dense plasmas". In addition it contains the recently added work on industrial applications of pulsed power techniques.

**Physik intensiver Strahlen leichter Ionen, Erzeugung hoher Energiedichten in Materie und Anwendungen der Pulsed Power Technik
Jahresbericht 1995****Zusammenfassung:**

In dem Bericht werden die in 1995 erzielten Ergebnisse zum Arbeitsthema "Physik intensiver Ionenstrahlen und gepulster dichter Plasmen" dargestellt. Zusätzlich wurden die neu hinzugekommenen Arbeiten zu industriellen Anwendungen der Pulsed Power Technik aufgenommen.

Contents

I.	Program goals and summary of results	1
	H. Bluhm, G. Keßler - INR	
II.	Machines and pulsed power techniques	
1.	Status of the HELIA accelerator	11
	P. Hoppé, W. Bauer, K. Baumann, H. Bluhm, J. Marek, H. Massier, D. Rusch, O. Stoltz - INR/FZK K. Leber, T. Petri, A. Völker, W. Ratajczak - HVT/FZK A. Arzhannikov - INR, Novosibirsk M. Desjarlais - SNL, Albuquerque	
2.	Low-intensity laser-triggering of railgaps applying metal- aerosol switching gases	25
	W. Frey - IEH, University of Karlsruhe	
3.	Fast change of magnetic flux in amorphous strip-wound cores	27
	S. König - IEH, University of Karlsruhe	
4.	Pulsed electron beam facility GESA for surface treatment	29
	of materials G. Müller, G. Schumacher, D. Strauß - INR/FZK V. Engelko, A. Andreev, O. Komarov, N. Schegolichin - Efremov, St. Petersburg	
III.	Production and focusing of high power light ion beams (Diode Physics)	
1.	Ion diode diagnostics to resolve beam quality issues	35
	H. Bluhm, A. Arzhannikov, L. Buth, P. Hoppé, V. Licht, A. Matveenkov, D. Rusch, O. Stoltz, J. Singer, C. Singleton, A. Tauschwitz, W. Väth, S. Yoo - INR/FZK	
2.	Post-focussing experiments performed on the KALIF accelerator ...	45
	using the $B_{\text{appl.}}$ - diode P. Hoppé, Y. Nakagawa, W. Bauer, H. Bluhm, L. Buth,	

	H. Massier, D. Rusch, O. Stoltz, A. Tauschwitz, W. Väth - INR/FZK	
3.	On the stationary applied - B ion diode impedance A Gretchikha - INR/FZK	53
4.	Ion beam emission from a rippled surface A. Gretchikha - INR/FZK	57
5.	Electron sheath collapse in an applied-B ion diode A. Gretchikha - INR/FZK	61
6.	Magnetic field calculations W. Bauer, R. Häfner - INR/FZK	65
7.	The Karlsruhe diode simulation program system KADI2D M. Boger, E. Halter, M. Krauß, C.-D. Munz, R. Schneider, E. Stein, U. Voß, T. Westermann - INR/FZK	69
IV.	Target physics	
1.	Hydrodynamic beam-target experiments on KALIF K. Baumung, L. Buth, R. Huber, D. Rusch, J. Singer, O. Stoltz - INR/FZK S.V. Razorenov, A.V. Utkin, G.J. Kanel - Inst. of Chem. Phys., Chernogolovka	83
2.	Foil acceleration experiments and equation of state for Aluminum B. Goel, W. Höbel, H. Marten - INR/FZK O. Yu. Vorobiev - Inst. of Chem. Phys., Chernogolovka	93
3.	Slowing down of an ablatively accelerated foil after impact on a stationary target H. Marten, B. Goel, W. Höbel - INR/FZK	99
4.	Temperature measurement for KALIF-targets by soft X-ray spectroscopy G. Meisel, H. Bluhm, P. Hoppé, R. Hüttner, D. Rusch, E. Sängner, T. Schön, J. Singer - INR/FZK	107

V. Applications	
1. Light ion beam driven inertial confinement fusion: requirements and achievements	117
H. Bluhm, G. Keßler - INR/FZK	
R.R. Peterson - Fusion Technology Institute, University of Wisconsin	
2. Results of recent investigations conducted on the pulsed proton beam facility PROFAs	129
H. Giese, S. Schalk - INR/FZK	
V. Engelko - Efremov, St. Petersburg	
3. Plasma radiation in ITER tokamak hard disruption events	137
F. Kappler, G. Piazza, H. Würz - INR/FZK	
B. Bazylev - Lykov Inst. of Heat and Mass Transfer, Minsk	
J. Landman - Troitsk Inst. for Innov. and Fusion Research, Troitsk	
4. Modification of material surfaces by the pulsed electron beam facility GESAs	147
G. Müller, G. Schumacher, D. Strauß - INR/FZK	
V. Engelko, A. Andreev, V. Kavaljov - Efremov, St. Petersburg	
5. Process and device for electrodynamic fragmentation of solids - FRANKA	151
V. Neubert, C. Schultheiß - INR/FZK	
H. Wierzch - TTM/FZK	
W. Edinger, R. Sträßner - Ingenieurbüro D.T.I., Karlsruhe	
6. ELBA deposition of glass layers on hydrocarbon foils	159
M. Konijnenberg, G. Schmitt, C. Schultheiß, M. Söhner - INR/FZK	
G. Krafft - TTM/FZK	
7. Production and compaction of nano-crystalline metal oxides by pulsed power techniques	165
R. Böhme, G. Schumacher, A. Weisenburger - INR/FZK	
VI. Publications	171

I Program goals and summary of results

Program goals and summary of results

H. Bluhm, G. Keßler

I. General goals

At the end of 1995 external decisions forced us to shift the main emphasis of the program from intense light ion beam production and high energy density matter research to the development of high voltage pulsed power techniques for industrial processes.

After that less than 40% of the personal and financial resources stay in the initial field of intense particle beams and pulsed dense plasma. The remaining part is concentrated on electrodynamic fragmentation of solid materials, surface modification with pulsed electron beams and generation of nanocrystalline materials by electrodynamic methods.

This report includes work done until April 1996 and therefore, already reflects the general change.

II. Machines and pulsed power technique

The schedule for the begin of operation of the 6 MV, 2TW generator KALIF-HELIA had to be shifted once more till the end of 1997 because of a pending management decision on the site for operation. Thanks to a new Marx-generator that was ordered in 1995 KALIF-HELIA can now be operated and installed independently from KALIF. Therefore, it was finally agreed to install it in the same hall where KALIF is located now (building 423). We believe that KALIF-HELIA operated in negative polarity has a larger potential for the exploration of possible industrial applications than with positive polarity. Therefore, the magnetically insulated voltage adder (MIVA) and the arrangement of the cavities was modified such that both polarities become possible. In addition we revised the dimensions of the inner conductor of the adder in accordance with recent theories developed at Sandia. Also we have begun with design studies for an electron diode (P. Hoppé et al, p. 6).

The investigation of laser triggered multichannel railgap switches carried out at the University of Karlsruhe has been completed in 1995. It was found that metal-aerosols in the switching gas improve the switch characteristics drastically (W. Frey, p. 20).

A test circuit was set up at the High Voltage Institute (IEH) of the University of Karlsruhe to study the behaviour of Vitrovac ferromagnetic cores at fast magnetic flux changes. The results of these measurements shall be used to optimize the design of magnetic switches for repetitive pulsed power generators (S. König, p. 22)

The pulsed electron beam facility GESA designed and fabricated by the Efremov Institute of Electrophysical Apparatus in St. Petersburg was taken into operation in 1995. A wide range of beam parameters can be realized with GESA to optimize the conditions for material surface treatment. Electron kinetic energies range from 50-150 keV, power and energy densities can reach up to 2 MW/cm² and up to 50 J/cm² respectively and pulse durations are controllable from 5 to 40 μ s (G. Müller et al. p 24).

III. Diode physics

Various diagnostic methods and instruments are under development at FZK to measure important physical quantities in the accelerating gap of the KALIF-diode. These methods include optical spectroscopy, refractive index measurements, dispersion interferometry, and high resolution ion energy analysis (H. Bluhm et al. p. 28).

An experiment was set-up to study the post-focusing of the ion beam from the KALIF B_{appl.}-diode by self-fields and by solenoidal fields. So far only the action of the self-fields was studied. A perceptible influence of the self-fields on the power density distribution in the beam focus was not observed. However, the experimental results suggest a strong dependence of the degree of current neutralization on the radial position inside the beam. This result may become important for the recently proposed scheme of self-pinched intense ion beam propagation (P. Hoppé et al., p. 38).

Several analytical approaches have been worked out to explain the operating characteristics of applied-B high power ion diodes. An analytical model based on

electron mixing and magnetic Debye shielding was developed. It predicts unstable diode operation beyond a critical current density. The problem of ion beam emission from a rippled plasma surface in a Child-Langmuir diode was reinvestigated. A differential equation was derived and analytically solved which is valid for most practical cases. Finally, the collapse of the electron sheath in applied-B-diodes, which may occur in the presence of a resistive anode plasma has been investigated (A. Gretchikha, p. 45).

The transient magnetic flux diffusion into the anode of applied-B diodes and its compensation by the superposition of slow and fast fields was studied with the ANSYS-code (W. Bauer, R. Häfner, p. 57).

A first version of the time dependent, two-dimensional particle in cell diode code KADI2D was completed in 1995. An adequate graphical user interface is under development. The extension to three dimensions on a Cartesian grid is planned for 1996 (M. Boger et al. p. 61).

IV. Target physics

The hydrodynamic beam-target experiments with thin foils were continued in 1995. To improve the hydrodynamic efficiency triple layer targets consisting of a gold tamper, a diamond ablator and a Ti payload were used for the first time. Although the observed velocity profile of the flyer looked quite promising, it turned out that the gold tamper was much thicker than desired.

For the first time, spatially resolved dynamic tensile strength measurements were performed across a grain boundary. It was shown that for high strain rates individual crystal grains fail independently (K. Baumung et al., p. 73).

The foil acceleration experiments performed at KALIF were simulated with the target code KATACO and an equation of state in Mie-Grüneisen form was derived which satisfactorily reproduces the experimental data (B. Goel et al., p. 83).

Simulating the impact of Al-flyers on thick LiF-crystals showed distinct differences to the experimental data. Compared to the experimental results the "velocity plateau" of the contact surface after impact was shorter and the decay of the "velocity tail" was less steep. Isolating different involved phenomena it could be demonstrated that radiative heat transport from the hot ablated plasma to the

cold accelerated flyer which was neglected in the initial calculations was responsible for the discrepancy.

In addition it was found that the shape of the "velocity plateau" depends on the phase of the compression wave in the flyer at the instant of impact (H. Marten et al. p. 89).

The K_{α} emission spectroscopy was successfully applied to infer the central temperature of thin targets heated by the KALIF-ion beam. It was found that with Al-foils temperatures above 20 eV were achieved. The X-ray emission from NaF targets initially foreseen for these experiments was too weak to be recorded with the present equipment (G. Meisel et al., p. 96).

The experimental data that become available from the high power plasma gun facility 2 MK-200 CUSP at Troitsk were used to verify the theoretical modeling of the plasma surface interaction during hard disruptions in ITER. Temperature and density distributions of the carbon plasma shield as well as total and line radiation transport to the wall could be reproduced satisfactorily (B. Bazylev et al., p. 123).

V. Applications

In a paper presented at two conferences we compared the present achievements of the light ion beam approach to inertial confinement fusion with the requirements. It is shown that the largest technological gap exists in beam quality and repetition rate capability of high power ion diodes. Beam quality can very likely be improved to a level sufficient for driving a single shot ignition facility, if the potential of two-stage acceleration is used. Repetively operating pulsed power generators meeting the requirements for an ICF reactor driver can be based on presently developed technology (H. Bluhm et al., p. 104).

Significant improvement in the performance of the PROFA facility, which was built to develop the physical and technical basis for a Tokamak plasma disruption simulation generator, has been achieved. A maximum diode current of 100 A (100 mA/cm² at the anode) and a current density of 5-13 A/cm² in the target plane were obtained for pulse durations of up to 40 μ s. However, further improvements of the beam divergence are necessary (H. Giese et al., p. 115).

In a first application the GESA facility, whose characteristics are described in chapter II on machines, was used to treat the surface of the Superalloy MCrAlY, which is widely utilized for oxidation protection on gas turbine blades at high temperatures. An improvement in corrosion resistance has been demonstrated. In another application the wear resistance of tappets was more than 4 times increased by pulsed electron beam treatment (G. Müller et al., p. 133).

In 1995 we also took into operation the pilot generator FRANKA for electrodynamic fragmentation of solid dielectrics. This machine produces 250 kV pulses with a power of 1.5 GW and a pulse duration of 200 ns at a repetition rate of 5 Hz. The pulses are applied to a water filled discharge vessel which contains the material to be fragmented on its grounded metallic bottom. Because of the difference in the dynamic electric strength of water and most solids the pulsed current is forced to flow through the solid material and breaks it into pieces. The unique features of this method is that it separates metallic and dielectric components. Therefore it is well suited for many tasks in the recycling of multicomponent materials. Because of the enormous industrial interest we plan to build more generators of this type adapted to special fragmentation tasks (W. Edinger et al., p. 137).

ELBA uses the electron beam from a channel spark discharge to deposit thin glass layers on organic foils to create a barrier against diffusion of gases. Together with an industrial partner we are presently setting up two channel spark arrays to demonstrate the deposition of a 60 cm wide foil at a speed of 10 cm/s in a pilot-rollcoater (M. Konjinenberg et al., p. 144).

Finally we use the pulsed electrical discharge through a thin wire to generate nanopowder for the production of advanced ceramics and coatings. Sinterable greens of different forms are produced by pulsed magnetic field compression (R. Böhme et al., p. 150).

II Machines and pulsed power techniques

Status of the HELIA accelerator

P. Hoppé, W. Bauer, K. Baumann, H. Bluhm, J. Marek, H. Massier, D. Rusch O. Stoltz - INR/FZK
K. Leber, T. Petri, A. Völker, W. Ratajczak - HVT/FZK
A. Arzhannikov¹ - INP, Novosibirsk
M. P. Desjarlais², SNL, Albuquerque

Abstract

Related to new guidelines for the future use and accomodation of the HELIA accelerator the work in the past period concentrated on the investigation whether this machine can be operated in negative polarity and in another building as yet foreseen. Based on a new theory describing the operation of magnetically insulated transmission lines the diameters of the inner conductor were reconsidered. This report also gives a review of the HELIA related activities performed during the last year [1] and summarizes the tasks to be accomplished to get the accelerator operational under these new conditions.

I. Introduction

During the last month the work on the High Energy Linear Induction Accelerator HELIA was strongly influenced by the following new guidelines: the intention to use HELIA for the generation of an electron beam and to install and operate the accelerator in another building as yet foreseen.

The linear induction accelerator HELIA was designed to deliver an electrical impulse with a voltage of 6 MV and a current of 400 kA for a time interval of 50 ns (FWHM). The conversion of this electrical energy of 120 kJ into energy of a particle beam requires positive polarity at the inner conductor of the accelerator for the extraction of an ion beam and negative polarity for the extraction of an electron beam. HELIA was originally designed for positive polarity operation. Motivated by the increasing interest in technological applications the possibility to operate HELIA in negative polarity for the generation of an electron beam was investigated. The design of the magnetically insulated voltage adder (MIVA) and the magnetically insulated transmission line (MITL) was optimized on basis of a new theory. These new results - compared to those achieved from earlier approaches - are discussed for either polarity in sect. II. The preliminary design parameters of a diode converting the electrical energy delivered by the accelerator into beam energy for either ions or electrons are summarized in sect. III.

In the past years the plans for the construction and operation of HELIA were based on its accomodation in hall I of the building 630. The space available in this hall allowed a coupling of the existing KALIF Marx generator to the HELIA accelerator. Due to financial reasons the reconstruction of hall I in building 630 turned out to be not feasible. As an alternative solution it was considered whether HELIA could be constructed and operated in the building 423. This is only possible if the concept of coupling the two machines by one common Marx generator is abandoned and each accelerator is powered by its own Marx. A more detailed description of the new HELIA Marx ordered for this purpose is given in sect. IV. In section V a review will be given of the different arrangements considered so far for the accomodation of KALIF and HELIA in the different buildings.

¹ permanent address: Institut of Nuclear Physics, Novosibirsk, Russia

² permanent address: Sandia National Laboratories, P.O. Box 5800, Albuquerque, NM 87185, USA

HELIA still would be a unique accelerator in Europe³ with respect to the projected peak power of 2.4 TW and to the technology used for the generation of a peak voltage of 6 MV by adding up the voltages of about 1 MV delivered to 6 cavities. The maximum of information referring to this new domain of pulsed power technology will be assured by the instrumentation summarized in sect. VI. Finally the current status of the work on different components as well as the tasks which need to be completed before operation of this machine is given in sect. VII.

II. Redesign of the inner stalk of the magnetically insulated voltage adder

Based on the latest theory developed by Mendel [2] the design of the inner stalk of the MIVA for the HELIA accelerator was reconsidered [1]. The optimum transfer of the energy delivered by the 6 cavities to the load requires an optimum impedance sequence of the 6 coaxial sections, connecting the cavities to the load. This impedance sequence is strongly influenced by the electron vacuum flow. The electron flow is due to the high electric fields launching electrons into the vacuum gaps formed by the radial feed sections (impedance Z_{feed}) and the 6 coaxial sections formed by the bore diameter of the cavities and the 6 different outer diameters of the inner stalk. The term optimum is used here in the following sense. Most diode applications are geared towards higher voltage and lower current. In practice the best diode behavior is found in this limit. The optimum vacuum impedance sequence of the 6 coaxial sections is in Mendels theory defined by the vacuum impedance for each section (i.e $Z_{vac}(1) \dots Z_{vac}(6)$) that allows the highest value of the flow impedance for each section ($Z_{flow}(1) \dots Z_{flow}(6)$) without adding any unnecessary inductance slowing down the rise time of the pulse. In Mendels theory this optimum is clearly identifiable. In general, for a sequence of N adders, the Z_{flow} downstream of the last adder can be calculated as a function of the vacuum impedance in the final section. It is found that Z_{flow} saturates for some finite vacuum impedance. Beyond that point, Z_{flow} does not increase further, but the inductance of the last section continues to increase. The optimum for the purpose of a high impedance load performance occurs at that transition point.

The minimum feed impedance Z_{feed} for each of the existing HELIA cavities is approximately 8.25 Ω . Using this value and Mendels optimum ratio of $Z_{vac}(n)$ and $Z_{flow}(n)$ to Z_{feed} for each section $n = 1 \dots 6$ given by

$$\frac{Z_{vac}(n)}{Z_{feed}} = \sum_{i=1}^n \frac{1}{\sqrt{i}} \quad \text{and} \quad \frac{Z_{flow}(n)}{Z_{feed}} = \sqrt{n}$$

the optimum vacuum impedance sequence would be 8.25, 14.1, 18.9, 23.0, 26.7, and 30.0 Ω . The corresponding outer diameters of the stalk would then be 332, 301, 278, 260, 244, and 231 mm for a bore diameter of the cavities of 381 mm. These values are somewhat different from the diameters estimated previously (344, 305, 281, 240, 213, and 189 mm in [1]), the ones calculated on the basis of a minimum energy principle by Gordeev (349, 317, 286, 258, 232, and 209 mm in [3]) and the PSI design values (343, 317, 294, 273, 254, and 236 mm in [4]). Results from measurements performed on the PBFA-X MIVA and extension MITL strongly support Mendels theory. Therefore the inner stalk for HELIA-MIVA should be fabricated according to the diameters based on this theory. The mechanical deformation of the stalk is certainly not strongly affected by these diameter changes and therefore still can be considered as negligible [5].

³ Accelerators based on the Magnetically Insulated Voltage Adder principle are the HERMES III (20 MV) and SABRE (6 to 10 MV) machines at the Sandia National Laboratories, Albuquerque. The 4 MV COBRA accelerator will be operational before end of 1996 at the Cornell University.

Neglecting inductance and transmission line effects , a simple load line analysis of this configuration can be performed. The open circuit voltage V_{oc} is 18 MV arising from 3 MV of each of the 6 cavities [1]. The accelerator impedance Z_A as one lumped element is 6 times $5.5 \Omega = 33 \Omega$. Using the Z_{flow} relationship for the last section along with a simple resistive load gives

$$V_d = V_{oc} - Z_A (I_K^2 + V_d^2 / Z_{flow}^2)^{1/2}$$

where V_d is the diode voltage , and I_K is the cathode current entering the diode. Using the equation given before, the flow impedance of cavity number 6 is 20Ω . For the case of a zero cathode current the effective maximum voltage at the load would be 6.75 MV. Optimizing the power in the diode (assuming that the vacuum flow cannot be retrapped) by maximizing V_d times I_K gives a diode voltage of 4.6 MV, a cathode current of 333 kA and an anode current of 406 kA. The efficiency I_K/I_A is 82% and the ratio of the diode impedance V_d/I_K to Z_{flow} in the last section is 0.7, i.e. the diode is undermatched to the flow impedance. For a diode voltage of 6MV the expected cathode current would be 225 kA. These numbers do not include any breakdown of the efficiency within the diode itself, so the actual efficiency will be lower.

In positive polarity operation, these MIVA impedances should be close to optimum. In the case of negative polarity operation, the performance is a bit harder to predict. Considering the case of Hermes III at Sandia, it is found that in negative polarity the individual radial feeds do not appear to achieve sufficient voltage to cause the emission of a significant amount of electrons. In negative polarity, Hermes III seems to be modeled well by only including the electrons that are emitted by the central cathode. For the proposed HELIA configuration the amount of electrons emitted in the feed sections might be sufficiently large to give flow characteristics similar to the positive polarity operation.

Since it is a concern for HELIA generator to maintain a sufficiently low voltage at the oil/vacuum interface to avoid interface flashing, operation at a lower Marx charge voltage should be considered. An alternative would be to introduce a constriction into the radial feeds or central sections of the MIVA to limit the high voltage operation but without seriously compromising the operation at the desired operating point. This approach is currently being used successfully at the NRL to prevent their insulator stacks on the Gamble II accelerator from flashing.

III. Electron- vs. ion-beam generation with HELIA

III.1 Operation of HELIA in negative vs. positive polarity

The generation and extraction of an electron beam requires negative polarity at the inner conductor. Principally this can be achieved by either charging the Marx in negative polarity or by inverting the polarity of the voltage induced by each cavity.

The electric breakdown strength of coaxial transmission lines using water as dielectric depends on the polarity of the voltage applied to the inner conductor. In negative polarity the inner conductor can be charged about 2 times higher compared to a positive inner. Charging the Marx generator in negative instead of positive polarity would subsequently change the polarity on the 4 intermediate stores, the 4 lasertriggered gas switches and the 12 pulse forming lines (PFL). Hence the water insulated intermediate stores and PFL's would be operated with a positive inner conductor and might therefore breakdown prematurely. However, for lower Marx charge voltages (about 70% max.) one can presumably use the accelerator in the 'wrong' polarity.

Inversion of the polarity of the output voltage at full power can technically be achieved by just turning the inner conductor horizontally by 180 degrees, i.e. inserting it to the cavities from the right side

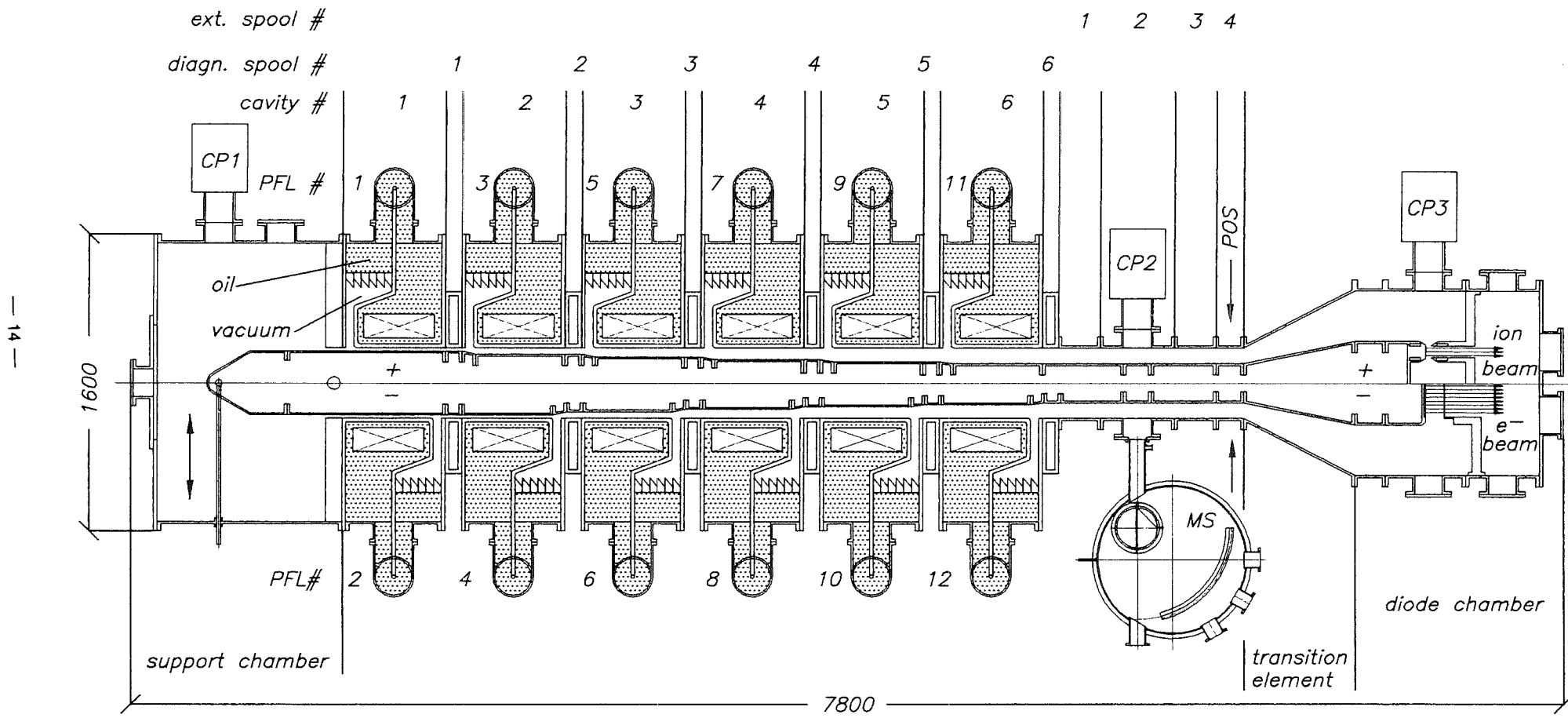


Fig.1: Schematic of the HELIA accelerator when operated in positive (upper half) or negative (lower half) polarity
 CP: cryo pump, PFL: pulse forming line, MS: magnetic spectrometer, POS: plasma opening switch

(Fig. 1) and also supporting (= grounding) it on the right side. The cavities themselves remain in place as foreseen for positive polarity operation. Consequently the area for experimental access as well as the location of the main radiation source would move to the left side. This strongly influences the complete support system already fabricated. It also influences the position of the auxiliary systems and the walls needed for radiation protection. These drawbacks can be avoided by turning horizontally 180 degrees each induction cavity (shown schematically in the lower half of Fig.1), leaving now the inner conductor in its position and also leaving the experimental area on the same side as required for positive polarity operation. However, compared to the positive inner conductor design (Fig. 1, upper half), the high voltage feed gaps of each cavity would move axially and correspondingly the stepwise reduction of the diameters of the inner conductor - needed for impedance matching (see sect. II) - must be moved too. This requires a redesign of the inner conductor with respect to the possibility of its adequate restacking. In addition, also the mechanical compatibility of all other components involved by this change of polarity must be verified and assured.

Between the cavity No. 6 and the diode generating the ion- or electron beam the MITL extension elements No. 1 to No. 4 and one transition element were inserted (Fig.1). These elements match to the vacuum impedance of the last MIVA stage, i.e. 30Ω . The four extension elements are necessary for the adaptation of a magnetic spectrometer MS foreseen for the measurement of the diode voltage, 3 plasma opening switches POS needed for the suppression of the precursor pulse and the mounting of the cryogenic pump CR2. Some distance between the diode and the cavities also helps to protect the oil to water interfaces of the cavities and reduces ringing effects from voltage reversals. The final diameter of the transition element is related to the design of the diodes (emitting the beam) and is considered in the following 2 sections.

III.2 Parameters of an ion beam diode

The ion beam delivered by the HELIA generator should deposit a specific power of about 1000 TW/g on a target. With the KALIF accelerator a specific power of 200 TW/g was achieved with a proton beam accelerated by a voltage of 1.7 MV. With the projected voltage of about 6 MV for HELIA the acceleration of protons will not result in a higher specific power deposition due to the extended range of protons at higher energies. The generation and acceleration of Lithium (or heavier ions like Carbon) is therefore mandatory for the success of HELIA when operated in positive polarity. The following considerations were used to achieve preliminary design parameters of a Lithium diode.

The anode surface of a diode accelerating and extracting a Lithium beam of about 400 kA is mainly determined by the density of the Lithium current which can be supplied by the Lithium plasma covering the emitting surface of the anode. Based on the present state of experience with Lithium plasma sources [6] a current density of the order of 1000 A/cm^2 seems to be achievable. A radially homogeneous ion emission can approximately be achieved with a ring shaped anode with a small aspect ratio $\Delta r / r$ where Δr is the difference between the outer and inner anode emission radius and r is their mean value. Another restriction for Δr is the voltage which can be supplied by the generator creating the anode plasma by the sliding gas discharge mechanism [7]. With peak voltages of about 40 kV achieved so far with these external plasma generators [8] the value of Δr should not exceed 3 cm limited by the electric field required for the breakdown of the Lithium vapor. Taking into account the space required for the outer and inner applied magnetic field coils on the anode side, the outer diameter of the anode stalk in the diode region should be around 45 cm (Fig.2, upper half). With this diameter of the anode stalk the inside diameter of 82 cm of the diode vacuum chamber and the corresponding side of the transition element is then fixed by matching these elements to the 30Ω vacuum impedance at the high voltage end of the MIVA. The ring shaped cathode tip must be placed at a distance of about 15 mm to the surface of the anode to achieve the 1000A/cm^2 current density. The ion beam is entering

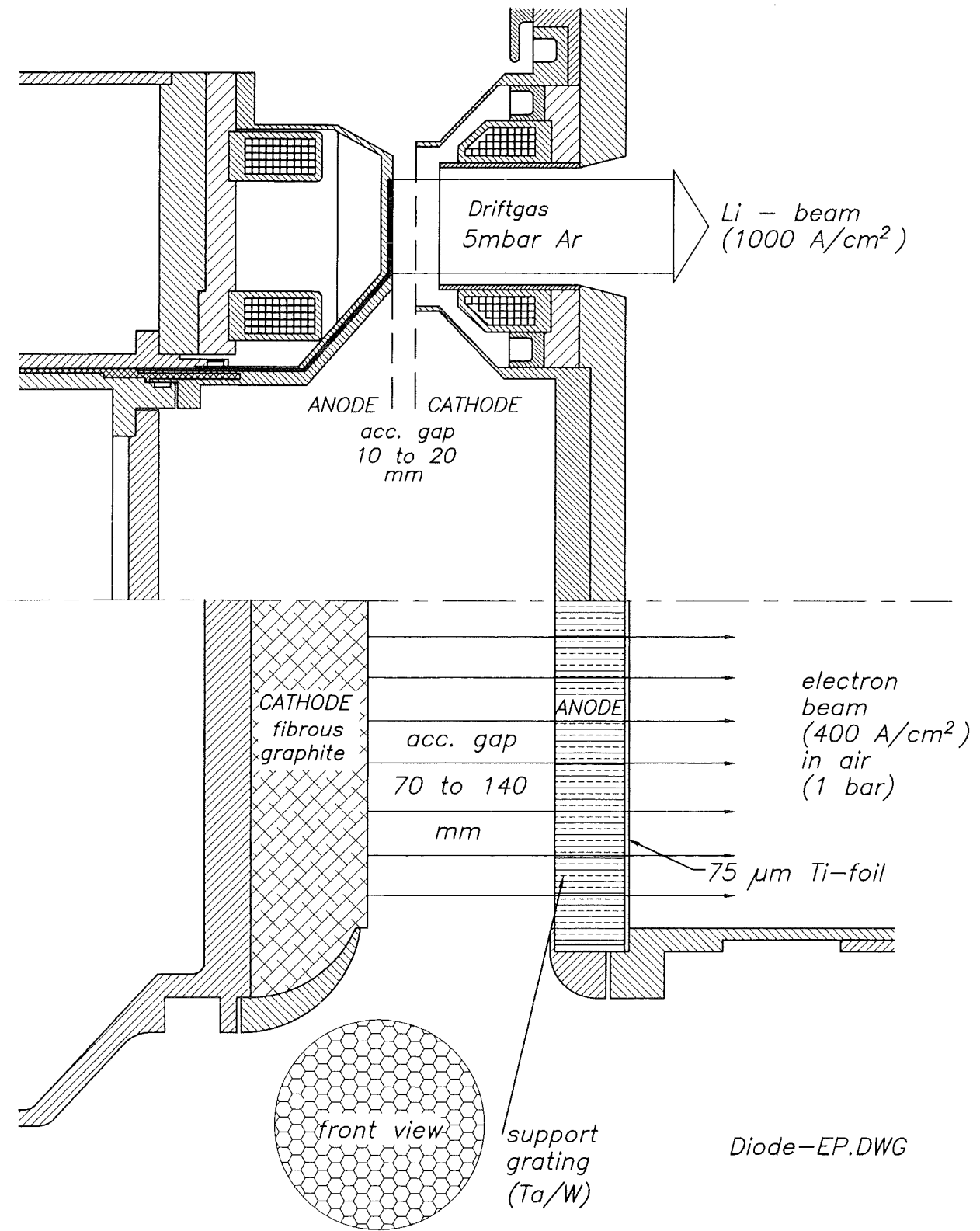


Fig.2: Schematic of an ion diode (upper half) and an electron diode (lower half) foreseen for the HELIA accelerator

into the drift section - requiring for beam propagation an Argon pressure of 5 mbar - through a 1.5 μm thick Mylar foil. The field coils for the production of the electron insulating magnetic field of about 4 T are arranged as close as possible to the acceleration gap and to the beam. Based on the SABRE operation of a similar extractor diode the driver banks for these coils should be able to store 200 to 500 kJ at a voltage of 10 kV. The supply of the energy required for the production of the anode plasma is fed to the Lithium layer on the anode by low impedance striplines (e.g. 6 lines in parallel with 2Ω each) led inside of the stalk of the MITL and via the support chamber to an external driver. Adequate striplines were designed, fabricated and tested [8].

At least the anode and the drift foil of this diode must be replaced after each shot which requires the opening of the vacuum chamber. In addition rather complicated cleaning- and cryogenic techniques and / or in-situ deposition of the Lithium will be necessary to avoid the formation of hydrogen plasmas which can be at the origin of a parasitic load in these Lithium ion diodes [10]. These cleaning protocols are also under investigation [11]. They will be effective only if a vacuum down to the 10^{-7} mbar range in the diode area can be achieved. Therefore the achievable shot rate with an ion diode will be down to about one to two shots per day.

III.3 Parameters of an electron beam diode

In contrast to the annular anode of the ion diode described before, an electron diode (Fig.2, lower half) can emit from a full surface. Using the same extension- and transition elements as for the ion diode the electron current density could in principle be as low as 250 A/cm^2 for a maximum accelerator current of 400 kA. This electron current density can be achieved by field emission from a fibrous graphite cathode. The anode of this electron diode must be placed at a distance of about 15 cm from the cathode surface. The intention to use the electron beam for technological applications like material- or waste treatment requires a beam outlet window. Depending on the pressure of e.g. the gas or water to be irradiated the anode titanium foil has to be supported by a grating structure made from tantalum or tungsten which ideally should absorb no beam energy. The technology of such outlet windows developed for similar conditions at the GOL III facility in Novosibirsk is as follows. The windows consist e.g. for an outside pressure of 1 bar of 10 mm wide meshes formed by 0.2 mm thin titanium strips with a width of 30 mm. The maximum outlet window diameter achieved so far with this technology is 300 mm. This would reduce the acceleration gap of the HELIA electron diode to 10 cm and thereby the current density would increase to about 600 A/cm^2 . Similar outlet windows with a size of 200 by 200 mm were used for coupling the electron beam to the laser amplifier of the NIKE KrF Laser [9]. For this application windows with a size of 600 by 600 mm are under development. However, for the high energy electrons considered here the tolerable thickness of the foil should allow the construction of larger outlet windows.

Based on the experience using fibrous graphite cathodes and grating anodes on the GOL III facility they can be operated under these conditions for hundreds of shots without damage and without opening of the vacuum chamber. Therefore the achievable shot rate might be as high as 10 per day. This high shot rate also will help to achieve a fast progress with respect to the new technology of this type of accelerator.

During the start up phase of the accelerator the electron beam can be dumped on a graphite disc with a at least a range deep thickness of 10 cm. This would reduce the production of radiation and would also allow to use the graphite disc as a calorimeter if equipped with thermocouples.

IV. Description of the new Marx generator for HELIA

The existing KALIF Marx, foreseen so far also for the operation of HELIA, consists of 50 capacitors of 1 μF each which can store a total of 250 kJ when charged to 100 kV. The new Marx for HELIA can

store about 400 kJ in 36 capacitors of $2.2\mu\text{F}$, also when charged to 100 kV. The energy delivered by either Marx to the HELIA accelerator is first charging up the 4 intermediate store capacitors (total of 36 nF) and then transferred to the 12 pulse forming lines (total of 46 nF) by 4 laser triggered gas switches. The capacitance of 9 nF of each intermediate store capacitor was selected as a compromise to the existing KALIF Marx. A maximum of 161 kJ can be accumulated in the intermediate store at a voltage of 3 MV. With the new HELIA Marx the voltage at the intermediate store will reach 2.85 MV and hence the stored energy will be 146 kJ only. These energies around 150 kJ may not be sufficient to reach the specified diode performance. However with the new HELIA Marx an increase of the capacitance of each intermediate store to a value of e.g. 18 nF (which can be achieved by changing the diameter of the inner conductor of the intermediate store capacitors) would allow to store about 210 kJ at a voltage of 2.4 MV. This energy is certainly sufficient to achieve the energy of 120 kJ to be delivered by the extracted ion or electron beam.

The 36 capacitors of the HELIA Marx generator are arranged in 3 rows with the HV side of 6 pairs of capacitors placed face to face in each row with the trigger spark gaps arranged between them. This modular Marx design, used in numerous pulsed power machines at the SNL in Albuquerque, proved very high reliability and easy service [12]. This Marx generator with a total weight of 4.2 t must be supported by an oil filled tank with a footprint of 4 by 4 m minimum, 4.5 m tall. The height of 4.5 m of this tank is required by the height of the existing intermediate store tank.

The Marx generator was adapted to the HELIA needs and an order was given end of 1995 to the Ktech company, Albuquerque. The Marx will be delivered with all auxiliaries (namely HV charging units, trigger systems, crowbar switch) end of Sept. 1996. As we have no possibility to test the Marx at FZK it will be tested prior to its delivery in Aug. 1996 at the SNL in Albuquerque.

V. Planning and safety considerations for the different arrangements of KALIF and HELIA

The following arrangements of KALIF and HELIA were considered:

- KALIF and HELIA in hall I of building 630 with both generators using the same, existing KALIF Marx as energy supply (Fig.3). This was the reference arrangement for the budget and building permit requested 1994 as well as for the safety report established in 1995.
- KALIF and HELIA in hall I of building 630 but both generators are powered now by their own Marx generators (Fig.4). This solution is to be considered as an ideal one because both generators can be operated completely independent and with enough space available for equipment and diagnostics. This arrangement would not have required any change in the building permit or safety report but control, cabling and supply etc. must be adapted.
- KALIF and HELIA in the hall of building 423 requiring power supply by 2 independant Marx generators (Fig.5, shown is HELIA only). For this arrangement most of the planning - and safety issues have to be reconsidered. This will be started as soon as formal decisions are available. However, this approach might show the advantage that the KALIF operation could be continued for most of the time needed for HELIA installation.

VI. Review of the instrumentation

The routine operation of HELIA requires the measurement of about 70 signals:

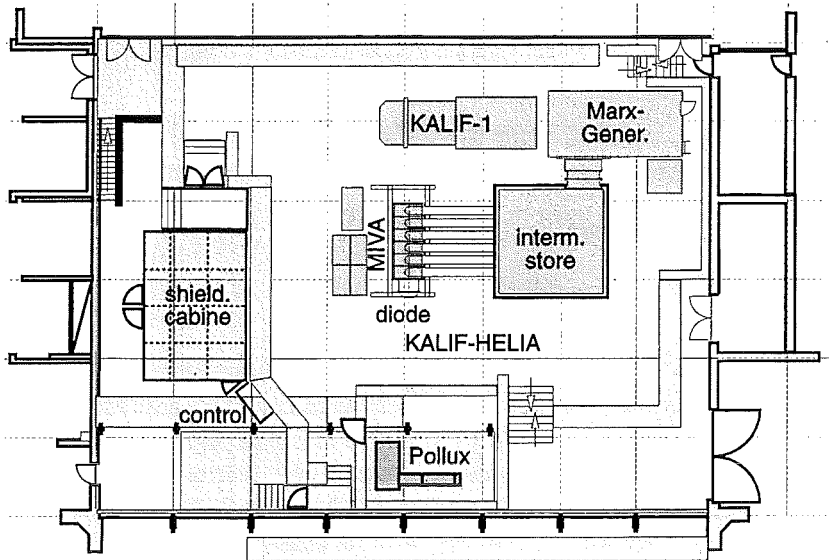


Fig. 3: HELIA and KALIF in Building 630 with common Marx generator

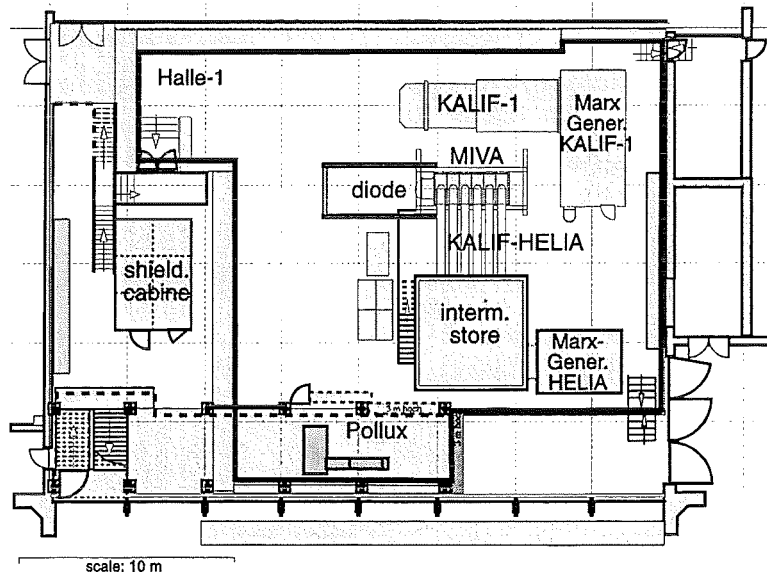


Fig. 4: HELIA and KALIF in Building 630 with separate Marx generator

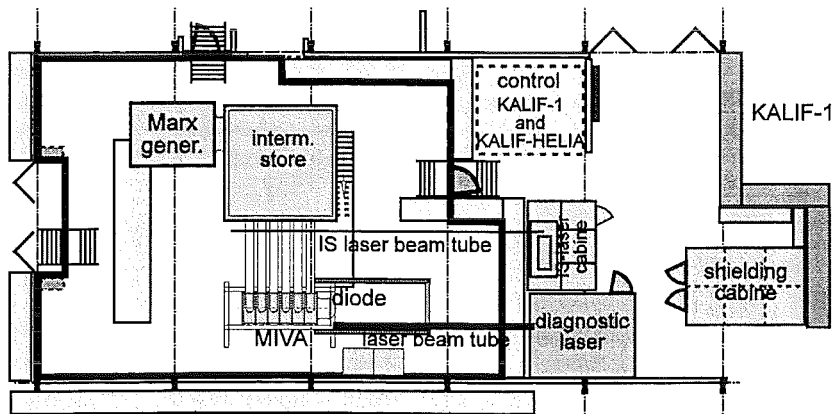


Fig. 5: HELIA in Building 423 KALIF with the original installation

- voltage and current at the interface of each of the 6 cavities (= 12 signals). These signals are needed for the control of the power supplied by each cavity to the MIVA as well as for monitoring the integrity of each interface.
- the voltages at the PFL section, after the pulse sharpening switch and at the output section of each of the 12 water transmission lines (=36 signals). These signals allow control of the proper operation of each line. With increasing experience the number of signals to be measured might be reduced to one per line or the monitoring of thresholds might become sufficient.
- the voltage at each of the 4 intermediate store capacitors (4 signals) for the control of the charge and discharge of each capacitor.
- the voltage delivered by the Marx generator and the trigger and loading units (about 5 signals).
- down the MIVA current measurements are needed after each adder section on anode and cathode side (ref. Fig.1, diagnostic spools no. 1 to 6). As long as azimuthal symmetry of the pulse is of no concern the measurement on one azimuthal position will be sufficient. However the possibility to measure on 4 azimuthal positions after each section is foreseen. These signals are necessary to observe the electron losses in each section (12 signals).
- The current delivered to the diode after the transition element (Fig.1) on 4 azimuthal positions (= 4 signals).

In this list are not mentioned the signals required for the measurement of the voltage at the MITL after the last cavity with the magnetic spectrometer MS located at extension spool no. 2 in Fig.1 (= 16 signals), for monitoring of the POS system (= 6 signals) and the field coils (= 4 signals). They are only required for the positive polarity option and when operating an ion diode.

Also not mentioned are signals which are needed for the control of the charging units, the auxiliary systems (e.g. water loops, reset loops, laser trigger loops, external plasma driver ...) and signals which are specific to an experiment.

During the start up phase of the accelerator the number of the signals to be measured must certainly be increased.

VII. Status and summary of the remaining tasks

Related to the doubts in the future use of the HELIA generator (e.g. polarity) and the building for its accomodation the design and fabrication of most components was slowed down. In early 1996 the status was as follows:

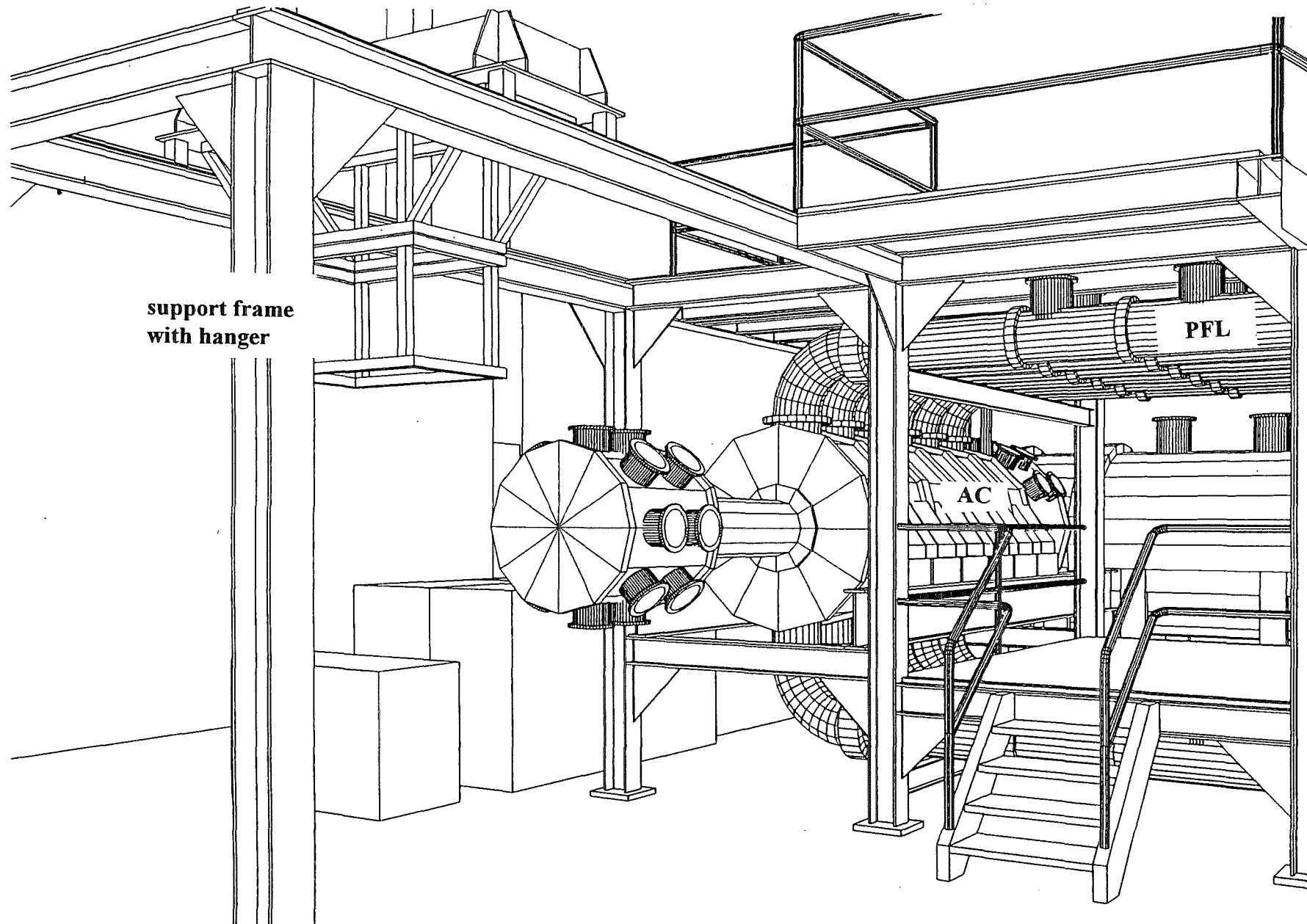
1. Auxiliary systems:

In 1995 the double wall storage tank for oil (200 m³) was fabricated, delivered to the building 630 and its components joint by welding inside of this building. Whether this tank can be disassembled and used in building 423 was not yet considered.

The support system (Fig.6) for the cavities, the PFL's etc. was designed, fabricated and delivered in due time after a test assembly was performed. The support components are stored now in the hall I of building 630. The support system also carries the movable hanger structure for the diode vacuum chamber (Fig.6). Delivery of the hanger as well as the components needed for the positioning and clamping of the cavities on the support rails is foreseen now for end of 1996.

For the assembly of the inner conductor a mounting rack is required which also should be available at the end of 1996.

The planning performed so far for the cabling, power supply, water and oil distribution systems in building 630 are obsolete now and have to be reconsidered for the new building.



support frame
with hanger

PFL

AC

Fig.6: Artists view of the high voltage end of the HELIA accelerator showing the adder cavities (AC), the pulse forming lines (PFL), the extension MITL, the diode vacuum vessel with the ports for the vacuum pumps and diagnostics and the support frames with the hanger

The control and operation system for HELIA (and KALIF as well) was based on computers allowing a high degree of automatization of the routine work. The studies done so far have to be revised and adapted to the new situation.

The reset circuits for the Vitrovac cores have to be designed. Monitors for the control of the magnetic state of the cores are needed. These cores have to be filled with oil under vacuum conditions which needs appropriate equipment.

The POS components (Fig.1) required for the suppression of the prepulse when operating an ion diode are available.

2. Marx tank and HELIA Marx generator:

The new HELIA Marx generator - described in more details in sect. III - was ordered in Nov. 1995 from the Ktech Corporation in Albuquerque, NM. This Marx with all auxiliaries will be delivered in Sept. 1996 after testing foreseen in Aug.1996 at SNL. The minimum dimensions of the oil tank required for this Marx are 4 x 4 x 4.5 m. This required footprint excludes the use of the existing stainless steel tank in the INR. In addition the height of the existing tank is too small and it has no entrance door for routine inspections of the Marx. This also would have required modifications of the stainless steel tank which are considered as too expensive. Specifications for the required new Marx tank were defined to get quotations from different companies.

3. Intermediate store tank:

The intermediate store tank (5 x 5 x 5 m) was delivered in due time and is stored now outside of building 630 in a protecting tent. The use of this tank in building 423 seems feasible, however the problem to get the tank into this building must be solved.

4. Power distribution elements between Marx, intermediate store and PFL's:

The following components - located inside the intermediate store tank and the Marx tank - need to be designed:

- the HV oil distribution lines from the Marx generator to the 4 intermediate store capacitors.
- the HV distribution lines from the output side of the 4 gas switches to the 12 pulse forming lines.
- the field grading rings for the gas switches.
- an emergency discharge of the intermediate store capacitors needed for the case the gas switches do not operate.

5. Laser triggered gas switches:

The operation of the 200 mJ KrF laser was tested: the specifications were fulfilled The optical path for the KrF laser light between the gas switches and the wall of the intermediate store tank should be designed next. The light distribution system between the laser screen room and this tank could not be considered because their details depend strongly on the arrangement of the laser which in turn is related to the building available.

6. Vacuum chambers and inner stalk of the MIVA / extension MITL:

The design of the vacuum chamber supporting the inner stalk (Fig.1) was completed for positive and negative polarity as well, quotations are on the way. The design of the inner stalk itself is actually being modified to allow its operation in both polarities. The diagnostic spools (fabricated in 1995 by PSI, delivery is expected early 1996) were also integrated into this redesign. The extension and

transition elements (inner and outer conductors of the coax lines) as well as the diode vacuum chamber are under design.

7. Diode design:

Preliminary design parameters for an ion diode as well as an electron diode are given in section III. A summary of the actual status is given below.

The development of an electron diode will not need an extensive R & D program and it allows a much higher shot rate of the accelerator. The more detailed design of an electron diode will be started as soon as decisions on the future use of HELIA were made.

For the ion diode investigated in 1995 only Lithium ions were considered as candidate species to be accelerated by HELIA. The status of the Lithium plasma source and the required external driver is described in [13]. The necessary magnetic insulation of the electrons in an ion diode also requires the development of a total of 4 pulsed coils for the generation of very high magnetic fields powered by 4 capacitor banks. Based on the experience with the KALIF proton diode the field coils as well as the capacitor banks with the corresponding connections need to be designed if HELIA will be operated in positive polarity. However due to the present situation the work on the coils, the capacitor banks and the Lithium source were stopped.

8. Instrumentation and data aquisition:

The magnetic spectrometer was designed in 1995 and was operated successfully up to voltages around 2 MV using the B_{\odot} diode as well as the B_{appl} diode on the KALIF accelerator [14]. About half of the monitors mentioned in section VI need to be designed and fabricated. The data aquisition system must be somewhat upgraded to allow the recording of about 70 signals.

9. Safety report and licensing:

The work done in 1995 was based on assumptions which are no longer valid. Most of the safety and licensing work has to be redone for the accomodation and operation of HELIA in building 423 instead of 630. The safety report must also be adapted to the production of an electron and an ion beam as well.

Acknowledgements

The authors would like to thank Prof. G. Keßler for his continous support of this project. In many discussions we got very valuable advice from M. Cuneo, J. Greenly and C. Mendel. We also want to acknowledge the excellent cooperation with H. Haas from the FZK purchase department.

References

- [1] W. Bauer et al., Annual Report 1994, Ed.: H. Bluhm, FZKA Bericht 5590, Karlsruhe, 1994, p.5
- [2] C. W. Mendel, Paper O-1-5, to be published in Proc. of the 11th Int. Conf. on High Power Particle Beams, Praque, Czech Republic, June 10-14, 1996
- [3] A. V. Gordeev, this report
- [4] I. Smith et al., KALIF-HELIA Review Meeting, Internal PSI report, Jan. 1991, unpublished
- [5] A. Grünhagen et al., Interner Bericht 51.03.01/15A, Juni 1995, unpublished

- [6] T. J. Renk et al., Proc. 10th Int. Conf. on High Power Particle Beams, Eds. D. Mosher and G. Cooperstein, May 25-30, 1993, Wash. DC, USA, Vol.I, p.51
- [7] H. Laqua et al., J. Appl. Phys. 77 (11), 1 June 1995
- [8] P. Hoppé et al., Paper P2-11, to be published in Proc. of the 10th IEEE Int. Pulsed Power Conf., Albuquerque, NM, USA, July 10-13, 1995
- [9] C. J. Pawley et al., Proc. of the 9th Int. Conf. on High Power Particle Beams, Wash. DC, USA, May 25-29, 1992, Vol.III, p.1912
- [10] T. A. Mehlhorn et al., Paper 18-6, to be published in Proc. of the 10th Int. Pulsed Power Conf., Albuquerque, NM, USA, July 10-13, 1995
- [11] M. Cuneo et al., Paper 18-5, to be published in Proc. of the 10th Int. Pulsed Power Conf., Albuquerque, NM, USA, July 10-13, 1995
- [12] J. M. Wilson, Proc. of the 6th IEEE Pulsed Power Conf., Arlington, Virginia, Eds. P. Turchi and B. Bernstein, p. 715
- [13] W. Vãth et al., this report
- [14] H. Bluhm et al., Paper P4-40, to be published in Proc. of the 11th Int. Conf. on High Power Particle Beams, Prague, Czech Republic, June 10-14,1996

Low-Intensity Laser-Triggering of Railgaps Applying Metal-Aerosol Switching-Gases

W. Frey - IEH, University of Karlsruhe

The simultaneous growth of spark channels between the rod-type electrodes reduces the impedance and increases the lifetime of railgaps, which operate as pulse-line switches of parallel-plate *Blumlein*-lines. In order to minimize the required trigger-laser energy for satisfactory multi-channeling, a high quantum-yield and low excitation energy seed-electron generation process like the photoemission of electrons must be applied.

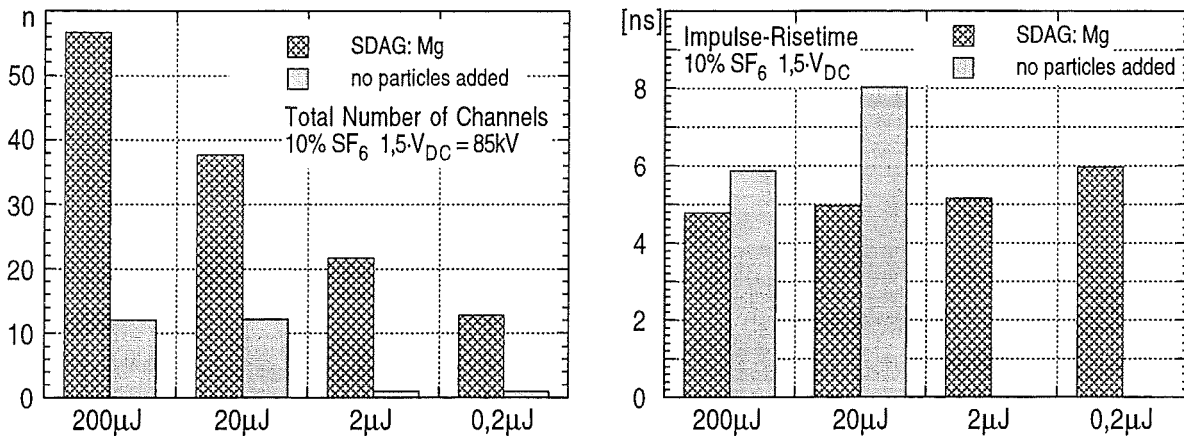


Fig.1 Total number of spark channels and impulse-risetime versus trigger-laser energy with and without the addition of Mg-aerosol particles to the Ar/SF₆ switching-gas.

Due to the photoemission of electrons from Mg-aerosol particles, which are produced by a spark discharge aerosol generator (SDAG) and then added to the Ar/SF₆ switching gas, multi-channeling can be observed with laser energies less than 200 nJ. In this case, the peak power of the N₂-laser beam is 60 W. Applying 200 μJ of unfocussed laser-radiation, the average number of spark channels increases from 12 to more than 50 channels along the 40 cm W/Cu-electrodes causing a low-risetime pulse-shape at the Blumlein generator's output, Fig. 1. If there are no particles added and if the beam energy is less than 20 μJ the triggering of the railgap fails.

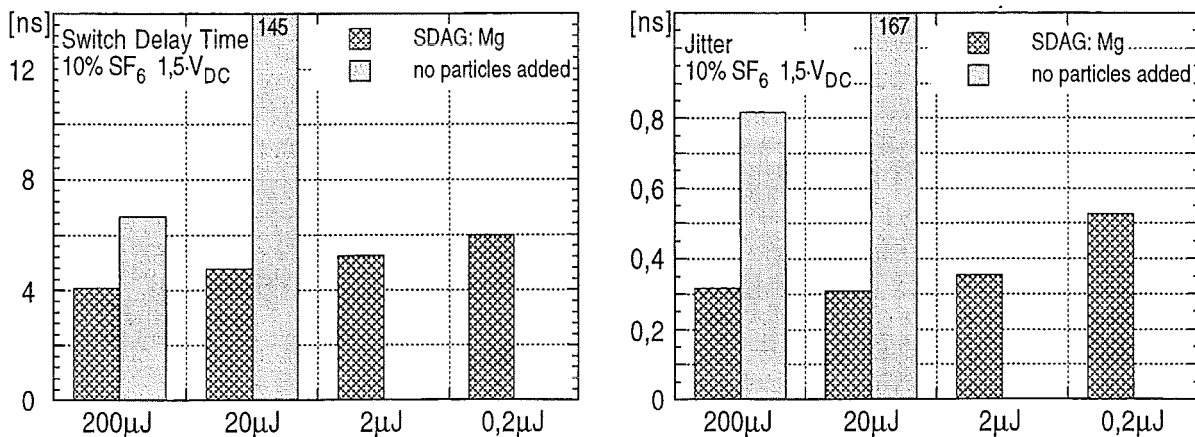


Fig.2 Delay time and jitter of the railgap versus trigger-laser energy with and without the addition of Mg-aerosol particles to the Ar/SF₆ switching-gas.

The emission of a seed-electron cloud from Mg-aerosol particles located in the irradiated gap volume shortens the avalanche phase during spark channel formation. This is the reason for the significant reduction of the switch delay time. The statistic behaviour of electron multiplication by impact ionization at the beginning of the avalanche growth starting from only one initial electron does not appear. Thus, the jitter of the switch is less than 350 ps, Fig. 2.

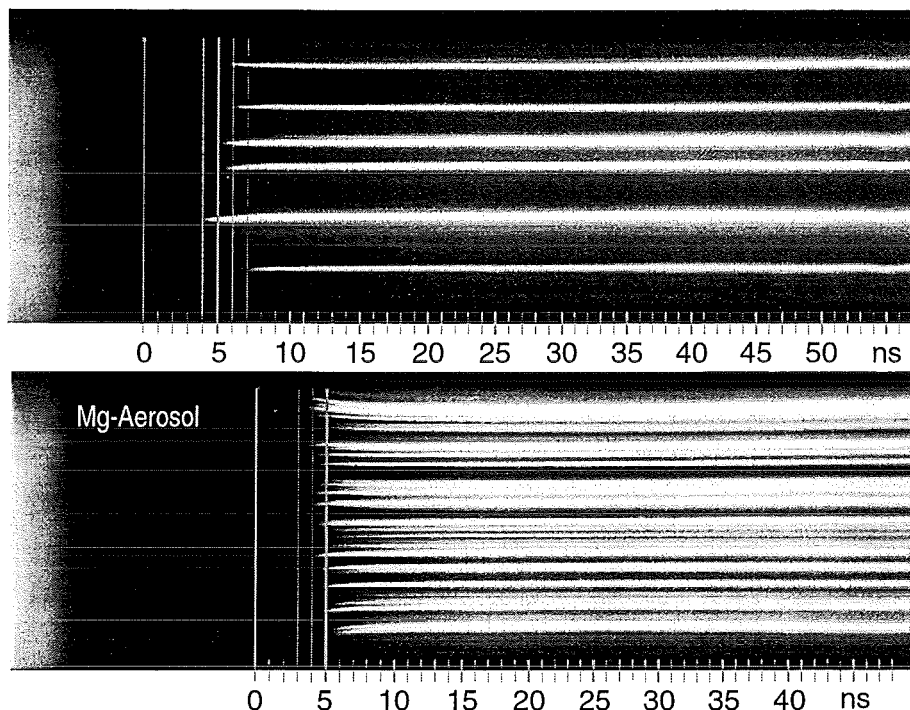


Fig.3 Streak photographs of the multichannel discharge with and without the addition of Mg-aerosol particles to the Ar/SF₆ switching-gas, Trigger voltage: $V_T = 1,5 \cdot V_{DC}$.

The streak photographs reveal the increase of the number of spark channels and the reduction of the closure-time jitter between the channels when adding Mg-particles.

Impulse breakdown experiments proved, that the presence of metal-aerosol particles does not reduce the self-breakdown voltage of the railgap, i.e. the upper trigger-voltage limit. The operating-voltage range is not affected by the addition of Mg-aerosol particles.

The "Metal-Aerosol Trigger-Methode" is well suitable to improve the switching performance of already existing laser-triggered facilities without demanding for changes of the switch design.

For further information please contact the author by e-mail: frey@ieh.etec.uni-karlsruhe.de

Fast Change of Magnetic Flux in Amorphous Strip-Wound Cores

S. König, - IEH, University of Karlsruhe

In order to investigate the fast magnetization behaviour of small amorphous softmagnetic strip-wound cores¹ a new test facility was built. Due to the voltage-time area of the core of 1,8 mVs the time for the reversal from the negative remanence to the positive saturation varies from 110 to 25 ns, when different values of the impulse amplitude are applied. Thus, the magnetic reversal velocity ranges from 30 to 132 T/ μ s. For setting the core to the negative or positive remanence a reset circuit was built.

The test equipment consists of a water-insulated coaxial pulse-forming generator, a gas-insulated core test-cavity and an electrolytic load, which absorbs the arriving output-pulse without almost any reflections. Capacitive voltage sensors and Rogowski-coils integrated in the outer conductor allow monitoring of the voltage and current at discrete points in the test facility, Fig. 1.

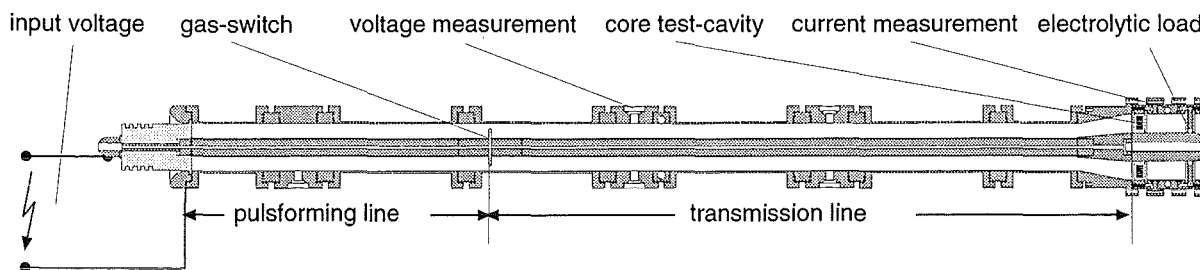


Fig. 1 Sectional drawing of coaxial test circuit.

Fig. 2 shows the charging voltage of the generator provided by a 140 kV marx-circuit. After self-breakdown of the gas-switch ($t = 0$ ns), an output-pulse (Fig. 3) propagates along the transmission line and passes the voltage monitor at 11 ns - 56 ns.

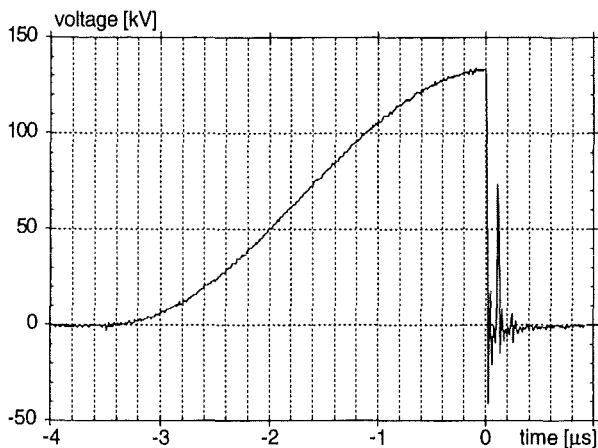


Fig. 2 Charging voltage of the puls-line.

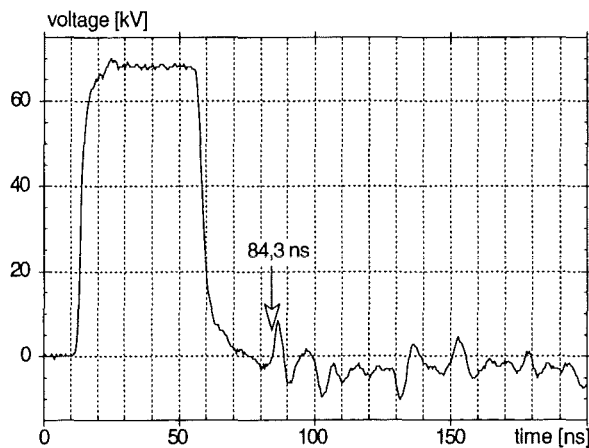


Fig. 3 Voltage on the transmission line when no core is inserted in the test-cavity.

¹ VITROVAC 7600Z, Vacuumschmelze Hanau, Germany.

The voltage curves measured in the transmission line demonstrate the well matched integration of the test-cavity into the pulse-forming arrangement. The traveling-wave propagates along the test-cavity without almost any reflections. Only a small voltage-peak at 84.3 ns could be detected. This is a reflection of the main-pulse at the empty core test-cavity.

If the core is located in the test-cavity and set to its positive remanence a pulse shape (Fig. 4) is measured in the transmission line which is comparable to the measurement without the core. The main-pulse passes the core without almost any reflections. Additionally, the current measured behind the core is plotted in Fig. 4.

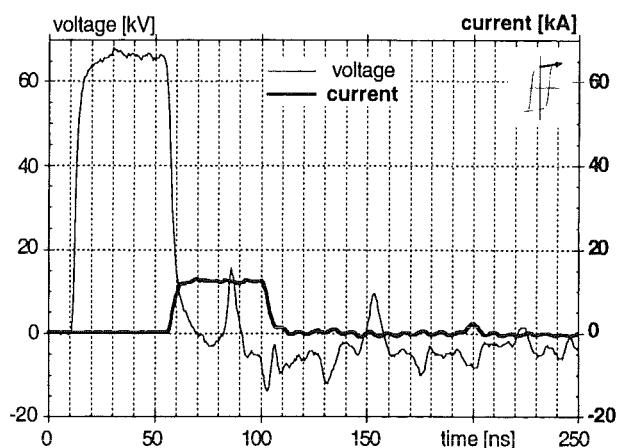


Fig. 4 Voltage and current measurement, core driven from positive remanence.

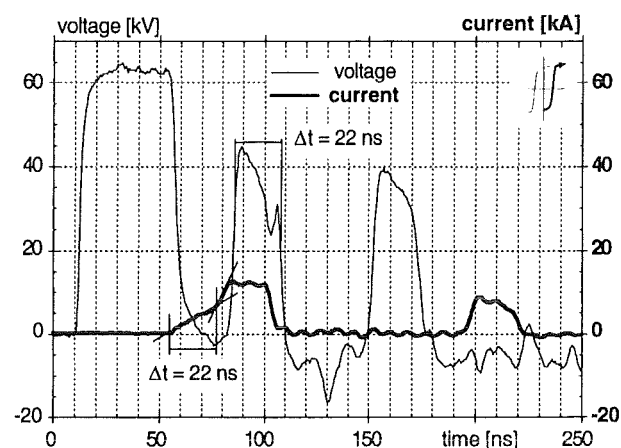


Fig. 5 Voltage and current measurement, core driven from negative remanence.

Setting the core to negative remanence the voltage and current measurements show the magnetization of the core, Fig. 5. During the magnetization the magnetic material of the core reacts on the arriving main-pulse with a high permeability. For the arriving main-pulse at the core test-cavity, this yields to a high surge impedance of the core and a high voltage reflection factor. After the magnetization is terminated the permeability quickly decreases to a very low value and the voltage reflection factor at the core test-cavity approaches to zero, providing the total transmission of the main-pulse.

The time to reach the saturation of the core can be taken either from the duration of the first reflected voltage pulse (it passes the voltage monitor at 86 ns - 108 ns, Fig. 5) or from the initial gradient of the current signal (55 ns - 77 ns). Both methods prove that the core is completely magnetized after 22 ns. Afterwards the current rises to its maximum level.

Because the main-pulse and its reflections do not superimpose at the presented voltage measurement position an easy discussion of the core saturation behaviour by travelling-wave analysis is possible. To give any final statement concerning the time-voltage area of the core or the hysteresis loop a measurement position in the vicinity of the core test-cavity is needed.

To get reliable data about the magnetizing behaviour the integration of additional measurement positions in front of and behind the core test-cavity will be done next.

For further information please contact the author by e-mail: koenig@ieh.etec.uni-karlsruhe.de

PULSED ELECTRON BEAM FACILITY GESA FOR SURFACE TREATMENT OF MATERIALS

G.Mueller¹, G.Schumacher¹, D. Strauss¹,

V.Engelko², A.Andreev², O.Komarov², N.Schegolichin²

¹Forschungszentrum Karlsruhe GmbH, INR, D-76021 Karlsruhe, Germany

²Efremov Institute of Electrophysical Apparatus, 189631 St.Petersburg, Russia

Abstract

The paper describes the new pulsed electron beam facility GESA developed for investigations in the field of pulsed heat treatment of materials and optimization of electron beam parameters. At present the electron beam has the following parameters: electron kinetic energy 50-150 keV; power density up to 2 MW/cm² and energy density up to 50 J/cm² at the target. The pulse duration is controllable with time increments of 1 μs in the range from 5 to 40 μs. The beam diameter at the target is 6÷10 cm.

1 INTRODUCTION

Pulsed heat treatment by intense electron beams is a modern and ecologically sound technique applicable in the field of material surface modification [1, 2]. For realization of the treatment procedure, electron beams capable of melting the surface layer of any material into depths of tens of μm at a rate of 10⁹ K/s are required. It is preferable to heat the treated layer without marked evaporation and boiling of the melted phase and also without significant energy loss due to thermal conductivity inside the bulk material. The conditions mentioned above can be satisfied by using a controlled volumetric heat source such as an intense electron beam of kinetic energy ≥ 100 keV. Calculations show that for an electron kinetic energy of 150 keV, the beam energy density and maximum pulse duration ensuring the heating of the treated layer without significant energy loss due to thermal conductivity lie in the range 20÷50 J/cm² and from microseconds to tens

of microseconds correspondingly. The microsecond range of the pulse duration is not only convenient for beam parameter control, but also essential to achieve sufficient energy deposition when the treatment chamber is separated from the electron injector by a drift channel which limits the max. achievable current [3]. On the base of these considerations the electron beam facility GESA for investigation of material surface modification was developed.

2 DESIGN OF THE FACILITY

The principle layout of the facility is shown in Fig.1. The main parts are the following: electron injector (EI); high voltage generator (HVG) with a pulse duration control unit; focusing magnetic coils (MC); drift channel (DC); chamber for samples treatment (SC); radiation protection (RP); controlling unit (CU).

The electron injector consists of a high voltage insulator, a multipoint explosive emission cathode, a controlling grid, and an anode, forming a triode arrange-

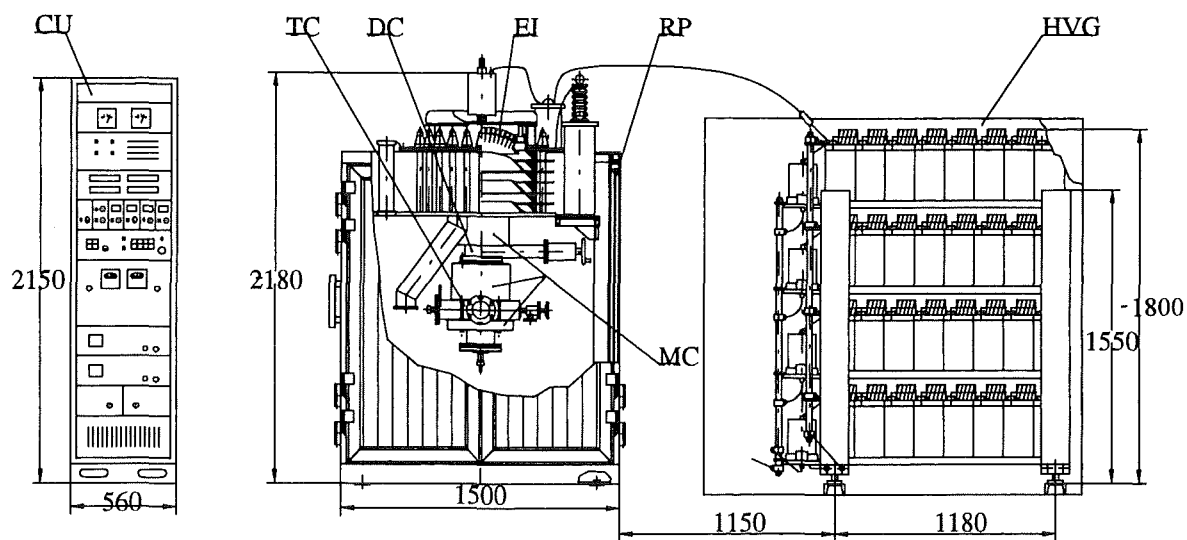


Fig. 1. Scheme of the GESA facility

ment. The controlling grid is connected with the grounded anode through the resistor R_g . This allows :

- 1) to control the current magnitude of the electron beam in a certain range without changing the kinetic energy of electrons at the outlet of the injector;
- 2) to create a sufficiently high electric field strength near the cathode surface at the beginning of the pulse, necessary for homogeneity of electron emission.

As a source of electrons a multipoint explosive emission cathode (MPC) with stabilised cathode plasma [4] is used. Such a cathode does not require heating, it operates under moderate vacuum conditions, and it is not poisoned by atmospheric gases or vapours from samples being treated. The area of the GESA cathode emissive surface is 700 cm^2 .

The high voltage generator (HVG) corresponds to the Marx scheme. It consists of four stages, which are artificial pulse forming lines, containing 8 cells with correcting RC networks. The duration of the flat part of the pulse is around $40 \mu\text{s}$, the amplitude on a matched load reaches 150 kV. The duration of the high-voltage pulse τ can be controlled by the pulse duration control unit with time increments of $1 \mu\text{s}$.

At the beginning of the pulse, the total voltage produced by HVG is applied to the cathode-grid gap, because the grid is grounded through the resistor. This ensures homogeneous excitation of the electron emission. After appearance of the electron current the total voltage is distributed among the cathode-grid and grid-anode gaps: $U_{cg}=U_0-U_{ga}$, $U_{ga}=IR_g(1-\alpha)$, where U_0 is the total voltage, I the electron current, R_g the grid resistors and $\alpha=0,8$ the grid transparency. In the grid-anode gap, electrons are accelerated to an energy corresponding to the total voltage applied to the injector. The electron beam is also magnetically compressed in this region.

The magnetic focusing system consisting of six coils provides formation, transport and variation of the beam diameter in the range of $6\div 10 \text{ cm}$.

The volume of the treatment chamber is separated from the volume of the injector by means of a gate valve. This allows to replace samples without distortion of the vacuum conditions in the injector and to use different treatment chambers. For transportation of the beam from the injector to the treatment chamber a drift channel is used, which is a stainless-steel tube with the diameter of 15 cm and a length of 50 cm. The residual gas pressure in the working volume is $10^{-5} \div 10^{-4} \text{ mbar}$.

3 BEAM PARAMETERS

Calculation of the electron beam parameters showed that the average value of the electron transverse energy E_{\perp} represents around 8% of the total kinetic energy E . Pulsations of the beam boundary in the drift channel are characterised by a wavelength of 4.0 cm and a magnitude of 2.5 mm for a beam radius of 5.0 cm. Nonuniformity of the current density distribution along the beam radius in the treatment chamber is about 20%. The angle distribution of the electrons is of Gaussian type with a mean angle of 16 degree.

The knowledge of the angle distribution of electrons $f(\theta)$ is necessary because of pulsed treatment conditions the temperature distribution inside the sample is sensitive to the beam energy deposition profile $E(z)$ affected by $f(\theta)$. This is illustrated by Fig.2 in which calculated results of $E(z)$ are shown with (curve B) and without (curve A) taking into account a homogeneous angle distribution of electrons.

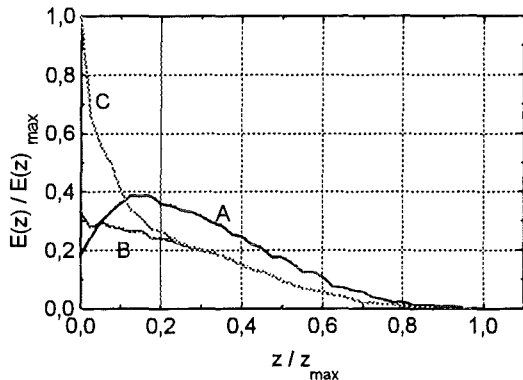


Fig. 2: Energy deposition vs. Depth

When calculating $E(z)$ it is necessary to take into account the part of electrons reflected by the treated specimen. In the presence of a magnetic field these electrons will reenter the specimen after reflection from the injector region. Since reflected electrons have a wide energy and angle spectrums, they increase significantly the energy deposition near the surface (curve C).

There are two sections limiting the beam current magnitude: the cathode-grid gap, and the drift channel. The limiting value of the cathode-grid current I_{cg} can be determined from the following equation

$$I_{cg} = k\alpha \frac{[U_0 - I_{cg}R_g(1-\alpha)]^{3/2}}{a^2(r_c/r_g)} \sin^2(\varphi/2) \quad (1)$$

where: $k=2.934 \cdot 10^{-5} \text{ A} \cdot \text{V}^{-3/2}$; α is the grid transparency; r_c and r_g are the cathode and grid curvature radii, respectively; a^2 is the Langmuir function for a spherical diode; $\varphi = \arctg(R_c/r_c)$, where R_c is the cathode radius. The limiting drift tube current I_{dc} can be estimated by the expression [3]

$$I_{dc} = 17 \cdot \frac{\gamma}{\gamma_{II}} \cdot \frac{(\gamma_{II}^{2/3} - 1)^{3/2}}{1 + 2 \ln(R_{chan}/R_{beam})} \quad (3)$$

where: $\gamma = (1 - v^2/c^2)^{-1/2}$, $\gamma_{II} = (1 - v_{II}^2/c^2)^{-1/2}$; R_{chan} and R_{beam} are the respective radii of the drift tube and the electron beam.

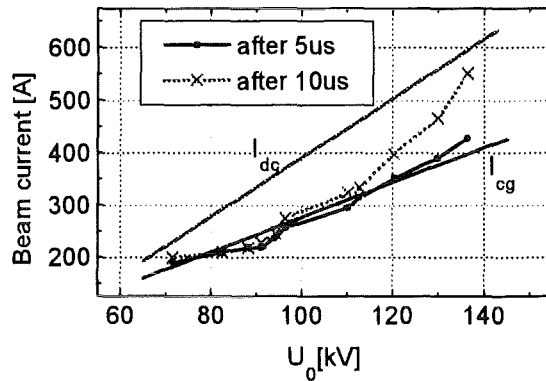


Fig. 3: Beam current vs. voltage for $R_g=575\Omega$

In Fig.3 the dependencies of I_{cg} , and I_{dc} on U_0 for the facility conditions realised presently are shown. Note that I_{cg} can be increased by means of changing of the corresponding gaps geometry. To increase the limiting current of the drift tube, neutralisation of the beam space charge is required.

Fig. 4 shows an example of the dependencies of the electron beam current on R_g . One can see that variation of R_g allows to change the electron beam current by a factor of two.

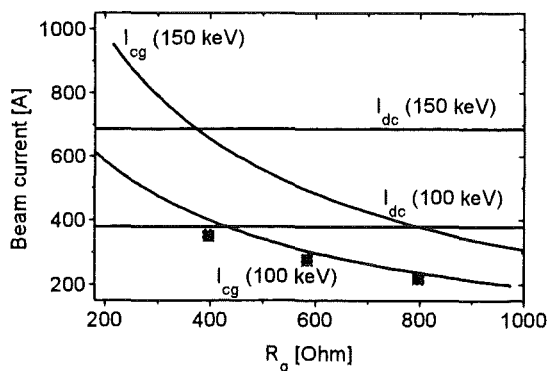


Fig. 4: Beam current vs. R_g

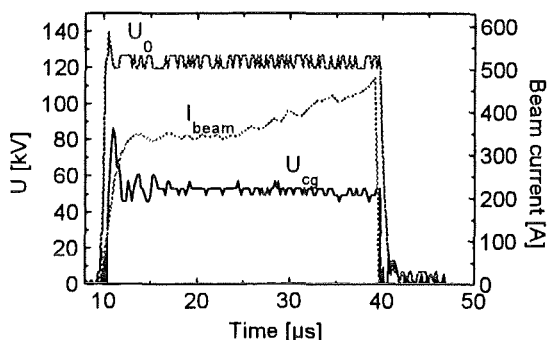


Fig.5. Typical oscillogrammes of the GESA facility operation

In Fig.5 typical oscillogrammes of the accelerating voltage U_0 , grid current U_{cg} and collector current I_{beam} are shown. One can see that the beam current magnitude reaches its quasi steady-state value 1-2 μs after the beginning of the pulse. During that time the formation of the cathode plasma emissive surface takes place. The increase of the beam current after 10 microseconds is caused by the influence of the gas desorbed from the controlling grid on cathode operation.

In Fig.2 the example of the measured electron beam current in the treatment chamber dependence on the total accelerating voltage U_0 is shown.

Some results of the measurement of the beam current dependence on the grid

5 REFERENCES

- [1] A.D.Pogrebnyak and D.I.Proskurovskii, *Phys. Stat. Sol. (a)*, 145, 9 (1994).
- [2] V.I.Engelko, A.V.Lazarenko, O.P.Pechersky, *Proc. Int. Conf. on High-Power Particle Beams*, edited by D. Mosher and G. Cooperstein (NTIS, Springfield, VA, 1992).
- [3] A.A.Ruchadze, L.S.Bogdankevich, S.E.Posinsky, V.G.Ruchlin, *Physics of high-current relativistic electron beams* (Atomizdat, Moscow, 1990) (in Russian).
- [4] M.A.Vasilevskii, I.M.Roife, V.I.Engelko, *Sov. Phys.-Tech. Phys.*, 26, 671 (1981).
- [5] G. Müller, G. Schumacher, D. Strauß, V. Engelko, A. Andreev and V. Kavaljov, *BEAMS 96*, in press

resistance are shown in Fig.3. One can see that under present conditions the possibility to change the beam current by means of R_g variation exist only in the range of $R_g > 400$ Ohm. At smaller R_g values the beam current is restricted by the limiting drift tube current.

The magnitudes of the current density, power density and energy density in the treatment chamber can be controlled in the range 1-12 A/cm², up to 2 MW/cm² and up to 50 J/cm² correspondingly. The radial current density distribution has a symmetrical shape. Its inhomogeneity is higher than calculated one (30% instead of 20%). The origin of the current density oscillations and its elevated inhomogeneity are so far not clear.

Some results of application of the GESA facility for heat treatment of materials is given in an accompanying paper [5].

4 CONCLUSION

The electron beam facility GESA was developed for investigations of material surface modification under pulsed intense electron beam treatment. The design of the facility allows to control all vital parameters of the electron beam (kinetic energy of electrons, beam current, pulse duration).

Presently the electron beam has the following parameters: electron kinetic energy 50-150 keV, power density on the sample up to 2 MW/cm², energy density up to 50 J/cm². The pulse duration is controllable in the range of 5-40 μs in steps of 1 μs .

Application of the GESA facility for pulsed heat treatment of materials is in progress.

III Production and focusing of high power light ion beams (Diode Physics)

Ion diode diagnostics to resolve beam quality issues

H. Bluhm, A. Arzhannikov, L. Buth, P. Hoppé, V. Licht, A. Matveenko, D. Rusch, O. Stoltz, J. Singer, C. Singleton, A. Tauschwitz, W. Väh, S. Yoo*

*Forschungszentrum Karlsruhe
Institut für Neutronenphysik und Reaktortechnik
Postfach 3640, 76021 Karlsruhe*

**Permanent address: Institute of Nuclear Physics, Novosibirsk, 630090*

Abstract

Various diagnostic methods and instruments are under development at FZK to measure important physical quantities in the accelerating gap of high power ion diodes on KALIF with high spatial and temporal resolution. These methods include optical spectroscopy, refractive index measurements, dispersion interferometry, and high resolution ion energy analysis. The paper describes the set-up of these diagnostics and first results obtained for applied and selfmagnetically insulated diodes.

Introduction

Beam quality is the main issue of intense light ion beam production and focusing. Beam quality does not only comprise divergence but also ion energy spread, purity, uniformity, ion canonical angular momentum, etc. Beam quality is tightly connected to diode operational stability. Most of the effects that influence beam quality have their origin inside the diode gap. Although substantial progress has been made, both theoretically and experimentally, to understand the sources of beam imperfections, many important details remain unknown. Especially, the dynamics of the anode plasma and the electron sheath in high power diodes is not well understood.

Optical diagnostics - spectroscopic, interferometric, deflection- can yield detailed information on the electromagnetic fields and particle distributions in the electrode plasmas as well as in the diode gap. Therefore, we have begun to set-up a diagnostic effort to measure some of the main quantities with high spatial and temporal resolution. This includes ion spectroscopy, dispersive interferometry, refractive index gradient measurements, and high resolution ion energy analysis. In this paper we report on the status of these developments and present first results.

Ion spectroscopy

The set-up used for spectroscopic measurements in the gap of the KALIF B_{appl} -diode is shown in fig. 1. The characteristics of the diode have been described elsewhere [1]. The spectroscopic system consists of two Cserny-Turner spectrographs with 1 and 0.5 m focal length respectively. An intensified gated diode array of 750 active elements is used as the detector at the exit of the 0.5 m system. A similar detector system or an array of 15 photomultipliers can be used with the 1 m system. The photomultipliers are coupled to the spectrograph via a quartz fiber bundle consisting of 15 columns with 40 fibers each. A spatial resolution of less than 0.5 mm and a temporal resolution of 10 ns for the diode array and of 2 ns for the photomultiplier array can thus be realized. A spectral resolution of 0.5 Å was obtained.

Since we tried to exploit the natural contaminants of our anode plasma, the major hindrance of the measurements became intensity. The intensity of most lines was insufficient to extend the measurements far into the gap. It turned out that doping of the anode surface either locally or globally changes the diode characteristics too much and therefore is of limited value.

Thus, mainly carbon (C I 2479 Å, C II 6578 Å, C III 2297 Å, C III 4647 Å, C IV 5802 Å) and hydrogen (H_{α} , H_{β}) lines are used to determine n_i , n_e , T_e , as well as the particle flux, the B-field, and the ion trajectory deflection.

The general structure of the C II - C IV line intensity evolution in the anode plasma is presented in fig. 2. Here the line of sight was 0.25 mm distant from the solid anode. The spatial resolution was 0.5 mm. Synchronously to H_{α} , the C II line is created during the initial phase of the sliding discharge across the Pd covered TiH film on the anode surface[2]. It is assumed that the origin of these carbon ions are surface contaminants released during the early heating of the metal

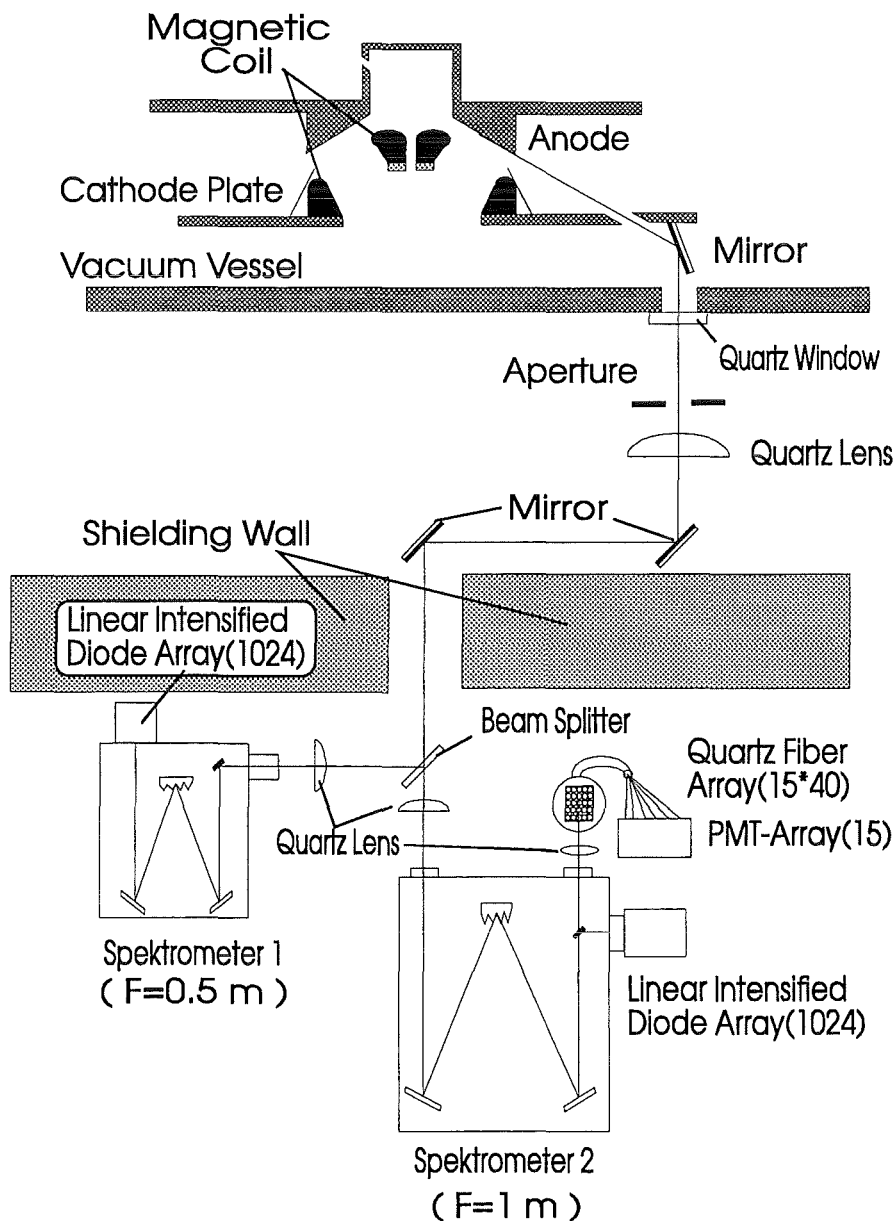


Fig.1 Schematic of set-up for spectroscopic measurements in the accelerating gap of the KALIF B_{app} -ion diode

films. After the beginning of ion current extraction the return current continues to heat the plasma and a transition from C II to CIV occurs. At the same time, the H_{α} line disappears, indicating complete ionization of the plasma. Since we observe a more rapid decay in space of the line intensities in the diode gap than expected from a space charge limited current density distribution, we must conclude that the electric field is shielded by a hydrogen plasma in front of the carbon plasma.

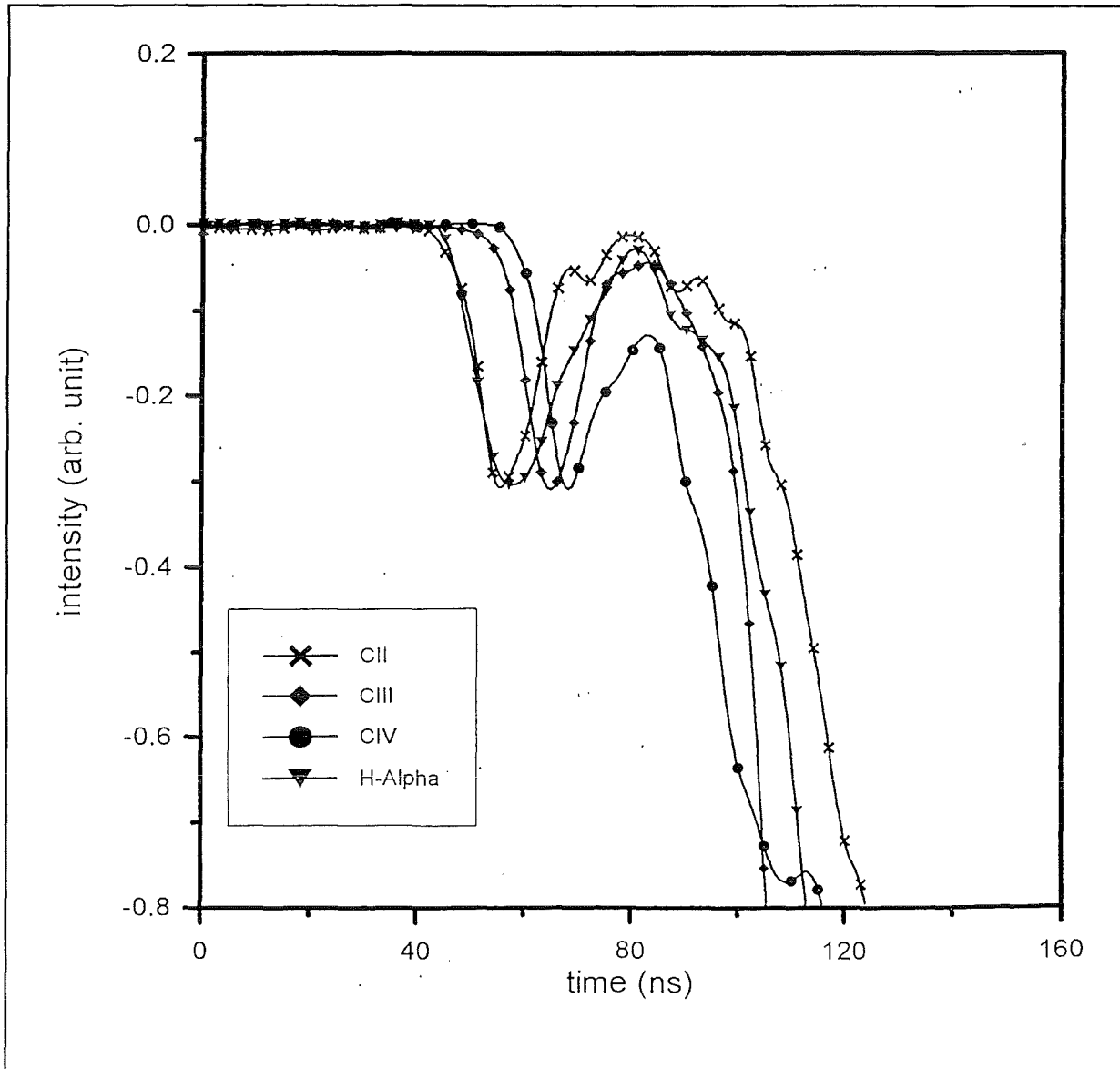


Fig.2 Time evolution of the emission intensity of C II, C III, C IV, and H_{α} lines

Shifting the line of sight of the spectrometer into the gap shows that the visible component of the anode plasma does not expand more than 1 mm into the gap during the whole pulse. This is confirmed by the refractive index diagnostics (see below).

Nonlinear dispersion interferometer

The main purpose of the dispersion interferometer is to measure the electron density in the ion diode acceleration gap. For a mean cord length of 3 cm through the ring shaped ion emitting

area the line density ($n \cdot l$) is expected to be around 10^{14} cm^{-2} . This line density will cause a very small fringe shift of less than 1/100 wavelength and therefore a very sensitive interferometer is needed. Besides sensitivity stability and simplicity are desirable in the hostile environment of the accelerator. The dispersion interferometer first proposed in [3] comes close to these requirements.

An important property of the dispersion interferometer is that its two probe beams use the same optical path through the object which makes it rather insensitive to mechanical vibrations of its optical elements. Thus additional measures for stabilization are unnecessary. The general set-up of the interferometer is shown in fig. 3. Both the fundamental wave of a Nd:YAG laser and its

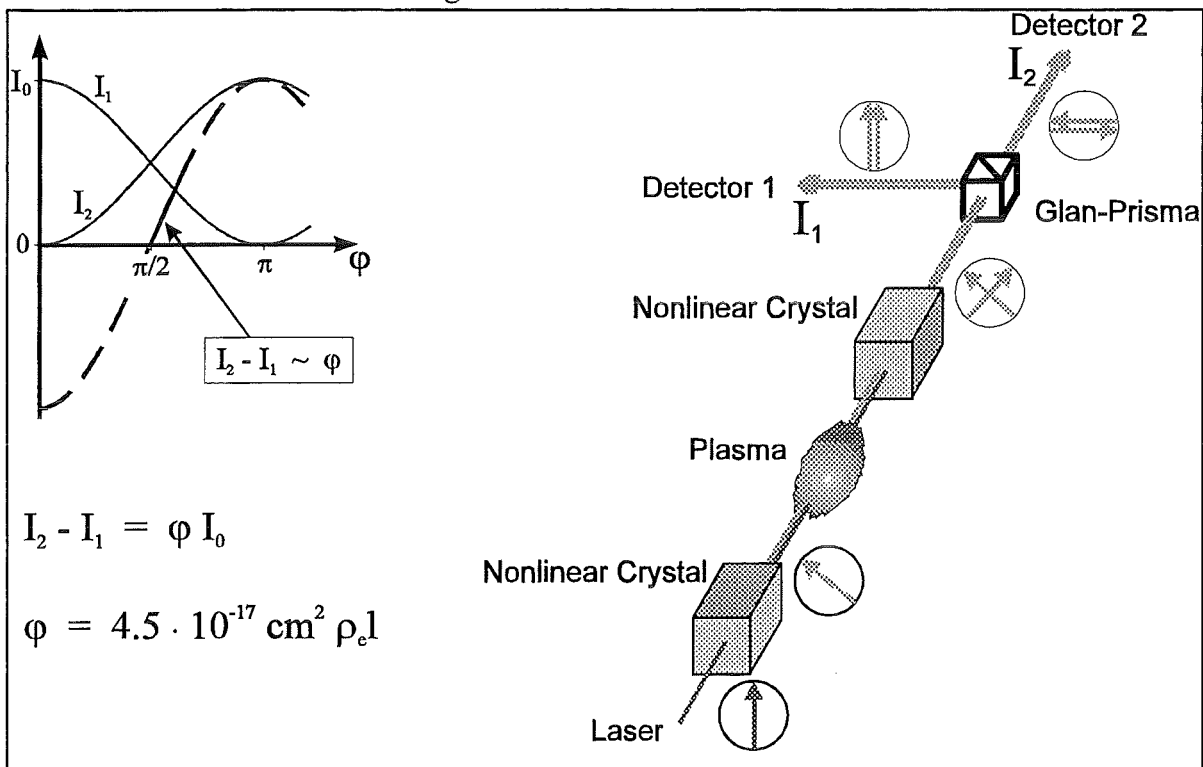


Fig.3 Set-up of the nonlinear dispersion interferometer system

second harmonic are transmitted through the plasma. After exiting from the plasma the infrared beam is frequency doubled a second time. Both green beams are polarized perpendicular to each other. Their relative phase shift is determined by the wavelength dependence of the optical pathlength. For a plasma this is proportional to the pathintegral of the electron density with a high degree of accuracy if the wavelengths are far away from any ionic or atomic resonances. A Glan polarizer whose transmission axis is fixed at 45° with respect to both beam polarizations splits the beams with equal intensities into both polarization directions. Thus the split beams can interfere at the position of the two detectors. However, the relative phase shift in both interference patterns is π . Thus subtracting the detector signals from each other can lead to complete cancelation of the difference signal. Using a Soleil-Babinet compensator in the beam path this phase shift can be adjusted before the experiment, i.e., without the object.

On the other hand there are special requirements to the laser system of the interferometer. The intensity must be high enough for frequency conversion, and single frequency operation is needed to get a smooth intensity profile on a ns time scale.

At present, a seeded, pulsed Nd:YAG laser with a pulsewidth of 10 ns and a pulse energy of about 100 mJ is used. As the short pulses give no complete measurement of the KALIF shot, the interference image must be compared to a reference measurement similar to a holographic

method. This limits the sensitivity to about 30 mrad corresponding to $d(r_e l) \sim 7 \times 10^{14} \text{ cm}^{-2}$ because of small drifts from pulse to pulse.

Presently an alternative single frequency cw laser system is under consideration. To achieve an intensity sufficient for frequency conversion the laser beam must be transmitted through several amplifiers. With the resulting quasistationary beam the complete KALIF pulse can be analyzed in one shot, and the sensitivity of the dispersion interferometer can be improved by one to two orders of magnitude.

First results with the short pulse laser system in the immediate neighbourhood of the anode showed that late in the KALIF pulse an electron density of more than 10^{16} cm^{-3} is reached.

RING-diagnostic

A Refractive INdex Gradient (RING)-diagnostic may be used to measure the gradient of electron and neutral densities in a plasma. It has been used previously by other authors [4,5]. It is based on the deflection of a laser beam transmitted through a plasma with density gradients. The angle of deflection is given by the following equation

$$\delta\phi = \frac{1}{\tilde{n}_0} \cdot \left| \int ds \cdot \nabla_{\perp} \tilde{n} \right|,$$

where $\tilde{n} = 1 + K_i n_i$ and \tilde{n}_0 are the perturbed and unperturbed indexes of refraction respectively. The integration has to be carried out along the laser beam path. The K_i are constants representing the different particle species. Their values range from $0.5 \cdot 10^{-23}$ to $50 \cdot 10^{-23} \text{ cm}^3$.

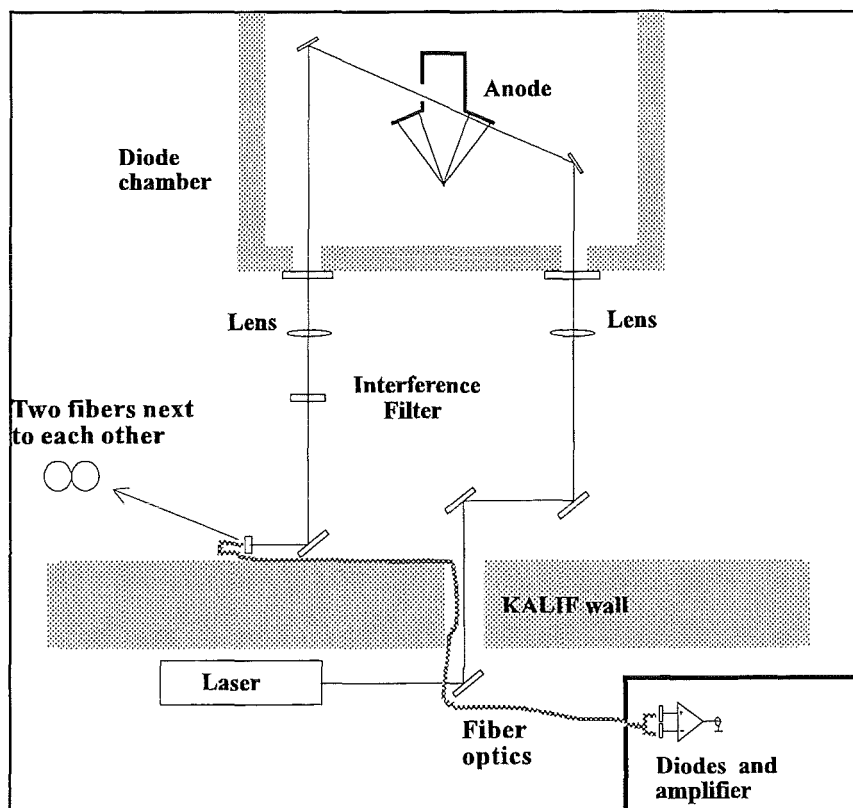


Fig. 4 Set-up of the RING-diagnostic on KALIF

In fig.4 the scheme of the diagnostic set-up on KALIF is depicted. After passing through the plasma the cw laser beam is focused onto two glass fibres positioned next to each other. The use

of fibres is the main difference compared to previous set-ups where bi-cell detectors have been applied [4,5]. The advantage of our arrangement is that much faster photodiodes can be used and the time resolution can almost be increased 10 times compared to bi-cell detectors. However, the sensitivity is somewhat reduced. We expect temporal and spatial resolutions of $\tau \approx 2$ ns and $\delta x \approx 0.2$ mm. The sensitivity of our instrument is $\nabla n_{\text{min}} \approx 3 \cdot 10^{16} \text{ cm}^{-3}$.

Fig. 5 shows the time evolution of the electron density gradient at different distances from the anode. It is realized that the electron density gradient diminishes by more than one order of magnitude on a scale length of less than 0.5 mm. Also, as expected the maximum gradient steadily decreases if the line of observation is shifted away from the anode. However, the plasma front does not reach farther than 1 mm into the gap before the end of the pulse.

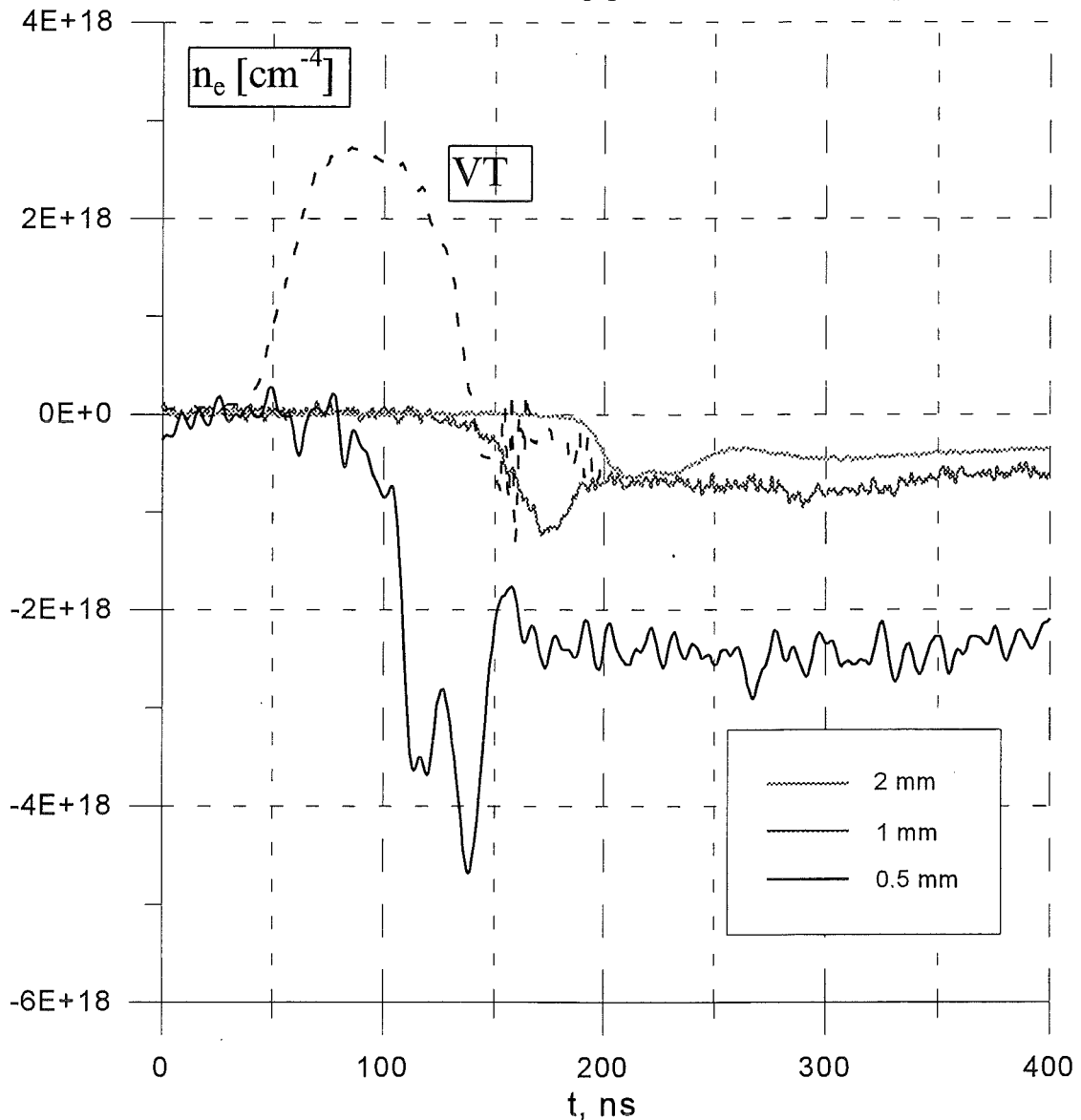


Fig.5 Electron density gradient at different lines of sight, 0.5, 1, and 2 mm from the anode. VT is the generator voltage

Phase shift of a laser beam passing through a cloud of relativistic electrons

Applying interferometric and refractive index diagnostics to high power ion diodes containing relativistic electron clouds requires a careful consideration of the effect of these electrons on the measurements. We assume that the incident laser beam propagates parallel to the magnetic field lines which are considered to be so strong that the electrons move along these lines too.

The fringe shift of the wave is proportional to the path integral of the refractive index and in case of a single energy group of electrons may be written in the following form $\delta\Phi(\gamma) = F(\gamma)\delta\Phi_0$, where $\delta\Phi_0$ is the fringe shift for the case of nonrelativistic electrons. $F(\gamma)$ is an additional coefficient that depends on the relativistic factor γ of the electrons. $F(\gamma) = \gamma(1+\beta)$ for a movement of the electrons into the direction of wave propagation (positive direction) and $F(\gamma) = 1/\gamma(1+\beta)$ for the opposite movement (negative direction). For the case of an ion diode the relativistic factor has to be calculated in accordance with the electrical potential at the position under consideration: $\gamma = 1 + e(\varphi - \varphi_c) / m c^2$.

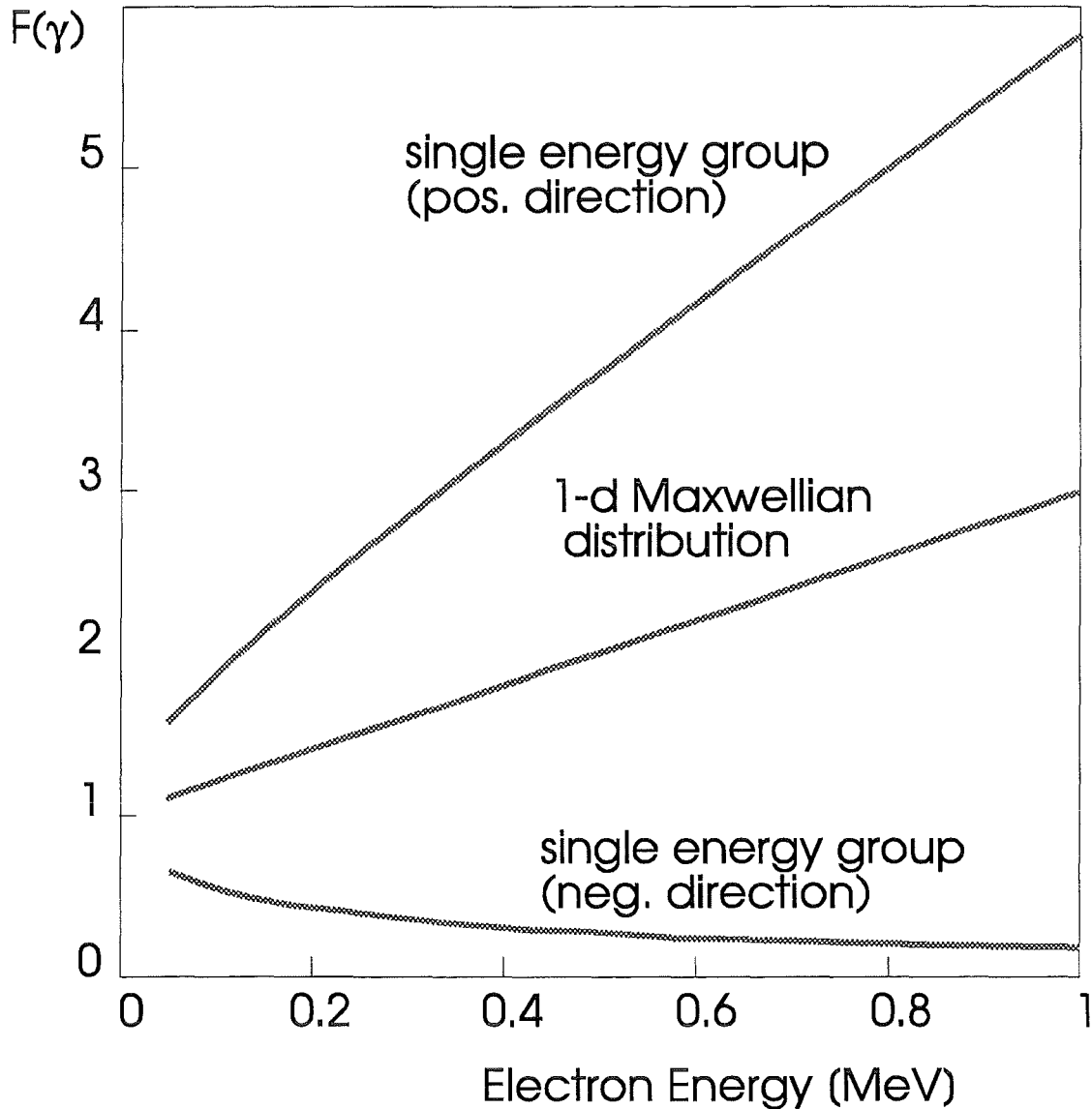


Fig. 6 $F(\gamma)$, the relativistic factor describing the phase shift multiplier for different electron energy distributions

The results show that in the presence of relativistic electrons the refractive index and the resulting fringe shift do not only depend on the electron density but also on their relative movement with respect to the laser beam path.

Magnetic Energy Analyzer

A high resolution magnetic energy analyzer has been built to measure the ion energy distribution. It consists of a circular permanent magnet system with a diameter of 0.22 m and a field strength of 0.76 T. An array of 16 1 mm^2 pin diodes is used to register the ion energy as a function of time. The system is shown in fig. 7. A 3000 \AA thick gold layer deposited on a 1.5 \mu m mylar foil positioned at the beam focus is used to Rutherford scatter the protons through the collimator in front of the magnet. The energy resolution of the system is better than 30 keV for the ion energy range below 2 MeV. The energy of the pin-diode channels was calibrated on a Van De Graaff generator.

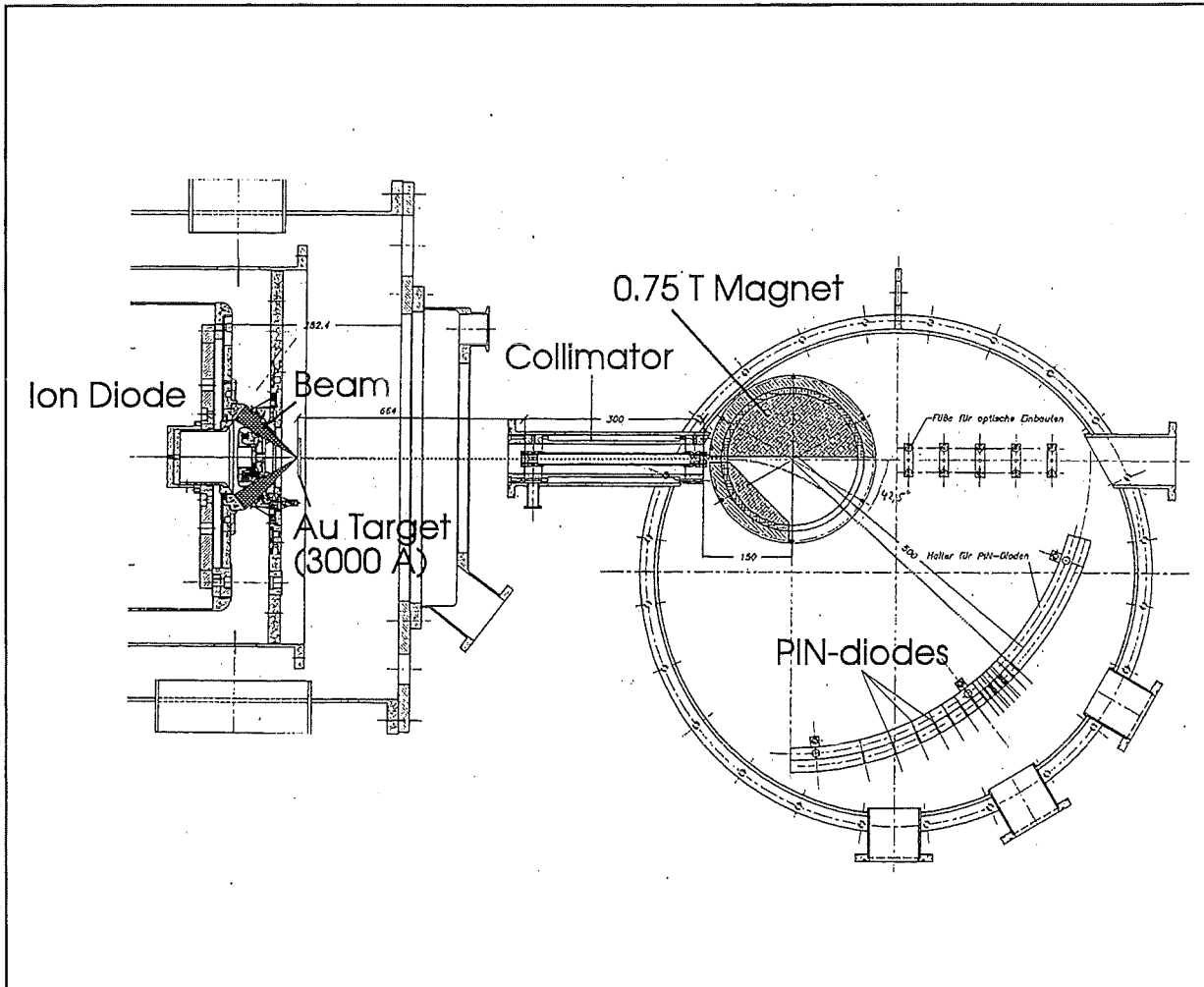


Fig. 7 Geometry of the magnetic energy analyzer on KALIF

Results are shown in fig. 8 and 9 for the B_0 and the B_{appl} diode respectively. Although certain differences appear between the electrically measured voltage pulse shape and the ion energy behaviour, there is no clear indication of ion energies greater than the applied voltage. However the width of the energy distribution is typically between 10 and 20% of the mean energy, i.e. between 100 and 200 keV. This is typical of energy spreads induced by electromagnetic instabilities as observed in 3-D simulations. It is somewhat larger for the selfmagnetically insulated diode. Systematic errors in the derived voltage curves become visible during the rising part of the

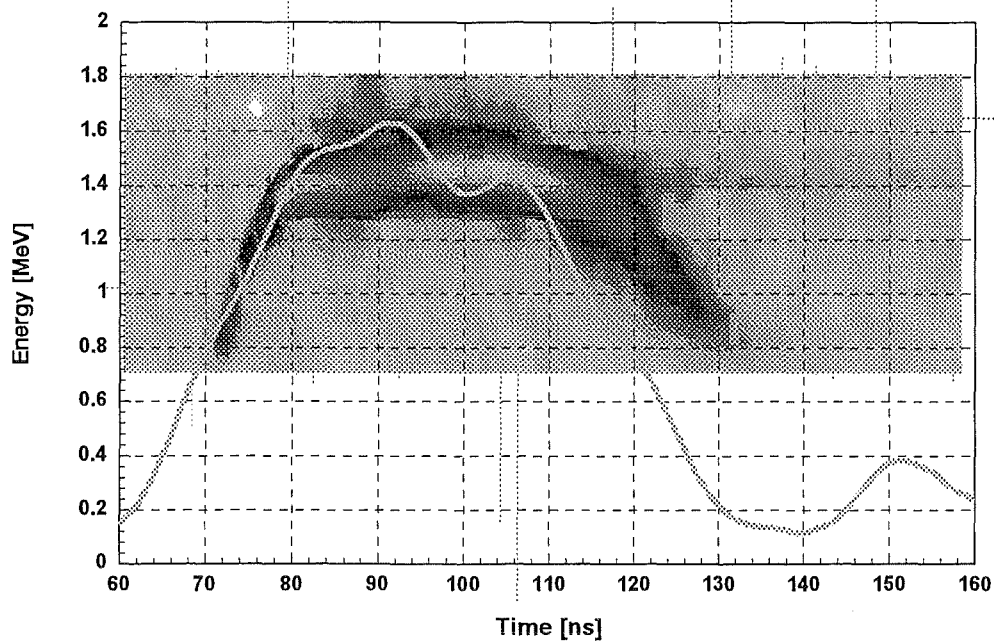


Fig. 8 Ion energy distribution measured with the magnetic energy analyzer (contour plot) compared to the voltage curve derived from the electrical (capacitive) monitor. The result shown was obtained for selfmagnetically insulated B_{σ} -diode

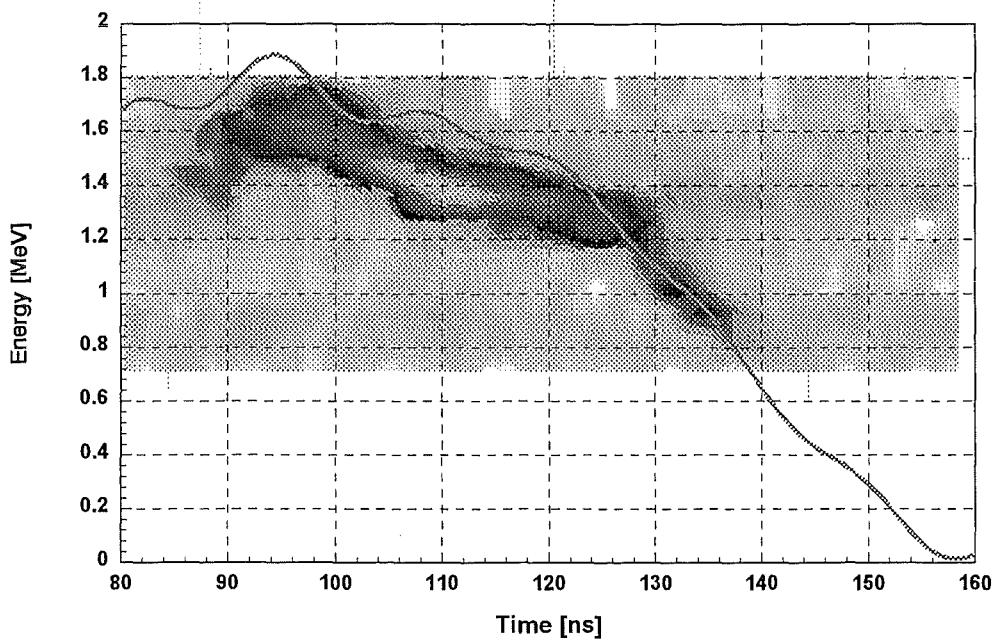


Fig.9 Same as fig. 8, but result obtained for the B_{app} -diode.

curve in case of the B_{appl} diode and during the falling part in case of the B_{θ} diode. These are probably due to the LdI/dt correction which, can be erroneous especially in the case of our B_{appl} diode because of the use of plasma opening switches in the power feed.

References

1. H.J. Bluhm, P. Hoppé, H. Laqua, D. Rusch, Proc. IEEE, Vol. 80, NO. 6, (1992), p. 995
2. H. Laqua, H. Bluhm, L. Buth, P. Hoppé, J. Appl. Phys. 77, (1995), p. 5545
3. P.A. Bagryanskii, V.P. Drachev, Yu. I. Krasnikov, Sov. J. Plasma Phys. 18(2), (1992), p.138
4. M. E. Cuneo, T.R.Lockner, G.C.Tisone, IEEE Trans. on Plasma Sci. 19, (1991), p. 800
5. B. A. Knyazev, J.B. Greenly, D.A. Hammer, E.G. Krastelev, and M.Cuneo, paper p4-10, Beams 96, Prague, June 10-14, 1996

Post-focusing experiments performed on the KALIF accelerator using the B_{appl} diode

P. Hoppé, Y. Nakagawa¹, W. Bauer, H. Bluhm, L. Buth, H. Massier, D. Rusch, O. Stoltz,
A. Tauschwitz², W. Väth - INR / FZK
H. Guth, A. Hellmann - IAI / FZK

Abstract

In 1995 experiments on the KALIF accelerator were prepared with the objective to study the influence of magnetic fields - induced by either the extracted proton beam itself or by an externally applied magnetic field - on the focusing properties of the B_{appl} diode. In a first set of experiments with a subdivided ion beam drift section the generation of net currents as well as their influence on the focusing properties was investigated. Net currents were found always delayed by typically 10 ns with respect to the ion current onset, reaching final values which strongly depend on the gas pressure in the second drift space. With vacuum in this second drift space the net current reached up to 50% of the ion current. The observed difference in the time histories of various net current monitors might be related to a radial dependence of the net current densities. The influence of these net currents on the focusing properties of the beam were investigated using, as the main diagnostic tool, a boron scattering foil in the focal plane and an ion sensitive film in a pin hole camera. In contrast to our expectations no influence of the gas pressure in the second drift space on the impact distribution patterns on the ion sensitive film was observed. In future experiments these results will be verified and the influence of an externally generated compression field on beam focusing will be investigated.

I. Introduction

On the KALIF accelerator a proton power density of up to 1 TW/cm^2 was reached in the focal plane of the B_{appl} diode [1]. Considering the emission of an annular proton beam (limited by the angles α_1 and α_2) from a spherical anode surface a beam of constant brightness B will produce an even higher power density $P = \pi B (\sin^2 \alpha_1 - \sin^2 \alpha_2)$ if the incident angle $\alpha = (\alpha_2 - \alpha_1)$ to the focal plane can be increased. Such increase of the incident angle can in principle be achieved by either magnetic fields induced by the beam itself (self-field focusing scheme) or by magnetic fields produced by external field coils placed close to the beam (external-field focusing scheme).

The external field focusing scheme suggested for the B_{appl} proton diode on KALIF [2] consisted of an additional single turn coil that was placed in the vicinity of the focal plane. A current of 100 kA through this coil produced the required external field for beam compression. This arrangement was investigated using the DRIFTPIC code [3]. The calculations showed that the focal spot size can be reduced by a factor of 2 assuming a monoenergetic beam, accelerated by 1.7 MV. For beams with realistic energy distributions a reduction of the spot size of about 30 % (increasing the power density by a factor of about 2) was predicted when using the same compression field. Due to this field the

¹ permanent address: Department of Electrical Engineering, Osaka City University, Japan

² permanent address: Physikalisches Institut I, Univ. Erlangen, D 91058 Erlangen, (Germany)

focal plane moved axially upstream by about 10 mm and hence the incident angle α was enhanced. For these calculations the degree of current neutralization of the beam was assumed to be 0.9 which seems to be somewhat low when using argon gas in the drift space at a pressure of 5 mbar. In its present version the DRIFTPIC code does not allow a self-consistent treatment of current neutralization. Therefore these results should be considered as preliminary only and adequate experiments might be useful for the development of this code in the future.

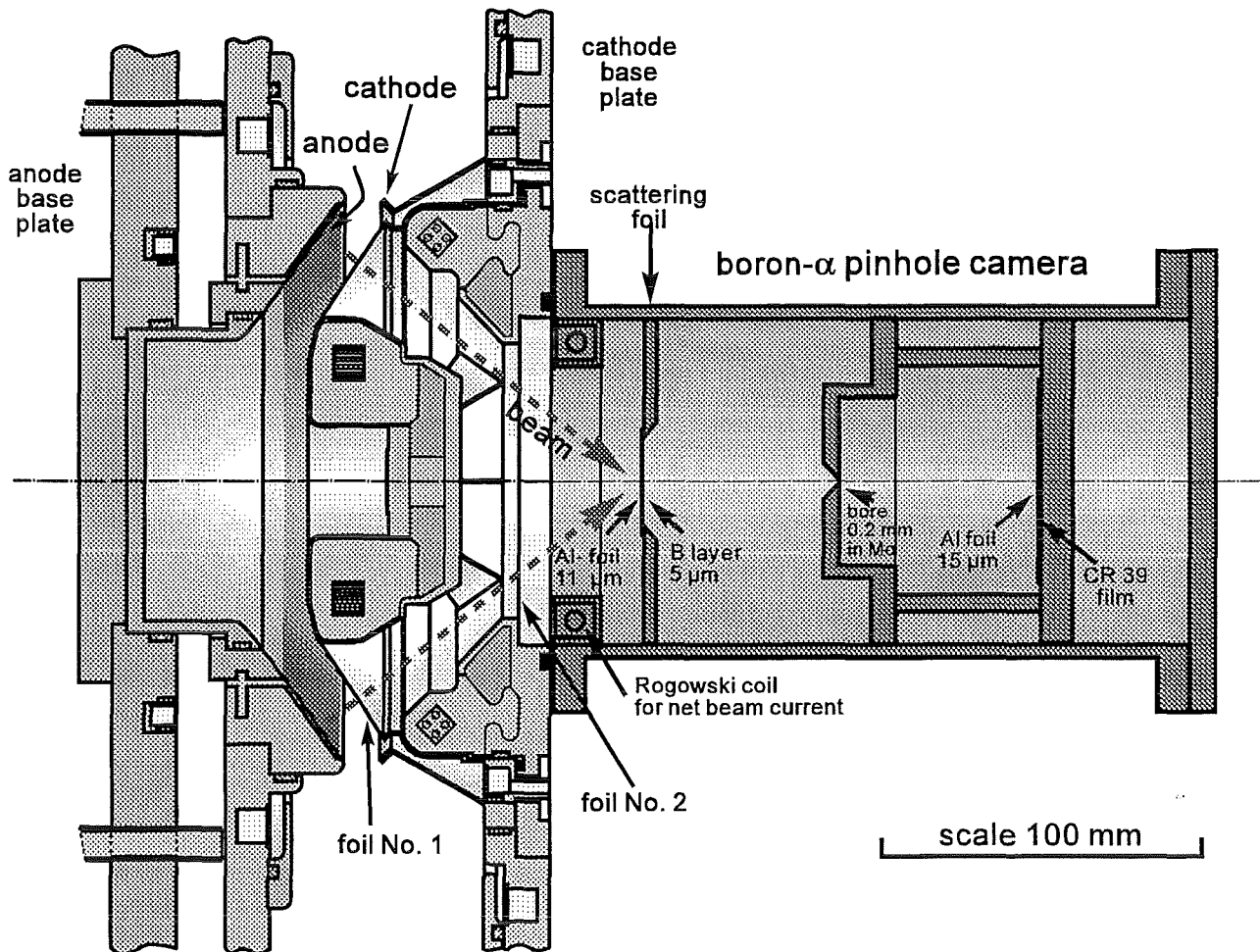


Fig. 1: Cross sectional view of the B_{applied} diode with two independent drift sections and the B_{α} diagnostics

The self-field focusing scheme is based on the generation of a B_{\ominus} field, induced by the non-current neutralized beam itself, in the drift section upstream of the focal plane of an extractor diode. Due to the resulting Lorentz forces this should also lead to a reduction of the focal length of the beam and hence to an increase of the incident angle α . The reduction of the focal length depends on the net current produced by the beam and on the distance the beam has to propagate non-neutralized. However, this distance is rather limited in the case of a sharply focusing diode using an applied magnetic field for electron insulation in the acceleration gap of this diode. The beam has to be maintained current neutralized in regions where it propagates through the return flux of the strong B_{appl} field. Therefore the drift section for the beam for self pinch experiments must be subdivided by a second foil into 2 independent sections which can be held at different gas pressures. In the first section an argon pressure of 5 mbar is needed in areas where the beam crosses the return flux of the insulating B_{appl} field. In the second section a sufficiently low gas pressure for the generation of net currents must be established. With the DRIFTPIC code, simulations for this self-field focusing scheme could not be performed

because this problem needs a self consistent treatment of current neutralization. Based on the calculation of single particle orbits a reduction of the focal length of about 2 mm was estimated for a net current of 200 kA in the beam.

II. Experimental arrangements and diagnostics

II.1 Experimental arrangement for the investigation of the self - field focusing scheme

In the experiments performed for the investigation of the self-field focusing scheme the first drift section was always held at an argon pressure of 5 mbar, normally used in the entire drift section. This neutralizing section was formed between a first Mylar foil (1.7 μm thick), placed as usual close to the cathode side of the acceleration gap, and a second Mylar foil (also 1.7 μm thick) placed on the backside of the coil producing the B_{appl} field (Fig.1). The argon pressure in the second drift section, formed by the second Mylar foil and the walls of the drift tube, could be varied from 5 mbar to vacuum.

The radial profile of a proton beam with power densities up to 1 TW/cm² was measured with the $B\alpha$ diagnostics [4]: the protons are scattered isotropically on an about 5 μm thick boron layer and the emitted α particles are imaged on an ion sensitive film (CR39) placed in a pin hole camera. The thickness of the aluminum filter foils (see Fig.1) in front of the boron layer (11 μm) and the CR39 film (15 μm) was chosen such that only protons with energies above 1.5 MV can be at the origin of tracks due to α particles on the CR39 film and that Rutherford scattered protons with energies below 1.7 MV cannot track the film. For a particular shot on KALIF the resulting net current induced by the chosen gas pressure in the second drift section as well as its influence on the position on the focal plane were not known in advance and hence the boron layer could not be properly positioned for the measurement of the radial beam profile in the presumed new focal plane. Therefore the boron layer was always placed in the nominal focal plane of the perfectly neutralized beam (Fig.1). With the boron layer in this position self pinch effects should produce a broadened or even a ring type image on the CR39 film.

The tracks on the CR39 films were counted using an automatic computer system [5]. With an excessive density of the tracks on the film, leading to an overlap of the impacts on the film, the count rates given by the automatic system will be erroneously low. In this case the non-linearly deformed track density distribution might be misinterpreted as an increase of the FWHM of the radial beam profile or as a ringshaped structure produced by post-focusing. Therefore the track density should not exceed about 300 to 400 tracks for a sample area on the CR39 film of 250 by 250 μm . The $B\alpha$ diagnostic was optimized in the first shots on KALIF with respect to its imaging ratio as well as to the impact density on the CR39 film.

For the measurement of the beam net-current, an integrating Rogowski coil was placed in the drift tube just behind the rear surface of the support plate of the B_{appl} field coils. In this position the entire beam must penetrate through the inner surface of the Rogowski coil and the Rogowski coil itself is protected as well as possible against plasma formation on its surfaces (Fig.1). For comparison with the signal of the Rogowski coil a shunt type current monitor (Fig.2) was used to measure the net current delivered to a metal cylinder

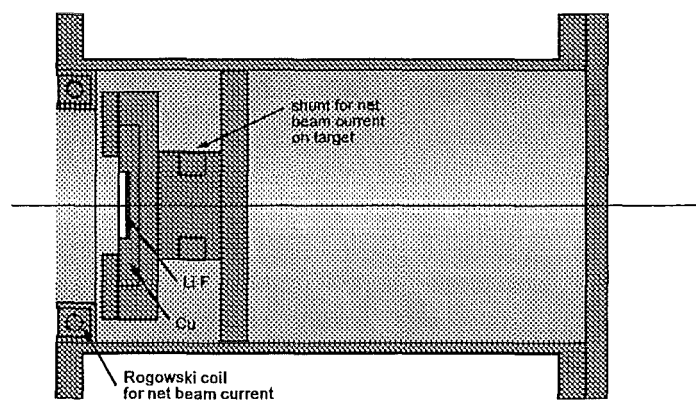


Fig. 2: Shunt monitor supporting the LiF-Cu activation target

(5 or 10 mm in diameter respectively) or to a LiF-Cu target with an outer diameter of 50 mm. This target measures the time and space averaged proton beam current delivered to its sensitive area with a diameter of 20 mm [6]. With the activation data from the LiF-Cu shots, and the radial track distribution from the $B\alpha$ diagnostic, the radial profile of the power density of the proton beam can be given in physical units.

Corresponding to the importance of the measurement of the net currents, the monitors were calibrated with reference to the current monitors close to the KALIF interface. The timing relations between all signals were carefully checked. Therefore the maximum timing uncertainty is below ± 2 ns.

Further experimental modifications used only in particular shots were as follows: an inner and an outer copper cone was used in one experiment that confines the beam after the second drift foil until close to the focus. In another experiment additional Mylar foils of 1.7 μ m thickness were attached to the Rogowski coil.

II.2 Experimental arrangement foreseen for the external-field focusing scheme

The experimental arrangement foreseen for the investigation of the external-field focusing scheme consisted of an additional coil that delivers the external magnetic compression field close to the focal plane. This post-focusing coil, attached to the rear surface of the insulating B_{appl} coil, excludes the use of the Rogowski coil for the measurement of the net-current (Fig.1) as well as the LiF-Cu activation diagnostics. Also, the possibilities for the application of the $B\alpha$ diagnostics and the current measurement with the shunt are rather restricted due to the available space.

The characteristics of 2 post focusing coils were investigated with a 2800 μ F capacitor bank chargeable to a maximum voltage of 5 kV. This bank was coupled by an inductance of 420 μ H to the 36 turn post-focusing coil having a mean radius of 4.25 cm and an inductance of 84 μ H. Both coils reached a current maximum of about 8.5 kA after 1.7 ms when charging the capacitor bank to its maximum voltage. The coil currents were proportional to the applied voltage: 1.66 kA/kV and 1.7 kA/kV were measured for coil#1 and coil#2 respectively.

The achievable maximum field on axis of these post-focusing coils is about 5T. This value seems to be somewhat low compared with the compression fields used in [2]. Post-focusing of the beam using these lower compression fields therefore might require the use of a second drift space that can be held at a lower gas pressure.

III. Experiments and results

In the 22 shots performed so far, only the self-field focusing scheme could be investigated. The diode and KALIF parameters remained unchanged in these shots and the KALIF Marx was always charged to 85 kV. The main results are summarized in the following.

III.1 Net current generation

The influence of the pressure of the argon gas in the second drift section on the generation of net-currents was investigated. The time-of-flight-corrected net-current time histories (Fig. 4) measured by the Rogowski coil and the shunt monitor supporting a LiF-Cu target showed 3 different phases. In phase 1 no net-current was measured for the time interval of about 10 ns following the onset of the diode current. This means that during this time the beam remained current neutralized. In phase 2 the net-current increased within about 20 ns (shunt monitor) and about 40 ns (Rogowski coil) to a plateau value. The gas pressure in the second drift section had a strong influence on this final value but

not on the net-current onset characteristics (Fig.4). In all shots the final values seen by the Rogowski coil were higher when compared with the shunt monitor. During phase 3 the mean signals of both monitors remained about constant. For pressures of 0.014 mbar and below, oscillations with a frequency around 80 MHz were observed during this phase. The net-current reached a maximum of about 50% of the diode current with vacuum conditions in the second drift space.

When replacing the LiF-Cu target on top of the shunt monitor by a metal rod (10 mm diam., 35 mm long) phase 1 was reduced to about 5 ns and the final values reached for the same gas pressure were lower. A reduction of the diameter of the rod to 5 mm did not modify the shunt signal.

III.2 Evaluation of the CR39 films

As examples for the evaluation of the CR39 films Figs. 5 and 6 show the track density as a surface plot for shot #3940 and #3942, respectively, while Figs. 7 and 8 present radial profiles (slices) of both functions. From the radial profiles of the track densities on the film, the 7 to 8 mm FWHM values of the beam at the position of the boron foil (i.e. in the nominal focus) were estimated. The values of the FWHM of the beam determined by this method for the other shots varied from 5.3 mm to 12 mm. This large spread could not be related to different pressures used in the second drift section. The minimum value of 5.3 mm was achieved with the double copper cone arrangement that should confine the beam. Damage at the inside of both cones and the very low track density on the film in this shot seem to indicate that most ions were absorbed by the walls of the cones.

The flat plateau of the track density distribution in shot #3942 (see Figs.6 and 8) is due to an excessive track density on the film. Above 300 tracks per sample the counting losses are sharply increasing and level off at about 700 tracks per sample. Therefore a FWHM reading may not be taken from Fig. 8. Though the measured net-current in the beam was 100 kA the change of the track density function may not be attributed to a focusing effect. Even shots performed with vacuum in the second drift section, inducing net-currents up to 200 kA, still showed FWHM values from 7 to 8 mm which are in agreement with results from shots performed with a 5 mbar argon gas pressure in the entire and undivided drift section.

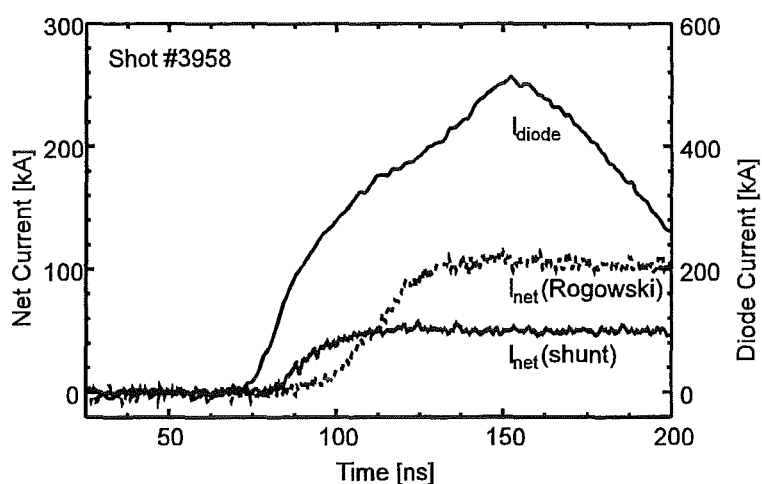


Fig. 3: Time histories of the net current measured by the Rogowski coil and the shunt compared with the diode current

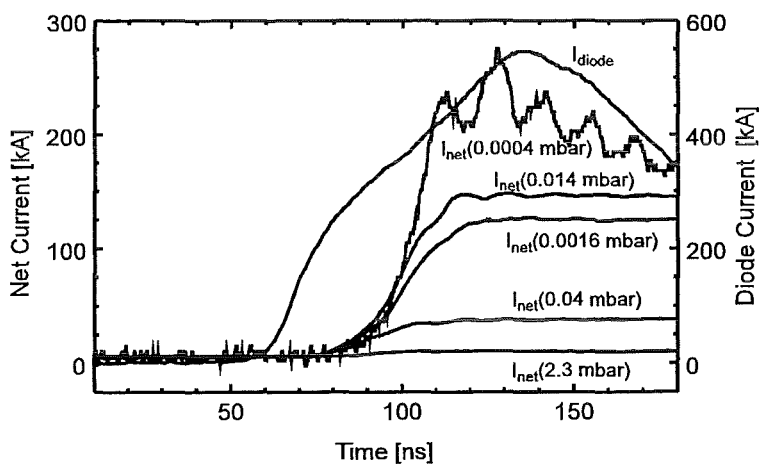


Fig. 4: Time histories of the net currents measured by the Rogowski coil for various Argon pressures in the second drift section

IV. Conclusions and outlook

The time histories of the net-currents as well as the differences between the signals are not yet well understood. As one possible explanation one might assume a non-homogeneous radial current distribution that develops when the beam propagates through the second drift section. Depending on time the number of electrons required for the neutralization of the inner beam regions cannot be supplied either by the low density background gas or by the neighboring surfaces. However this assumption needs to be verified by adequate modeling and numerical simulations.

In contrast to our expectations, the experiments did not show a noticeable influence of the gas pressure in the second drift section, and the related net-current, on the radial beam profile. This might indicate that the self-field focusing scheme does not act as foreseen on this sharply focused beam. However the following items must also be considered as possible explanations:

- the $B\alpha$ diagnostic might not be sensitive enough to measure the estimated small axial shifts of the focal plane of 2 mm.
- the measurement of the net-current is not reliable.
- the shot to shot reproducibility of the position of the focal plane may mask shifts of the focal plane related to net current generation.

In future experiments these items must be investigated in more detail. If however it could be confirmed that vacuum in the second drift section has no influence on the focusing properties of the beam, this result would be significant with respect to the current understanding of beam neutralization. It also would allow the application of a laser generated back lighter plasma for the measurement of the target temperature by absorption spectroscopy. Furthermore experiments using the available and already tested compression coils should be performed.

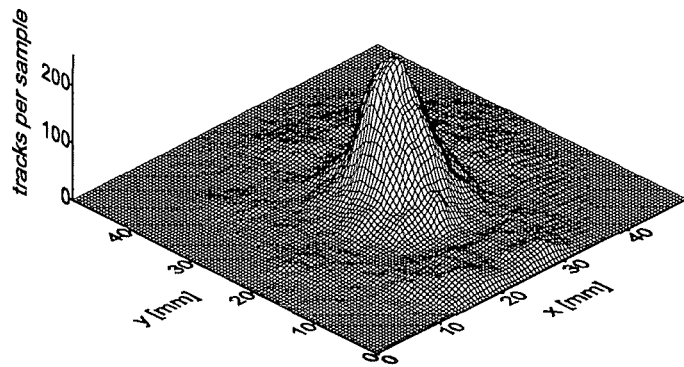


Fig. 5: Track density distribution on the CR 39 foil for shot #3940 with the boron foil in the nominal focal position

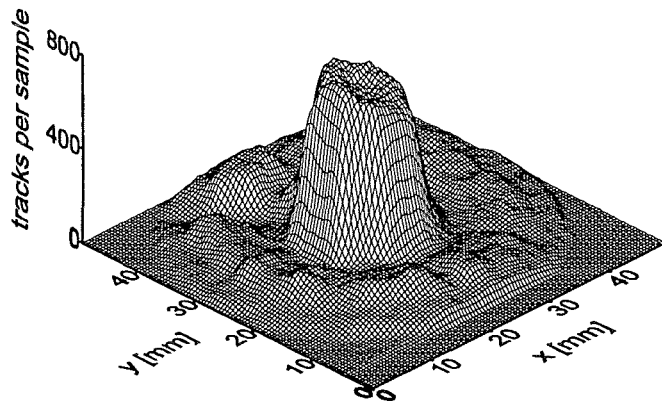


Fig. 6: Track density distribution on the CR 39 foil for shot #3942 with the boron foil in the nominal focal position. Excessive track density in the center

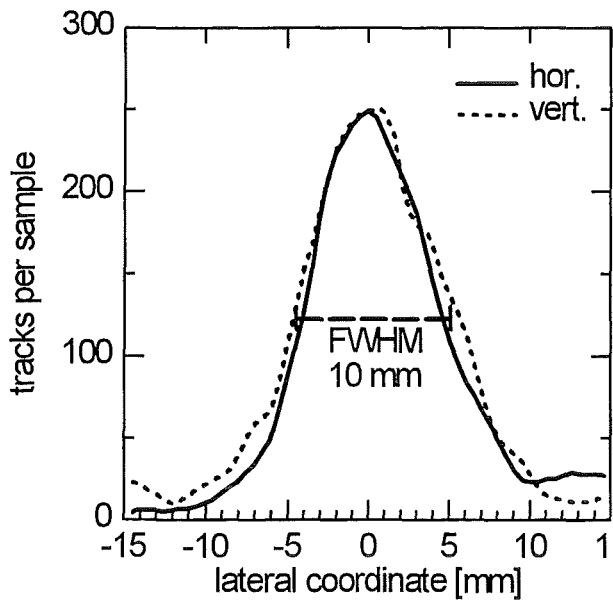


Fig. 7: Radial profiles (slices) of the track density of shot #3940

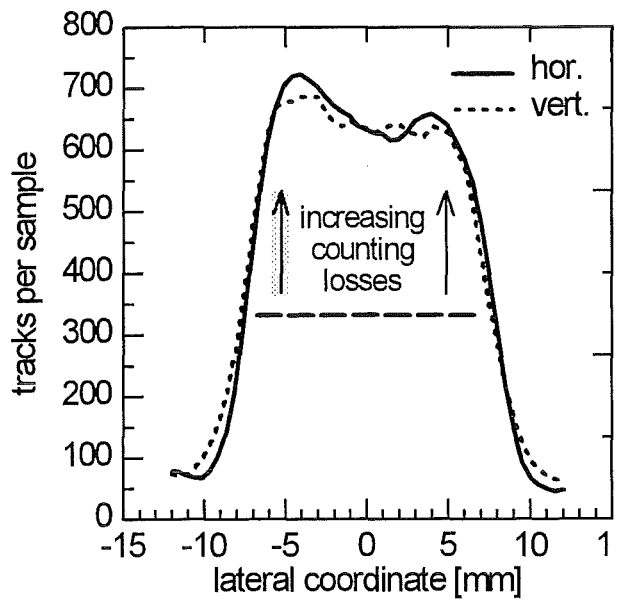


Fig. 8: Radial profiles (slices) of the track density of shot #3942

References

- [1] H. Bluhm et al., Proc. 9th Int. Conf. on High Power Particle Beams, Eds. D. Mosher, G. Cooperstein, May 25-30, 1993, Wash. DC, USA, Vol.I, p.51
- [2] W. Bauer et al., Annual Report 1994, Ed.: H. Bluhm, FZKA Bericht 5590, Karlsruhe, 1994, p.58
- [3] L. Feher et al., KfK Bericht 5207, Karlsruhe, 1993
- [4] A. Klumpp, H. Bluhm, KfK Bericht 4130, Karlsruhe, 1986
- [5] H. Guth, A. Hellmann, FZKA Bericht 5523, Karlsruhe, 1995
- [6] P. Hoppé et al., Annual Report 1994, Ed.: H. Bluhm, FZKA Bericht 5590, Karlsruhe, 1994, p.51

On the Stationary Applied-B Ion Diode Impedance

A.Grechikha

Abstract

The stationary impedance of the applied-B ion diode is found in the frame of an electron mixing model. It is shown that the diode voltage as a function of current has a maximum and behaves as $U \sim B^4_{app}/I^2$ at large currents. The consequences are discussed.

The voltage-current characteristics of the applied-B diode were the main subject of consideration in the previous report [1] where the effects of electron mixing and screening on the magnetic Debye scale $r_B = B/4\pi en_e$ in the diode were introduced. This theory was developed for the far-from-equilibrium state with a delta-function peak in the electron distribution at the virtual cathode. As a consequence it contained a free parameter describing the fraction of mixed electrons in the gap in comparison to the total electron distribution and expressing the 'distance from the equilibrium'. A further comparison with results from 3D nonstationary simulations[2] showed that the best agreement with the theory (Fig 1)

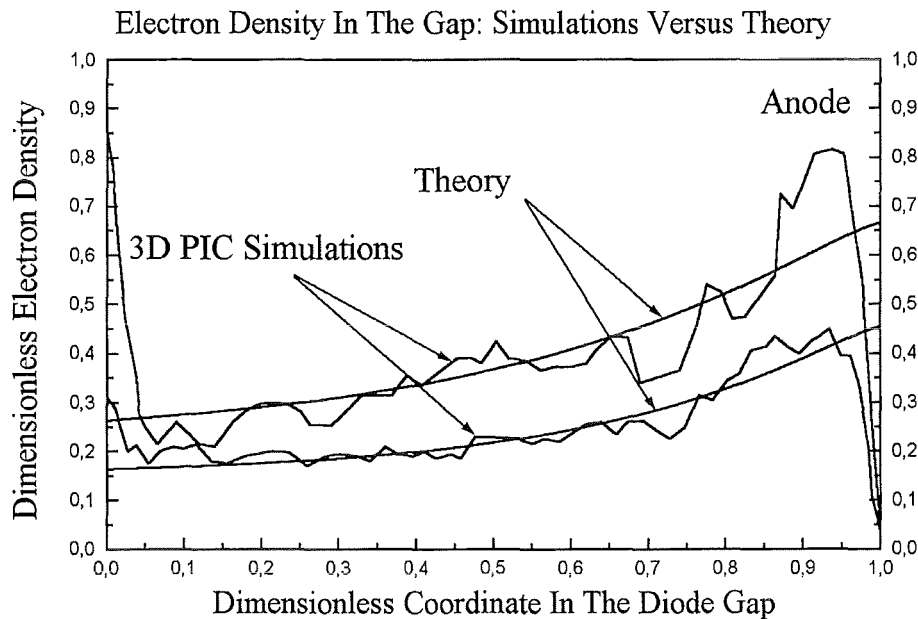


Fig. 1 Distribution of the electron density in the gap in the theory and in the 3D PIC simulations [2]

is reached in the opposite case of the equilibrium state where all electrons in the gap are uniformly mixed (more accurately, the uniformity does not concern the electron density n_e but the ratio n_e/B which is the integral of motion for drifting electrons). Consequently there is no delta-function electron layer in the vicinity of the virtual cathode as assumed in [1]. This case,

however, requires that we consider the magnetic pressure in the charge-neutral region of the diode which was possible to neglect in [1]. The basic equations should include the conservation of two magnetic fluxes: one corresponding to the vacuumic gap and one corresponding to the charge-neutral region

$$F = B_{appl}d ,$$

$$B(x)(L - x) = B_{appl}(L - d).$$

Here F is the magnetic flux in the gap, B_{appl} is the initially applied B-field, x is the distance from the anode to the virtual cathode, d is the geometric gap, L is the distance from the anode to the cathode foil. As a result the calculations become more complicated. Using dimensionless variables $\eta = x/r_B$, $f = F/B_a r_B$, $h = B/B_a$, $u = U/F$ (B_a is the B-field value at the anode surface) one arrives at the dimensionless equations for the flux conservation

$$B_a r_B f = B_0 d ,$$

$$B_a h \left[\frac{L}{d} - \eta \frac{r_B}{d} \right] = B_0 \left[\frac{L}{d} - 1 \right]$$

The resulting formulas for the voltage-current characteristics are

$$u = \frac{1-h}{f} ,$$

$$J = J_1 f^{1/2} \left(\left(1 - \frac{d}{L} \left(1 - \frac{\eta h}{f} \right) \right) / h \right)^2 ,$$

where $f = \int_0^1 h d\eta$, function h satisfies the equation

$$h'^2 = 4J_1 \sqrt{1-h} + h^2 - 1$$

with the boundary conditions $h(0) = 1$, $h'(\eta) = 0$, and the parameter J_1 is

$$J_1 = j/j_1 , \quad j_1 = (B_a^3 2e/M_i r_B)^{1/2} / 4\pi .$$

These relationships provide the solution in the implicit form $u = u(J_1)$, $J = J(J_1)$. Fig.2 exhibits the behavior of the dimensionless diode voltage $u = U/F$ as a function of the dimensionless current density $J = j/j_0$ where

$$j_0 = (B_{appl}^3 2e/M_i d)^{1/2} / 4\pi .$$

Plots are shown for different diode geometries fixed by the ratio d/L .

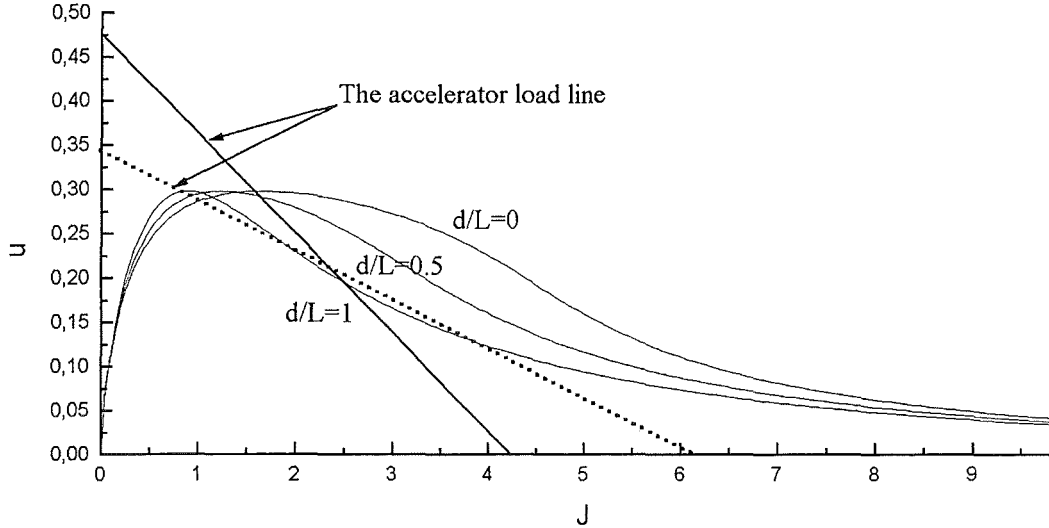


Fig. 2 The dimensionless diode voltage u versus the dimensionless current J , the load line (solid) for Kalif ($U = 1.8MV$, $I = 0.5MA$, $j = 4KA/sm^2$, $B_{appl} = 2.5T$, $d = 0.85sm.$) and an example load line (dotted) with switching rather than smooth regime.

It should be mentioned that if the loading line (solid) would be less steep (dotted) it would cross the curve at three points rather than one point and instead of a smooth decrease in voltage at large current one would have a sudden drop when the load line passes the top of the plot (see the Discussion also).

Physically the behavior of the diode voltage as a function of ion current density may be understood without calculations. At small current densities the magnetic insulation is strong enough and the voltage is provided by the formula for a Child-Langmuir ion diode uniformly filled with a charge-neutralizing electron component. At large current densities the magnetic pressure cannot counteract the electrostatic attraction of the electron cloud towards the anode

except in a the small region of the order of the magnetic Debye scale near the anode. In that case the physical diode gap d_{eff} no longer coincides with the geometric one but is of order r_B :

$$d_{eff} = \frac{9}{8}r_B.$$

This results in a scaling $U \propto B_{appl}^4/j^2$ which can be understood in crude hydrodynamic terms. The momentum flux continuity

$$M_i n_i V_i^2 + \frac{B^2}{8\pi} - \frac{E^2}{8\pi} = const = \frac{B_a^2}{8\pi},$$

the continuity equation

$$n_i V_i = \text{const} = j_i / e$$

and the energy conservation

$$M_i V_i^2 / 2 = eU$$

result in the relationship

$$U = \frac{e (B_a^2 - B_c^2)^2}{2(8\pi)^2 M_i j^2}$$

where we have taken into account the zero values of the electric field at the electrodes. This relationship is true as long as we can neglect the heat pressure of the electron gas, otherwise one should add it to the magnetic pressure. At large currents the theory provides $B_a = 3B_{\text{appl}}$, $B_c = B_{\text{appl}}$ and we arrive at the expression

$$U = \frac{e B_{\text{appl}}^4}{2\pi^2 M_i j^2}$$

for the diode voltage.

Discussion

The existence of the falling part of the voltage curve can lead to important consequences. First, the negative derivative of the voltage over the current density means instability of the ion current emission. Entering the falling part of the curve, the ion diode should immediately switch into the regime with local ion current density oscillations. That can probably explain what is actually observed in the experiments where the strong slow oscillations of the local ion current density can suddenly arise. Another consequence is the ability of the diode to switch from one voltage to the smaller one when the load line passes the top of the voltage plot. That is also what the experiments show. A very important point is that the voltage drop and switching to the slow oscillations will strongly correlate in time, since they both result from the falling branch of the voltage curve.

It should be mentioned here that although the qualitative conclusions are not too sensitive to the chosen model, the digits could be. Thus, finite electron gyroradii lead to an appreciable increase in the voltage due to vacuum layer formation near the anode: electrons cannot approach the anode closer than their gyroradii allow. The finite pressure of hot electron gas is also important when considering the pressure balance in the diode. The finite electron mass is negligible only with relativistic voltages on the diode, otherwise one should consider the effect of the c/ω_{pe} scale which is no longer small. All these effects are too unmanageable to be correctly considered analytically and require us to combine theory with numerical examination.

Literature

1. A.V.Gordeev, A.V.Grechikha. JETP Lett., Vol. 61, No. 3, 10 Feb. 1995. p.196
2. T.D.Pointon, M.P.Desjarlais, D.B.Seidel et.al., Phys. Plasmas 1, 429 (1994)

Ion Beam Emission From a Rippled Surface

A.Gretchikha

Abstract

Child-Langmuir emission of an ion beam from a rippled surface is considered. It is shown that the beam divergence has zeros at distances from the emitting surface which asymptotically form the geometric progression with a progression factor $q = \exp(6\pi/\sqrt{7}) \approx 1242$. The effect of a weak adiabatic cooling of the beam is found.

The problem of the Child-Langmuir emission of a beam from a rippled surface is important if we are interested to predict the beam angular divergence created by the wavy shape of an emitting metal or plasma boundary. Let us assume that the beam moves along the x axis and that the emitting surface is directed along the y axis. We shall derive an equation describing the stationary spatial distribution for the beam of arbitrary geometry and examine its linear properties for the case of a slightly rippled anode where the δx coordinate of the anode surface is behaving as $\delta x = \delta x_{\max} \exp(iky)$, $k\delta x_{\max} \ll 1$ (Fig.1).

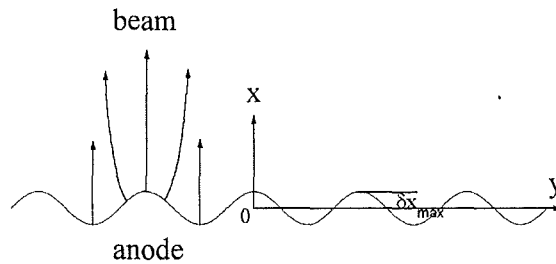


Fig. 1. The initial geometry.

The equations describing the beam should include the continuity of flow

$$\nabla(nv) = 0, \quad (1)$$

zero vorticity of the flow

$$\nabla \times v = 0 \quad (2)$$

which allows us to represent the velocity v as a gradient of some scalar function

$$v = \nabla S, \quad (3)$$

energy conservation

$$v^2 \sim U \quad (4)$$

valid for the stationary case,- and the Poisson equation

$$n \sim \Delta U \quad (5)$$

that relates the beam density with the potential U . The zero vorticity results from its being frozen in the flow and from zero initial conditions at the emitting surface. Substituting these

relationships one into another, we arrive at an equation describing the beam in the general case:

$$\text{div}(\text{grad}S * \Delta((\text{grad}S)^2)) = 0. \quad (6)$$

It should be emphasized here that we did not assume anything but stationarity when deriving this equation, therefore, it is valid for all geometries of the emitting surface where beam particles do not start to intersect the trajectories of others.

Now we are proceeding to examine the linear properties of equation (6). Splitting the solution S into a nonperturbed one S_0 and into the perturbation S_1 where

$$S_0 = j^{1/3} x^{5/3} \quad (7)$$

corresponds to the standard one-dimensional Child-Langmuir flow (we are omitting all the dimensional factors except for the dependence on the current density and space coordinate) and

$$S_1 = a(x)\exp(iky) \quad (8)$$

where the dependence on x is to be found. Substituting $S = S_0 + S_1$, $S_1 \ll S_0$ into the general equation we arrive at a linear equation for the factor $a(x)$:

$$(a' S_0'^{2//} + 2S_0'(S_0' a')'')' - k^2(a S_0'^{2//} + 2(S_0'^2 a')') = 0. \quad (9)$$

Substituting $a = j^{1/3} x^{2/3} (-\frac{5}{3} \delta x) f$ and taking into account the dependence of S_0 on x we finally arrive at the equation

$$x^2 f^{(4)} + \frac{16}{3} x f^{(3)} + \frac{40}{9} f^{(2)} = k^2 (x^2 f^{(2)} + \frac{8}{3} x f^{(1)} + \frac{8}{9} f) \quad (10)$$

for the dimensionless function f that provides the angular beam divergence

$v_y/v_x = -ik\delta x f \exp(iky)$. It should be completed by the boundary conditions at the anode reflecting the fact that in the vicinity of the emitting point where two-dimensional effects are negligible the solution coincides with the usual Child-Langmuir law. That means that the asymptotic solution for $x \rightarrow \delta x$ should look like

$$S = (j + \delta j)^{1/3} (x - \delta x)^{5/3} \quad (11)$$

or, in terms of f ,

$$f = 1 - \frac{1}{5} \frac{\delta j}{j} \frac{x}{\delta x} + \dots \quad (12)$$

As the fourth order equation has four linearly independent solutions we can conclude that this asymptotic completely determines the solution excluding two solutions which have $1/x$ - and $1/x^2$ - singularities at $x \rightarrow 0$ and selects the weights at which the two regular ones

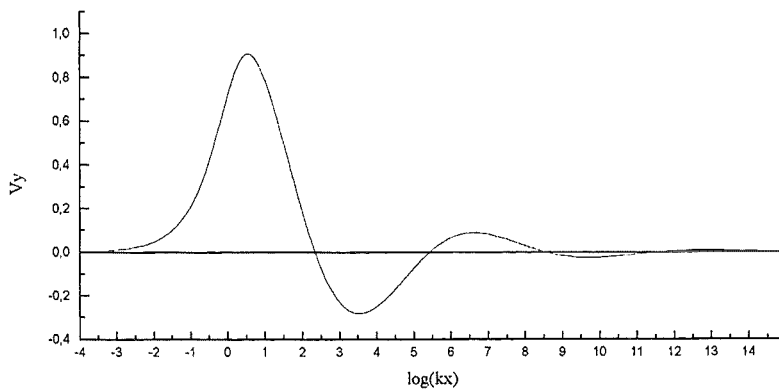


Fig. 2. The dimensionless transverse beam velocity v_y as a function of kx .

(having respectively zero value and zero derivative at $x = 0$) should be taken to provide $f(x)$. Done numerically it results in the relationship $\frac{\delta j}{j} \approx 1.82k\delta x$ between the amplitudes of the current density and the anode surface perturbations.

The numeric solution of the equation for $f(x)$ by a finite-difference scheme is not possible (the equation has exponential solutions which lead to exponentially rising numeric errors killing the right solution almost immediately) and it is reasonable to look for a solution matching numerically the Taylor series for $x \rightarrow 0$ and for $x \rightarrow \infty$. The resulting transverse velocity of the beam

$$v_y(x) = -ik\delta x v_{cl}(x)f(x) \quad (13)$$

is shown in Fig. 2 where a logarithmic scale for kx is chosen and v_y is normalized by

$$v_o = -ik\delta x v_{cl}(k^{-1}) \quad (14)$$

where $v_{cl}(x) = v_x$ is the longitudinal velocity of the Child-Langmuir at the distance x from the anode and the imaginary unit implies that the perturbations in v_y are shifted by the phase $\pi/2$ relative to the perturbations of the surface. One can see a sequence of zero values for v_y has at the distances forming asymptotically the geometric progression and weak reduction of the amplitude of v_y oscillations at $x \rightarrow \infty$. The analytic result provides

$$v_y \sim (kx)^{-1/6} \exp(i\frac{\sqrt{7}}{6} \ln(kx)) \quad (15)$$

for the v_y asymptotic at large kx which results in a value of

$$q = \exp(6\pi/\sqrt{7}) = 1241.98... \quad (16)$$

for the progression factor (the next distance with zero v_y is q times greater than the previous one). The numeric solution shows that the first zero occurs at $kx \approx 217.1$. Fig. 3 exhibits the angular beam divergence as a function of kx . The physical meaning of the slow decrease of the v_y amplitude with kx is the following. When the particles are far away from the anode (compared to the wavelength of perturbation $\lambda = 2\pi/k$) the only surviving degree of freedom for perturbation is the oscillations of the particles parallel to the anode with the plasma frequency

$$\omega_p = (4\pi e^2 n/m)^{1/2} \quad (17)$$

As the ratio E/ω is an adiabatic invariant ($E = mv_y^2/2 + e\delta U$ is the total transverse energy of the oscillating particle), the amplitude of $v_y \sim E^{1/2}$ should go down as $\omega_p^{1/2} \sim n^{1/4} \sim x^{-1/6}$. i.e. the reduction of v_y means adiabatic cooling of the beam. Let us finally determine the limit of applicability of the linear approximation. It is provided by the condition that particle shifts in y direction should be small relative to the wavelength: $k\delta y_{\max} \ll 1$. The expression for v_y results in $k\delta y_{\max} \sim k\delta x_{\max}(kx)^{1/6}$ and the limit of applicability should therefore be

$$k\delta x_{\max}(kx)^{1/6} \ll 1 \quad (18)$$

which is not very restrictive, for most cases it coincides with the condition of small surface modulation $k\delta x_{\max} \ll 1$. As $\delta j/j = \delta n/n = -ik\delta y$ for the linear oscillations, the condition (18) is also responsible for the smallness of $\delta j/j$, $\delta n/n$.

Let us apply the theory developed to estimate the real angular beam divergence that could result from a rippled plasma surface created on the anode. The typical wavelength is determined by the distance between the slots filled by epoxy to provide the flashover surface on the anode and is of the order of 1mm . The typical diode gap is about 5mm . Assuming the parameter $k\delta x$ to be of order 1 one finds the beam output divergence for $kx = 2\pi * 5 = 31.4...$

$$\alpha = |v_y|_{\max}/v_x \approx 40\text{mrad} \quad .$$

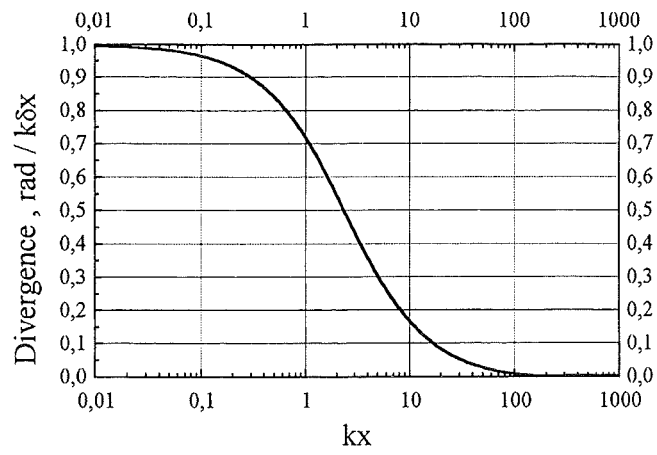


Fig. 3. The angular beam divergence as a function of kx .

ELECTRON SHEATH COLLAPSE IN AN APPLIED-B ION DIODE

A.Grechikha

*Forschungszentrum Karlsruhe, Institut für Neutronenphysik und Reaktortechnik
Postfach 3640, 76021 Karlsruhe, Germany*

Abstract

The effect of the electron sheath collapse in an applied-B ion diode due to the presence of the resistive anode plasma layer is found. It is more damaging at higher diode voltages and it may be responsible for the parasitic load effect observed in the experiments.

Introduction

Applied-B ion diodes are used for the generation and focusing of intense ion beams in the Inertial Confinement Fusion Program. The basic effort has been to increase the energy and improve the quality of the beams. Experiments show that there are many obstacles to this, and the unstable behavior of the magnetized electrons is among them. Describing the electron component is one of the basic problems in the theory of ion diodes. The reason is that, in contrast with a classical Child-Langmuir diode, in which the electrons are freely accelerating between the electrodes, an ion diode requires magnetic insulation of the electrons, which would otherwise carry most of the current. Magnetic insulation, however, makes the behavior of the electrons extremely complicated.

The basic goal of the present work is to investigate the role of the anode plasma in the problem of stability of the electron sheath in the diode. Both analytic and numerical approaches are used. It is shown analytically that the infinitely thin electron sheath is generally speaking unstable in the presence of a resistive anode plasma and the threshold thickness of the plasma layer is less, the greater the ion current enhancement is. The numerical part of the work is to study the role of finite electron gyroradii which are assumed to be zero in the theory. The main result is that low-voltage diodes exhibit better stability due to the limiting effect of larger gyroradii.

Theory

Let us consider an infinitely thin electron sheath in the diode (Fig. 1), the position of which is determined by the balance [1] between electrostatic attraction to the anode and resulting magnetic pressure defined by the extent of the compression of the magnetic flux captured in the gap and the extent of the expansion of the magnetic flux captured in the charge-neutral region

$$B_{gap}^2/8\pi - E_{gap}^2/8\pi = B_{cn}^2/8\pi . \quad (1)$$

Here the left side represents the net force acting on the sheath from the anode and the right side represents pressure of the magnetic flux captured in the charge-neutral region of the diode. The presence of the anode plasma results in a different scaling for the two forces: the magnetic one and the electrostatic one. The pressure of the magnetic flux captured to the diode gap is proportional to the inverse square of the distance from the sheath to the anode, while the electrostatic force for the given voltage is proportional to the inverse square of the

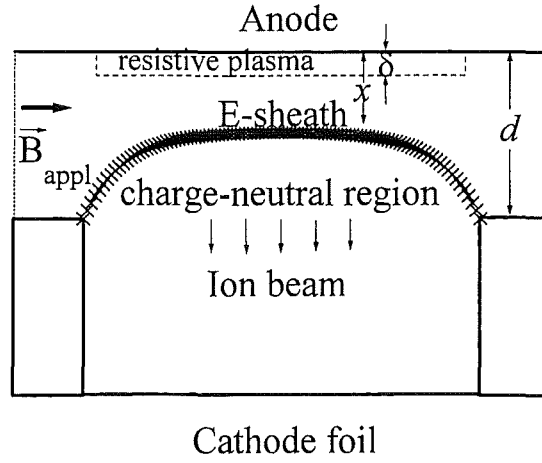


Fig. 1. Geometry of the model.

distance from the sheath to the boundary of the plasma layer (we assume here, for this simple argument, the skin time for the magnetic field penetrating into plasma to be small compared with the pulse duration). If both forces are large enough compared with the pressure of the magnetic flux captured in the charge-neutral region (the case of the large current enhancement), the stability of the electron sheath is impossible as the electrostatic force (directed to the anode) rises faster than the magnetic one (having the opposite direction) when the sheath position is shifting towards the anode. The theory provides the expression

$$1 - \frac{\tanh \sqrt{\gamma\tau}}{\sqrt{\gamma\tau}} = \frac{1-qx/\delta}{1-q} \quad (2)$$

for the growth rate γ where $\tau = 4\pi\sigma\delta^2/c^2$ is the plasma skin time and $q = \left(\frac{x(L-d)}{d(L-x)}\right)^2 \frac{L-\delta}{L-x}$. One can find that $\gamma > 0$ at

$$\delta > d \left(\frac{x(L-d)}{d(L-x)}\right)^3 \frac{L}{L-d} / \left(1 + \left(\frac{x(L-d)}{d(L-x)}\right)^3 \frac{d}{L-d}\right). \quad (3)$$

If $L \gg d$, one can neglect the change in the pressure of the magnetic flux in the charge-neutral region and the condition of instability simplifies to:

$$\delta > d \left(\frac{x}{d}\right)^3. \quad (4)$$

This means that at the large enhancement ($x \ll d$) a smaller plasma layer is sufficient to cause the electron sheath instability. The physical meaning of the threshold is that the spatial derivative of the force F acting on the unit square of the electron sheath, where

$$F = B_{gap}^2/8\pi - E_{gap}^2/8\pi - B_{cn}^2/8\pi \quad (5)$$

changes its sign from negative to positive and instead of returning the sheath to the equilibrium position, the force F acts to increase the deviation from equilibrium. One can

show that the inequality (3) is equivalent to the condition $dF/dx > 0$.

Simulations: The Model

Simulations using the 2D PIC code KARAT [2] were carried out in order to clarify the nonlinear stage of the instability, its sensitivity to the physical parameters, and its possible effect on the ion diode behavior. A simple model for the simulations was chosen: the resistive plasma was modelled by a region with constant resistivity; the ion beam was absent. This simple model is more preferable than an exact one in the sense that it cuts off all the features which are not related to the studied effect, such as the two-fluids electron-ion instabilities as well as by the instability of the plasma surface due to the ion beam emission. (See the Discussion also.) The only quantitative consequence of the absence of ions in the simulations is that the voltage and electric field in the gap are related by the factor $\alpha = 1$ rather than $\alpha = 0.75$ as it would be in the case of a Child-Langmuir diode.

Results

Figure 2 exhibits the pattern of the sheath instability for the high-voltage case $U = 100MV$ which is closer to the theory's assumptions as the electron gyroradii are small and the approximation of an infinitely thin electron sheath works well enough. One can see that the instability results in spot-like regions where the electron sheath penetrates into the resistive plasma. Figure 3 exhibits the same case with half the anode width along the magnetic field. Only one spot develops. Figure 4 exhibits a lower voltage case with $U = 10MV$. One spot develops, but it is much more diffuse. The depth of the electron sheath penetration into the plasma is much less.

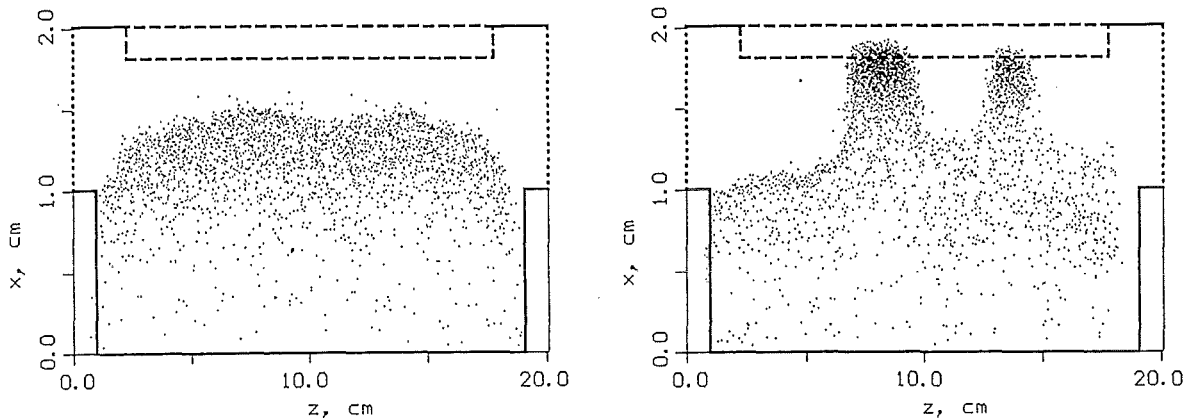


Fig. 2. Instability at $U = 100MV$ for $t = 9.0ns$ and $t = 10.3ns$.

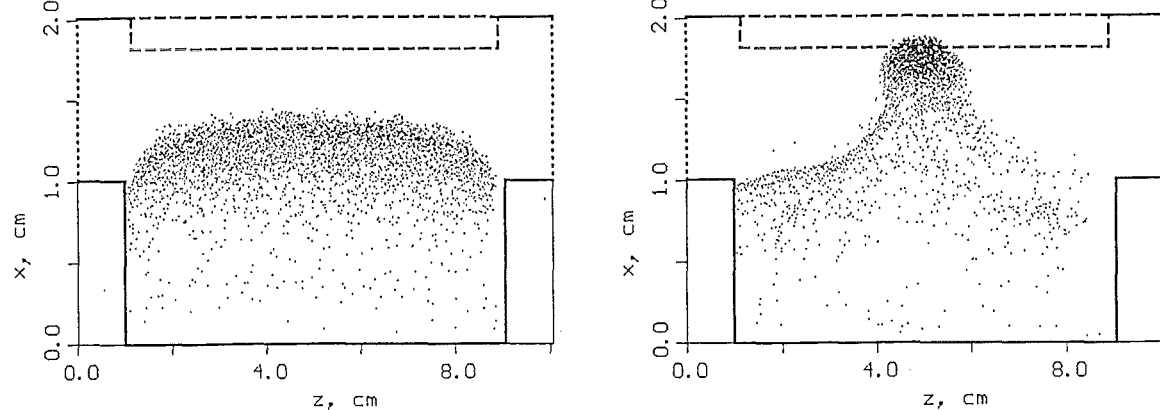


Fig. 3. Instability at the same voltage and an anode that is half as wide in the direction of the magnetic field for $t = 3.0ns$ and $t = 3.8ns$.

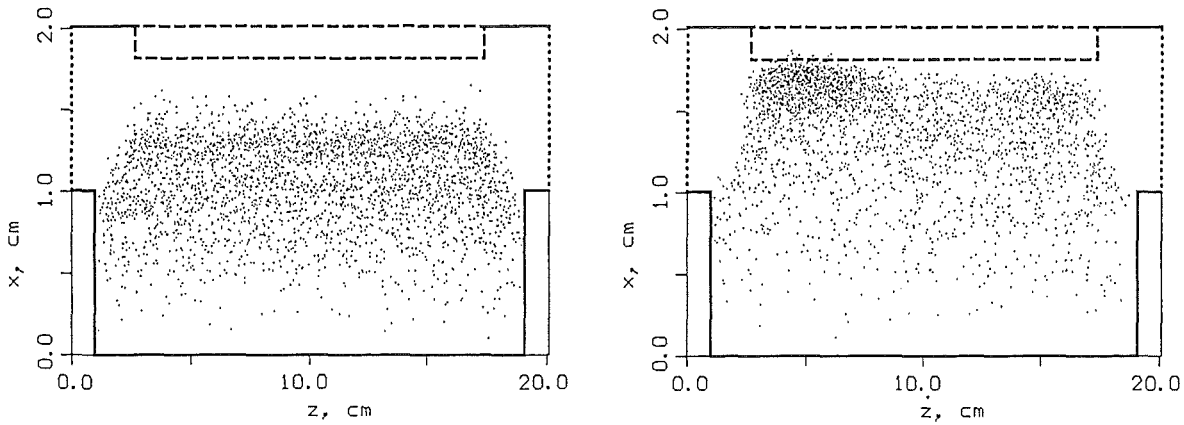


Fig. 4. Instability at $U = 10MV$ for $t = 21.5ns$ and $t = 25ns$.

Discussion

It has been shown that in the case of higher voltages, the instability is more damaging in the sense of the electron sheath uniformity and insulation. Better performance of the diode is expected at lower voltages due to the stabilizing effect of the relatively larger electron gyroradius, which obeys the scaling

$$r_L/d \sim m_e c^2 / U. \quad (6)$$

The simulations with the low voltage $U = 1MV$ did not exhibit any significant effect of the instability at all. This conclusion, however, may be too optimistic because in the real 3D electron dynamics their gyroradii could be less due to the possibility of energy transfer from gyrorotation to other degrees of freedom - e.g. to ion beam. The described effect may be responsible for the parasitic load effect both because of the breakdown of the electron insulation at the spots and the enhancement in ion current emitted from the spots; the ion beam from the spots would not contribute to the focussable beam because of strong local defocussing.

This instability due to the presence of the anode plasma is not the only one. It can be shown that the ion emission from the plasma leads to instability of the plasma boundary, with a growth rate provided by the dispersion relationship

$$\omega^2 = 1.81 \dots i |k| B j_i / c \rho \quad (7)$$

which is consistent with the observed time dependence of the anode plasma layer broadening. Here ρ is the mass density of the plasma and the wavenumber k is directed across the magnetic field. The physical meaning of this instability is that rippling of the plasma surface leads to the modulation of the emitted ion current density which is larger at the tops of the ripples, and this, in turn, causes modulation of the magnetic pressure acting on the plasma surface which results in the further development of the ripples. This instability may also significantly limit the ion beam quality, but its detailed description is beyond the scope of the present paper.

[1] M.P.Desjarlais, Phys.Fluids B 1, 8 (1989).

[2] Ignatov A.M., Tarakanov V.P., Phys.Plasmas, 1, 741 (1994).

MAGNETIC FIELD CALCULATIONS

W. Bauer, R. Häfner

Forschungszentrum Karlsruhe GmbH, Postfach 3640, 76021 Karlsruhe, Germany

In this report Ralph Häfner's diploma work is summarized, where first time resolved magnetic field calculations using the finite-element-program „ANSYS“ on our applied-B-diode were carried out. The results show that the magnetic flux penetrating the anode is minimized at the time instant, when the diode is fired.

1. INTRODUCTION

An important part of the particle-in-cell-simulations reported earlier [1] was the calculation of the magnetic field generated by external coils for the applied B-Diode. The program „PROFI“ [2] was used for this purpose, and the results of these calculations on rectangular grids were interpolated to fit into the boundary-fitted grids used in our particle-in-cell-codes „BFCPIC“ and „DRIFTPIC“ [3]. In these magnetic field calculations only a harmonic, sinusoidal time dependence of the magnetic field was assumed, without taking into account the real time dependence of the pulsed magnetic field.

The transition from the centralized vector computer, used earlier, to distributed work-stations and the new development of a time-resolved PIC-code (see the following paragraph) initiated considerations of using a new finite element program for the calculation of transient (time-dependent) magnetic fields. It was expected, that the Program „ANSYS“ [4] should be easier to handle and better suited for our type of boundary fitted grids. Especially it is planned to use the same grid for the particle-in-cell-code and for the magnetic field code, which is not possible in PROFI. In order to test ANSYS some calculations on a model of our present Applied-B-Diode were carried through, the results of which are reported in [5]. A short summary of this work follows here.

2. RESULTS

The purpose of the magnetic field in Ion Diodes is to prevent direct electron flow from the cathode to the anode. To accomplish this, the magnetic field lines have to be as exact as possible parallel to the anode. In addition it is necessary, that the canonical momentum of the ion beam leaving the anode is zero, in order to enable a focus point on the axis. The minimum radius r_{\min} of the focus spot is given by [6]

$$r_{\min} = \frac{1}{\sqrt{2 \frac{U}{q/m}}} r_0 A(r_0) \quad (1)$$

where U is the accelerating voltage, q and m are charge and mass of the ions and $r_0 A(r_0)$ is the vector potential at the anode surface. This means that a small focus point is only possible, if the magnetic field does not penetrate into the anode while the ions are emitted. This is approximately achieved by applying a current pulse as shown in fig. 1 to the magnet coils. The small pulse of 15 kA with a risetime of 6.25 ms (160 Hz) produces a magnetic field of opposite direction, thus compensating the 50 kA pulse at 4400 Hz at the instant when the high voltage pulse of 60 ns duration extracts the ions from the anode.

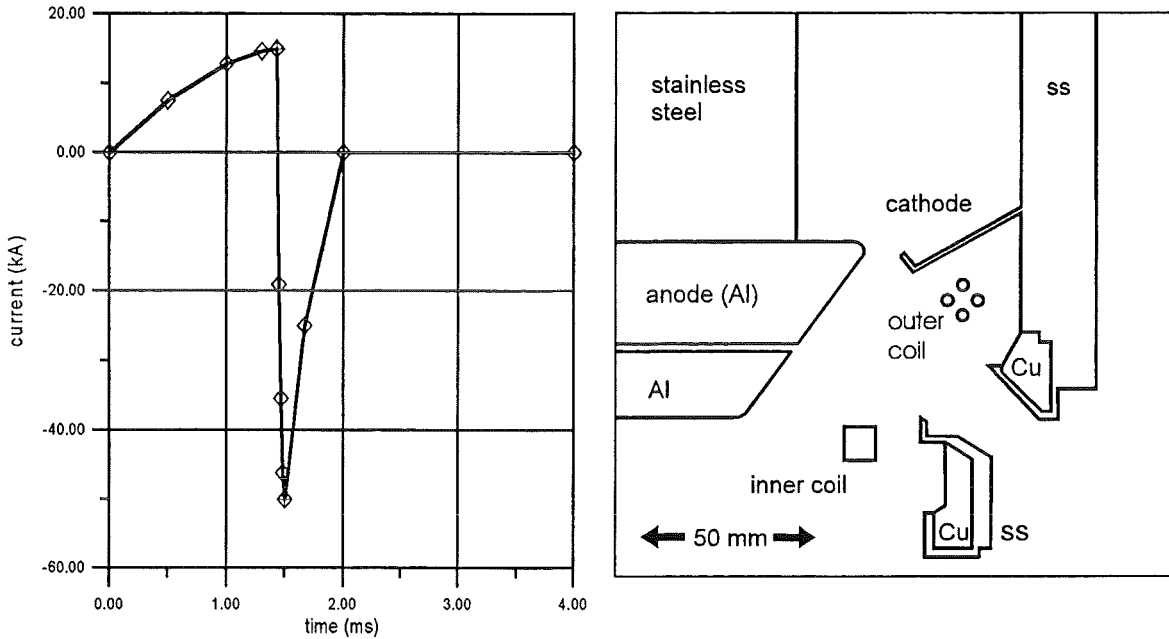


Fig. 1: Current pulse used for simulation Fig. 2. Applied-B-Diode model

Fig. 2. shows the outlines of the Applied B-Diode as it is modeled in ANSYS. In fig. 3. the absolute value of the magnetic induction B is plotted as a function of time. The B -values are given for 6 different locations defined in Table I. The radial coordinate is 83.5 mm for all points.

Table I. Evaluation points for B plotted in Figures 3 and 4.

in Anode1	3mm inside the anode
in Anode2	1mm inside the anode
vAnode3	0.5 mm in front of the anode
vAnode4	2 mm in front of the anode
vAnode5	5 mm in front of the anode
vAnode6	9.5 mm in front of the anode

The curves resemble the current pulse of fig. 1. The dip at the end of the compensation field is due to the isolation field that goes into the opposite direction. The maximum value reached close to the anode surface (vAnode3) is 3.2 VS/m^2 .

The magnetic vector potential rA_0 is plotted as a function of time in Fig. 4 for the same points as defined in Table I. Here it can be clearly seen that the vector potential approaches zero at the time, when the diode is fired (about 1.5 ms after the start of the compensation field). To show this in more detail a blow-up of fig. 4 around the time interval from 1.464 to 1.544 ms is shown in fig. 5.

Taking from this simulation a value of $rA_{\theta} = 0.2 \cdot 10^{-3}$ Vs a minimum possible focus radius of 1mm is obtained in equation (1) for the parameters of our diode.

These calculations will be continued with the aim to further optimize the magnetic field in the diode gap and thereby improving the isolation by using separate capacitor banks with different current time histories for the inner and outer coils.

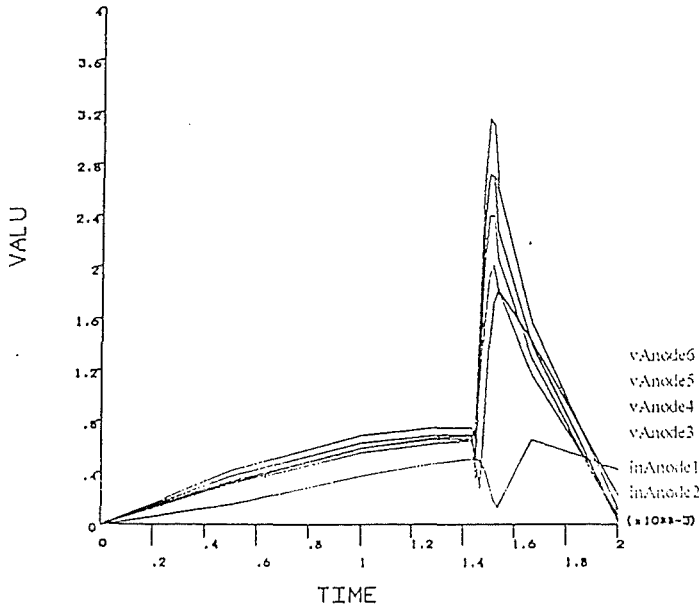


Fig. 3. Absolut value of the magnetic induction B as a function of time at the locations defined in Table I.

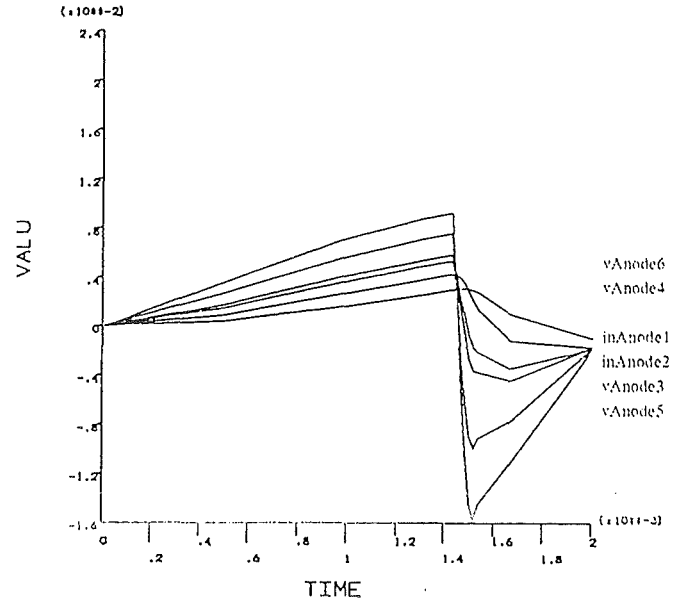


Fig. 4. Magnetic vector Potential rA_{θ} as a function of time at the same locations

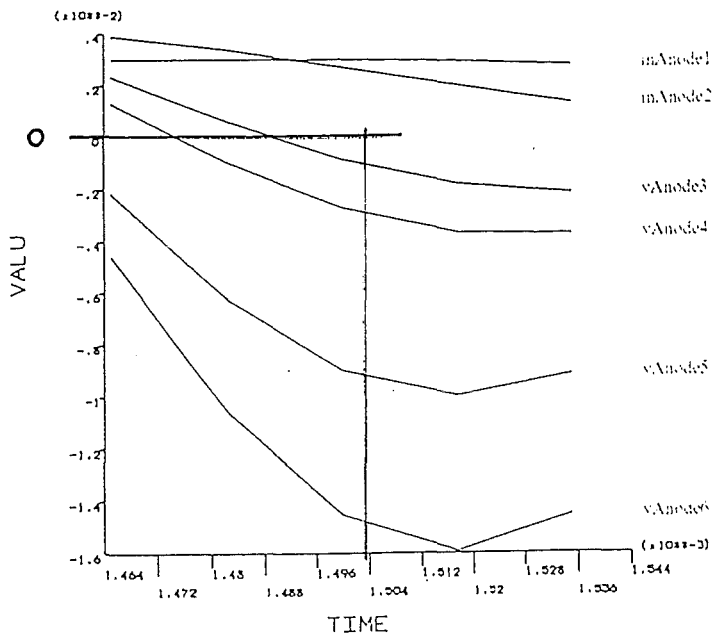


Fig. 5. Blow-up of fig. 4. around $t = 1.5$ ms

References:

- [1] W. Bauer, W. Höbel, A. Ludmirsky, E. Stein, T. Westermann, „A contribution to the magnetic focusing in an applied-B-Extractor Ion diode“, Annual report 1994, FZKA 5590, Forschungszentrum Karlsruhe, page 58 (1995)
- [2] PROFI program documentation Version 7.4, PROFI-Engineering, Otto-Röhm-Staße 26, 64293, Darmstadt
- [3] T. Westermann, „Numerical Modelling of the Stationary Maxwell-Lorentz System in Technical Devices“, Int. J. Num. Modeling: Electronic Networks, Devices and Fields, 7, (1994), p, 43 - 67
- [4] ANSYS Program documentation, Swanson Analysis Systems, Inc., available from Fa. CADFEM, Marktplatz 2, D-85567 Grafing bei München.
- [5] R. Häfner, „Finite Elemente - Rechnung von Magnetfeldstrukturen in technischen Anwendungen“, Diplomarbeit Fachhochschule Karlsruhe und Forschungszentrum Karlsruhe (1995)
- [6] H. J. Bluhm, „Die Erzeugung gepulster Megaampere-Ionenströme für die Materie- und Trägheitsfusionsforschung“, Forschungszentrum Karlsruhe, Wissenschaftliche Berichte, FZKA 5528 (1995)

The Karlsruhe Diode Simulation Program System KADI2D

M. Boger, E. Halter¹, M. Krauß², C.-D. Munz,
R. Schneider, E. Stein, U. Voß, T. Westermann³

Forschungszentrum Karlsruhe — Technik und Umwelt,
Institut für Neutronenphysik und Reaktortechnik,
Postfach 3640, D-76021 Karlsruhe

The numerical concept realized in the the Karlsruhe Diode Code KADI2D is briefly reviewed. Several new aspects concerning the Maxwell field solver based on high resolution finite-volume methods are presented. A new approach maintaining charge conservation numerically for the Maxwell-Lorentz equations is shortly summarized.

1. INTRODUCTION

For experiments with the object of optimization as well as for further developments of ion diodes it is very important to get a deep physical understanding of the fundamental time-dependent phenomena occurring inside those diodes. Elaborate computer simulations are an effective and ideal tool to enhance the knowledge about the complex ion diode physics and, additionally, could force time and reduce costs of further developments. Extensive experimental investigations [4, 5] accompanied by guiding analytical works [12, 13] and comprehensive three-dimensional, time-dependent simulations [14] stamp our present understanding of the ion diodes which is closely related with the non-linear dynamics of the non-neutral plasma inside the ion diode gap. This physical observation is modelled mathematically by the Maxwell-Vlasov equations (see e.g. [10, 11]). However, for numerical calculations it is more convenient to replace the Vlasov equation by its characteristic equations resulting in the Maxwell-Lorentz system.

The numerical simulation of concrete field problems such as the stationary or nonstationary Maxwell equations in relevant technical geometries require an adequate computational grid. This grid should cover the domain of interest as good as feasible. Therefore, we adopt a grid model based on boundary-fitted coordinates (BFC) [34] resulting in quadrilateral meshes which possesses the great advantage that the data structure is regular.

Practical grid generation is often cumbersome and connected with great effort: High quality simulations of electrical devices require an appropriate replica of the boundary of the computational domain, where several kinds of boundary conditions could be imposed. To fulfil the high accuracy requirements for the discrete solution of Maxwell equations it is necessary that the grid zones are not distorted too much and that the grid fineness is controllable. To simplify the grid generation procedure the program package InGrid (**I**nteractive **G**rid generation) [16] has been developed in close collaboration with the Fachhochschule Karlsruhe. This program system is a

¹Fachbereich Feinwerktechnik, FH Karlsruhe, Postfach 2440, D-76012 Karlsruhe

²Forschungszentrum Karlsruhe, Hauptabteilung Informations- und Kommunikationstechnik, Postfach 3640, D-76021 Karlsruhe

³Fachbereich Naturwissenschaften, FH Karlsruhe, Postfach 2440, D-76012 Karlsruhe

combination of the powerful construction tool AutoCAD with extended BFC grid generation techniques [17, 15], which enables to generate interactively a computational grid in two dimensions in an effective and comfortable manner.

The numerical solution of the Lorentz and stationary Maxwell equations based on the above mentioned BFC grid concept is realized with the simulation program BFCPIC [38] which has been developed at the Forschungszentrum Karlsruhe during the last years. It has been turned out that BFCPIC is an excellent tool for the optimization of the design of technically relevant diodes and their resulting focussing properties [2, 36]. Furthermore this code is successfully applied to the simulation of numerous devices at the Forschungszentrum where stationary fields are dominant (see e.g. [7] and references therein). However, it is not possible to study with the BFCPIC code important time-dependent phenomena. Urgent problems like the origin and consequences of electromagnetic instabilities inside the ion diode gap and, especially, their influence to the stability and quality of the ion beam require the numerical solution of the full nonstationary Maxwell equations. For that purpose, the recently developed Karlsruhe Diode code KADI2D is now available. Modern numerical techniques based on finite-volume (FV) methods are employed in KADI2D to attack the nonstationary Maxwell equations numerically [15]. The application of FV methods, which are known to be very robust even when strong gradients occur, is a new approach in electromagnetics [24] and self-consistent particle simulation using Maxwell-Lorentz equations. Well-established subroutines for the particle treatment are carefully adapted from the BFCPIC code to the new data structure of the KADI2D program system. For a detailed discussion of numerical results obtained with the time-dependent, $2\frac{1}{2}$ -dimensional BFC version of KADI2D we refer to [26].

After a brief overview of the numerical model in its entirety we will focus our attention to a few selected aspects concerning the Maxwell as well as the Maxwell-Lorentz equations. Some results obtained with KADI2D will be presented, demonstrating the properties and quality of the applied numerical methods. Concluding remarks about the further program development and on planned activities finish this paper.

2. THE NUMERICAL MODEL

The self-consistent numerical solution of the Maxwell-Lorentz equations is obtained by applying the well-established particle-in-cell (PIC) method [3, 19]. This method is an attractive computational tool for studying kinetic phenomena, in particular in plasma physics: The orbits of electrically charged particles have to be determined with respect to externally applied as well as self-generated electromagnetic fields. Especially, for pulsed power ion diodes the magnitude of the self-generated fields is of the same order as that of the applied ones. The basic idea of the PIC method can be skilful summarized by a representation of several steps within an iteration circle.

Therefore, we suppose that the external as well as the self-consistent charge and current density ρ^{ext} , \mathbf{j}^{ext} and ρ^{sc} , \mathbf{j}^{sc} , respectively, is given at a certain time level $t = t_{n-1/2}$. In solving the Maxwell equations

$$(2.1) \quad \partial_t \mathbf{E} - c^2 \nabla \times \mathbf{B} = -\frac{1}{\epsilon_0} (\mathbf{j}^{ext} + \mathbf{j}^{sc}) ,$$

$$(2.2) \quad \partial_t \mathbf{B} + \nabla \times \mathbf{E} = 0 ,$$

$$(2.3) \quad \nabla \cdot \mathbf{E} = \frac{1}{\epsilon_0} (\rho^{ext} + \rho^{sc}) ,$$

$$(2.4) \quad \nabla \cdot \mathbf{B} = 0 ,$$

for instance numerically with a FV field solver, we obtain the electric field \mathbf{E} and magnetic induction \mathbf{B} at the new time level $t = t_n$ at the barycenters of the computational grid zones. Here, ∂_t and ∇ are the usual abbreviations for the time and space

derivation, respectively, and the permittivity ϵ_0 and permeability μ_0 of vacuum are related to the speed of light according to $\epsilon_0\mu_0c^2 = 1$. Afterwards, the electromagnetic fields \mathbf{E} and \mathbf{B} have to be interpolated to the actual position $\mathbf{x}_k(t_n)$ of the charged particles, where the index k runs over all particles inside the computational domain. The used interpolation scheme is an extension of the standard area-weighting method [25], properly calculates the interpolation weights for arbitrary quadrilateral BFC grid zones [31]. The electromagnetic fields at the particle position set up the Lorentz force

$$(2.5) \quad \mathbf{F}_k(t) = q_k [\mathbf{E}(\mathbf{x}_k, t_n) + \mathbf{v}_k \times \mathbf{B}(\mathbf{x}_k, t_n)] ,$$

acting on the charge q_k with the velocity $\mathbf{v}_k(t_n)$, which is responsible for the redistribution of the charged particles within the domain of interest. The new phase space coordinates are determined by solving the relativistic (electrons) and non-relativistic (ions) Lorentz equations:

$$(2.6) \quad \frac{d\mathbf{U}_k(t)}{dt} = \frac{\mathbf{F}_k(t)}{m_k} ; \quad \mathbf{U}_0 = \mathbf{U}_k(t_{n-1/2}) ,$$

$$(2.7) \quad \frac{d\mathbf{x}_k(t)}{dt} = \mathbf{v}_k(t) ; \quad \mathbf{x}_0 = \mathbf{x}_k(t_n) ,$$

where m_k denotes the mass and $\mathbf{U}_k = \gamma_k \mathbf{v}_k$, with $\gamma^2 = 1 + (\mathbf{U}/c)^2$, the relativistic velocity of the k -th charged particle. The particle-pushing according to the Lorentz equations (2.6), (2.7) is numerically performed by applying the second-order leapfrog-scheme [35] which possesses the advantage of time-centeredness and, hence, time reversibility. In order to obtain the new charge and current density distribution due to the movement, the particles have to be located with respect to the computational grid [37]. The resulting interpolation weights for the four barycenter corners surrounding the new particle position $\mathbf{x}_k(t_{n+1})$ are calculated, necessary for the assignment of the contribution of the k -th particle to the self-consistent charge and current density at the new time level $t = t_{n+1/2}$ [15].

Now, the iteration cycle is closed and the electromagnetic fields used for the next cycle have to be determined from the solution of the nonstationary Maxwell equations (2.1)-(2.4). Proceeding in this way by considering the linked interplay of Maxwell and Lorentz equations the self-consistent solution of this non-linear system is obtained.

3. THE FINITE-VOLUME METHOD BASED MAXWELL FIELD SOLVER

Solving Maxwell equations numerically we use in the KADI2D code high resolution FV methods [22] which are from the point of construction very evident and known to be very robust and able to resolve strong gradients without generating spurious oscillations. Numerical algorithms in the time domain are usually based only on the Maxwell equations (2.1) and (2.2). These equations may be recast in conservation form [15]

$$(3.1) \quad \partial_t u + \partial_{x_1} f_1(u) + \partial_{x_2} f_2(u) = q(u) ,$$

where we restricted ourselves to two space dimensions and assume that the vector of the electric field and magnetic induction

$$(3.2) \quad u = (E_1, E_2, E_3, B_1, B_2, B_3)^T$$

does not depend on x_3 . The essential aspect in this formulation is that the curl operator appearing in (2.1), (2.2) is replaced by component-by-component divergence applied to the fluxes $f_i(u) = K_i u$, $i = 1, 2$, where the K_i are constant (6×6) matrices (see e.g. [15]). The vector of the source terms $q(u)$ essentially contains the current densities of equation (2.1).

We assume that the physical domain is covered by a structured boundary-fitted grid composed by quadrilateral zones V_{ij} with the area $|V_{ij}|$. A FV scheme is obtained integrating the conservation equations (3.1) component-by-component over the space-time volume $V_{ij} \times [t_n, t_{n+1}]$. With the average of u over the grid cell V_{ij} at time $t = t_n$ defined as $u_{ij}^n = \frac{1}{|V_{ij}|} \int_{V_{ij}} u(x, t_n) dV$ we get the explicit standard FV scheme in conservation form

$$(3.3) \quad u_{ij}^{n+1} = u_{ij}^n - \frac{\Delta t}{|V_{ij}|} \sum_{\beta=1}^4 G_{ij,\beta}^n + \Delta t q_{ij}^n,$$

where the vector q_{ij}^n approximates the source terms averaged over V_{ij} and the time interval $\Delta t = t_{n+1} - t_n$. The so-called numerical flux through the boundary segments of V_{ij}

$$(3.4) \quad G_{ij,\beta}^n \approx \int_{S_{ij,\beta}} \left[n_{ij,\beta}^{(1)} f_1(u) + n_{ij,\beta}^{(2)} f_2(u) \right] dS$$

is an approximation of the dot product between the physical flux vector $(f_1(u), f_2(u))^T$ and the outwards directed unit vector $n_{ij,\beta} = (n_{ij,\beta}^{(1)}, n_{ij,\beta}^{(2)})^T$ normal to the edges $S_{ij,\beta}$ of V_{ij} . FV schemes are completely defined if the numerical fluxes are specified. The suitable calculation of these fluxes from averaged quantities at the time level $t = t_n$ is the main task in the context of FV methods.

One possibility of flux estimation is based on the solution of the so-called Riemann problem (RP) [15, 27], which can be solved exactly in the present case of linear hyperbolic equations. By the use of the RP solution the local structure of wave propagation is directly incorporated into the numerical approximation, responsible for the inherent robustness of these schemes. The simplest numerical flux approximation based on the solution of the RP known as Godunov method, is only first-order accurate in both space and time and, in general, not applicable for most practical purposes. To heighten the order of the schemes it is sufficient to improve the order of the numerical flux calculation: Applying the MUSCL (Monotonic-upwind-schemes for conservation laws) approach proposed by van Leer [21] a second-order space and time accurate TVD (Total Variation Diminishing) FV upwind-scheme is obtained [15, 27], which is implemented as the standard Maxwell field solver for the KADI2D program system.

Typical test problems for validating the implemented Maxwell solvers are the approximation of TM and TE standing waves, for which exact solutions are available [20].

The contour plots shown in Figure 1 are recorded at $t = 90$ ns (left) and $t = 180$ ns (right) and give an impression of the spatial distribution of the E_3 field component of a TM problem, where two wave trains are excited in each direction. The numerical results (lower two pictures) are obtained for a quadratic computational domain parallel to the axis but the grid lines inside the domain are strongly disturbed according to a sine curve [27]. The comparison with the exact solution (upper two pictures) plotted at the same computational grid convincingly shows the quality of the approximation.

An important part of solving numerically hyperbolic Maxwell equations is to specify the boundary conditions imposed at the border of the computational domain properly. Therefore, the finite-sized physical domain is surrounded by two additional stripes of grid zones called dummy cells in the following. If these dummy cells are covered with suitable values an effective flux calculation at the boundary of the computational domain is guaranteed and automatically incorporated into the FV

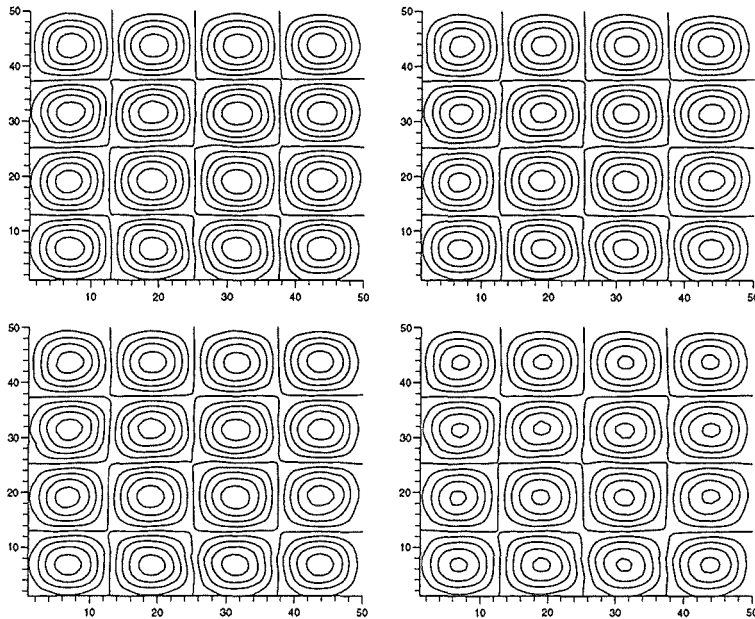


FIGURE 1. Spatial distribution of the E_3 field of a TM calculation on a strongly disturbed grid at $t = 90$ ns (left two plots) and $t = 180$ ns (right two plots). The inspection reveals that the numerically obtained result (lower two pictures) is in nearly perfect agreement with the exact solution (upper two pictures).

scheme. The numerical realization of both physically (like perfect conducting wall or irradiation of electromagnetic energy) and computationally (like open boundaries) motivated boundary conditions is founded in the framework of RP [15]. Checking simultaneously the numerical treatment of different kinds of boundary conditions for the Maxwell equations, we consider the radiation field of a simple 2d-dipole located at the origin of the (x, y) -plane for which a closed-form solution is known [15]. The finite-size computational domain for this problem is shown in Figure 2 consisting of a quarter ring with an inner and outer radius R_i and R_o , respectively. At R_i the theoretical result of the oscillating dipole is irradiated into the domain while open boundary conditions are imposed at R_o and symmetric considerations are necessary at the axis. The contour plot seen in Figure 2 is a snapshot of the numerically obtained B_2 dipole field distribution at $t = 30$ ns, clearly indicating that no visible wave reflection occur at the truncated numerical domain at R_o . By scanning the time variation of the B_1 field component at four fixed points in space ($R_1 = 1.01\text{m}$, $R_2 = 1.41\text{m}$, $R_3 = 2.59\text{m}$, $R_4 = 2.99\text{m}$) lying at the bisector of the angle of the first quadrant the exact solution (solid lines) and numerical approximation (open circles) reveal the high quality and accuracy of the applied methods.

For long-range calculations finding the existing stationary solution numerically as well as for problems showing high-oscillatory behavior or/and steep gradients in their solution high-order methods are necessary. Modern ENO (Essentially Non-Oscillatory) extensions of FV methods have been proposed recently [32, 33, 9, 18], exhibiting excellent improvements in numerical accuracy. This ENO approach is investigated with respect to our purposes and implemented as a further optional

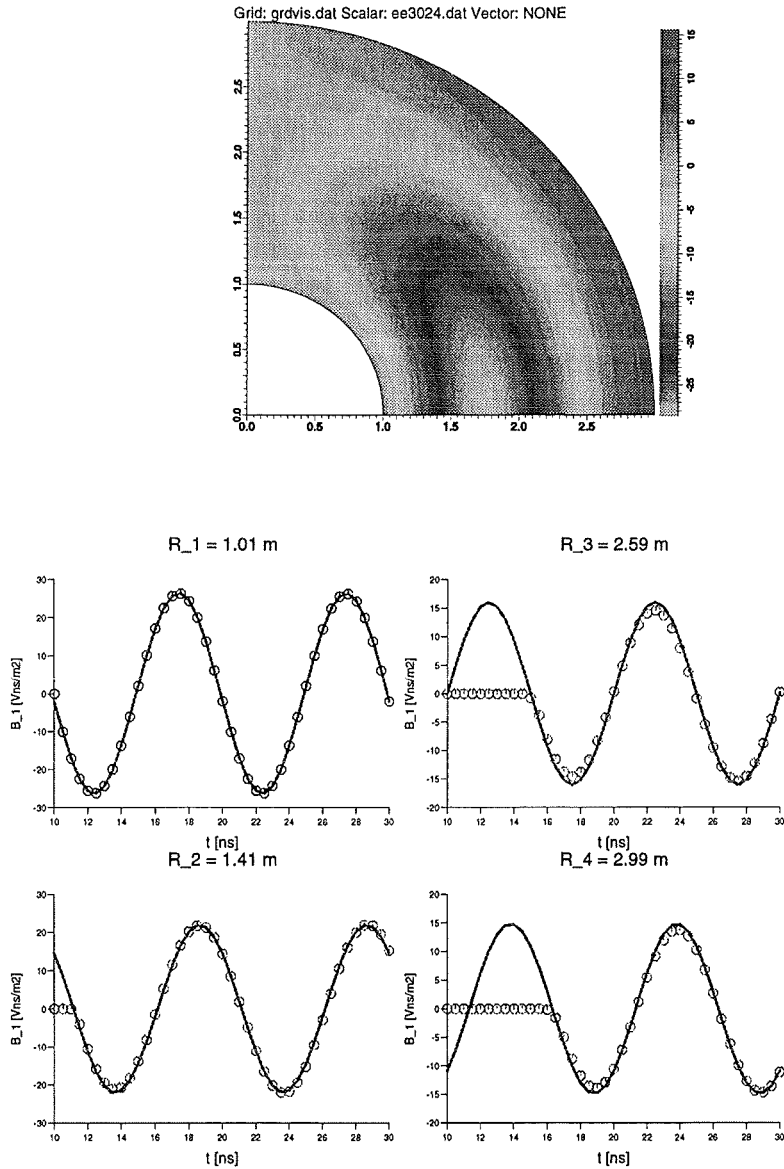


FIGURE 2. The upper picture shows the spatial distribution of the numerically obtained and exact B_2 dipol field solution. The exact solution is plotted left and the numerical approximation is plotted right of the bisector of the angle of the first quadrant at $t = 30$ ns. A quantitative comparison between the exact solution (solid lines) and the numerical result (open circles) of the B_1 field component at four different fixed points is depicted in the lower plot.

Maxwell field solver in KADI2D. The desired high-order numerical flux calculation is obtained by applying ENO-reconstruction methods. To achieve consistent numerical accuracy in time Runge-Kutta schemes are used to solve numerically a semi-discretized formulation of FV schemes in conservation form [6].

The result of a numerical experiment for a simple TM problem is depicted in Figure 3. There, the exact E_3 field solution (solid lines) is compared with three different numerical approximations at $t = 75$ ns (left) and $t = 150$ ns (right).

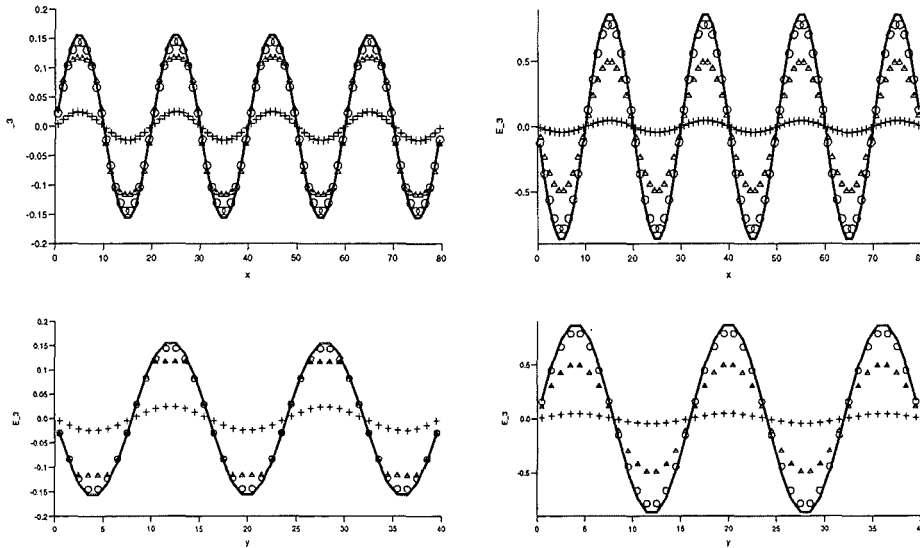


FIGURE 3. Comparison of the exact TM solution of the E_3 field component (solid lines) with three different numerical approximations at $t = 75$ ns (left) and $t = 150$ ns (right). The crosses, triangles and circles indicate the first-order Godunov, TVD MUSCL and ENO results, respectively.

Obviously, the first-order Godunov result (crosses) shows strong numerical damping while second-order TVD MUSCL approach (triangles) reproduce the exact standing wave solution very well. Clearly, the third-order both in space and time accurate ENO approach (circles) produce the best results: The form and amplitude of the wave shown are in nearly perfect agreement with the exact result. Furthermore, a series of numerical calculations with different grids have been performed, revealing a qualitative picture of the approximation quality of ENO schemes with different order. It is found out [27, 6] that the number of grid points could be considerably reduced using sophisticated ENO implementations and, hence, these schemes seemed to be very attractive for extension of the KADI2D code up to three dimensions in space.

4. A NEW APPROACH TO IMPROVE CHARGE CONSERVATION

A direct consequence of the fact that the divergence of the curl of a vector field is zero results in the equation of charge conservation

$$(4.1) \quad \partial_t \rho + \nabla \cdot \mathbf{j} = 0,$$

which is true for all times if \mathbf{E} , \mathbf{B} , \mathbf{j} and ρ fulfil the Maxwell equations (2.1)-(2.4). Otherwise, if (4.1) is valid for all times and initial data satisfy the divergence equations (2.3) and (2.4) then the solution of (2.1) and (2.2) automatically fulfil Gauss law (2.3) and the absence of magnetic monopole statement (2.4) for all times.

An important situation occurs when the Maxwell field solver is applied as one part in a self-consistent simulation of charged particles in electromagnetic fields: Each step of the PIC approach outlined in section 2 introduces numerical errors and a discrete analogue of the charge conservation (4.1) does not hold exactly or even with a defect of a certain order. Since only current density is used for the numerical field calculation, the consistency of $\epsilon_0 \nabla \cdot \mathbf{E}$ with charge density ρ may be lost. Several sophisticated correction methods imposing directly the divergence conditions by the introduction of correction potentials have been proposed [3, 23]. Since for practical

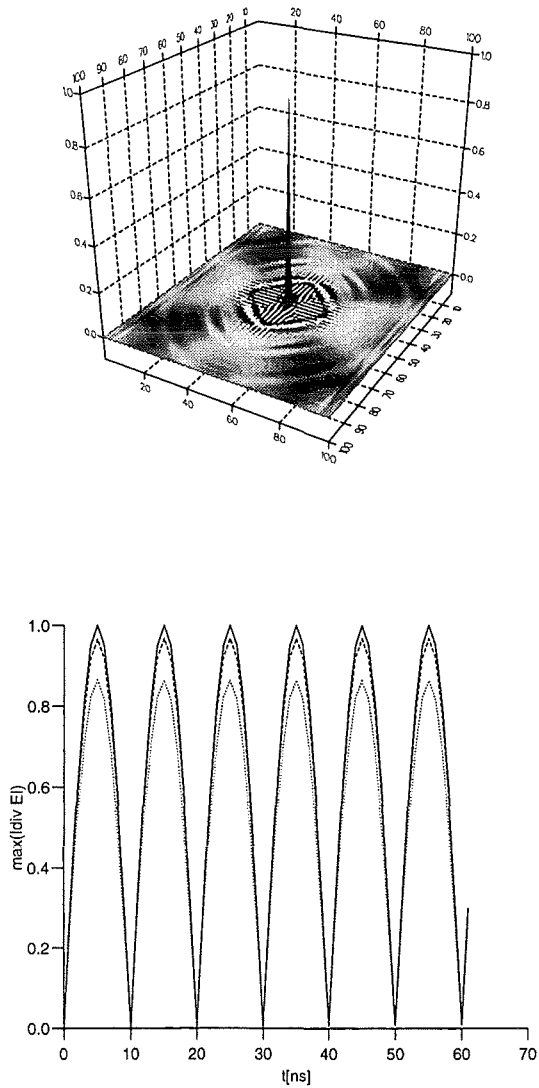


FIGURE 4. An overview of the exact solution of $|\nabla \cdot \mathbf{E}|$ at a certain time is given in the upper picture. The time history of the error $\max|\nabla \cdot \mathbf{E}|$ between the exact solution (solid line) and the numerical result (dashed line $\beta = 30$, dotted line $\beta = 20$) based on the strictly hyperbolic model (4.1)-(4.3) is depicted in the lower plot.

purposes the correction of the electrical field is much more important than those of the \mathbf{B} -field, we restrict ourselves only to the \mathbf{E} -field correction. Therefore, we adopt the approach of Assous et al. [1] and introduce the Lagrangean multiplier φ , which may be considered as a potential correcting the actual electric field. Additionally, we modify this system by introducing the term $\frac{1}{\beta^2} \partial_t \varphi$ and study the constrained,

strictly hyperbolic problem [28]:

$$(4.2) \quad \partial_t \mathbf{E} - c^2 \nabla \times \mathbf{B} + c^2 \nabla \varphi = -\mathbf{j}/\epsilon_0,$$

$$(4.3) \quad \frac{1}{\beta^2} \partial_t \varphi + \nabla \cdot \mathbf{E} = \rho/\epsilon_0,$$

$$(4.4) \quad \partial_t \mathbf{B} + \nabla \times \mathbf{E} = 0.$$

Here, β denotes the magnitude of the yet unknown parameter, which has to be estimated numerically. In contrast to the usual correction methods [8] this purely hyperbolic approach possesses the property that the information of correction or equivalent the errors due to Gauß law propagate with a finite velocity βc .

Without going into further details [28] we will briefly discuss the results of the simple test problem

$$(4.5) \quad \mathbf{E}_0 = 0, \quad \forall x$$

$$(4.6) \quad \mathbf{B}_0 = 0, \quad \forall x$$

$$(4.7) \quad \mathbf{j}_0 = 0, \quad \forall x, t$$

$$(4.8) \quad \rho(x, t) = \begin{cases} \rho_0 \sin(\omega t) & (x, y) = (x_0, y_0) \\ 0 & \text{elsewhere} \end{cases},$$

indicating that charge conservation is violated. The upper picture depicted in Figure 4 give a global idea of what happened: At a certain time the absolute value of $\nabla \cdot \mathbf{E}$ is, essentially, in a small circle around (x_0, y_0) nonzero, which means that the oscillatory behavior of a point charge is considered. A quantitative comparison between the exact and numerically obtained maximum of $\nabla \cdot \mathbf{E}$ on a nanosecond time scale is seen in the lower part of Figure 4. An acceptable small deviation from the exact solution is visible at the peaks only, indicating that the numerical result based on the hyperbolic model (4.1)-(4.3) establishes the consistency of $\epsilon_0 \nabla \cdot \mathbf{E}$ with the charge density ρ in a very impressive manner for this time-dependent test problem, which is difficult to deal with numerically.

5. ACTUAL AND FURTHER ACTIVITIES

An important building block to close the chain of field and particle treatment and consequently to verify the entire Maxwell-Lorentz program system is the particle generation module. At the moment, the field emission of electrically charged particles from the plasma surface is established by applying Gauß law under the Child-Langmuir condition. Two further emission scenarios describing the response of the preformed plasma surface to the fields inside the computational domain are under discussion [30] and are implemented to some extent in the KADI2D program. Extensive numerical experiments for idealized ion diode geometries are in progress to clarify the impact of different emission models to self-consistent particle simulations.

The computational effort running KADI2D on a present high performance computer is on the order of ten CPU-hours. A distinct reduction of the elapsed-time of the calculation can only be achieved if certain appropriate parts of the total simulation program are performed parallel on different processors. Hence, one important aspect within all stages of the present code development is the far-sighted choice and effective implementation of the algorithms, especially, in view of parallelization. First experience and preliminary results for an optimized version of parallelized particle treatment running on the CRAY J916 with 16 processors were reported in [7] recently. Further appropriate parallelization strategies for the Maxwell field solver based on domain decomposition methods are under investigation.

To ease the handling and to raise the attractivity of complex program systems such like KADI2D an adequate graphical user interface (GUI) is necessary. Based

on the tool command language Tcl and their toolkit extension Tk [29] a user friendly GUI for the KADI2D program system is under development. The acceptability of test releases indicate the possibility of effective handling and checking data files and the comfortable controlling of the BFCPIC and KADI2D code using powerful GUI.

Finally, combining the acquired knowledge and experience made with KADI2D and focussing our present endeavor it should be possible that a three-dimensional nonstationary extension of KADI2D for Cartesian grids is available during the course of this year.

Acknowledgements

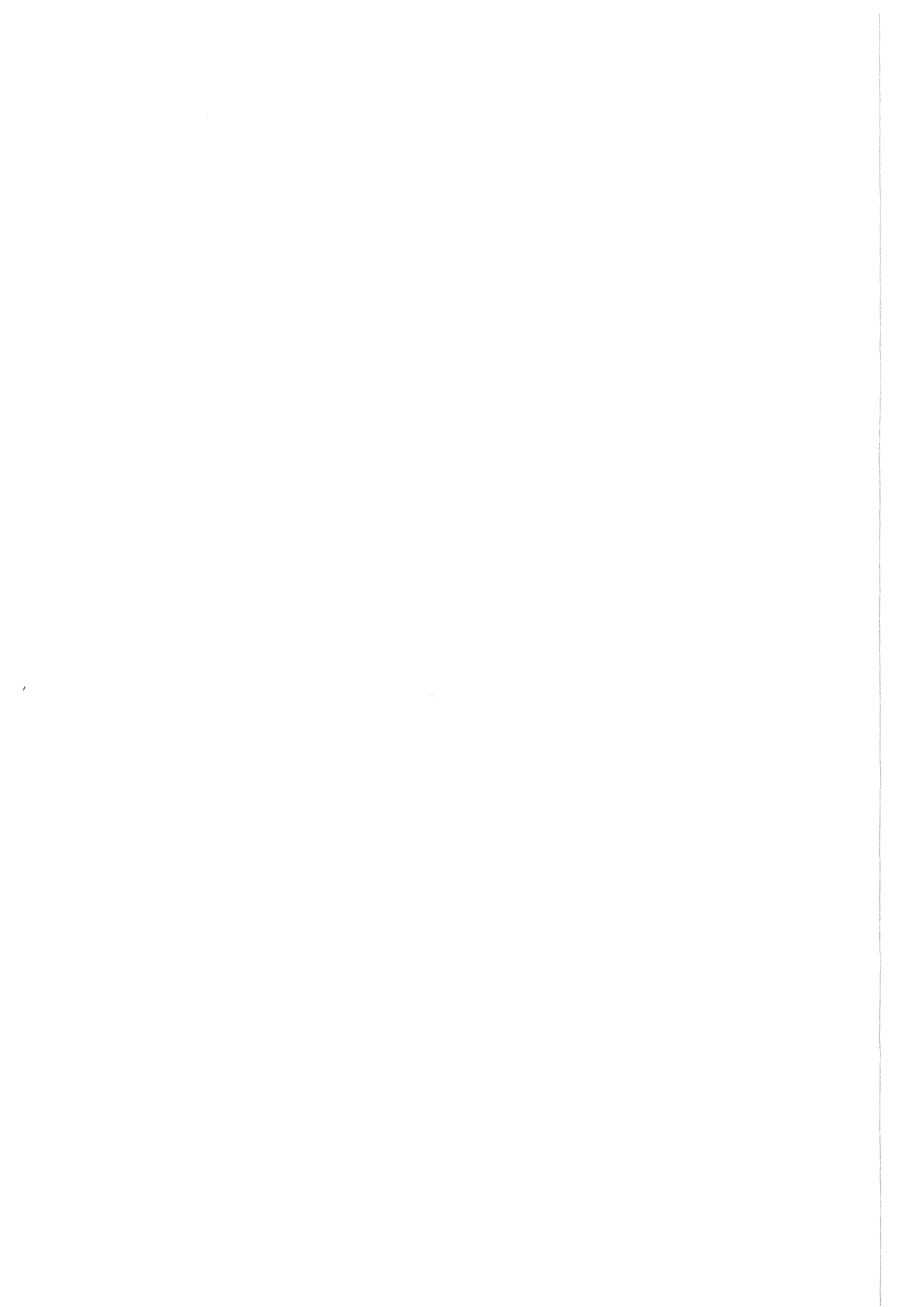
It is a pleasure to thank E. Borie and S. Illy for numerous stimulating and very helpful discussions as well as for fruitful mutual support. The authors furthermore gratefully appreciate advice by S. Illy concerning technical details in testing the Maxwell field solver.

REFERENCES

- [1] F. ASSOUS, P. DEGOND, E. HEINTZE, P. RAVIART, AND J. SEGRE, *On a finite-element method for solving the three-dimensional Maxwell equations*, J. Comput. Phys., 109 (1993), pp. 222–237.
- [2] W. BAUER, W. HÖBEL, A. LUDMIRSKY, E. STEIN, AND T. WESTERMANN, *A contribution to the magnetic focusing in an applied-B-extractor ion diode by a laser pulse driven solenoid*, in Proc. 10. Int. Conf. on High-Power Particle Beams, San Diego, San Diego, 1994.
- [3] C. BIRDSALL AND A. LANGDON, *Plasma Physics via Computer Simulation*, McGraw-Hill, New York, 1985.
- [4] H.-J. BLUHM, P. HOPPÉ, H. LAQUA, AND D. RUSCH, *Production and investigation of TW proton beams for an annular diode using strong radial magnetic fields and a preformed anode plasma source*, Proc. IEEE, 80 (1992), p. 995.
- [5] H.-J. BLUHM, H. LAQUA, L. BUTH, P. HOPPÉ, AND D. RUSCH, *Formation of a homogeneous hydrogen plasma layer for the production of Terawatt ion beams*, IEEE Trans. Plasma Sci., 21 (1993), p. 560.
- [6] M. BOGER, *Hochauflösende Finite-Volumen-Verfahren für die instationären Maxwellgleichungen*, PhD thesis, Fakultät für Mathematik der Universität Karlsruhe, 1996. Diploma thesis.
- [7] E. BORIE, E. HALTER, S. ILLY, M. KRAUSS, C.-D. MUNZ, R. SCHNEIDER, E. STEIN, U. VOSS, AND T. WESTERMANN, *Die numerische Simulation von elektrischen Apparaturen an gepulsten Hochspannungsanlagen*, FZKA-Nachrichten, Jahrg. 28, 2 (1996).
- [8] J. BORIS, *Relativistic plasma simulations – Optimization of a hybrid code*, in Proc. 4th Conf. on Num. Sim. of Plasmas, NRL Washington DC, 1970, pp. 3–67.
- [9] S. CHAKRAVARTHY, B. ENGQUIST, A. HARTEN, AND S. OSHER, *Uniformly high-order accurate nonoscillatory schemes III*, SIAM J. Numer. Anal., 24 (1987), pp. 279–309.
- [10] P. CLEMMOW AND J. DOUGHERTY, *Electrodynamics of Particles and Plasmas*, Addison Wesley, Reading, 1969.
- [11] R. DAVIDSON, *Theory of Nonneutral Plasmas*, Benjamin, Reading, 1974.
- [12] M. DESJARLAIS, *Impedance characteristics of applied-B ion diodes*, Phys. Rev. Lett., 59 (1987), p. 2295.
- [13] ———, *Theory of applied-B ion diodes*, Phys. Fluids B, 1 (1989), p. 1709.
- [14] M. DESJARLAIS, T. POINTON, D. SEIDEL, R. COATS, M. KIEFER, J. QUINTENZ, AND S. SLUTZ, *Evolution and control of ion-beam divergence in applied-B diodes*, Phys. Rev. Lett., 67 (1991), p. 3034.
- [15] E. HALTER, M. KRAUSS, C.-D. MUNZ, R. SCHNEIDER, E. STEIN, U. VOSS, AND T. WESTERMANN, *A concept for the numerical solution of the Maxwell-Vlasov system*, Forschungszentrum Karlsruhe – Umwelt und Technik, FZKA 5654, (1995).
- [16] E. HALTER AND J. KÜNDAHL, *InGrid, interaktive Gittererzeugung in der Produktsimulation*, tech. rep., Institut für Innovation und Transfer der FH Karlsruhe, FH Karlsruhe, Postfach 2440, 76012 Karlsruhe, 1994.
- [17] E. HALTER, J. KÜNDAHL, M. KRAUSS, C.-D. MUNZ, R. SCHNEIDER, E. STEIN, U. VOSS, AND T. WESTERMANN, *Interaktive Gittererzeugung im Rahmen eines offenen CAD-Systems*, 9. DGLR/AG STAB-Symposium 1994, Erlangen, (1994).
- [18] A. HARTEN AND S. CHAKRAVARTHY, *Multidimensional ENO schemes for general geometries*, ICASE Report no. 91-76, NASA CR-187637, 1991.
- [19] R. HOCKNEY AND J. EASTWOOD, *Computer Simulation using Particles*, McGraw-Hill, New York, 1981.
- [20] J. JACKSON, *Classical Electrodynamics*, Wiley, New York, 1975.
- [21] B. LEER, *Towards the ultimate conservative difference scheme V. A second order sequel to Godunov's method*, J. Comput. Phys., 32 (1979), p. 101.
- [22] R. LEVEQUE, *Numerical Methods for Conservation Laws*, Birkhäuser, Basel, 1990.
- [23] B. MARDER, *A method incorporating Gauss' law into electromagnetic PIC codes*, J. Comput. Phys., 68 (1987), pp. 48–55.
- [24] V. MOHAMMADIAN AND W. HALL, *Computation of electromagnetic scattering and radiation using a time-domain finite-volume discretization procedure*, Computer Physics Communications, 68 (1991), pp. 175–196.
- [25] R. MORSE AND C. NIELSON, *Numerical simulation of the Weibel instability in one and two dimensions*, Phys. Fluids, 14 (1971), p. 830.
- [26] C.-D. MUNZ, R. SCHNEIDER, E. STEIN, AND U. VOSS, *Simulation of charged particles in self-consistent electromagnetic fields for technical relevant devices using KADI2D*, in Preparation, (1996).
- [27] C.-D. MUNZ, R. SCHNEIDER, AND U. VOSS, *A finite-volume method for Maxwell equations in time domain*, submitted, (1996).

- [28] C.-D. MUNZ AND U. VOSS, *A purely hyperbolic method for incorporating Gauß' law into Maxwell solvers in time domain*, in Preparation, (1996).
- [29] J. OUSTERHOUT, *Tcl und Tk*, Addison Wesley, Bonn, Paris, 1994.
- [30] R. SCHNEIDER AND C.-D. MUNZ, *The numerical approximation of two-fluid plasma flow with explicit upwind schemes*, Int. J. Num. Modelling, 8 (1995), pp. 399–416.
- [31] D. SELDNER AND T. WESTERMANN, *Algorithms for interpolation and localization in irregular 2D meshes*, J. Comput. Phys., 79 (1988), p. 1.
- [32] C.-W. SHU AND S. OSHER, *Implementation of essentially non-oscillatory shock capturing schemes I*, J. Comput. Phys., 77 (1988), pp. 439–471.
- [33] ———, *Implementation of essentially non-oscillatory shock capturing schemes II*, J. Comput. Phys., 83 (1989), pp. 32–78.
- [34] J. THOMPSON, Z. WARSİ, AND C. MASTIN, *Boundary-fitted coordinate systems for numerical solution of partial differential equations - A review*, J. Comput. Phys., 47 (1982), p. 1.
- [35] T. WESTERMANN, *Teilchenfortbewegung in elektro-magnetischen Feldern*, Kernforschungszentrum Karlsruhe GmbH, KfK 4325, (1988).
- [36] ———, *Optimization by numerical simulation of the focusing properties of self-magnetically insulated ion diodes*, Appl. Phys. Lett., 58 (1991), p. 696.
- [37] ———, *Localization schemes in 2D boundary-fitted grids*, J. Comput. Phys., 101 (1992), p. 307.
- [38] ———, *Numerical modelling of the stationary Maxwell-Lorentz system in technical devices*, Int. J. Num. Mod., 7 (1994), p. 43.

IV Target physics



Hydrodynamic Beam-Target Experiments on KALIF

K. Baumung, L. Buth, R. Huber, D. Rusch, J. Singer, O. Stoltz, *INR*
S.V. Razorenov*, A.V. Utkin*, G.I. Kanel*

The hydrodynamic response of 10- to 100- μm -thick targets can provide information on ion beam parameters like proton range, power density, and ablation pressure, as well as the dynamic tensile strength of the target matter under intense stress at nanosecond load durations. The primary information in all experiments is the velocity of the target surface opposite to the ion beam measured by high-resolution laser Doppler velocimetry. In the report period, beam diagnostics experiments concentrated on the later time period of the ion pulse. For the first time, spatially resolved dynamic tensile strength measurements were performed across a grain boundary showing that in polycrystalline materials, with short pressure wavelengths, individual crystal grains fail independently.

1. Introduction

The interaction of a pulsed high-power ion beam with condensed matter leads to a rapid energy deposition within a layer of finite thickness. The thermal expansion can not follow the temperature rise, and high pressure builds up. In the hydrodynamic target experiments performed on KALIF we utilize the mass flow induced by this pressure build-up, and the resulting motion of the target surface opposite to the beam to investigate the beam properties, the beam-target interaction, and properties of condensed matter under nanosecond loading at pressure levels of several tens of GPa [1]. The measured quantity is the velocity of the rear target surface. This can be a free surface velocity u_{fs} , or - if the target surface is in contact with an appropriate transparent barrier - directly the mass flow, or particle velocity, u_p can be measured. The measurements are performed by remote laser Doppler velocimetry at a high temporal resolution (≥ 0.2 ns), and zero-dim, or 1-dim spatial resolution at a maximum resolving power of ~ 10 μm [2]. In the report period, experiments on beam diagnostics, dynamic tensile strength of solids, and hypervelocity launching were performed.

2. Beam-target interaction diagnostics: improving the sensitivity up to peak voltage

A space-time-, or x,t -diagram, of the hydrodynamic phenomena encountered with the beam target interaction is shown in fig. 1. Protons leaving the anode plasma move at a velocity corresponding to the actual diode voltage. On their 15-cm-trajectory to the target (with the B_\ominus -diode), protons starting at a low acceleration voltage earlier in the pulse can be overtaken by more energetic ones starting later. With time constants of the pulse rise of 8-12 ns in a normal KALIF shot protons with energies between 0.3 and 0.8 MeV may reach the target within ~ 1 ns (see fig.2). This time-of-flight compression or "bunching" of the ion beam front results in a short burst of the power density that can be comparable with the peak value

* Permanent address: Russian Academy of Sciences, Inst. of Chemical Physics, Chernogolovka 142432

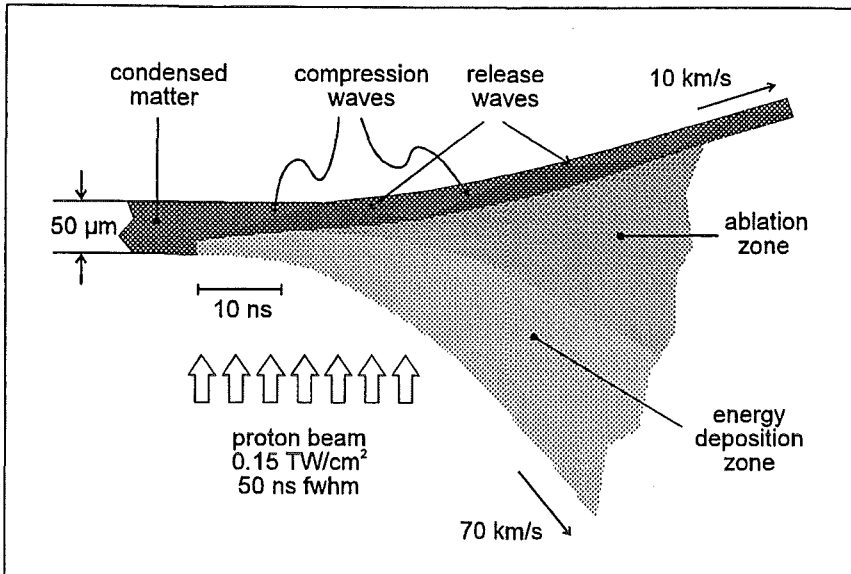


Fig. 1:

Schematic of the processes during the beam target interaction with a thin target. x, t -diagram with typical figures for an experiment with the 0.15 TW/cm^2 beam of the B_{θ} -diode and an aluminum target

reached at the voltage maximum. In aluminum, these intermediate energies correspond to proton ranges of up to $10 \mu\text{m}$. As a result, a substantial specific energy is deposited into cold - that means little compressible - and dense material that the thermal expansion can not follow. High pressure builds up which causes a compression wave to propagate with the so-called bulk sound velocity of $c_b \approx 7 \text{ km/s}$ into the adjacent cold material (the sound velocity under normal conditions is $c_0 = 5.3 \text{ km/s}$). Associated with this first compression ($\rho/\rho_0 \approx 1.2$) is a mass flow or particle velocity u_p of typically $\sim 1.25 \text{ km/s}$ in aluminum targets. On its arrival at the rear free surface the compressed matter expands and thereby accelerates the surface to a velocity $u_{fs} \cong 2 \times u_p$. This is the first information of the beam interaction at the rear surface that can be recorded by the laser Doppler interferometer. The material expansion propagates as a release wave back into the target. On contact with the energy deposition zone the expanded matter is again pressurized, and another compression wave propagates to the rear surface. Reverberations of compression and rarefaction waves successively accelerate the residual condensed part of the target (see fig. 1). On the beam side the decompression goes along with a rapid expansion or ablation of the hot plasma that forms in the energy deposition zone. As the acceleration voltage rises the proton range δ increases and makes the energy deposition zone advance into the adjacent condensed matter at a velocity v_R . However, this together with the increase of the power density only results in a $\sim 10 \text{ ns}$ pressure stabilization at a level below the initial peak value (see fig. 3). As soon as the slope of the power density rises reduced the pressure starts to fall. In the beginning, the pressure - and thus the particle velocity u_p - at the

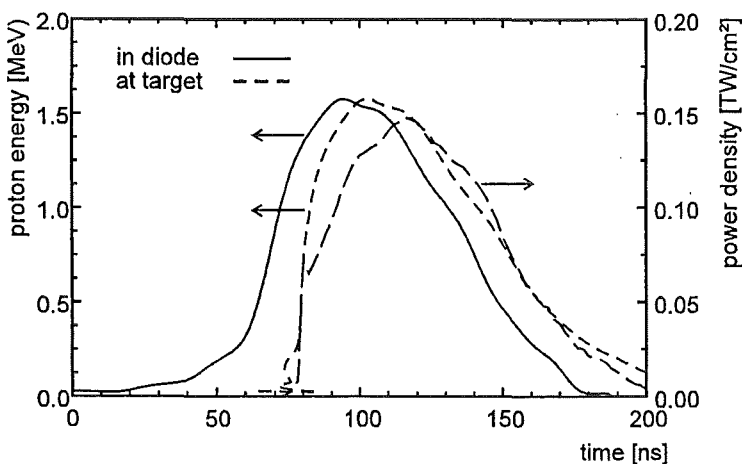


Fig. 2:

Acceleration voltage in the diode, time of flight corrected proton energies in the position of the target, and power density on target as a function of time

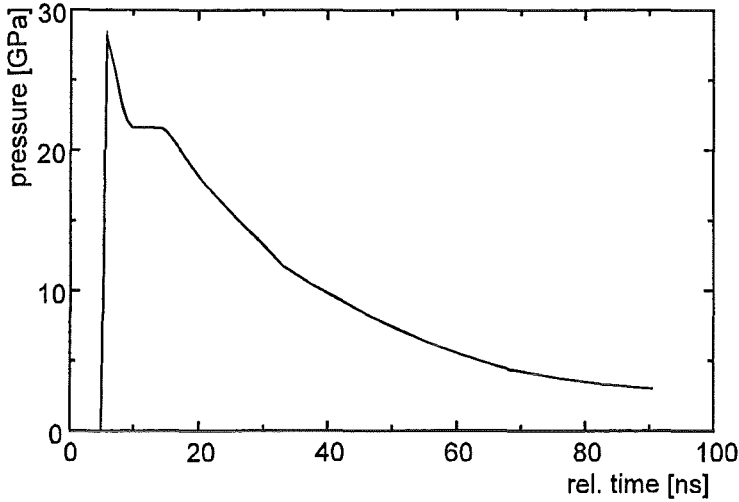


Fig.3

Ablation pressure generated in aluminum by the 0.15 TW/cm² beam of the B_θ-diode

boundary of the energy deposition zone to the cold target material (located at δ_{\max}) rise until, at time $\tau = \delta_{\max} / c_b$ after the onset of the interaction, the expansion wave starting from the free surface of the energy deposition zone reaches this boundary. This causes the slope of the u_p -rise to decrease drastically or, depending on the particular power history, even leads to a decrease of u_p . In our case, the expansion wave propagates at a bulk sound velocity c_b that is close to the “shock velocity“ u_s , at which the pressure wave propagates, and that is determined from the particle velocity as

$$u_s = c_0 + S u_p \approx 7 \text{ km/s} \quad (1)$$

where S is a material constant. With initial ranges of up to 10 μ m we obtain $\tau \approx 1$ ns. Equ. (1) is a commonly used fit of the Hugoniot equation of state to experimental data. The other hydrodynamic quantities, density ρ , and pressure p can be determined from the mass conservation (2) and the momentum conservation (3) laws. For initial zero particle velocity and pressure these relations are

$$\rho_0 u_s = \rho_1 (u_s - u_p) \quad (2)$$

$$p = \rho_0 u_s u_p \quad (3)$$

The Hugoniot EOS is not a complete thermodynamic EOS since temperature is contained only implicitly in the specific internal energy E

$$E = E_0 + \frac{1}{2} (V_0 - V) p \quad (4)$$

where $V=1/\rho$ is the specific volume. The specific energy and the pressure can be split into a “cold” contribution that is due to the compression of the condensed matter, and a “thermal” contribution that is due to the thermal excitation of atoms, molecules, or ions, and conduction electrons. In the Mie-Grüneisen approximation, this thermal contribution to the pressure is

$$p_{\text{th}} [\text{GPa}] = \frac{\Gamma}{V [\text{cm}^3/\text{g}]} E [\text{kJ/g}] \quad (5)$$

where the Grüneisen coefficient $\Gamma = \Gamma(V)$ depends on the density only. During the first few nanoseconds of the interaction of the beam front with the cold target the pressure in the energy

deposition zone can be attributed to the thermal part only. Assuming furthermore that in this early phase the density has not yet changed significantly the power density in the beam front can be estimated as follows. As mentioned above, the maximum proton range δ_{\max} in the beam front can be determined from the rise time τ_r of the initial acceleration of the rear target surface as $\delta_{\max} = c_b \tau_r \approx u_s \tau_r$. The initial pressure is calculated from the measured jump of the particle velocity reached at time τ_r using equ. (1) and (3). Taking the Grüneisen coefficient for normal density ($\Gamma = 2.0$ for aluminum) the average over τ_r of the power density I in the beam front is

$$I = \frac{P_0}{\Gamma} u_p (c_0 + S u_p)^2. \quad (6)$$

The first jump of the free surface velocity is typically $u_{fs} = 2.5$ km/s with the B_o-diode in aluminum giving $u_p = 1.25$ km/s. This yields an initial power density of $I \approx 0.01$ TW/cm². This is much less than the value shown in fig. 2. However, since in the B_o-diode the proton current cannot be measured directly it is assumed that it amounts to 25% of the total KALIF current, the other part being mainly due to electrons, to some contributions from other ion species, and probably to other effects. A more detailed analytical treatment employing an acoustic approximation [3] based on the same assumption on the Grüneisen coefficient, and allowing for the power density increase rate yields similar values for the initial jump, and increase rates $dI/dt \approx 0.001-0.02$ TW cm⁻²ns⁻¹ depending on the respective power trace. Since the time of flight of the protons is comparable with the rise time of the KALIF pulse minor changes of the voltage pulse shape introduce significant changes in the power density profile of the pulse front. The above results for I and dI/dt are in reasonable agreement with Faraday cup, and nuclear activation measurements of the power density [4].

Because the KALIF pulse is longer than the wave transit times in both the energy deposition zone and the cold part, the wave reverberations induced in the beginning of the interaction superimpose and blur the effects of further energy input. Later into the pulse, in addition to these perturbations, the hydrodynamic response of the residual condensed part of the target to the power density history is reduced and finally canceled by two effects: At first, the massive energy deposition leads to a rapid decrease of the density by material ablation. This, in turn, increases the compressibility of the matter, and reduces the Grüneisen parameter to a stationary value of $\Gamma = 0.25$ for aluminum plasma of 0.01 g/cm³, respectively. According to equ. (5), the pressure can be maintained only if the expansion (increase of the specific volume V) is compensated by a corresponding increase rate of the power density [5]. Later into the pulse, the energy deposition zone hydrodynamically uncouples from the residual condensed part (cf. fig. 1), at first due to shortening effects on the proton range in the hot ablation plasma [6], and eventually by the KALIF voltage decrease. At the end of the KALIF pulse the expansion velocity is of the order of 100 km/s. This is by one order of magnitude greater than the bulk sound velocity. As a consequence, beyond a certain time close to the time of peak voltage the energy deposition zone “disappears behind the sonic horizon”, that means no more hydrodynamic effects due to further energy deposition can reach the residual target.

However, the sensitivity of the hydrodynamic response at least up to this uncoupling can be improved with experiments using filter foils upstream the target (see fig. 4). In order to avoid hydrodynamic interactions between the two foils during the 30 ns of interest the filter was placed 2 mm in front of the target. The filter thickness was varied from 10 to 22.5 μm , and the total thickness was adjusted to approximately 30 μm in order to obtain results comparable with previous single foil experiments using 33 μm foils. The filters act as energy threshold discriminators keeping away from the target protons with effective ranges smaller than the filter foil thickness. The penetrating protons lose a significant part of their energy in the filter

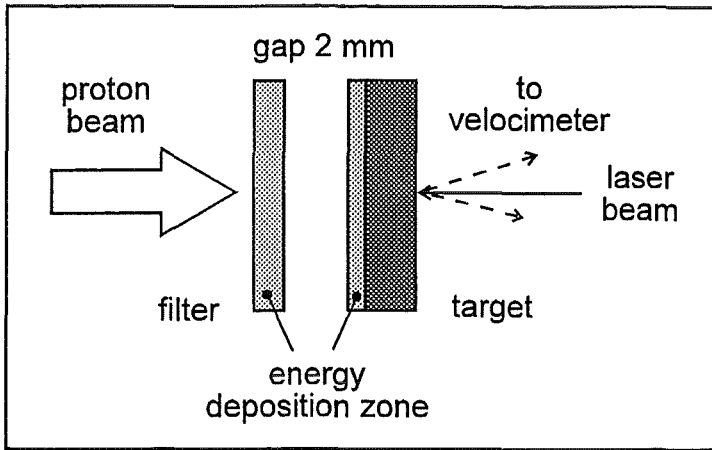


Fig. 4:

In composite targets, the hydrodynamic response of the energy deposition in the filter is separated from the target by a gap. Protons penetrating the filter deposit their residual energy in cold target material generating a clear signal that can be interpreted by an analytical model.

but deposit their residual energy in cold material, and generate a clear hydrodynamic response (see fig. 5) which again can be analyzed by an acoustic approximation assuming the constant Grüneisen coefficient for cold material. In contrast to the above case of the beam front interaction where the proton range could be assumed constant, too, in experiments with filters the first protons reaching the target have energies close to zero (since they just succeeded in penetrating the filter) but then the range increases rapidly according to the voltage rise.

To interpret these experiments, an improved analytical model was established allowing for the linear increase in time of both power density and range [7]. If the proton range, or the boundary of the energy deposition zone to the cold material, respectively, propagate at a subsonic velocity $v_R < c_b$ the particle velocity u_p should rise as long as the proton range increases. However, decompression waves starting from the free surface propagate at the bulk sound velocity c_b which is approximately twice the range increase velocity $v_R \leq 3.5$ km/s in experiments with filters. As a consequence, the rise time is given by the oppositely directed effects of increasing energy deposition, and the advancement of the deposition zone into cold material on one side, and the decompression by material ablation on the other side. The proton range in the target is determined from the wave reverberation period $\Delta t = \tau_2 - \tau_1$ (cf. fig 5) for the instant when the rarefaction wave coming from the rear target surface contacts the boundary of the energy deposition zone. This instant, and thus the proton energy, can be chosen by the appropriate target and filter thicknesses. The total proton range is determined by the filter thickness plus the range in the target. This method allowed to determine the range of 1.35 MeV protons in the hot aluminum ablation plasma to be 5.6 mg/cm^2 ($21 \mu\text{m}$). Keeping in

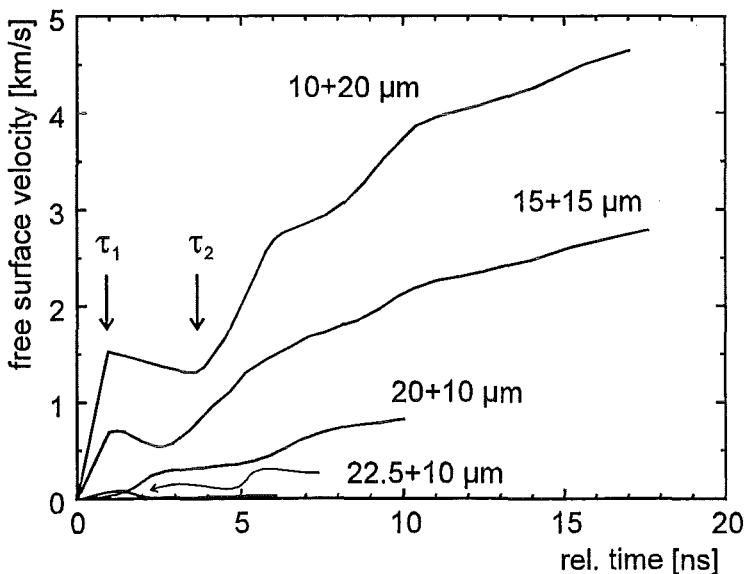


Fig. 5:

Free surface velocity profiles measured with different filter + target foil thicknesses. The two foils are hydrodynamically uncoupled by a 2 mm gap. The hot plasma shows an enhanced stopping power compared with cold material. The 22.5- μm -thick filter nearly absorbs all protons while the range corresponding to the peak energy in cold material is 27 μm .

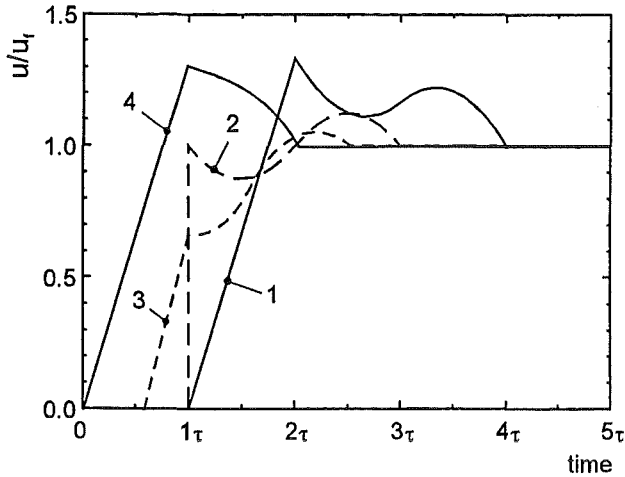


Fig. 6:

Particle velocity profiles at the position of the maximum range obtained from the analytical model for different range increase velocities v , normalized to the final velocity u_f . The peak amplitudes depend on the power density increase rate. (1): $v_R < c_b$; (2) $v_R = c_b$; (3) $v_R > c_b$. Curve (4) holds for constant, non-zero range corresponding to $v_R = \infty$.

mind the experimental uncertainties and the simplifications of the model, this compares well with the range of 1.53 MeV protons of 6.1 mg/cm^2 ($22.5 \text{ }\mu\text{m}$ at normal density) found in transmission experiments (cf. fig. 4). This latter value is significantly less than the range of 7.3 mg/cm^2 ($27 \text{ }\mu\text{m}$) given in tables for cold material and reflects the enhancement of the stopping power in hot matter.

The analysis of the dependence of the velocity profile on the range increase velocity v_R (see fig. 6 showing the normalized particle velocity in the position of the maximum proton range δ_{max}) gives a result that, at first, is somewhat surprising: the rise time of the velocity is finite for both subsonic ($v_R < c_b$, case 1) and supersonic ($v_R > c_b$, case 3) regimes. Only if the range increase velocity *exactly equals* the bulk sound velocity ($v_R = c_b$, case 2) the rise time becomes zero, that means a shock wave forms directly by the beam interaction. In single aluminum targets the rise times are 1-2 ns, and the pressure pulse has to propagate through a layer of 20-30 μm of condensed matter before steepening to a shock front discontinuity. The time unit $\tau = \delta_{\text{max}}/c_b$ chosen for fig. 6 is the wave transit time through the layer of thickness δ_{max} . The beam target interaction starts at $t = 0$. Consequently, in case 1, and 2, the first information about the onset of the beam interaction arrives in this position at time τ . In case 3, the velocity starts to increase at time $t = \delta_{\text{max}}/v_R < \tau$ and changes the slope upon the arrival, at time τ , of the release wave starting from the free surface of the energy deposition zone. Case 4 is the approximation for the interaction of the bunched beam front with a constant range δ_{max} considered above. The particle velocity (in the position δ_{max}) starts increasing as soon as the beam hits the target ($t = 0$) until, at time τ , the decompression wave arrives from the free surface.

The increase rate of the power density deduced from this model for filter-target-combinations give values $dI/dt < 10^{-3} \text{ TWcm}^{-2}\text{ns}^{-1}$ that are by one order of magnitude lower than the values given above for the single target. The analysis also confirms that the particle velocity and pressure, respectively, not only depend on the power conditions but also on the proton range. The greater the range the longer pressure builds up at the boundary of the energy deposition zone, the material layer behind acting as a tamper. This lead us to the iconcept for the improvement of the hydrodynamic efficiency presented in the next section.

Because of the interest in the simulation of experiments [8] in which an ablatively accelerated aluminum foil impacts a thick window made of LiF single crystal showing nearly identical hydrodynamic behavior, some additional measurements were made varying the time of impact by choosing different initial gaps between the flyer foil and the window.

2.2. Hypervelocity launching of composite targets

Launching projectiles to hypervelocities (i.e. to velocities beyond the scope of military guns which is several km/s) is a challenging task in shock wave physics. In particular, the velocity interval between 10 and 20 km/s closing the gap between what can be achieved with sophisticated two-stage gas guns, and explosives-driven multi-layer arrangements, respectively, and the domain of underground explosions is of interest, and seems to call for new approaches. The impact of flyers at these velocities allows to generate pressures > 1 TPa (10 Mbar).

On KALIF we have launched 10 to 20- μ m-thick aluminum flyers to velocities > 12 km/s. However, the hydrodynamic efficiency, i.e. the ratio of kinetic energy per cm^2 of the projectile and ion beam energy input per cm^2 is 1% with the B_Θ -diode, and 0.5% with the appl-B-diode

only. It is lower for the appl.-B diode because of the time delay of ~ 10 ns needed to reach the design working point. As a result, the current carried by the bunched beam front is relatively small and induces a particle velocity which is by a factor of 4 smaller than with the B_Θ -diode. On the other hand, the energy input is high enough to pre-heat and expand the energy deposition zone and thus reduce the Grüneisen coefficient. Therefore, the main energy deposition causes a smaller effect than in cold matter.

The above analysis has shown that the ablation increases until the release wave caused by material ablation reaches the boundary of the energy deposition zone to the cold material. That means that the pressure can be increased by increasing the range. This can be achieved by increasing the ion energy or by a low-density target material. Although the specific energy deposition increases for low-density materials the achievable pressure is higher in high-density materials (cf. equ. 5, $\Gamma = 1.5 \div 3$ for condensed materials) for a given accelerator voltage and beam energy. On the other side, the pressure achievable with a given specific energy is determined by the reduction of the Grüneisen coefficient and, above all, by the drop of the density due to the material ablation. Finally, as follows from fig. 1, the acceleration results from the reverberation of compression and release waves between the free surface and the energy deposition zone which propagate at the bulk sound velocity c_b .

Keeping in mind all these details we conceived the following scheme of a triple layer target in order to improve the hydrodynamic efficiency (see. fig 7). The ablator consists of a layer of polycrystalline diamond. This material has a comparatively high density of $\rho = 3.51 \text{ g/cm}^3$ and a very high bulk sound velocity ($c_b \approx 12 \text{ km/s}$). The thickness of 11 μm was chosen in order to stop completely 1.5 MeV protons, which are slightly slowed down by the tamper, inside the ablator. The diamond samples were fabricated by CVD-deposition on 0.5-mm-thick Si-wafer substrates of 30 mm diameter. The wafers were laser cut to four quarters, and the silicon removed by chemical etching over an area of $\sim 4 \times 8 \text{ mm}^2$ in order to obtain free-standing diamond films (office by H. Bachmann, Philips Res. Labs , Aachen). The films are smooth on the side on which they grew on the polished substrate and show 1- μm -roughness on the opposite side. The payload of 10 μm titanium was deposited on the smooth side by sputtering (Forschungsinst. f. Edelmetalle u. Metallchemie, Schwäbisch Hall). The method and the

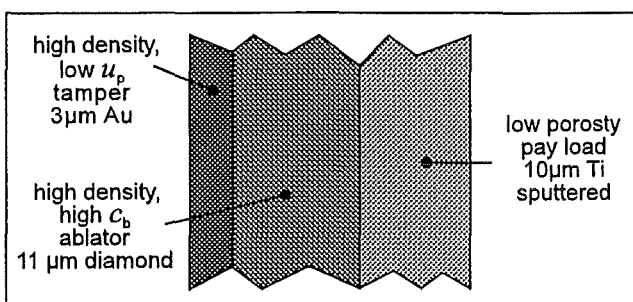


Fig. 7:

Triple layer target combining a tamper with low particle velocity u_p , an ablator with high bulk sound velocity c_b , and a payload of low porosity.

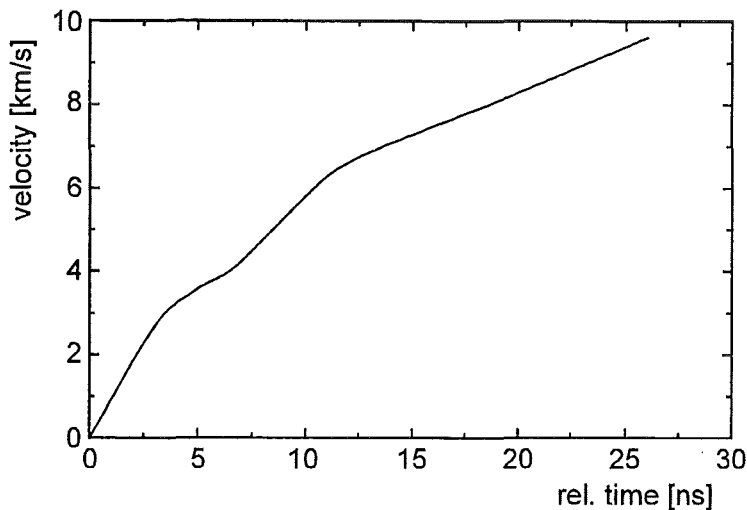


Fig.8:

Acceleration of a triple-layer target consisting of a 11 μm diamond ablator, a 3 μm Au tamper and a 10 μm Ti payload (cf. fig. 7).

material were chosen because they are best suited to provide homogeneous layers of nearly theoretical density. The gold tamper was applied in a vacuum vaporizer. The final thickness of $\sim 3 \mu\text{m}$ was much more than the initially intended value of "at least $2 \mu\text{m}$ " due to the failure of the thickness gauge during the coating process. The two experiments we performed with these targets showed (see fig. 8) that the tamper thickness was definitely too large. The acceleration is steady, and in particular, does not show the steep jump caused by the bunched beam front with simple targets. The measured peak velocity of $\sim 10 \text{ km/s}$ looks promising (cf. fig. 8). Upon impact, this flyer would induce a pressure of +2.3 Mbar in titanium and $\sim 4 \text{ Mbar}$ in a heavy material like gold.

2.3. Dynamic tensile strength measurements at high strain rates

The possibility to generate very short compression pulses in solid samples, and to perform

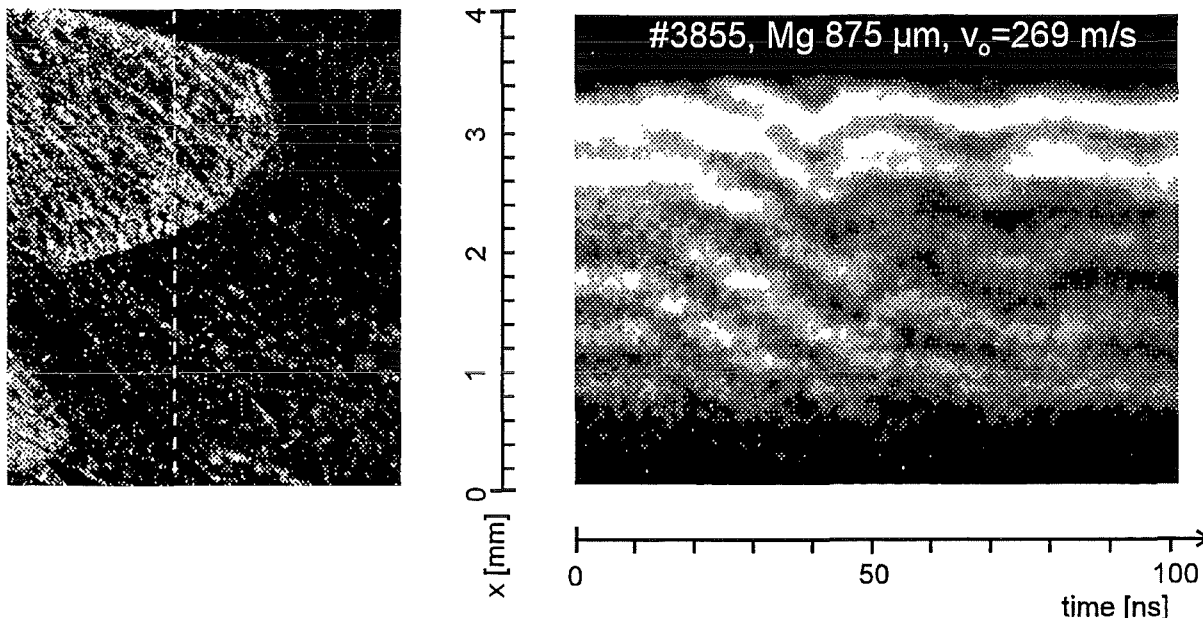


Fig. 9: Spalling of a magnesium sample across a grain boundary. The picture on the left shows a close-up of the sample with the measuring line indicated. Depicted on the right side is the 2D-ORVIS record, showing spall pulses of different lengths in the upper and lower crystal grains, indicating different tensile strengths due to different orientations relative to the strain normal to the surface.

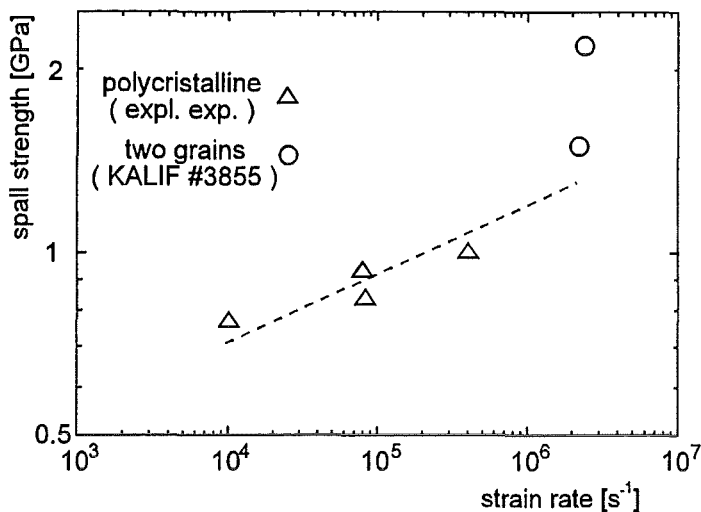


Fig. 10:

Spall strength of 99.95 magnesium as a function of the strain rate. Comparison of the results obtained on two millimeter-size adjacent grains on KALIF in the experiment shown in fig.8 and on polycrystalline material using explosive loading (courtesy G.I. Kanel).

free surface velocity measurements with high temporal resolution provides a unique opportunity to study the strength of materials under nanosecond load duration. The dynamic tensile strength is measured by the analysis of spall phenomena under shock pulse action.

Spalling is the process of internal failure or rupture of a body due to tensile stresses generated as a result of the reflection of a short compression pulse from a free surface of the sample. The reflected wave is a stress wave running back into the material thereby increasing its amplitude until the failure threshold is reached. The stress amplitude leading to fracturing, the so called "spall strength", can be unambiguously determined from the free-surface velocity profiles as detailed in the 1994 report [9].

The characteristic thickness of the fracture zone at nanosecond load durations is comparable with or probably even less than the grain size of the sample. Consequently, it is interesting to perform measurements on homogeneous specimen like single crystals. They are largely free from various stress concentrators that can be damage nucleation sites in usual materials. The investigation of spalling of single crystals therefore provides information about the conditions of damage nucleation on a structure level close to ideal crystal structure and is of fundamental interest in physics of strength. This is why we performed tensile strength measurements on single crystals in earlier experiments [10,11].

On the other hand, there is also an interest in understanding the failure mechanism in polycrystalline bulk material. With our spatially resolving velocimeter we have demonstrated for the first time that the tensile strength of polycrystalline materials shows a clear spatial variation [9].

To investigate in more detail the spall process in the vicinity of a grain boundary magnesium samples with grain sizes of the order of millimeters were investigated. The sample thicknesses were in the range of 0.8 mm. Since the amplitude of very short shock waves generated by the impact of 10-30 μm thick foils would significantly decay on passing through a sample of that thickness we used the compression wave generated by the direct beam interaction. In fig. 9 a macro picture of a Mg sample showing a grain boundary is displayed together with the spatially resolved ORVIS record of the spall process. The velocity decrease in the time interval from 15 to 50 ns - recognizable by the negative slope of the interference fringes - is due to the build-up of tensile stresses which form after the reflection of the initial pressure wave at the free boundary. This deceleration is stopped when the material disrupts. Obviously, that happens at different tensile stresses in the two crystal grains, the grain boundary being a boundary for the rupture process, too.

The tensile strengths determined from this measurement is displayed as a function of the strain rate together with data obtained by the explosive loading technique on polycrystalline samples in fig. 10. The increase of the spall strength with the strain rate is due to the finite

relaxation times of the damage processes leading to rupture. The relaxation length of the stress wave is several millimeters in explosive driven experiments and thus much smaller than the grain size. Since, in particular, grain boundaries act as damage nucleation sites the spall strength is smaller in this material. Single crystals are largely free from imperfections and show higher spall strengths. The difference in the two grain is probably due to the different orientation of the lattices relative to the plane of the stress wave.

3. Conclusions

In the report period, one experimental campaign was conducted investigating beam-target interaction issues with composite samples, hypervelocity launching of triple-layered targets, and the spatial variation of dynamic tensile strength of coarse-grained samples across single grain boundaries. The beam-target experiments have improved our understanding of the main factors governing the ablative acceleration and the state of thin flyer plates and will help us to optimize the launching process for applications in the range beyond 10 km/s. This would open the possibility to investigate, by impact experiments, the state of matter in the 100- to 1000-GPa-range. For the first time, we measured the spall strength across a grain boundary. We found that, on our time scale, the rupture does not cross this border. The investigation of the ICF-related issue of the development of hydrodynamic instabilities during the ablative acceleration is scheduled for the next campaigns.

Acknowledgment

This work was partially supported by the German-Russian Scientific and Technological Cooperation Treaty and The NATO Science Programme. The authors would like to thank the KALIF operators for conducting the shots.

References

- [1] K. Baumung, H. Bluhm, B. Goel, P. Hoppé, H.U. Karow, D. Rusch, V.E. Fortov, G.I. Kanel, S.V. Razorenov, A.V. Utkin, and O.Yu. Vorobjev, Shock-wave physics experiments with high-power proton beams, to be publ. in *Laser Part. Beams* 14(2), 1996.
- [2] K. Baumung and J. Singer: A Novel High-Resolution Line-Imaging Laser-Doppler Velocimeter, Report FZKA 5590, Forschungszentrum Karlsruhe, 88(1995).
- [3] K. Baumung, H.U. Karow, D. Rusch, G.I. Kanel, A.V. Utkin, V. Licht: High-Power Proton Beam-Matter Interaction Diagnostics by Analysis of the Hydrodynamic Response of Solid Targets, *J. Appl. Phys.*, 75(12), 7633 (1994).
- [4] P. Hoppé, H. Bachmann, W. Bauer, H. Bluhm, L. Buth, H. Massier, D. Rusch, O. Stoltz, and W. Vöth, Characteristics of the Ion Beam Produced by the B₀ Diode, Report FZKA 5590, Forschungszentrum Karlsruhe, 51 (1995).
- [5] O.Yu. Vorobjev and B. Goel: Reinvestigation of Aluminum Foil Acceleration Experiments, KfK Internal Report 51.03.02/03A, October 1994.
- [6] B. Goel and H. Bluhm, *Journ. de Physique - Coll. C7*, 49, C7-169 (1988).
- [7] A.V. Utkin, G.I. Kanel, S.V. Razorenov, K. Baumung and D. Rusch, Diagnostics of high-power ion beam interaction with composite targets, *J. Appl. Phys.* 79, 2180 (1996).
- [8] H. Marten, B. Goel, and W. Höbel, Slowing down of an ablatively accelerated foil after impact on a stationary target, this report.
- [9] K. Baumung, D. Rusch, J. Singer, S.V. Razorenov, A.V. Utkin, G.I. Kanel: Measurement of the Tensile Strength of Solids at Very High Strain Rates, report FZKA 5590, Forschungszentrum Karlsruhe, 82 (1995).
- [10] G.I. Kanel, S.V. Razorenov, A.V. Utkin, V.E. Fortov, K. Baumung, H.U. Karow, D. Rusch, V. Licht, "Spall Strength of Molybdenum Single Crystals", *J. Appl. Phys.* 74, 7162 (1993).
- [11] S. V. Razorenov, A. V. Utkin, G. I. Kanel, V. E. Fortov, A. S. Yarunichev, K. Baumung, and H. U. Karow, "Response of high-purity titanium to high-pressure impulsive loading", *High Pressure Research* 13, pp. 367-376 (1995).

Foil Acceleration Experiments and Equation of State for Aluminium

B. Goel, W. Höbel, H. Marten, O.Yu. Vorobiev¹

Forschungszentrum Karlsruhe, PO Box 3640, D76021 Karlsruhe

1) Institute of Chemical Physics, Chernogolovka, Russia

Abstract

We have analysed foil acceleration experiments performed at KALIF. The available equation of state data can not describe these experiments satisfactorily. Therefore, we have formulated an equation of state in Mie-Grüneisen form. This equation of state describes these foil acceleration experiments as well as the available shock compression data. The parameters of this equation of state are given in this report.

1. Introduction

The dynamics of foil acceleration experiments performed at KALIF with the B₃-diode[1,2] were analysed previously and reported in the last years annual report[3]. It was found that the newly determined temporal behaviour of beam parameters[4] give an adequate replication of the observed rear-surface velocities if uncertainties in the equation of state data are taken into account. KALIF experiments are sensitive to the equation of state data of dense plasma in the region of a few 10's of eV. This is the region of strongly coupled plasma. In the present paper we analyse the implication of these experiments on the equation of state data. We present results of our semi-empirical equation of state formula and compare it with other available equation of state data.

2. Mathematical Model and Calculations.

Calculations were performed by solving the Euler equations of motion using the Godunov method in a moving grid. The beam energy was coupled to the target using the wide range energy deposition formula developed by Polyschuk[5]. Radiation transport was performed in conduction approximation. The details of the mathematical model and calculations are given elsewhere[3,6]. In the followings we concentrate on the equation of state data.

It is seen in figure 1 that the results of calculations using SESAME [7] and Bushman *et al.* [8] EOS tables do not reproduce the experimental data adequately[3,6]. There are two main disagreements.

- 1) The duration of the first step in the velocity evolution does not agree with the experimental observation and depends on the equation of state used. This duration should correspond to the shock reverberation time in the unablated part of the target and should depend on the sound velocity in the cold material only. In a hydrodynamic code the matter is kept together or expands depending upon the value of the pressure inside the material. To prevent

material expansion before melting the lattice binding energy can be represented as negative pressure. In the SESAME equation of state table this negative pressure is present. However, to obtain accurate data between the tabulated points logarithmic interpolation is required and thus negative pressures are truncated.

- 2) The disagreement between calculation and measurement is large for the time interval between 10 and 20 ns. At these times the density of the target is reduced by more than an order of magnitude and the temperature increases beyond 10 eV. These states of matter correspond to the region of strongly coupled plasma and the uncertainty in EOS models in this region is large.

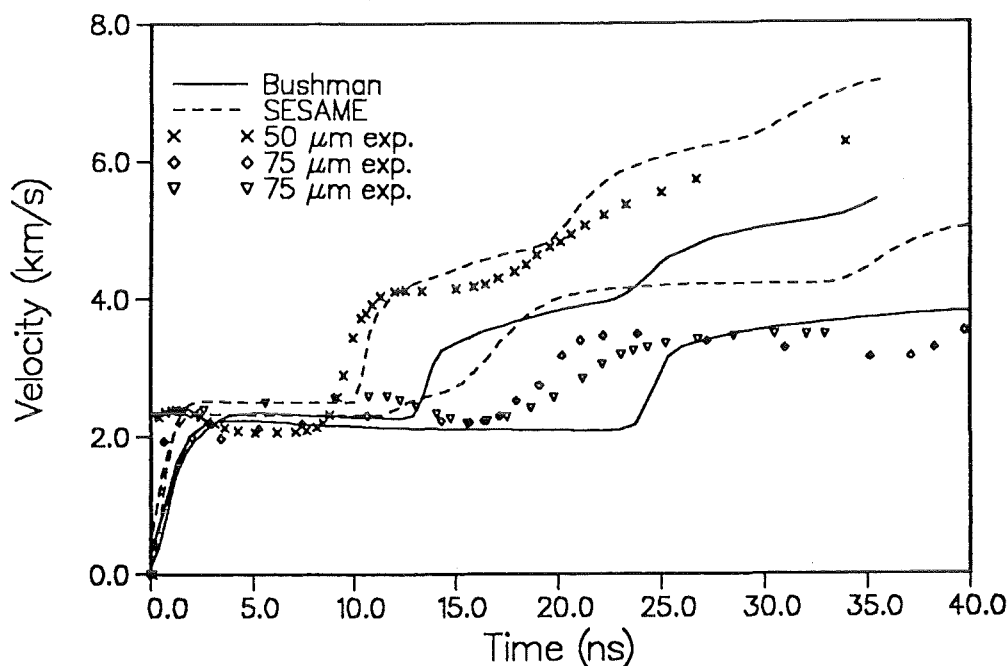


Figure 1: Comparison of experimental (symbols) and calculated rear surface velocities of 50 μm and 75 μm aluminium foils ablatively accelerated by the KALIF proton beam. Simulations are carried out using SESAME and Bushman EOS data.

To rectify this situation we formulate a semiempirical EOS model in a generalised Mie-Grüneisen form that contains several fitting parameters. It well describes the experimental data of shock compression of solids in the pressure range up to several megabars. Adopting the usual procedure, the internal energy of matter is divided into two parts. The cold energy E_c is a function of density only. The thermal component of the energy E_t is a function both of temperature (internal energy) and density. We use (p, ρ) variables.

$$E(p, \rho) = E_c(\rho) + E_t(p, \rho) \quad (1)$$

To describe the Hugoniot data for solid matter we choose for the cold pressure the conventional form (Bushman *et al.* [8], Eliezer *et al.* [9]):

$$p_c(\rho) = \sum_{i=1}^5 a_i \delta^{(i/3+1)}, \quad \delta \geq 1 \quad (2)$$

$$p_c(\rho) = \frac{\rho_0 c_{s0}^2}{n-m} (\delta^n - \delta^m), \quad \delta \leq 1 \quad (3)$$

where $\delta = p/p_0$, and ρ_0 , and c_{s0} are the normal density and sound velocity, respectively. Coefficients a_i are found by solving the system of linear equations that ensure the properties of material under normal conditions and by using the Thomas-Fermi-Dirac model at high compression. The cold component of the total pressure strongly dominates the thermal component in shocked states of solid matter up to several megabars. The thermal pressure is related to the thermal energy through the Grüneisen parameter Γ , which is a function of energy and density

$$p_t = \Gamma(E, \rho_0) E_t \rho. \quad (4)$$

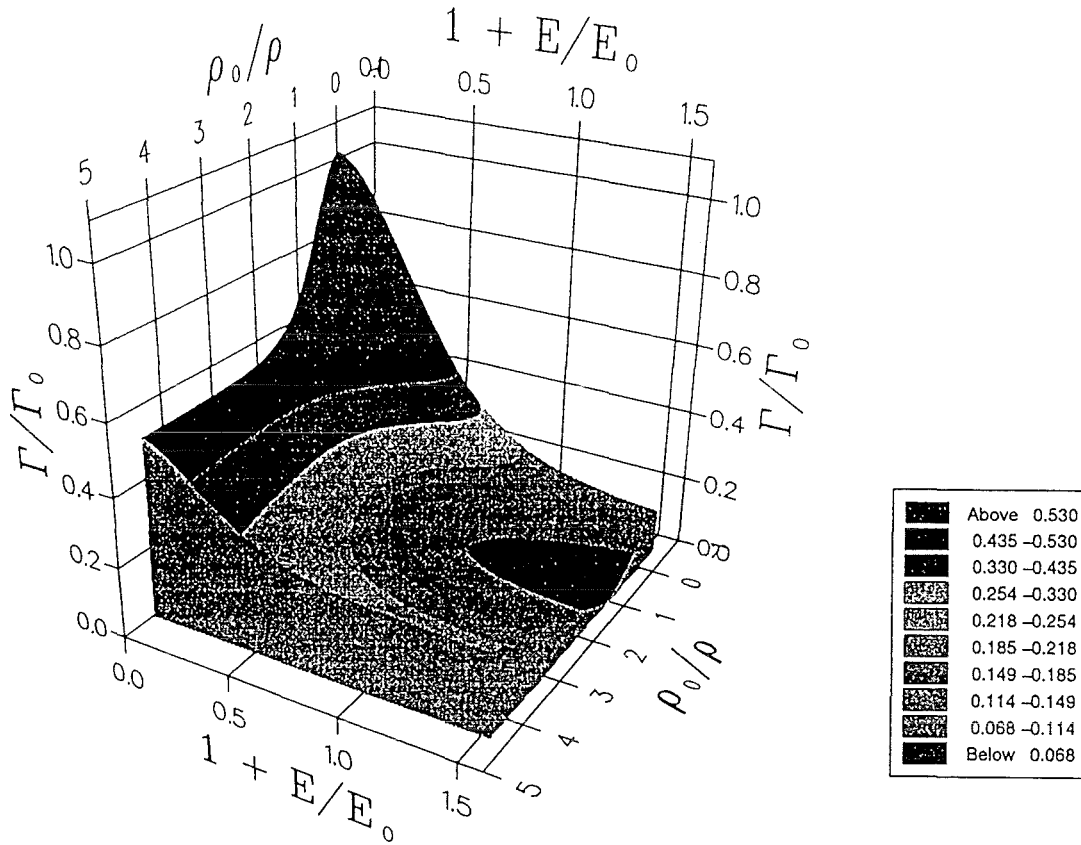


Figure 2: Grüneisen parameter as a function of specific energy and density for aluminium calculated with coefficients are give in Table 1.

The following dependence of the Grüneisen parameter on the internal energy is used.

$$\Gamma = \Gamma(\rho)_\infty + \frac{\Gamma(\rho)_0 - \Gamma(\rho)_\infty}{1 + (E/E_0)^\alpha} \quad (5)$$

Here E_0 and α are fitting parameters. To describe the asymptotic behaviour of Γ in the limit of high compression (Fermi gas) and expansions (ideal gas) we choose both functions Γ_0 and Γ_∞ having an asymptotic value $2/3$ for $\rho \rightarrow \infty$ and $\rho \rightarrow 0$.

$$\Gamma(\rho)_0 = \frac{2}{3} + \left(\Gamma_s - \frac{2}{3} \right) \frac{2}{(\rho_0/\rho + \rho/\rho_0)}, \quad (6)$$

$$\Gamma(\rho)_{\infty} = \frac{2}{3} + \left(\Gamma_{\min} - \frac{2}{3} \right) \left(\frac{2}{y + 1/y} \right)^{\beta}, \quad y = \frac{\rho_0}{\rho} \xi, \quad (7)$$

where Γ_s is the Grüneisen coefficient at normal conditions, β and ξ are fitting parameters. To fit the parameters Hugoniot and unloading isentropes of solid and porous aluminium were analysed in the pressure range up to 2 Mbar. An additional constraint was that in the plasma region these parameters should give reasonable agreement between the results of experiments and calculations. The Grüneisen parameter as a function of specific energy and density is shown in Fig. 2.

Table 1. Coefficients for the calculation of Grüneisen parameter for aluminium .

α	β	E_0	γ_{\min}	γ_s	ξ	
1.1	0.02	30 kJ/g	0.2	2.1	0.1	
a_1	a_2	a_3	a_4	a_5	n	m
-15009.612	51732.56	-66509.87	37631.99	-7845.07	3.5	1.93633

3. Results

Results of numerical simulations using the analytical EOS with parameters presented in Table 1 are shown in figure 3 together with the experimental data for foils of different thickness launched by the ion beam. The EOS is able to describes all experiments with aluminium foils of different thickness.

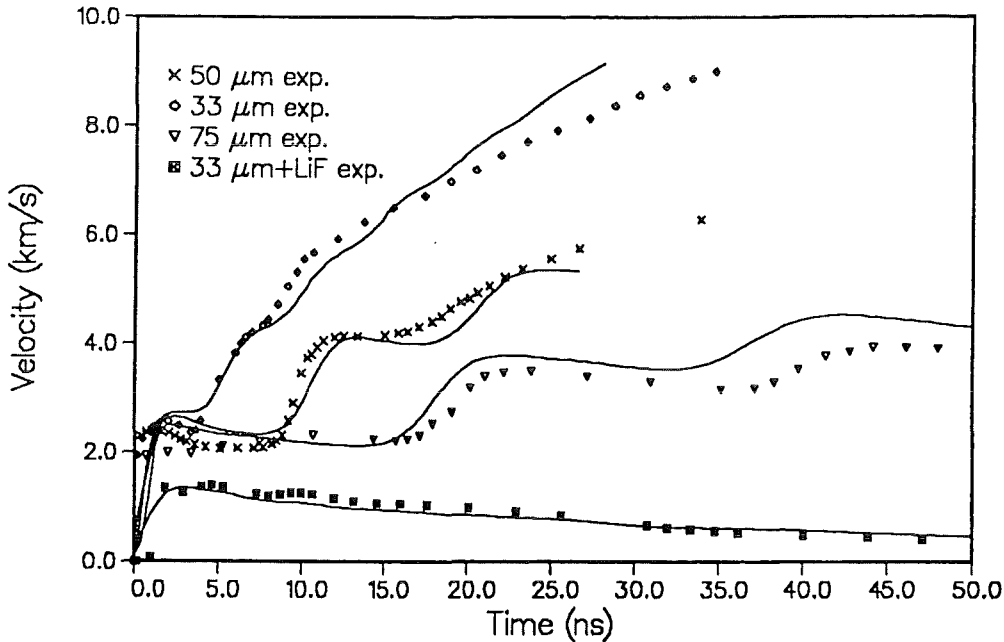


Figure 3: Simulation results for different foil thicknesses using analytical equation of state as described in the text. Satisfactory agreement between experiment and simulation is observed. This is a large improvement against the results of obtained with other equations of state.

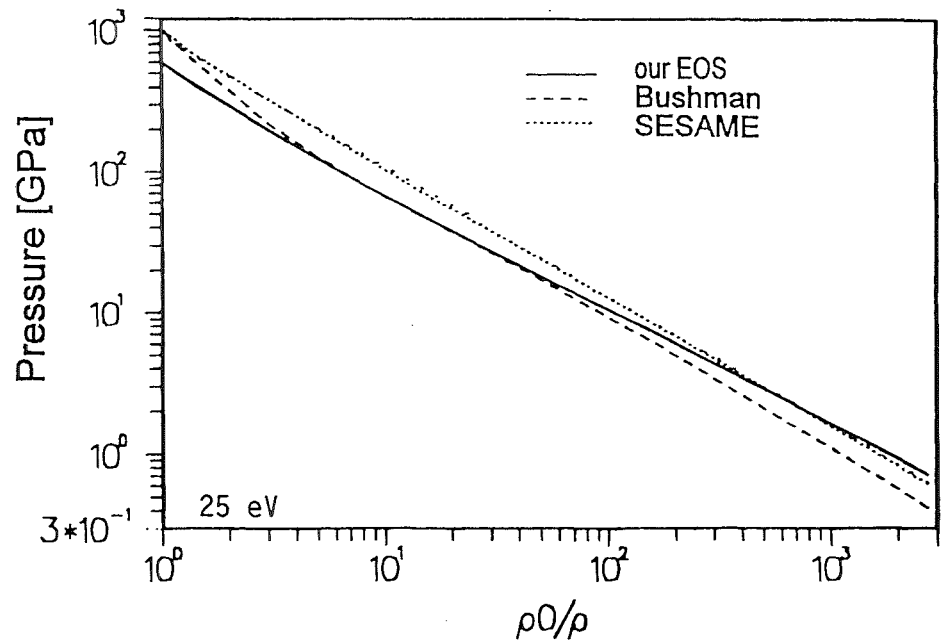
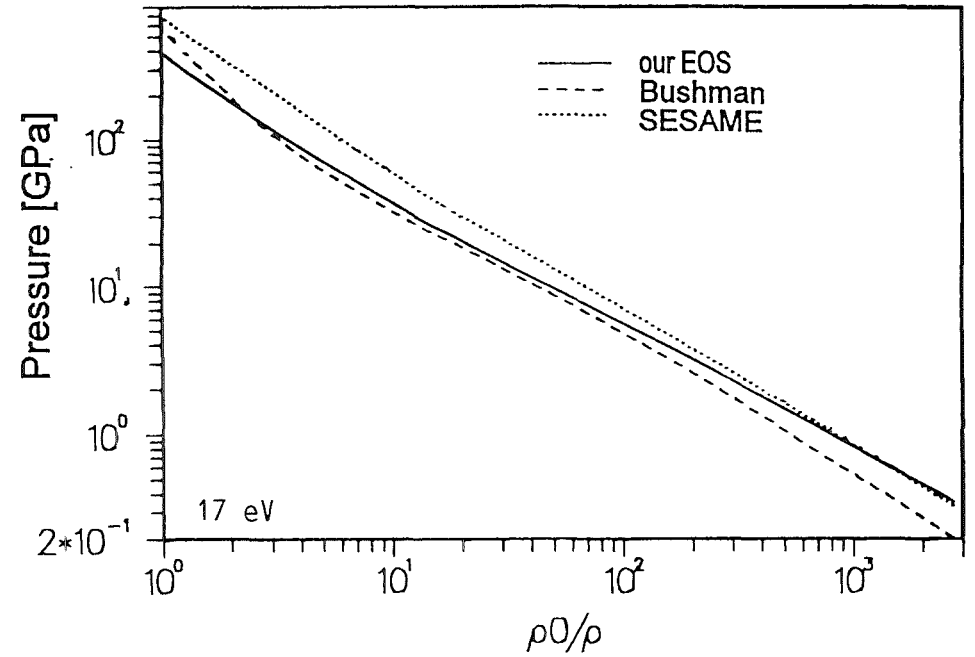
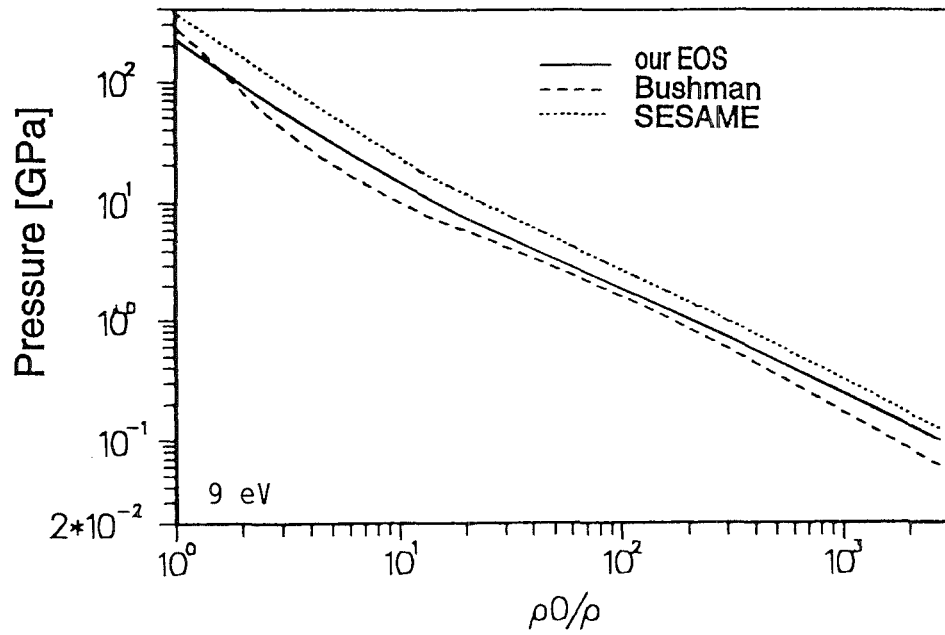


Figure 4: Pressure as function of density calculated with different EOS models at different temperatures, (a) 9 eV (b) 17 eV and (c) 25 eV.

In figure 4 we compare the pressure calculated with our equation of state with that given in SESAME and Bushman tables as a function of density for a few selected temperatures. It is seen that our data are between those of SESAME and Bushman. Near the solid density they are closer to Bushman's data whereas for low densities SESAME data seem to be more appropriate.

4. Conclusions

We have analysed the foil acceleration experiments performed at KALIF using the B_q-diode. The analysis provides information on the equation of state in the region of strongly coupled plasma. In this region experimental information is scarce and theoretical models have large uncertainties. We have postulated an equation of state formula in the Mie-Grüneisen form. The pressures calculated with this equation of state formula in the region of interest are between the tabulation of SESAME and Bushman. The accuracy of the equation of state determined by this method depends on the accuracy of beam parameters. Improving accuracy of beam parameters will also improve the accuracy of equation of state data. The main uncertainty in the beam parameter is the value of peak power. From our experience in analysing different experiments with the same beam parameters i.e. assuming complete reproducibility of KALIF and diode operation we conclude that the uncertainty in the beam parameters may be less than that given in [4] and is of the order of 10-20%.

5. References

- [1] BAUMUNG, K. *et al.* 1992 In *Proc. 9th International Conference on High-Power Particle Beams*, Washington DC, Vol. I.,68.
- [2] BAUMUNG, K. *et al.* 1995a In *Report FZKA 5590*, Forschungszentrum Karlsruhe, p. 88.
- [3] GOEL, B., VOROBIEV, O. YU., In *Report FZKA 5590*, Forschungszentrum Karlsruhe 1995, p. 109.
- [4] HOPPÉ, P. *et al.* In *Report FZKA 5590*, Forschungszentrum Karlsruhe 1995, p.51.
- [5] POLYSHCHUK, A.YA. *et al.* 1991 *Sov. J. Plasma Phys.* **17**, 523.
- [6] GOEL, B., VOROBIEV, O. YU., In *Equation of State Information from Beam-Target Interaction Experiments at KALIF*, Laser and Particle Beams, To be Published
- [7] SESAME Library, Lawrence Livermore National Laboratory, Report UCID-118574-82-2 (1982).
- [8] BUSHMAN, A.V. *et al.* *Intense Dynamic Loading of Condensed Matter*. (Taylor & Francis, Washington DC, London) 1992
- [9] ELIEZER, S *et al.* *An introduction to equation of state* (Cambridge University Press) 1986

SLOWING DOWN OF AN ABLATIVELY ACCELERATED FOIL AFTER IMPACT ON A STATIONARY TARGET

H. Marten, B. Goel, W. Höbel
Institut für Neutronenphysik und Reaktortechnik

Recently, Baumung et al. (1995) observed a nontrivial slowing down of an ablatively accelerated aluminum foil striking a non-moving LiF crystal. We analyze these experiments using a radiation-hydrodynamic code. Isolating different involved phenomena we conclude that the behaviour observed in the experiment is caused by the radiative transport of heat energy from the hot ablated plasma into the cold accelerated aluminum flyer.

1. Introduction

In foil acceleration experiments performed with the high-voltage pulsed power generator KALIF, intense proton beams generated in the ion diode are used to irradiate thin foils, thus generating ultrahigh pressures of up to 60 GPa in condensed matter. Once the proton beam starts depositing energy inside the foil, a part of the matter is ablated and heated to high temperatures. The high pressure of this plasma then drives a compression wave into the remaining solid and cold part. At the rear surface of the target (interface between solid state and vacuum, the so-called “free surface”) the compression wave is reflected as a release wave running back into the target, the release wave is reflected at the ablation-plasma boundary as a pressure wave, and so on. Experiments as well as numerical simulations show that these wave reverberations in the condensed part of the foil lead to a stepwise increase of the targets rear-surface velocity (Fig. 1), and ablatively driven velocities of up to 12 km/sec have been measured in these experiments.

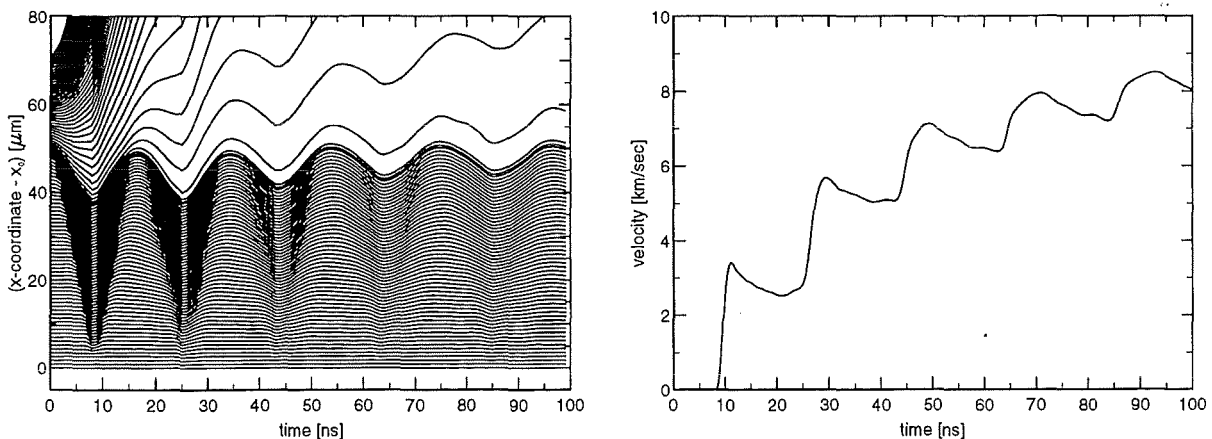


Figure 1: left: Evolution of the numerical cell boundaries in the reference frame of the targets rear surface (from a 1D-Lagrangian simulation of a beam-target interaction with a beam impinging from the top). Note the periodically reflected waves reaching the free surface at about 9, 26, 44, ... ns. right: Velocity of the targets rear surface in the observers frame for the same model.

Recently, Baumung et al. (1995) presented velocity measurements of an ablatively accelerated aluminum foil striking a stationary target. In these experiments, a laser-Doppler interferometer records the rear-surface velocity of the Al-foil of 71 μm initial thickness through a non-moving LiF-window (thickness about 5 mm) initially placed at a pre-defined distance behind the Al-foil.

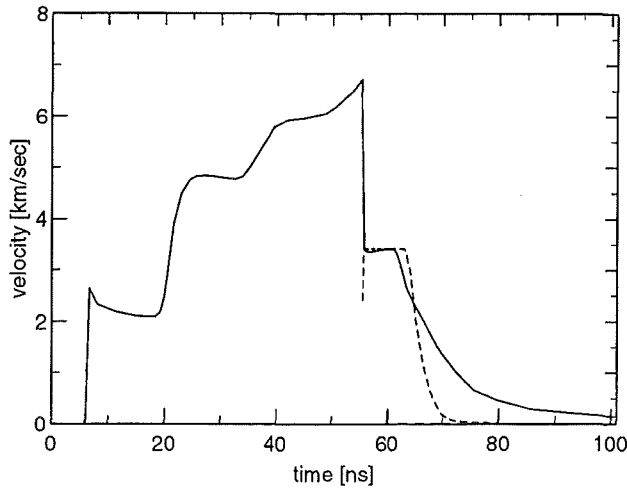


Figure 2: Measured velocity of an ablatively accelerated Al-foil striking a stationary target at about 55 ns (Baumung et al. 1995). The dashed curve is a simplified theoretical model for the impact of two cold foils (see text).

The collision of the Al-flyer with the LiF-foil generates two compression waves propagating into both materials and leads to a typical velocity signal as shown in Fig. 2 at about 55 ns. Because of the nearly identical dynamic properties of the two materials the flyer velocity first drops to about one half of its impact velocity, remains almost constant until the pressure wave generated in the flyer reaches the ablation-plasma interface, and finally starts to drop. The dashed curve shown in Fig. 2 is a simplified model of a collision of two “cold” targets, i.e. the collision of two cold foils with an impact velocity taken from the experiment and a flyer thickness of $48.5 \mu\text{m}$ (= initial thickness minus range of 1.5 MeV-protons). Compared to the experimental results of Fig. 2, two remarkable differences are noticed: In the experiment the “velocity plateau” after the impact is shorter and the decrease of the “velocity tail” is less steep than expected from the cold-target estimates. In the following sections, these differences are examined in more detail by numerical simulations performed with the hydrodynamic code KATACO (Goel et al. 1993).

2. Model Calculations

2.1. The influence of the phase of the pressure wave at impact

Since the wave reverberation inside the cold part of the Al-foil is a quasi-periodic phenomenon, as seen from Fig. 1, with the period slightly changing in time due to changes of the target thickness, one may define a phase of the pressure wave, ϕ , starting with $\phi = 0$ at that time when the pressure wave just reaches the targets free surface. Numerical simulations have shown that the “velocity plateau” after the target impact is in general not as flat as found in the experiment, but shows a structure which depends on ϕ at the time of impact. Fig. 3 shows two computed velocity signals after the impact at two different phases. In model A (impact at $\phi = 0$), the rear-surface velocity of the flyer drops to about one half of the initial value but soon increases by about 1 km/sec due to acceleration by the just arriving pressure wave. In model B (impact at $\phi = \pi$) the arrival of the pressure wave at the rear surface is seen as a velocity hump near the end of the plateau. Also, the length of the plateau is somewhat increased in this case. In an experiment it is difficult to control the phase of impact. Nevertheless, from our simulations we can estimate that in the experiment shown in Fig. 2 the impact took place at about $\phi = 0.1 \cdot 2\pi$.

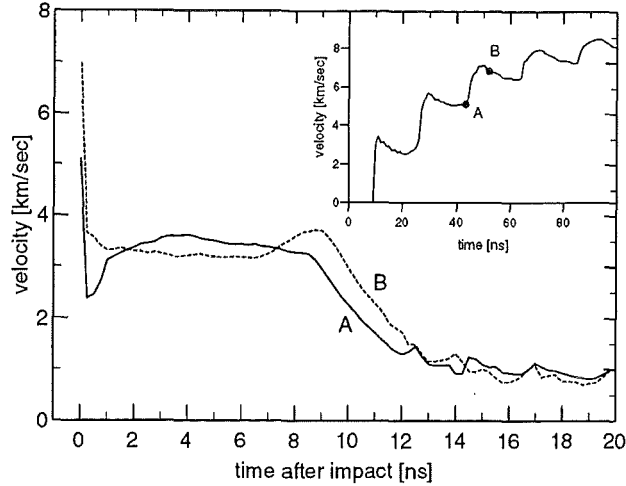


Figure 3: Simulated velocity evolution of the LiF-Al interface after the impact at two different phases of the pressure wave (A: $\phi = 0$; B: $\phi = \pi$). In the inset, the moments of impact for the two models are shown within the velocity curve of a free flying target.

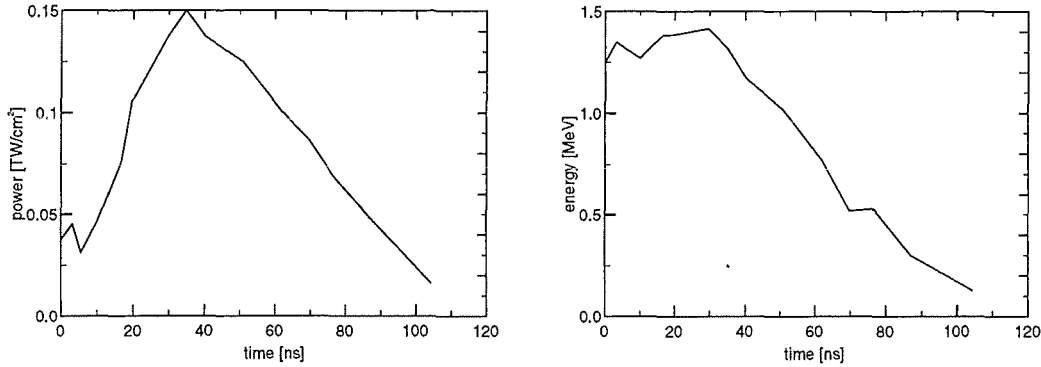


Figure 4: KALIF beam power and beam energy at the target as a function of time.

2.2. The influence of the proton beam and of the hot-plasma pressure

In Fig. 4, the KALIF beam power and energy are plotted as a function of time. According to Fig. 2, the target impact in the experiment took place at about 55 ns after the beam onset, i.e. about 20 ns after the beam-power maximum. In order to check whether the remaining beam pulse influences the further evolution of the target velocity, two impact calculations are compared in Fig. 5, one following the full KALIF-beam history, and a second one in which the beam has been switched off at the time of impact. Obviously, there are no significant differences in the velocities of both cases. Due to range shortening effects, but mainly due to the decreasing particle-beam energy after the beam-power maximum, the proton range in the plasma decreases so that the energy deposition-zone moves into the ablated plasma, away from the accelerated (solid) part. The relative velocity between the solid Al and the energy deposition-zone becomes even larger than the signal velocity in the ablated plasma so that the pressure information generated by the energy deposition is not able to reach (and thus further accelerate) the Al-flyer. Consequently, details on the temporal behaviour of the beam profile after about the beam-power maximum do not influence the velocity of the foil after impact any more. Similar results have also been found by Goel & Vorobiev (1996) for a free flying target. The dashed curve in Fig. 5 represents the simulated velocity signal after the impact of two “cold” targets. In contrast to the previously discussed models, no “velocity tail” is seen in this case since there

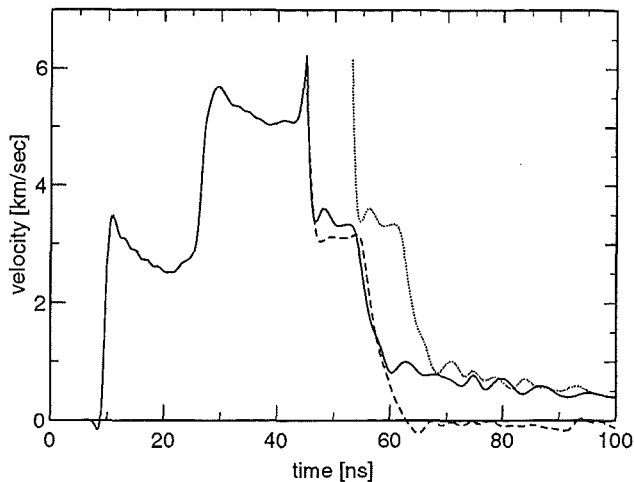


Figure 5: Velocity evolution of the Al-foil after impact at $t = 45$ ns. Straight line: including full history of the KALIF beam according to Fig. 4; dotted: beam switched off at impact; dashed: simulated impact of two cold targets (c.f. Section 1). The dotted curve has been shifted by 8 ns for the sake of clarity.

is no plasma exerting the Al-foil. Recalling that the beam *after* the beam-power maximum is unimportant for the target velocity we can conclude that the “velocity tail” observed in the experiment is due to the pressure of the hot plasma generated *before* the beam-power maximum.

2.3. The influence of thermal conduction

In contrast to the experiments, the computed “velocity plateau” in simulations including the full KALIF-beam history has about the same length as in the cold-target impact, and the decrease after the plateau in both cases takes place within about the same time (Fig. 5). A shorter velocity plateau after impact can in principle be achieved when the thickness of the remaining solid Al-foil is reduced by additional evaporation of matter beyond the proton range, e.g. by thermal conduction. In order to correctly consider the thermal conductivity in solids, new thermal conduction coefficients according to Bepalov & Polishchuk (1989) have been implemented in KATACO, with an additive correction accounting for the measured value of $\kappa_{\text{Al}} = 223$ W/Km at normal density. Fig. 6 demonstrates the enorme improvement of thermal conductivities compared to the values of Spitzer (1965) used in earlier calculations and which are strictly valid only in the range of high temperature plasmas. Nevertheless, the comparison of impact calculations with and without thermal conduction in Fig. 7 shows that this process is not responsible for the observed reduction of the target thickness. Thermal conduction is of only minor importance in these experiments.

2.4. The influence of radiative transfer

A second process that can reduce the thickness of the cold Al-foil by additional evaporation is due to heat transport by radiation. KATACO contains a formalism for multi-angle, multi-frequency radiative transfer. In these calculations we used 2 angular directions and 10 frequency intervals, with Planck-mean emission and absorption coefficients calculated with the code EOSOPC (Ping Wang 1993). In Fig. 8, the resultant velocities are compared for simulations with and without radiative transfer, the corresponding model structures at the time of impact ($t = 65$ ns) are shown in Fig. 9. Indeed, the additional transport of energy by radiation from the hot plasma

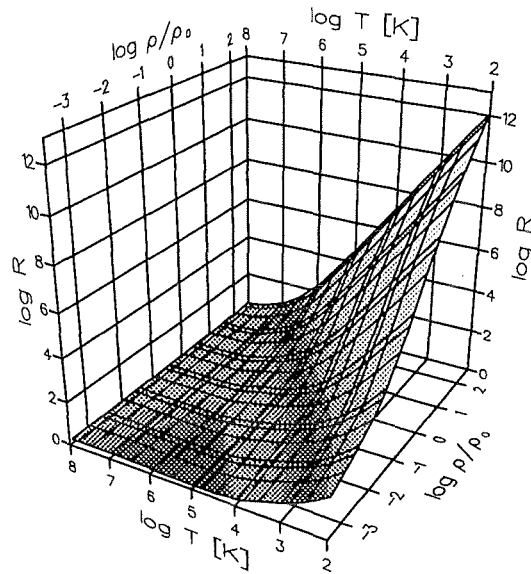


Figure 6: Ratio of thermal conduction coefficients of Bepalov & Polichshuk (1989) to those of Spitzer (1965) in a wide range of densities and temperatures (for aluminum).

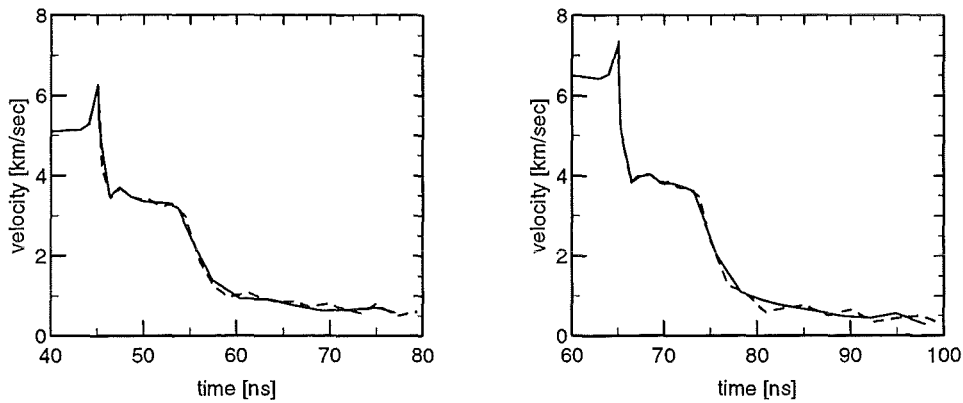


Figure 7: Comparison of impact calculations with (dashed) and without (straight lines) thermal conduction. **left:** velocity histories for impacts taking place at $t = 45$ ns. **right:** impact at 65 ns.

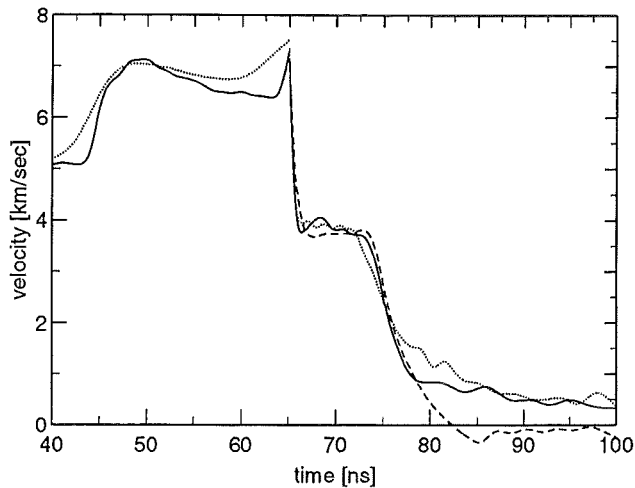


Figure 8: Computed target velocity as a function of time (impact at $t = 65$ ns) including radiative transfer (dotted), without radiative transfer (straight line) and for the impact of cold targets (dashed).

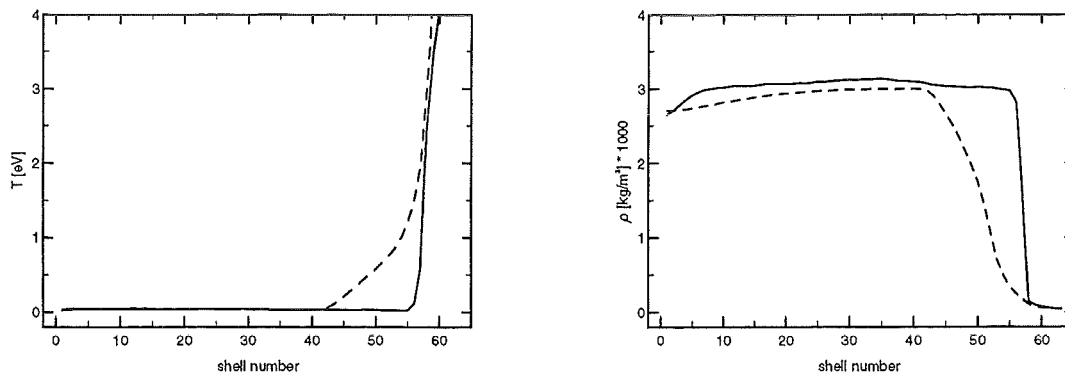


Figure 9: Temperature and density structure of models with (dashed) and without radiative transfer (straight lines) at the time of impact ($t = 65$ ns).

to the cold region leads to an evaporation zone (with a thickness increasing in time), which is seen in the temperature structure of Fig. 9. This results in an earlier reflection of the pressure wave generated at impact and thus in a shorter plateau of the rear-surface velocity (Fig. 8). The additional pressure of the evaporation zone retards the slowing down of the aluminum foil and leads to a less steep decrease of the velocity tail ($t < 72$ ns in Fig. 8), as observed in the experiment. Furthermore, the pressure of the evaporation zone reduces the density gradient at the ablation boundary so that any reflection of a compression or a release wave becomes less definit. As a result, the steps in the target velocity already become rounded before the impact takes place (Fig. 8). This behaviour is observed in the experiments as well (c.f. Fig. 2).

3. Conclusions

According to Section 2.1, the impact experiments depend on the phase of the pressure wave inside the solid part of the flyer *at* the time of impact. Since the latter is a complicated function of the initial distance d between the flyer and the impactor, as well as of the targets velocity

evolution which in turn is influenced by the targets equation of state (Goel & Vorobiev 1995), impact experiments at a definite phase are difficult to perform and the corresponding necessary initial distance d can only be found either by trial and error or by previous numerical simulations.

One of the most important assumptions for the interpretation of KALIF experiments is the reproducibility of the proton beam. In this respect, the results of Section 2.2 which have shown that details on the temporal behaviour of the beam history *after* about the beam-power maximum do not influence the velocity of the ablatively accelerated foil, are of major importance.

While thermal conduction was found to be unimportant for these experiments, radiative effects are not negligible. This is somewhat surprising at a first glance. The usual argument for neglecting radiation in numerical simulations comes from a comparison of the radiation energy with the thermal energy content. In the hot plasma generated by the KALIF-B₀ diode, the radiation energy is about 7% of the thermal energy content, and it might be enticing to neglect this "small fraction". However, radiation has always to do with *transport* of energy from a hot plasma into cold matter, where suddenly the situation may become just the opposite. It is this effect which significantly reduces the final thickness of the solid flyer in these experiments. A more detailed study of radiative processes with higher numbers of angular directions and frequency intervals is just under development.

References

- Baumung K., Rusch D., Singer J., Razorenov S.V., Utkin A.V., Kanel G.I., 1995, Hydrodynamic Beam-Target Experiments on KALIF. in: H.-J. Bluhm (ed.) Physics of Intense Light Ion Beams and Production of High Energy Density in Matter, Annual Report 1994, Forschungszentrum Karlsruhe FZKA 5590, p. 73
- Bespalov I.M., Polishchuk A.Ya., 1989, Sov.Tech.Phys.Lett. 15, 39
- Goel B., Vorobiev O.Yu., 1995, Reinvestigation of Foil Acceleration Experiments. in: H.-J. Bluhm (ed.) Physics of Intense Light Ion Beams and Production of High Energy Density in Matter, Annual Report 1994, Forschungszentrum Karlsruhe FZKA 5590, p. 109
- Goel B., Vorobiev O.Yu., 1996, Laser and Particle Beams, submitted
- Goel B., Höbel W., Würz H., 1993, Numerical Simulation of Radiation Transport on Supercomputers. in: H. Küsters (ed.) Proc. of the Joint Internat. Conf. on Mathematical Methods and Supercomputing in Nuclear Applications, Karlsruhe, April 19-23, 1993 Vol. 2, p.63
- Ping Wang, 1993, EOSOPC - A code for computing the equations of state and opacities of plasma with detailed atomic model, Interner Bericht Forschungszentrum Karlsruhe
- Spitzer L.jr., 1965, Physics of Fully Ionized Gases, 2nd Ed., Interscience Publishers

Temperature Measurement for KALIF Targets by Soft X-Ray Spectroscopy

G. Meisel, H. Bluhm, P. Hoppé, R. Hüttner, D. Rusch, E. Saenger, T. Schön, J. Singer

The K_{α} radiation emitted by Al and Mg targets upon interaction with the KALIF proton beam was spectroscopically investigated. From the time integrated spectra peak temperatures of ≈ 10 eV and ≈ 20 eV are estimated for the B_{\odot} diode and the B_{appl} diode, respectively. To allow for time resolved absorption experiments, a laser system was set up to generate soft x-rays to be used as backlighter. The system and its properties are described. First results of laser induced x-ray spectra are given.

1. Introduction

The high specific power deposition of 50 to 200 TW/g [1] as obtained in the focus of the KALIF proton beam allows one to generate a dense plasma in the $kT = 10 \dots 20$ eV range [2]. The temperature thus obtained can be determined by measuring high resolution K_{α} x-ray spectra of low Z elements contained in the plasma [3]. The temperature information essentially is contained in the satellite pattern that reflects the relative population of the different ionization and excitation states of the atoms inside the plasma. To get a uniform energy deposition inside the target, thin foils with subrange thickness were bombarded by the KALIF beam. Both spectroscopic alternatives, emission as well as absorption, were applied [4]. The emission scheme is less complicated to realize than absorption experiments; emission, though, gives only time averaged temperature information whereas absorption allows to perform time resolved experiments.

To evaluate the observed spectra with respect to the plasma temperature, calculations are required that give the spectra as function of various plasma parameters [2]. The plasma temperature basically is determined by comparing the detailed satellite structure of the observed spectrum with the calculated ones.

2. Emission Spectroscopy

2.1. Experimental details

The spectrometer setup requires flat Bragg crystals that can be rotated to define the wavelength region of interest. The spectrometer was equipped with two crystals that can be rotated independently. Cleaved RAP and KAP crystals [5] were used for $\lambda = 0.8$ to 1.6 nm in our experiments. The dispersed x-ray radiation was recorded on x-ray Kodak DEF-2 film [6] which was developed in Kodak GBX solution.

The spectrometer was placed inside a light-tight housing to avoid unwanted film exposure. A 2 μm thick mylar foil with 0.05 μm Al coatings on both sides (Type B(10 HH) by Alexander Vacuum Research Inc.) was used as x-ray entrance window. We found this foil sufficiently light tight; the soft x-rays of interest were only slightly attenuated by this window. The

exposed films were scanned by a microdensitometer which outputs a film optical density = $^{10}\log(1/\text{transmission})$ which is roughly proportional to the x-ray flux at the film position [6].

The quality of the spectrometer crystals was tested by recording soft x-ray spectra emitted from a laser induced plasma (see below, 3.1.). Both, the RAP as well as the KAP crystals were found to be similar in reflectivity and resolution. The ultimate resolution was determined to be about 1000 for both materials.

The spectrometer was mounted in a separate vacuum vessel that was attached to the KALIF diode chamber. The debris problem was solved as described recently for the B_θ diode [4]; it was found that the same debris protection is also sufficient for the B_{appl} diode. A permanent magnet was added to remove charged particles. The hard x-ray radiation from the KALIF diodes required some lead shielding to reduce it to a tolerable level.

The Al targets used so far were foils of 2 μm and 6 μm thickness. Magnesium targets were made by vacuum deposition of Mg metal onto 2 μm thick Al films as carrier. The same applies to NaF.

2.2. Results

Spectra were taken with the B_θ diode for Al, Mg, and NaF targets. With the B_{appl} diode spectra were recorded for Al and Mg only. The x-ray emission for NaF targets with thickness up to 12 μm was found to be too weak to be recorded with the present equipment.

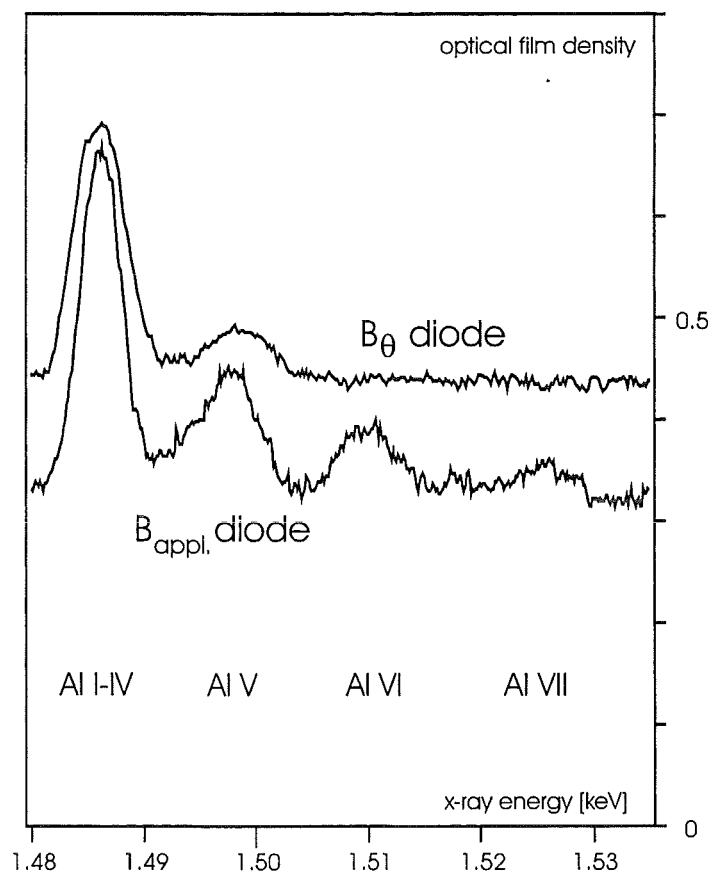


Fig. 1: K_α emission spectra for Al targets of 6 μm thickness as obtained with the two different KALIF diode types. The background results from film fog and hard x-ray radiation.

Fig. 1 gives the spectra obtained for 6 μm thick Al targets as obtained with the two different KALIF diodes. Both spectra show a strong low energy component which is emitted by neutral and weakly ionized Al atoms as is deduced from calculations [7]. The higher energy components are composed of many lines emitted by higher ionized Al as is indicated in figure 1. Obviously, the B_{appl} diode produces higher ionization states indicating that the plasma reaches a higher temperature for this diode as is expected from its emission characteristics.

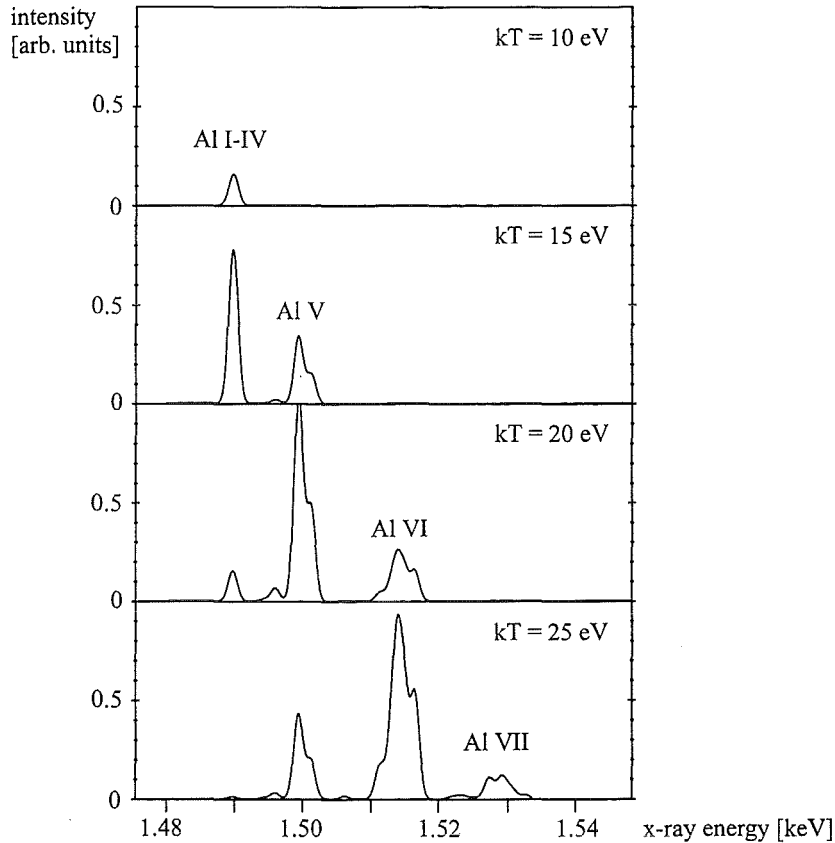


Fig. 2: Calculated K_{α} emission spectra for Al targets of 0.2 μm thickness for different fixed temperatures [8]. For a direct comparison with the experiment the temporal as well as the spatial variations of the temperature have to be taken into account.

A more detailed discussion of the observed spectra required a corresponding full calculation for different temperatures, also including the appropriate temporal and spatial averaging corresponding to the experiment. Such full calculations are not available at present. There are, however, results for fixed temperatures [8] (fig. 2). It is not surprising that none of them fits to the observed spectra. The calculations nevertheless allow some conclusions concerning the peak temperatures: The highest ionization states appearing in the two experimental spectra are Al V for the B_{\odot} diode and Al VII for the B_{appl} diode. From this we estimate that the peak temperatures reached for the two diodes are ≈ 13 eV and ≈ 23 eV for B_{\odot} and B_{appl} , respectively.

Since 6 μm is a rather large target thickness, we have also investigated the influence of the target thickness on the spectrum. Fig. 3 gives a comparison of the results for 2 μm and 6 μm thick targets. It demonstrates that the emission intensity is doubled for a threefold target thickness, i.e. there is some self absorption, though it is not extremely strong. It also shows that the self absorption for all ionization groups is about the same under our experimental conditions. These findings require more detailed experimental as well as theoretical work.

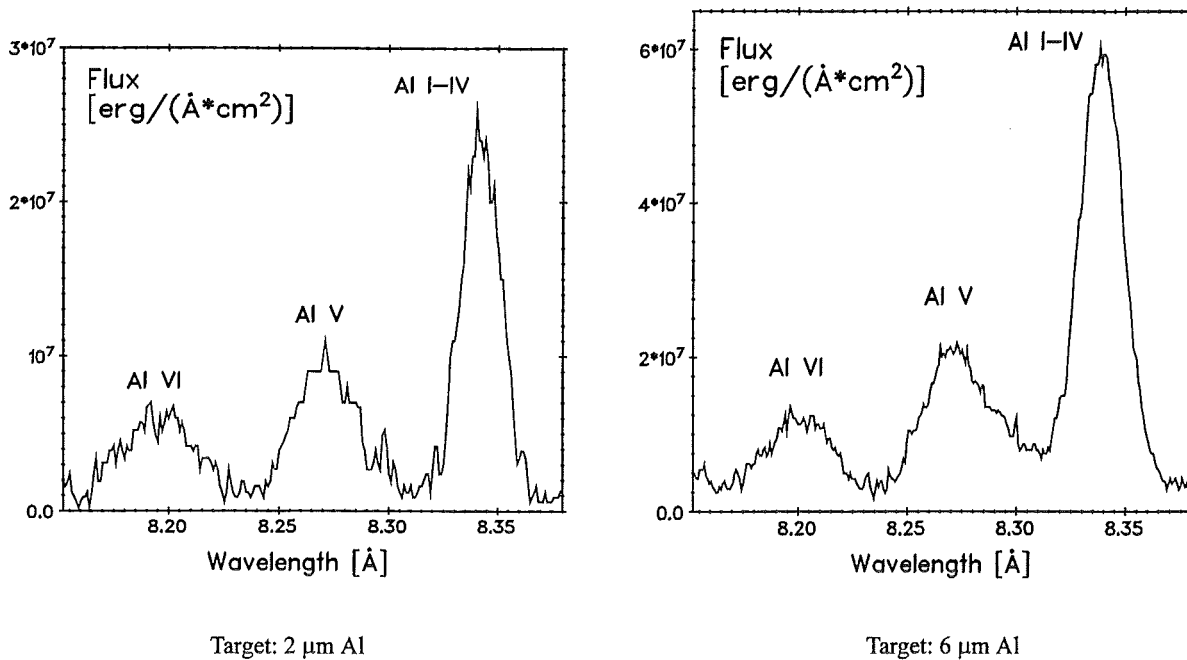


Fig. 3: K_{α} emission spectra for Al targets of 2 μm (left) and 6 μm (right) thickness as obtained with the B_{appl} diode. Note that the ordinates differ by a factor of 2 for the two curves.

A Mg spectrum is given in Fig. 4; its structure is similar to that one found for Al. In comparison with the corresponding Al spectra it is weaker by about a factor of two. This still is in agreement with a rough theoretical estimate [9]. Comparative calculations for Al and Na [7] predict slightly lower fluxes for Na resulting in a signal on the film that is down by a factor of 3. If we assume an additional overall uncertainty factor of two, the Na signal might be barely visible under our present instrumental conditions. Further investigations are required to clarify the reason why no Na signal is observed.

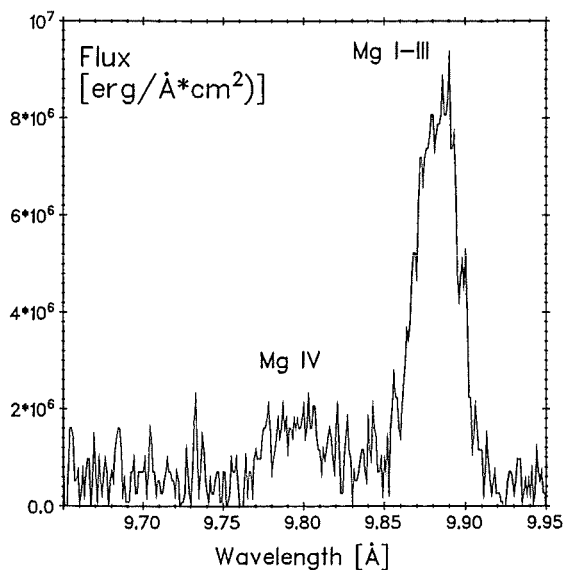
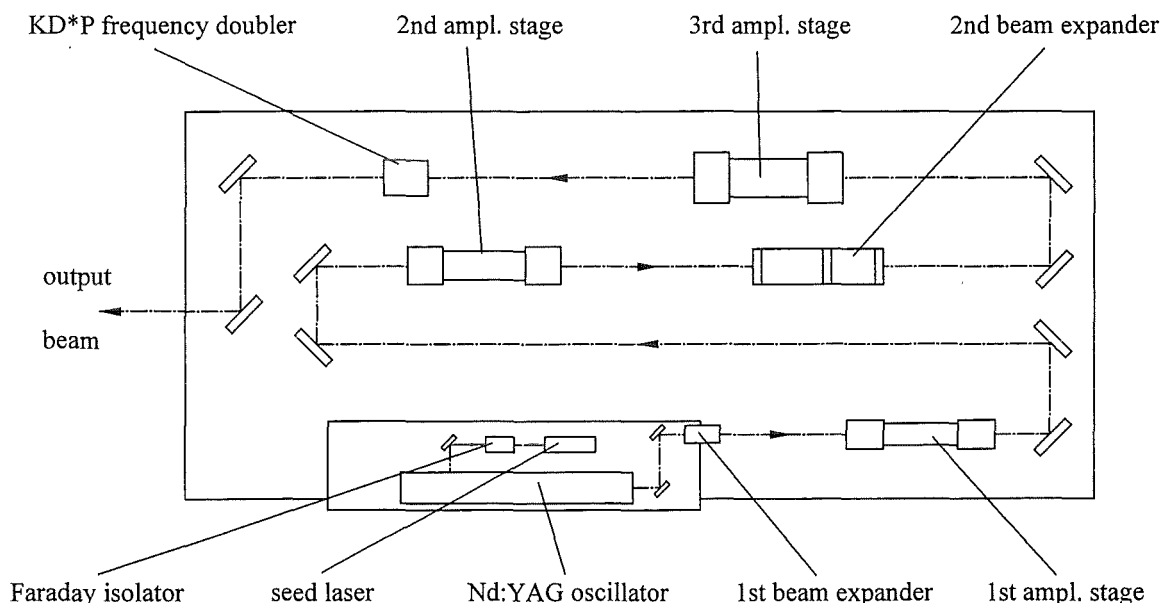


Fig. 4: K_{α} emission spectrum for a Mg target of 6 μm thickness (with 2 μm Al backing) as obtained with the B_{\odot} diode.

3. Absorption Spectroscopy

3.1. Experimental details

The absorption scheme requires a backlighter source that emits a soft x-ray continuum in the respective K_{α} region. A laser generated plasma is used for this purpose. Therefore a laser system was installed (see fig. 5). It has a Q switched Nd:YAG oscillator which is seeded from a single mode cw Nd:YVO₄ laser such that its output is a single frequency pulse of 200 mJ at 1064 nm. It operates at a repetition rate of 10 Hz. The oscillator pulse duration is about 7 ns. The oscillator output is amplified in three Nd:Glas amplifiers. At the 3rd amplifier output the pulse energy reaches 10 to 15 J. The output beam diameter is about 28 mm. The amplifier can be fired every 5 minutes. The output beam is frequency doubled in a KD*P crystal leaving a pulse energy of 4 to 8 J at 532 nm. Its duration is about 7 ns, too.



*Fig. 5: Schematic diagram of the laser system. The output of the seeded Q switched Nd:YAG oscillator is a single frequency pulse of 7 ns duration. It is amplified in 3 stages and frequency doubled in a KD*P crystal.*

To prepare experiments with KALIF, a synchronization of the laser system with the KALIF pulse generation was set up. A special feature of this device is that the laser system and KALIF interchange their role as far as their master/slave relation is concerned. The reason is that the laser oscillator has to run at its 10 Hz rate to enable the seeding feedback system to operate and to assure the thermal stability of the laser. Thus the KALIF discharge procedure is triggered (after appropriate delay) by the last oscillator pulse before the one which is to be amplified and focussed into the KALIF chamber. The trigger delay is chosen such that the next oscillator pulse (which is 100 ms later) coincides to within a few μ s with the arrival of the KALIF shot at the diode. Thereafter KALIF takes over as master, i. e. the light from the spark gap of the intermediate switch drives an electro-optical device which in turn triggers the Q switch driver of the laser oscillator.

3.2. Results

The output beam was focused onto different targets to generate a plasma. The radiation emitted by the plasma was analyzed by the x-ray spectrometer. As an example, fig. 6 gives a spec-

trum with many lines that was obtained from a copper target. The widths of the narrowest lines in this spectrum were used to determine the spectrometer resolution to be about 1000 (see above, 2.1.).

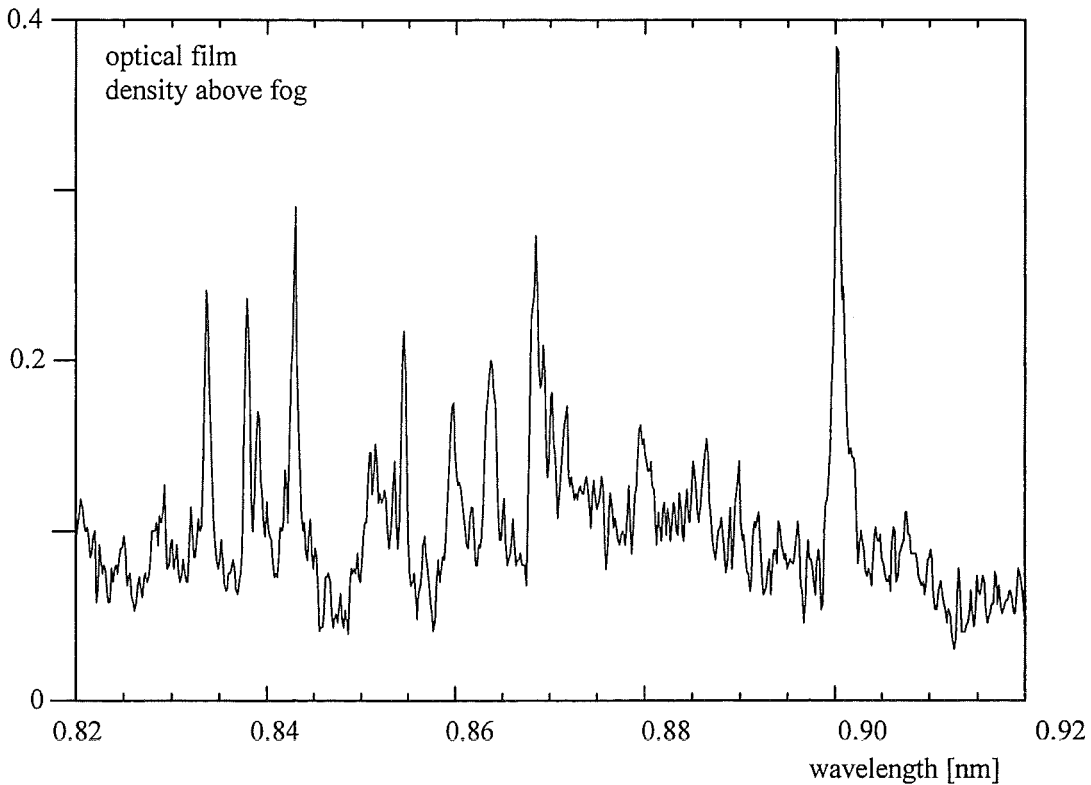


Fig. 6: Emission spectrum from a laser induced copper plasma. The laser beam had an energy of 5.4 J; the lens focal length was 500 mm.

In the same way the M_{α} spectra for the oxides of Ce, Dy, and Gd were recorded in the spectral range where Na has its K_{α} lines. The spectra were relatively weak, showing some line structure, so the search for a good backlighter material is continuing.

Tests with the laser/KALIF triggering device revealed that the overall jitter of the laser synchronization is ± 12 ns. The main contribution to the jitter is from the light output function of the KALIF spark gap which is only loosely correlated to the electrical switching function.

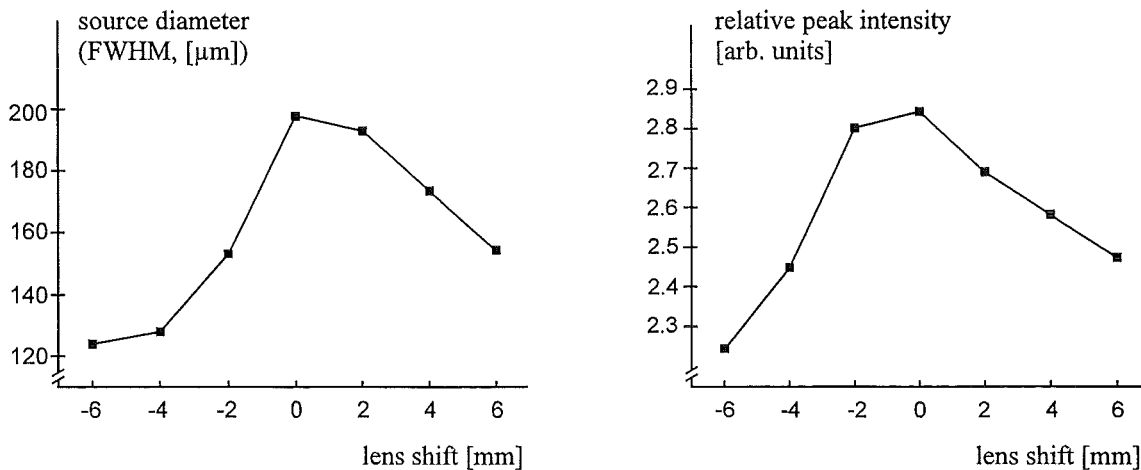


Fig. 7: The effect of laser defocussing on the backlighter source diameter and on the x-ray intensity as obtained from pinhole images.

An important parameter of the backlighter source is its diameter since it can be a resolution limiting factor. Pinhole camera images were taken to determine the source size and how critical it depends on the focussing. To ensure that only x-rays reach the film, two layers of protecting foil (2 μm mylar with two 0.06 μm Al coatings each) were used as filter. It was found (cf fig. 7) that tighter focussing leads to higher x-ray intensities, but the source diameter increases, too. However, for the diameters observed for tightly focussed pulses the source size allows for sufficient resolution.

4. CCD soft x-ray detection

The x-ray film material used so far has two essential drawbacks: The film fog represents an optical density of about 0.2 which increases with storage duration. Thus the minimum detectable intensity is severely limited, as was seen in the negative Na results (see above, 2.2). On the other hand, the highest useful optical density ("saturation") is about 3. The saturation to background ratio is only about 15 which limits the dynamic range considerably.

A CCD device has the potential to extend the detection range by its lower background and its higher saturation to background ratio. It is planned to use linear diode arrays such as model RL1024SAU-811 by EG & G Reticon with a reduced protective oxide layer thickness.

Several problems arise if delicate electronic equipment is operated near the KALIF diode since intense hard x-rays and strong microwave fields are produced. We therefore have performed measurements of the electromagnetic pollution levels for different rf shielding conditions. We used an 18 mm long wire as antenna to pick up the rf signals. They were recorded by an SCD 5000 oscilloscope by Tektronix with more than 4 GHz bandwidth. Unshielded signal levels up to 150 V_{pp} for the B_θ diode were observed, while for the B_{appl} diode the level was only 20 V_{pp} .

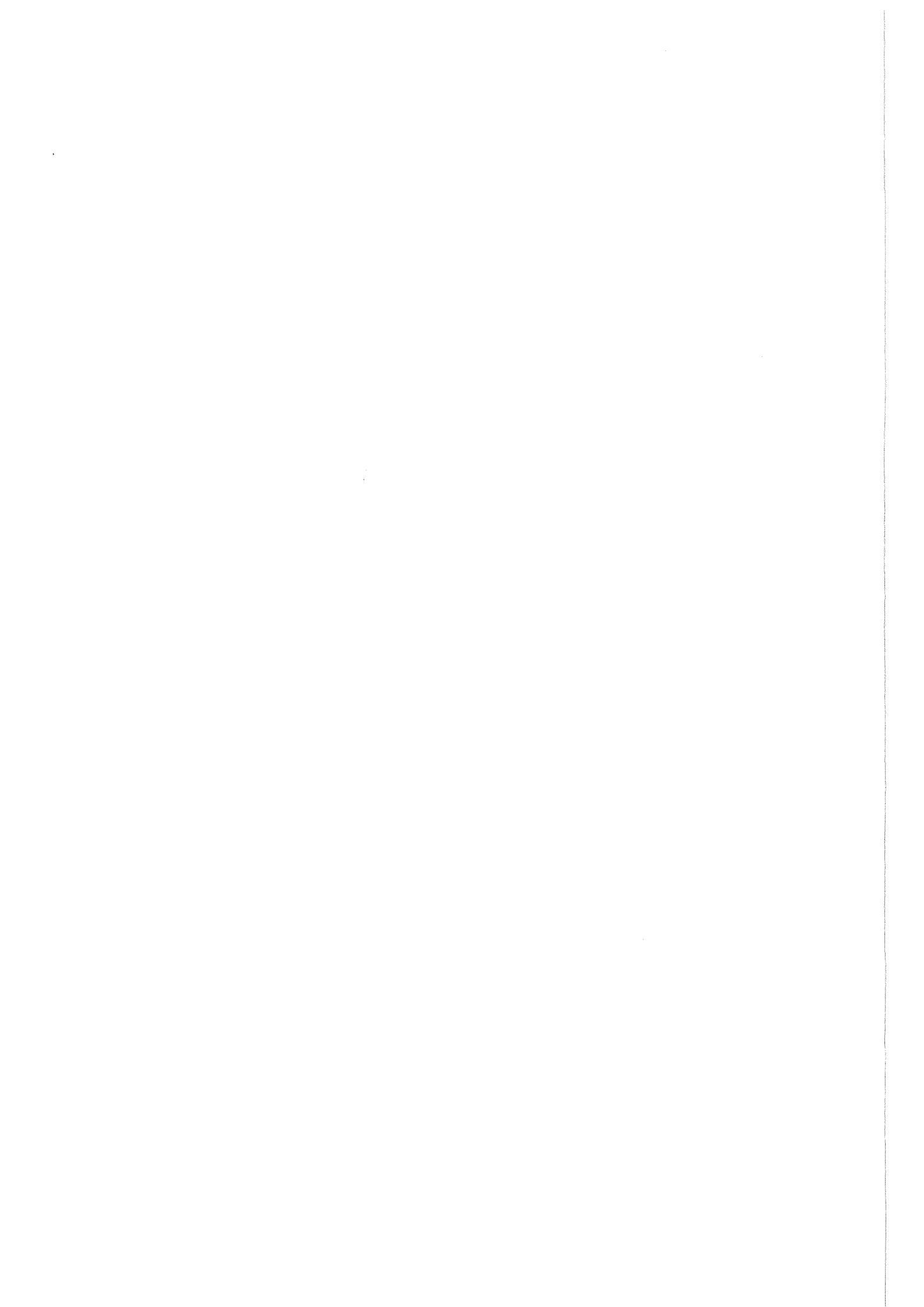
The rf shielding must leave open a path with cross section of about 6 mm by 25 mm to serve as entrance window for the dispersed x-rays. Using 90 mm long wave guides with this cross section as entrance window to a shielding box we found for the more critical B_θ diode signals from 0.8 to 8 V_{pp} depending strongly on the configuration of the vacuum lines connecting the diode and the spectrometer vacuum chambers.

References

- [1] H. Bluhm, G. Keßler: Report FZKA 5590 (1995) 1
- [2] B. Goel, W. Höbel, A. Ludmirski, J. J. MacFarlane, and P. Wang: Report FZKA 5590 (1995) 99
- [3] E. Nardi and Z. Zinamon: J. Appl. Phys. **53** (1981) 7075
- [4] G. Meisel, A. Ludmirski, J. Singer, H. Bluhm, and T. Schön: Report FZKA 5590 (1995) 95
- [5] B. L. Henke, P. Lee, T. J. Tanaka, R. L. Shimabukuro, and B. K. Fujikawa: Atomic Data and Nuclear Data Tables **27** (1982) 1

- [6] B. L. Henke, J. Y. Uejio, G. F. Stone, C. H. Dittmore, F. G. Fujiwara: *J. Opt. Soc.* **B3** (1986) 1540
- [7] J. J. MacFarlane and P. Wang: Report FZK FPA-95-3 (1995)
- [8] B. Goel: private communication (1996)
- [9] J. J. MacFarlane: private communication (1995)

V Applications



Light Ion Beam Driven Inertial Confinement Fusion: Requirements and Achievements

*H. Bluhm, G. Keßler, R.R. Petersen**
Forschungszentrum Karlsruhe
Institut für Neutronenphysik und Reaktortechnik
P.O.Box 3640, D-76021 Karlsruhe

**Fusion Technology Institute*
University of Wisconsin-Madison
1500 Engineering Drive, Madison, WI 53706

Abstract. In this paper we compare the requirements for a light ion beam driven inertial confinement fusion reactor with the present achievements in pulsed power technology, ion diode performance, beam transport and target physics. The largest technological gap exists in beam quality and repetition rate capability of high power ion diodes. Beam quality can very likely be improved to a level sufficient for driving a single shot ignition facility, if the potential of two-stage acceleration is used. Present schemes for repetition rate ion diodes allow either too low power densities or create too large beam divergence. On the other hand repetitively operating pulsed power generators meeting the requirements for an ICF reactor driver can be built with present technology. Also a rather mature target concept has been developed for indirect drive with light ion beams.

INTRODUCTION

The use of light ions to implode DT filled targets in future commercial fusion reactors has been studied for over more than 10 years. The first self consistent light ion driven power plant design LIBRA was published by the University of Wisconsin (UWM), Sandia National Laboratories (SNL) and the Nuclear Research Center Karlsruhe (KfK) in 1989 [1]. The specific issues to be solved for any light ion beam driven ICF power plant are related to the repetitive operation of the high voltage pulse generator and the ion source, to the production of high quality beams and to their transport to the target. Although the reaction chamber and the targets driven by a light ion beam also have their peculiarities, these seem to be at least not more demanding than for any other driver option.

So far the LIBRA reactor studies have been restricted to detailed investigations of the generator, the beam transport, and the reaction chamber issues. They did not address the very difficult problem of high quality repetitive beam production to any depth. The physical and technical foundations of this challenging problem must be solved first in a separate experimental and theoretical research and development program. Such programs are underway

at Sandia National Laboratories, Cornell University, NRL Washington, ILE Osaka, and at the Research Center Karlsruhe.

Meanwhile three versions of the LIBRA reactor study have appeared that mainly differ from each other by their schemes for beam transport. They considered

- preconditioning of beam channels by laser beam and pulsed direct current [1]
- ballistic transport and final focussing of the ions with robust solenoidal magnetic lenses (LIBRA-LITE) [2]
- self propagating ion beams in a self pinched mode (LIBRA-SP) [3]

From a reaction chamber design point of view the self propagating beam would be preferable. In this paper we attempt to compare the present status of R&D results with the key design parameters of the conceptual reactor design studies.

LIBRA-SP CONCEPTUAL DESIGN

The LIBRA-SP conceptual reactor design study of UWM-SNL-KfK is a 1000 MWe Inertial Confinement Fusion Reactor which utilizes 30 MeV Li⁺ ion beams propagating in a self-pinched mode from the ion diodes to the targets [3]. There are 24 Li⁺-ion beams transporting 7.2 MJ onto the target. These modules are fired in a two-step sequence to provide the desired power pulse shape. Out of these 24 beams 12 are operated in a prepulse mode delivering 1.2 MJ and 12 beams hit the target with 6 MJ in the main pulse. The prepulses have a half width of 40 ns whereas the main pulses are bunched with a pulse width of 40 ns at the diodes and 20 ns at the target. The pulses overlap at the target to impact it with 300 TW peak power. The main beam parameters are listed in Table I.

Table I. LIBRA-SP General Ion Beam Parameters

Parameter	Main Pulse	Pre-Pulse
Ion species	Li ⁺	Li ⁺
Ion energy [MeV]	30	30
Energy on Target [MJ]	6.0	1.2
Transport efficiency [%]	90	90
Number of beams	12	12
Pulse width at diodes [ns]	40	40
Pulse width at target [ns]	20	40
Total Diode current [MA]	5.56	1.11
Total current on target [MA]	10	1
Total power at diodes [TW]	167	33
Total power at target [TW]	330	30

The 24 Li⁺ ion beams are generated by Li⁺ ion diodes which are loaded by 24 driver modules. The driver modules are of the same technology as used in the electron accelerator Hermes III at Sandia National Laboratories [4]. This technology uses alternators and step up transformers in charging pulse lines to convert wall plug electrical power into 0.75 μs pulses

of 2.7 MV. The charging pulse lines then feed pulse forming lines that drive Metglas induction cells in 1.15 MV, 39 ns pulses. Each main module is made of 26 induction cells whereas each prepulse module is constructed with 18 induction cells. The driver modules are situated around the reactor chamber at two levels. Fig. 1 shows a cross sectional view of the reactor chamber with its beam lines aiming at the target.

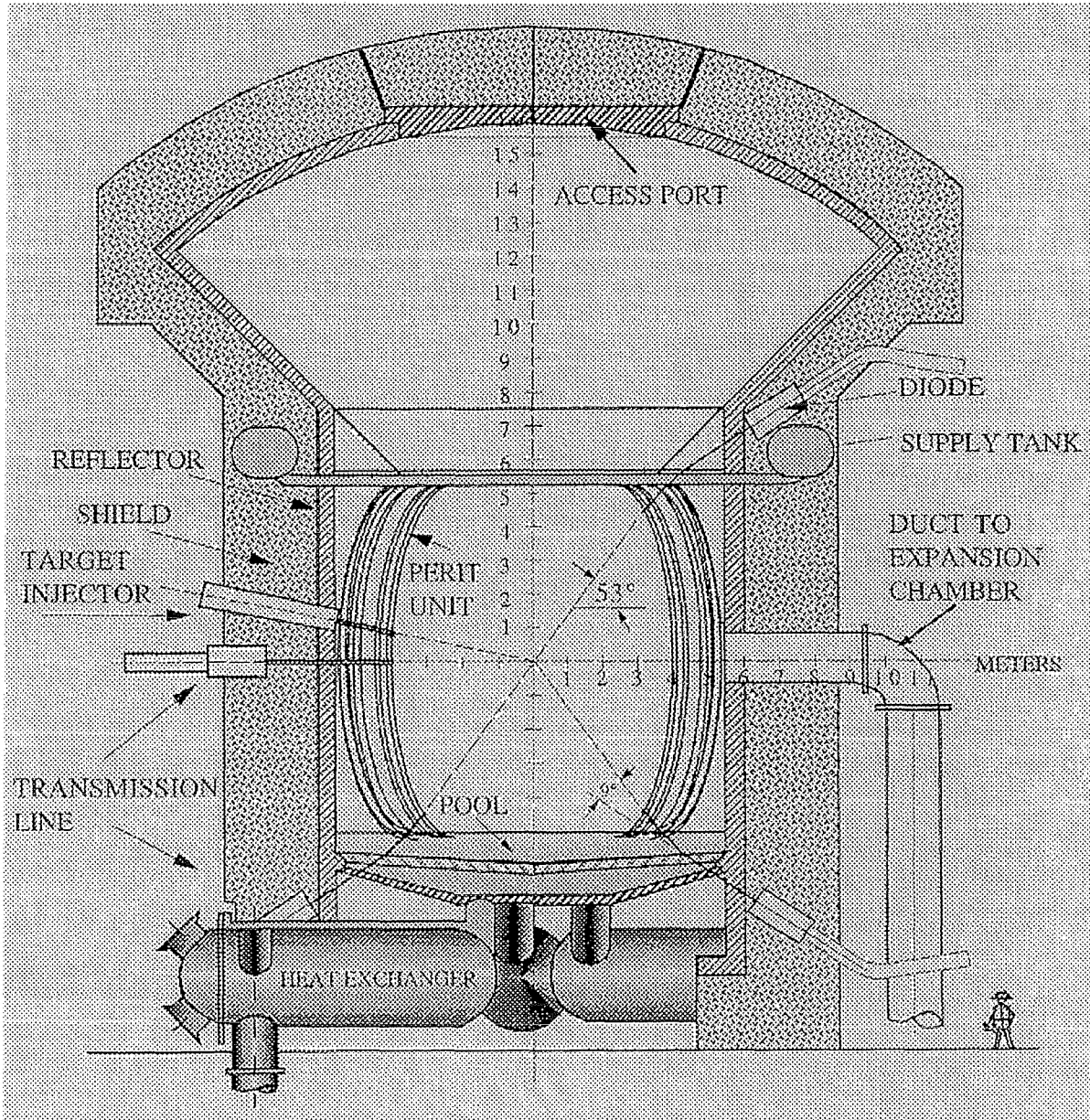


Figure 1. Cross-section of the Libra-SP target chamber

The reaction chamber is an upright steel cylinder (HT-9) of 5.7 m diameter and 13.6 m height which has an inverted conical roof extending an additional 9 m above the cylindrical position. The floor of the chamber consists of a perforated drain plate followed by a sump

leading to the intermediate heat exchangers. The cylindrical wall of the reactor chamber is shielded by a bank of curved tubes which carry the PbLi coolant and breeder material. These coolant tubes have a system of spray fan nozzles (Perforated Rigid Tubes: PERIT) through which coolant flows and forms sheets of liquid metal in front of the main tubes. These sheets will mitigate the shock waves hitting the tubes and will shield the tube surfaces from the target X-rays.

The schematic picture of a possible 2-stage diode concept for LIBRA-SP is presented in Fig. 2. Three sets of magnets are shown, one on the anode side and two on the cathode side, each consisting of an inner and an outer ring coil. The annular ion beam passes through the ring shaped gap between the inner and outer coil on the cathode side. The focal length of the

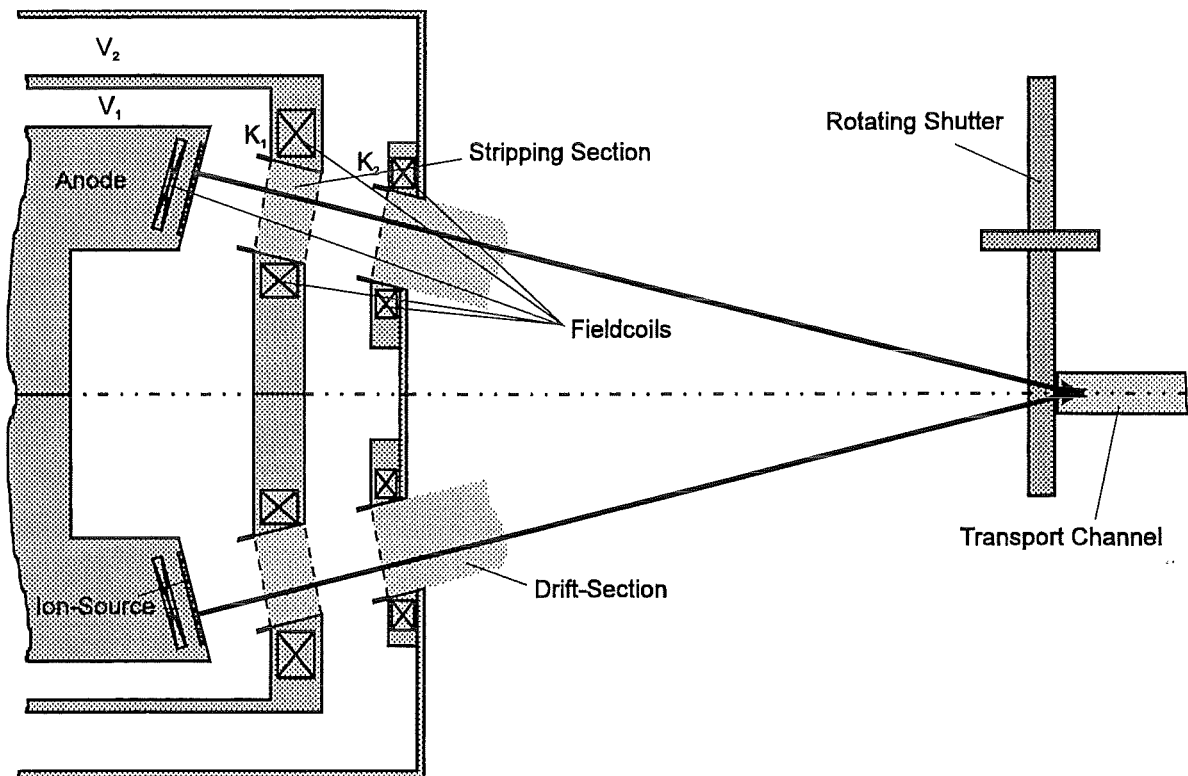


Figure 2. Schematic presentation of a possible two-stage diode design for LIBRA-SP

diode is given by the shape of the anode, the external magnetic fields acting upon the ions and by the degree of neutralization of the ion beam. The outer radius of the anode is an important parameter for the self pinched transport of the beam. The inner radius must be large enough to contain the magnetic field coils, the power feeds and the cooling channels. Rotating shutters between the 2 stage diode and the atmosphere of the reactor chamber separate the different vacuum conditions of the diodes and of the reactor chamber. It is assumed that the beams will propagate in a straight line without any pre-ionizing by a laser. The beam lines must therefore be aimed precisely at the targets.

The spherical target which is based on the target design for the Laboratory Microfusion Facility [5] is shown in Fig. 3. The peak beam power on target is 330 TW in a pulse width of

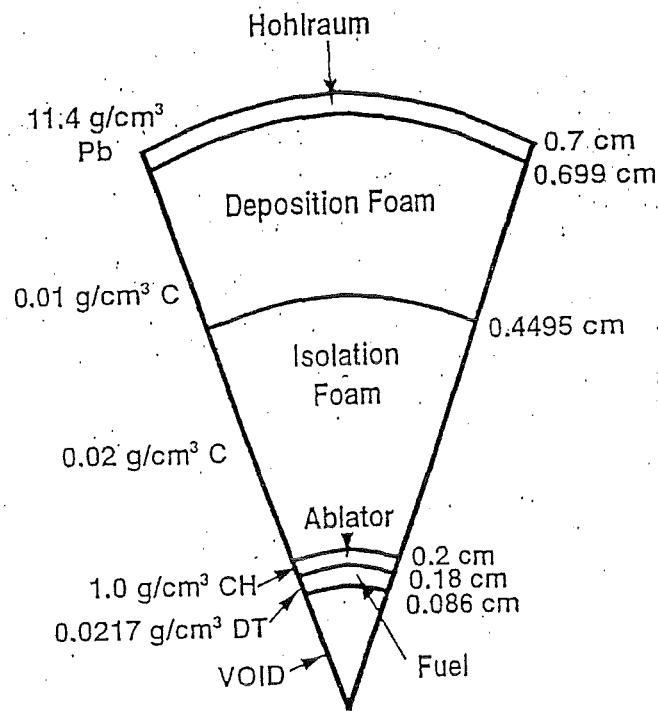


Figure 3. Schematic of initial target configuration for LIBRA-SP

20 ns. Internal pulse shaping of the X-ray flux on the inner DT-capsule is expected to lead to a gain of about 80, thus producing a total yield of 560 MJ, at a frequency of about 4 Hz. Some target data are given in Table II.

Table II. LIBRA-SP Target and Ion Beam Parameters

Total absorbed beam energy	7.2 MJ
Peak beam power (main + prepulse)	330 TW
Hohlraum radius	0.7 cm
Target gain	82
Fusion energy Yield	560 MJ
Peak beam intensity	54 TW/cm ²

STATUS OF R&D RESULTS

In the second part of this paper we analyze the present status of light ion beam reactors and compare it with the actual state of the art in driver technology, diode technology as well as experimental and theoretical results for target physics.

Driver Modules

The LIBRA-SP accelerator modules are based on the same successful technology used for the HERMES III and SABRE accelerators in Sandia, and for the KALIF-HELIA-facility at Karlsruhe as well.

This technology couples a self-magnetically insulated transmission line (MITL) with the induction linac technology. By this technique the voltage pulses from separate inductively insulated pulseforming lines are added on a coaxial vacuum line. The outer conductor of this line is formed by the inner bore of induction cells filled with laminated ferromagnetic cores. The central conductor of this line extends along the entire length of all induction cells. The voltage pulses reach the vacuum line through annular feed gaps between the cells. They propagate down the line and superpose to a pulse whose amplitude is proportional to the number of cells. This pulse can be coupled into single or two-stage ion diodes and converted into an intense ion beam.

To extract an ion beam from the accelerator the inner conductor of the vacuum line must be operated in positive polarity. In this configuration the magnetically insulated electron flow in the line is rather complex. Nevertheless experimental experience on HERMES III and Sabre has shown that the magnetically insulated voltage adder can operate with efficiencies of more than 80% [6].

In Table III the main data of a LIBRA driver module are compared to those of existing machines like HERMES III and KALIF-HELIA. It is evident that both, the electrical power and the pulse energy of HERMES III are similar to those of the main pulse beam lines of LIBRA-SP, while the electrical parameters of KALIF-HELIA are in the same class as those of the prepulse beam lines.

Table III. Comparison of LIBRA-SP driver Modules with Hermes III and KALIF-HELIA

Parameter	LIBRA-SP		Hermes III	KALIF-HELIA
	Prepulse	Main pulse		
Voltage at diodes [MV]	30	30	22	6
Number of 1 MV cavities	30	30	20	6
Current at diodes [kA]	93	463	730	400
Electrical power (1 beam) [TW]	2.8	14	16	2.4
Pulse width at diode [ns]	40	40	26	50
Polarity	+	+	- (+)	+
Energy into diode [kJ]	120	500	400	100
Type of diode	two-stage Li ⁺	two-stage Li ⁺	one-stage electron	one-stage and two-stage H ⁺ and Li ⁺

The successful operation of the RHEPP facility [7], which is based on the same technology, has demonstrated that repetitive operation of pulsed power generators can be achieved with high voltage alternators, step-up transformers and pulse compression with

magnetic saturable core switches in the charging circuit. A necessary prerequisite for long lifetime repetitive operation is to eliminate all spark gap switches in the machine by magnetic - or some other type of nonwearing-switches (semiconductor switches). This also has the advantage to increase the efficiency of the generator from typically 40-50% with spark gaps to more than 80% with magnetic switches.

Summarizing, high power pulse generators with 3-4 Hz repetition rate complying with the requirements for ICF-driver modules can be built with present day technology.

Extraction Ion Diodes

The conclusion of the last paragraph cannot be drawn for ion beam production. With respect to ICF reactor applications the main issue is to develop a technology that allows repetitive diode operation together with sufficiently small beam divergence. Presently both requirements are attacked independently. Although this may be reasonable for a single shot ignition facility and for other industrial applications of ion beams, a unified approach is necessary for an ICF reactor ion diode.

The lowest measured ion beam divergence from single stage diodes is around 17 mrad [8]. Until today two-stage diodes have mainly been operated on rather low power machines [9,10]. In these experiments values as low as 10 mrad have been found. For reactor applications less than 5 mrad are needed while 10 mrad maybe sufficient for an ignition facility. A prerequisite for divergence reduction is to identify the main sources, and to understand their origin and their dependence on important parameters like current density, voltage, magnetic field, ion mass etc. A large experimental and theoretical effort is presently underway in several laboratories to accomplish this task.

So far two main sources of beam divergence have been identified inside the diode accelerating gap: inhomogeneities and surface roughness of the anode plasma which delivers the ion beam and instabilities of the free electron sheath containing the virtual cathode. While the first source can be mitigated by improved anode plasma production it is not yet clear whether the most damaging electron sheath instabilities can be suppressed. Although reliable scaling laws are not yet available, it seems obvious that the effect of instabilities decreases with decreasing current density, and increasing voltage and ion mass. The advent of new high voltage accelerators like PBFA-X, KALIF-HELIA and Sabre shall accelerate the determination of the required scaling laws.

In addition it will become possible to investigate two-stage diodes on higher power machines. Two-stage diodes allow an independent control of voltage and current and much stiffer diode impedances are predicted. This kind of impedance behavior is necessary if beam bunching shall be utilized to increase the power density on target. However, the largest potential of two-stage diodes in reducing the beam divergence is probably given by post acceleration. 3-dimensional particle in cell code simulations have shown that the ion divergence scales with the injected current density [11,12]. If the current density is kept close to the value at which the formation of a virtual anode occurs only longitudinal velocity is added to the ions in the second stage and thus their divergence is reduced. Since the physics of the second acceleration stage is even more complex than that of the first, an experimental verification of the predicted

results on high power machines seems necessary. Generally it appears desirable to increase the particle energy and mass of light ion driver beams.

Although the voltage adder technique may allow accelerating voltages of up to 60 MV single stage acceleration looks completely unrealistic at these voltages. It would require very large insulating magnetic fields, exceeding the yield strength of any coil material. If a two-stage scheme is used high particle energies are easier to realize. Utilizing charge stripping between the stages high particle energies can be achieved with much lower voltage pulses. E.g. connecting two 10 MV accelerating stages by a stripping cell 40 MeV Li^{3+} ions can be produced.

Although a repetition rate capability is not necessary for a single shot ignition facility, it needs to be developed for a reactor diode. A good starting point for this development is the MAP-diode [13]. However, a strong increase in current density and a drastic reduction of beam divergence is necessary before this diode satisfies the requirements for a reactor driver. Therefore, other schemes should be considered.

Summarizing it is very likely that the big experimental and theoretical effort to understand the physics of the accelerating gap in high power ion diodes will lead to a beam divergence reduction compatible with the requirements for an ignition facility. Two-stage ion acceleration has an even larger potential to improve the beam quality. However, more experimental results from high power accelerators are needed. The development of ion diodes with repetition rate capabilities is still in its infancy. New schemes that do not sacrifice the beam quality have to be created.

Beam Transport

Several different transport schemes have been considered for light ion beam driven reactors. The most promising among these are ballistic transport combined with solenoidal focusing [2, 14] and self-pinch transport [3]. In the first scheme a background gas provides charge and current neutralization. The gas pressure must also be chosen to prevent excessive small angle scattering and energy loss and to avoid the occurrence of filamentation instabilities. If 30-40 MeV Li^{3+} ions are considered about 100 Pascal of helium gas pressure complies with these requirements. A disadvantage of this approach is that the solenoidal lens must still be rather close to the target and therefore, will be exposed to a large neutron and soft X-ray radiation flux.

No transport apparatus in the reactor chamber is required for the self-pinch transport scheme. Since it would allow small holes in the chamber wall and thus easy protection of the diode hardware it is considered as the most preferable concept for high yield repetitive target ignition. Self-pinch transport requires a low pressure ± 10 Pascal gas background in the chamber. A net electrical current

$$I_{\text{net}} = 0.5 \left(\frac{R_o}{r_f} \right)^2 \Theta_m^2 I_A$$

is needed to trap the ion beam. (I_A = Alfvén current, R_o = radius of the beam envelope, r_f = focal spot size, Θ_m = beam microdivergence). The details of this transport scheme have not yet

been studied adequately. The key issue is the gas breakdown process, which occurs at the head of the beam. If the breakdown process occurs too fast the net current frozen in the plasma may become too small to confine the beam. Theoretical modeling suggests that fast electrons with mean free path greater than the beam radius produce non-local breakdown effects which may influence the net current amplitude [15].

Summarizing, both transport schemes need further theoretical and experimental investigations. This is especially true for the self-pinch transport, where very little experimental work has been done.

Target Physics

The concept of the foam filled light ion driven hohlraum target shown in Fig. 3 is probably one of the most attractive target designs. It takes advantage from the proper range of 30 MeV Li-ions, which is large enough to penetrate the hohlraum wall, yet short enough to be completely stopped in the foam. This target concept avoids some of the nonsymmetry problems resulting from rather localized converters and therefore does not need any shims to smooth the radiation. In addition the foam filled hohlraum reduces the hydrodynamic inward motion of the hohlraum wall.

Conversion of light ion beam energy into a soft X-ray radiation field has been carried out with foam filled hohlraum capsules at specific power depositions around 1000 TW/g on PBFA II [16]. In these experiments hohlraum temperatures around 60 eV have been achieved and it has been shown that a transparent hohlraum fill was created. Also another basic LIF target concept has been investigated: Internal pulse shaping using shells of BeO and Be was demonstrated in laser driven hohlraums [16].

The target experiments on PBFA II with specific power depositions above 1000 TW/g allow to study the physics in the prepulse of an ignition target. Besides this several other issues of ICF targets can be studied at even lower power densities around 200 TW/g attainable on KALIF and comparable generators of the 1 TW class. Target layers have been accelerated to approximately 1/10 of the implosion velocity necessary to ignite a target [17]. We have started in our own laboratory to study the hydrodynamic stability of perturbed accelerated foil targets. In addition from these target experiments fundamental quantities of intense ion beam target interaction like specific energy loss, ion range, eos data, opacities, and soft X-ray conversion efficiency can be determined.

Summarizing, a very attractive target concept has been developed for LICF. Fundamentals of this target concept have been verified experimentally. The presently achieved power density in the focus of intense light ion beams is sufficient to study several quantities that are important for ICF.

CONCLUSIONS

We have compared the requirements for a light ion beam driven inertial confinement fusion reactor with the present achievements in pulsed power technology, ion diode performance, beam transport and target physics. It is obvious, that the largest technological

gap still exists in the production of high quality (low divergence) intense ion beams. Therefore, a continued strong research effort is necessary to solve this issue. A large potential lies in the utilization of two-stage acceleration. Using this potential and improving our knowledge about the physics of the diode accelerating gap will very likely lead to beam qualities matching the requirements for an ignition facility. Besides beam quality, repetition rate capability is the next big issue of ion diode development. Although not necessary for a single shot ignition facility, new schemes should be investigated as early as possible. Here the main problem is not to lose beam quality in return.

After the diode issues the second largest needs for development are in the beam transport. Especially, the self-pinched propagation scheme requires further experimental and theoretical investigations.

In contrast to the diode and transport problems the achievements in driver technology and target design look very mature. Suitable pulse power generators with repetition rate capability (3-4 Hz) can be built based on available technology. In addition some ion beam-target interaction experiments with relevance to ICF targets can be carried out with presently achievable beam intensities.

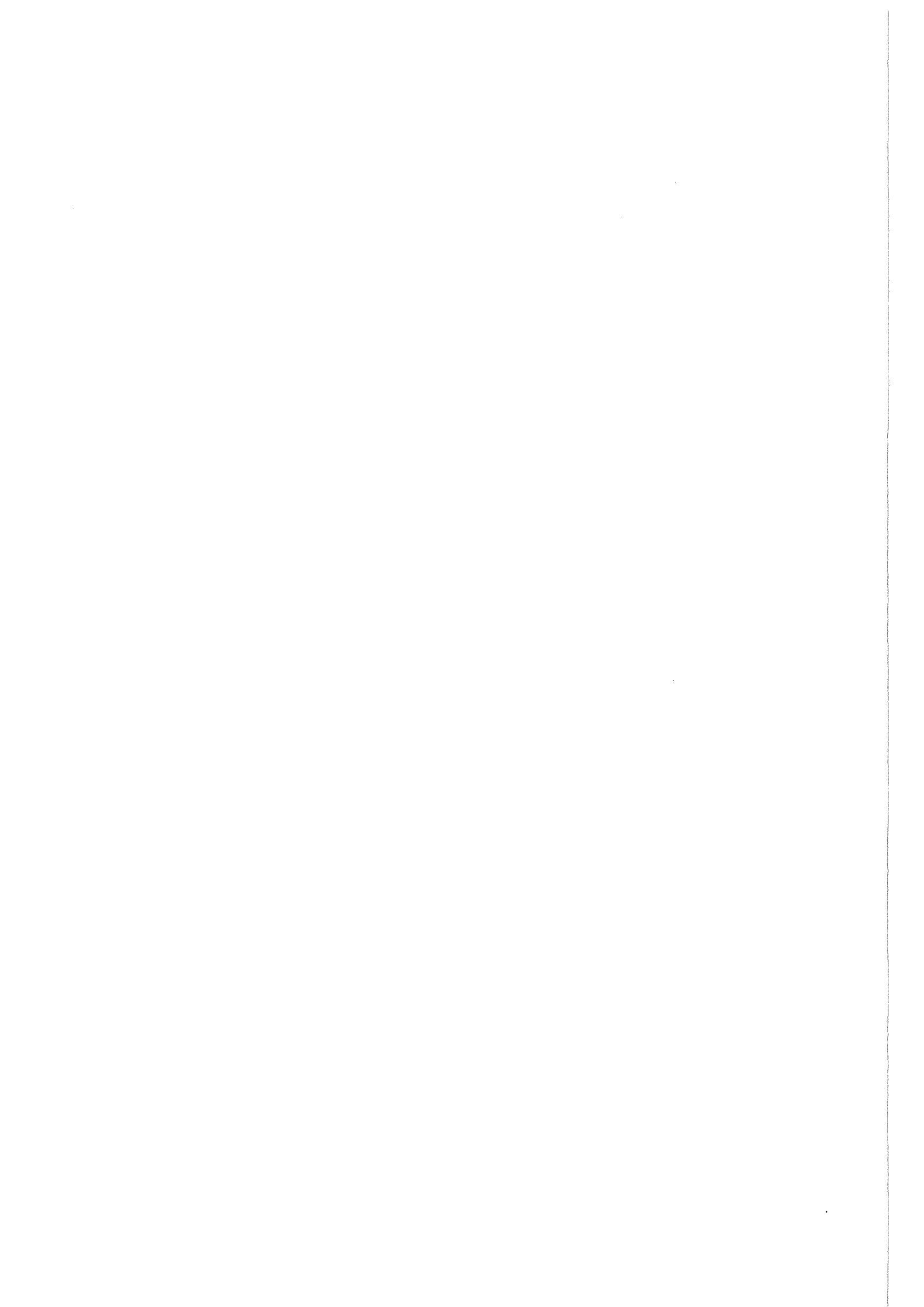
The large research and development effort that is still needed to match the requirements for light ion beam driven ICF seems justified by two potential advantages of the light ion approach:

1. Its outstanding low costs and high efficiencies;
2. The prospect that this technique is likely to meet the requirements for a high gain ignition facility, which then could be built at affordable costs.

REFERENCES

- [1] B. Badger, et al., Res. Rep. KfK, KfK-4710 (1989)
- [2] B. Badger, et al., Res. Rep. Univ. of Wisconsin, UWFD880 (1991)
- [3] B. Badger, et al., Res. Rep. Univ. of Wisconsin, UWFD892 (1995)
- [5] R.J. Leeper, Paper presented at Int. Workshop on Ion Beam Driven ICF, Osaka, (May 1, 1995)
- [4] J.J. Ramirez, K.R. Prestwich, J.D. Smith, Proc. of the IEEE, 80, 946 (1992)
- [6] J.W. Poukey, M.E. Cuneo, T.R. Lockner; Proc. 10th Int. Conf. on High Power Particle Beams, San Diego, p. 394 (June 1994)
- [7] D.L. Johnson, et al., Proc. 9th Int. Pulsed Power Conf. Albuquerque, New Mexico, (June, 1993)
- [8] H. Bluhm, P. Hoppe, H.P. Laqua, and D. Rusch, Proc. IEEE 80, 995 (1992)
- [9] S. Miyamoto, A. Zakou, K. Imasaki, C. Yamanaka, S. Nakai, Proc. 8th Int'l Conf. on High Power Particle Beams, Novosibirsk, p. 190, (July 2-5, 1990)
- [10] T.R. Lockner, S.A. Slutz, J.W. Poukey, and W. Stygar, Proc. IEEE 1993 Pulsed Power Conf., Albuquerque, (1993)
- [11] S.A. Slutz, M.P. Desjarlais, J. Appl. Phys. 67, 6705 (1990)
- [12] S.A. Slutz, paper presented at the Workshop on High Energy Density in Matter, Hirschegg, (Febr. 1993)

- [13] W.A. Noonan, S.C. Glidden, J.B. Greenly, and D.A. Hammer, *Rev. Sci. Instr.* 66, 3448 (1995)
- [14] P.F. Ottinger, D.V. Rose, J.M. Neri, C.L. Olson, *J. Appl. Phys.* 72 395 (1992)
- [15] C.L. Olson, J.P. Quintenz, R.O. Bangerter, B.G. Logan, J.D. Lindl, *Proc. IAEA Techn. Com. Meeting on Drivers for Inertial Confinement Fusion, Paris*, p. 259, (November 1994)
- [16] R.J. Leeper, et al., *Proc. 12th Int. Conf. on Laser Interaction and Related Plasma Phenomena Osaka*, (April 1995)
- [17] K. Baumung, H.U. Karow, D. Rusch, H. Bluhm, P. Hoppé, G.J. Kanel, A.V. Utkin, V. Licht, *J. Appl. Phys.* 75, 7633 (1994)



RESULTS OF RECENT INVESTIGATIONS CONDUCTED ON THE PULSED PROTON BEAM FACILITY PROFA

H. Giese, V. Engelko*, S. Schalk

Forschungszentrum Karlsruhe GmbH, Postfach 3640, D-76021 Karlsruhe, F.R.G.

*permanent address: Efremov Inst. of Electrophys. Apparatus, 189631, St. Petersburg, Russia

ABSTRACT

Recent activities at the pulsed proton beam facility PROFA [1, 2, 3] include optimization of the mechanical and electrical diode parameters, assessment of the limiting operational parameters of the diode (maximum achievable pulse duration, diode current and current density), measurements of the radial and axial ion beam current density profiles in the drift space, and first tests of the beam space charge neutralization in the target plane.

The presently achieved maximum proton current densities at the emitting anode surface, in the ballistic focus plane and in the target plane of PROFA are of the order of $0.1\text{A}/\text{cm}^2$, $1\text{A}/\text{cm}^2$ and $5\text{A}/\text{cm}^2$ respectively. The maximum diode current is 100A. Residual problems are: insufficient space charge neutralisation, premature diode breakdown in the high current operating regime and higher than expected beam divergence.

Complementing the work performed at FZK, side investigations run at the St. Petersburg State University aimed at measuring the composition of an ion beam produced by a PROFA type diode and to quantify the effects of anode aging and reconditioning on the beam composition.

1. INTRODUCTION

The principal layout of the PROFA facility in its present state is shown in Fig.1. An extraction type diode of 44cm diameter with concave electrode surfaces for ballistic beam focusing is accommodated in a stepwise tapered vacuum vessel. The magnetic coil system surrounding the vessel has been designed to allow an adiabatic compression of the beam within a short distance [4].

The PROFA diode comprises an anode discharge electrode (ADE) for plasma production and a set of stainless steel grids for ion extraction. The ADE is a perforated concave stainless steel shell containing 750 spark units with an average distance of 2cm. Each of these spark units consists of a polyethylene plug of 6 mm diameter and a central needle electrode. All needle electrodes have series resistors R_o and are jointly connected to ground via an external RC network R_a, C_a .

Applying a positive high voltage pulse to the ADE leads to a surface discharge across each polyethylene plug from the ADE body to the central needle electrode, and to the formation of a hydrogen-rich plasma cushion on the ADE surface. Adequate choice of the series resistors R_o ensures homogeneous firing of the spark units over the ADE surface. After expansion of the plasma cushion to the anode grid AG, ions are extracted under the influence of the diode electric field and accelerated towards an accel-decel configuration consisting of an adequately biased double grid arrangement CG1, CG2. After passing through the ballistic focus at a distance of 60 cm from the diode, the proton beam diameter is further reduced by approx. a factor of 3 by magnetic compression.

Initial measurements performed at PROFA in 1994 were focused on component tests and exploratory studies, like e.g. the vacuum operating range of the facility, the applicability of different methods of beam space charge neutralisation and measurements of the beam envelope. The majority of these early measurements was run using relatively small diode currents. It was found that in this operating regime, the diode could deliver proton pulses of up to $40\mu\text{s}$

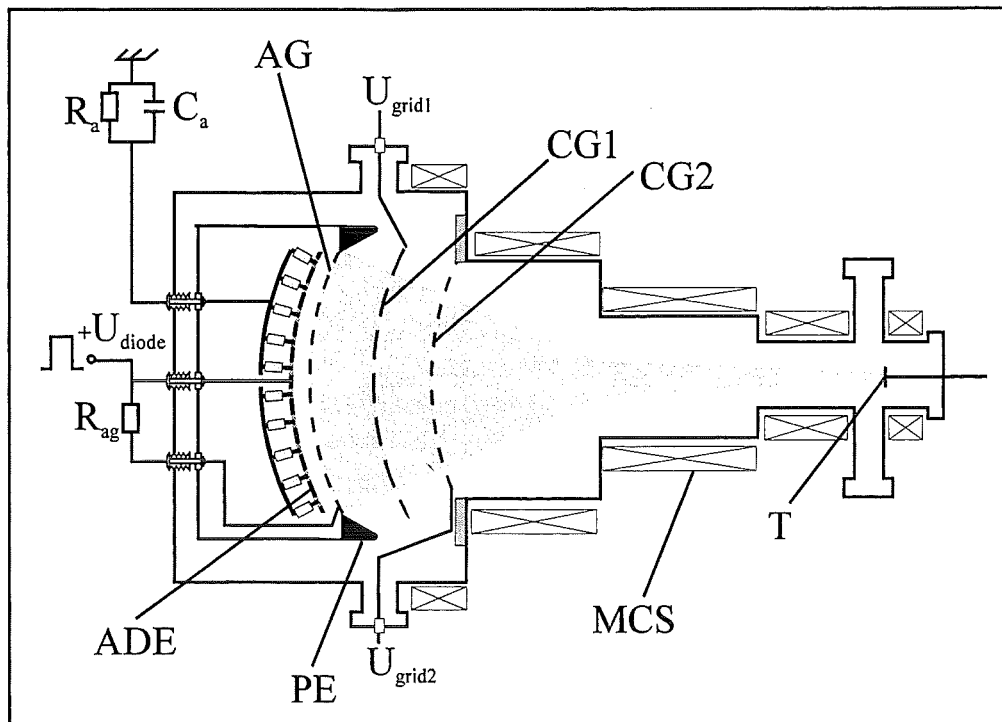


Fig. 1: Schematic layout of the pulsed proton beam facility PROFA.

ADE: anode discharge electrode; AG: anode grid; PE: Pierce electrode;
CG1,CG2: cathode grids; MCS: magnetic coil system; T: target.

in length, limited only by the capability of the high voltage pulse generator. The maximum beam current density recorded in the target plane was about 40 mA/cm^2 .

In 1995 the key issue of the investigations was the transition to higher beam currents. Activities included the mechanical and electrical optimization of the PROFA diode and the development of more reliable diagnostic equipment. Detailed studies were then made of the diode operation limiting parameters, of the radial and axial beam current density profiles and of the beam space charge neutralisation.

Complementing the studies performed at FZK, experiments conducted at the St. Petersburg state university on a scaled down replica of the PROFA diode, concentrated on measurements of the beam composition and divergence.

Reported hereafter are the hardware improvements of predominant importance and some selected results of the experiments performed in 1995.

2. OPTIMIZATION OF THE PROFA DIODE:

This campaign comprised the following steps:

1. The PROFA anode originally had two perforated stainless steel plates with a combined transparency of only about 7% installed in front of the anode discharge plate. These two plates were replaced by one anode extractor grid with 70% transparency. The new grid (AG in Fig.1) was fabricated from 1mm stainless steel wires with a pitch of 2cm and formed to a spherical shape of 60cm radius. A fine stainless steel cloth was welded on top of this support structure to minimize electric field waviness along the ion extraction boundary.
2. Parametric studies showed a significant influence of the potential of the anode extractor grid on the diode current. It was found that the diode current reached a maximum when AG was allowed to adopt the anode plasma floating potential. This was achieved by connecting AG to the anode discharge electrode through a resistor of adequate magnitude, given by:

$$R_{AG} \gg \frac{T_e}{eI_{i0}(1-\alpha)} \quad (1)$$

where T_e is the electron temperature, α is the anode grid transparency and $I_{i0} = 0.49 \cdot enA(T_e/m_i)^{1/2}$ (n = anode plasma density, m_i = ion mass, A = anode grid area) is the ion saturation current. In our case, using $R_{AG} = 1k\Omega$ an increase of about 50% in diode current was observed with respect to the situation, when AG was held at the potential of the ADE.

3. The PROFA cathode grid arrangement was improved in two respects: The total transparency was increased using similar grids as for the anode, and both grids are now independently biased to optimize space charge neutralisation by secondary emission electrons originating from ion collision with the cathode grids. The first cathode grid is presently held at a high negative bias of -1 to -2kV and the second at a low negative bias of about -100V. In the presence of the ion beam, this type of biasing establishes an electric field distribution between the two grids, that maximizes trapping of the secondary emission electrons inside the beam and minimizes both, electron backflow to the anode and oscillations of the beam current.
4. The diode gap was reduced from originally 4.5 to 1.5cm. It should be mentioned that the curvature of the cathode grids has not yet been adjusted to the new gap width, leading to an increase of the gap width from the central value of 1.5cm to an edge value of about 1.7cm. This deficiency introduces a certain steering error that contributes to the total beam divergence, the magnitude of which has not yet been quantified.

3. PERFORMANCE OF THE PRESENT DIODE ASSEMBLY

A substantial number of experiments has been devoted to the assessment and optimization of the operational parameters of the diode.

The integral ignition behavior of the anode discharge units was surveyed during source operation by taking long exposure photographs of the ADE through a window in the bottom of the vacuum vessel. These showed that the distribution of fired spark units across the surface of the ADE was rather homogeneous, and that their number ($\approx 75\%$ of the total number for a diode voltage of 22 kV) corresponded well with the number deduced from measurements of the voltage drop across the series resistors R_0 .

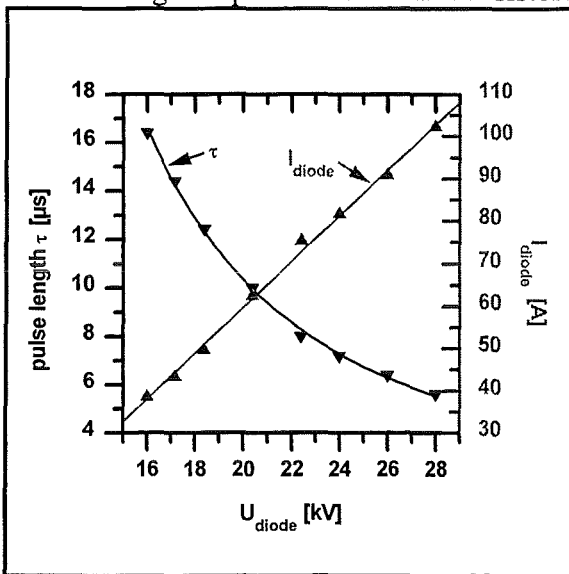


Fig. 2: Pulse length and total diode current as a function of voltage for $R_a = 8\Omega$. A linear fit for I_{diode} is included.

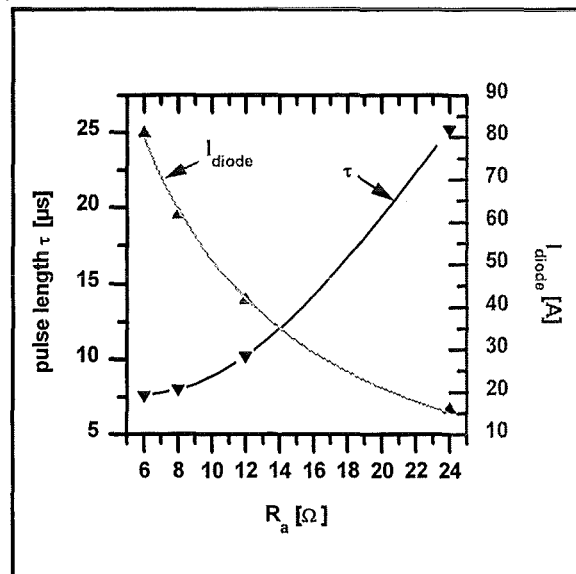


Fig. 3: Pulse length and total diode current against anode resistor R_a for $U_{diode} = 20.4$ kV.

Numerous measurements were made of the dependence of the diode current I_{diode} and of the total pulse length τ on the diode voltage U_{diode} , the diode gap, the external anode resistor R_a , and on the potential of the anode grid AG.

It was found that the diode current is directly proportional to the discharge current I_{dis} , i.e. the total current through all discharge units which determines the anode plasma production rate, with a fixed ratio $I_{\text{diode}}/I_{\text{dis}} = 0.05$. Since I_{dis} is mainly governed by the ratio U_{diode}/R_a , the diode current can simply be controlled by R_a .

Two representative examples of the measured dependence of τ and I_{diode} on U_{diode} and R_a are given in Fig. 2 and 3. One can see that I_{diode} exceeds 100 A at $U = 28$ kV. The space charge limited diode current predicted by Child-Langmuir theory is 112 A. Unfortunately τ is only about $5.5 \mu\text{s}$ under such conditions. The exact breakdown mechanism responsible for the pulse length decrease with increasing U is not fully understood to date. It seems likely that filling of the diode gap by neutrals generated in the arc units could lead to a gas breakdown.

4. PROTON BEAM CHARACTERISTICS

Various diagnostic tools have been employed in the course of the experiments, like integrating calorimeters, capacitive probes, damage paper and ion sensitive films. The measurements most thoroughly interpreted to date, some selected results of which are shown hereafter, are those using a three electrode collector (TEC). This device comprises a collector cup and a repeller electrode, both accommodated in an outer stainless steel housing. Adequate negative biasing of the repeller allows to completely remove comoving electrons from the beam and to measure the clean ion current [5].

It should be mentioned that results referring to the ballistic region were obtained without applying the compressing magnetic field.

Fig. 4 shows two measured angular distributions of the maximum ion current density \hat{j}_i recorded at a distance of 7 cm below the second cathode grid under similar operating conditions ($U_{\text{diode}} \approx 20$ kV, $R_a = 8 \Omega$, diode gap ≈ 1.5 cm, cathode grid distance 3 cm). Both measurements were made using a 11.5 mm entrance aperture TEC, supported by articulated rods in such a way that it could be swiveled around the machine axis with the centre of rotation positioned in the ballistic beam focus. While dis. 1 was recorded using the anode configuration shown in Fig. 1, dis. 2 was obtained using an additional grid of 35% transparency installed

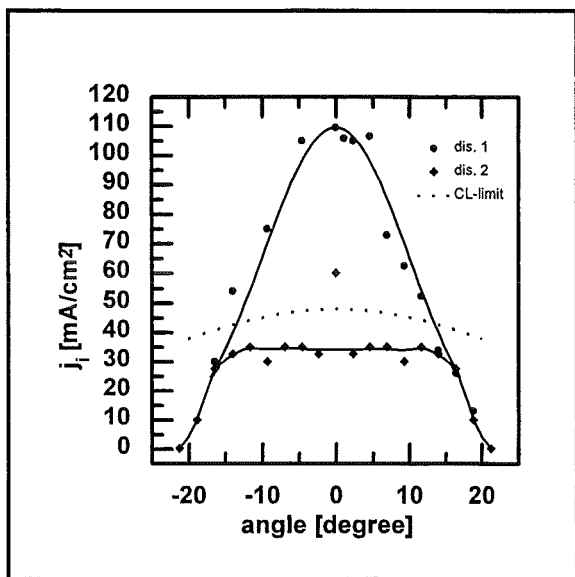


Fig. 4: Maximum ion current density as a function of angle, recorded 7 cm below second cathode grid for two conditions. (see text for details).

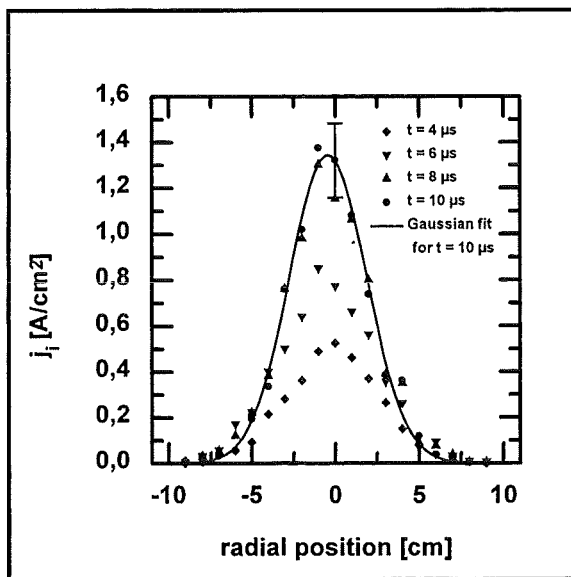


Fig. 5: Ion current density against radial position in the ballistical focus plane for different times.

between the anode discharge electrode and the anode grid. Dis. 1 shows a Gaussian profile, with \hat{j}_i near the beam axis exceeding 0.1 A/cm^2 . Considering the focusing effect and the grid transparencies, this value corresponds to 0.11 A/cm^2 at the emitting boundary, the AG. The directly measured total diode current is 55 A , which is in good agreement with the current obtained from integration of dis.1.

Dis. 2 shows that the introduction of an additional anode grid has substantially improved homogeneity of the plasma profile, but at the cost of reduced current density.

For comparison, Fig. 4 also shows the ion current density obtained from Child Langmuir theory. The reduction of j_i at large angles is due to the increase of the diode gap originating from the inadequate curvature of the cathode grids (see section 2.4).

Fig. 5 shows the ion current density distribution in the plane of the ballistic focus under the same conditions as dis. 1 in Fig. 4 for different moments in time. A detailed study of beam emittance utilizing a multiaperture or scanned aperture technique has yet to be done. Nevertheless, it is viable to make a simple estimate of the emittance based on the known geometry of the configuration and the radial beam profile in the ballistic focus plane. This estimate implies the calculation of the beam divergence half-angle corresponding to the half-width radius (HWHM) of the Gaussian fit, which is given by

$$\Theta_{\text{HWHM}} = \frac{r_{\text{HWHM}}}{L} \quad (2)$$

where L is the ballistic focal length of the system ($L = 60 \text{ cm}$). The beam emittance is then approximated by

$$\varepsilon = r_0 \Theta_{\text{HWHM}} \quad (3)$$

where r_0 is the extractor radius ($r_0 = 22 \text{ cm}$); this assumes that the beam envelope is at a waist in the ballistic focus plane. With $r_{\text{HWHM}} = 2.7 \text{ cm}$ (for $t = 10 \mu\text{s}$) one obtains a divergence half-angle of 45 mrad and thus an emittance of $100 \pi \text{ cm mrad}$ (this is equivalent to a normalized emittance of $0.64 \pi \text{ cm mrad}$).

In a similar way, the radial current density distributions shown in Fig.5 also allow to derive the fraction of the total diode current that can be attributed to a given beam divergence range (Fig.6). One can see that only a fraction of about 25% of the total beam current possesses a divergence $\leq 30 \text{ mrad}$, and that the total beam divergence amounts to 150 mrad . This is important, since the magnetic compression system of PROFA had been designed for an anticipated maximum beam divergence value of 30 mrad [4]. In this context it should be noted,

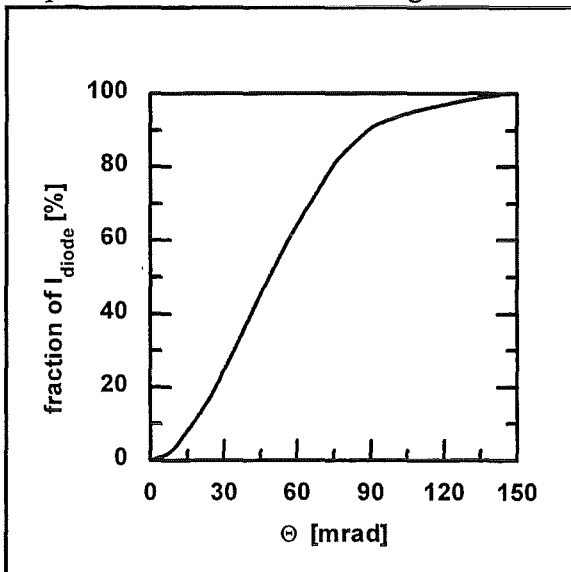


Fig. 6: Fraction of diode current that can be attributed to a beam divergence range from 0 to Θ .

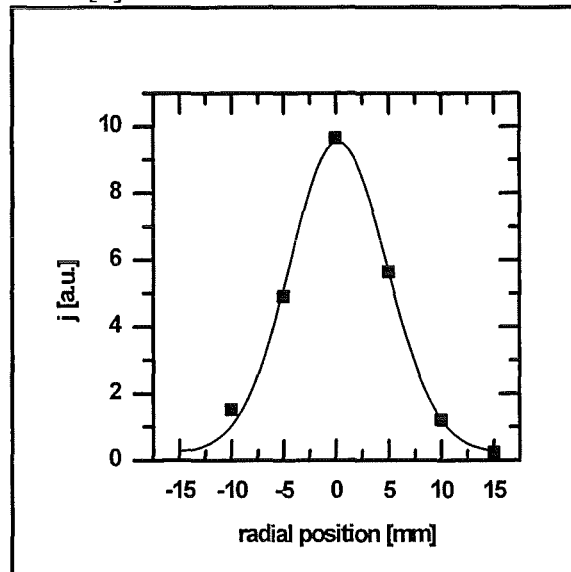


Fig. 7: Radial profile of the ion current density in the target plane.

that the total divergence value of 150mrad is composed of several contributions: (1) The source divergence (transverse velocity component in anode plasma), (2) steering errors and (3) beam widening due to insufficient space charge neutralisation. Present investigations aim at a quantification of these different components.

For the position on the center axis (radial pos. 0 cm in Fig. 5) 7 shots were taken to get a better understanding of the reproducibility of the beam. The error bar for this point at 10 μs is also displayed in Fig. 5 and corresponds to a relative statistical standard variation of 12%. In contrast it was found that the relative statistical standard variation for the diode current is only about 3.5%. This indicates that there are local fluctuations of the current density, although the total beam current from shot to shot remains very stable.

An example of the latest results obtained using calorimetric measurements is presented in Fig.7. Shown here is a radial beam profile recorded in the target plane using a linear array of PT1000. platinum resistors. Each resistor has a surface of 2.3 by 2.0 mm The spacing between the resistors was 5 mm.

Corresponding measurements using the three electrode collector positioned on the beam axis showed a maximum ion current density of 5 A/cm² for a target area of about 1 cm². More recently, peak target current densities of even up to 13 A/cm² have been observed. The operating conditions leading to these high values are not yet fully understood. Assuming an ideal transport efficiency for the beam of 1 [4] a current density of about 25.6 A/cm² is expected, based on the current magnitude measured in the ballistic region.

5. SPACE CHARGE NEUTRALISATION

A first series of measurements was made to judge the degree of space charge neutralisation of the proton beam in the target plane. For this purpose the same three electrode collectors were used, that had already been employed for the beam profile measurements. However, instead of using a sufficiently high negative bias on the repeller electrode to remove all co-moving electrons from the beam, this voltage was now varied between zero and a negative value of -250V. In the course of these measurements the collector cup was held at a positive

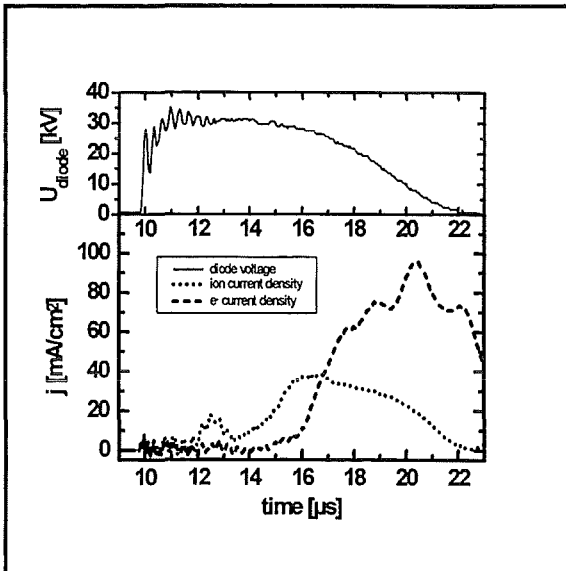


Fig. 9: Time evolution of target electron and proton current.

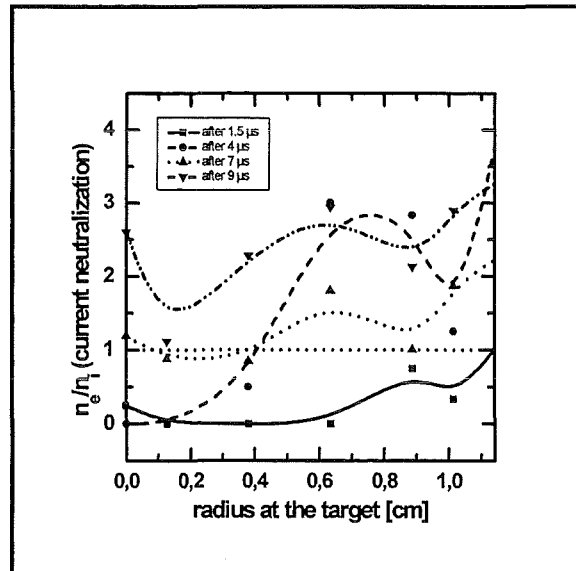


Fig. 8: Radial dependence of the current neutralization (I_e/I_i) at different times after pulse onset.

bias to avoid errors in the current measurements provoked by secondary emission electrons escaping from the collector.¹

Some of the first results obtained are shown in Figures 8 and 9. The electron current density was obtained by subtracting the collector signal measured with the repeller at high negative bias from the signal obtained with the repeller at zero bias.

Fig. 8 shows the time development of the protonic and of the electronic component of the beam current on the axis. One observes that after a certain delay of about 5 μ s, the electron current exceeds the proton current, i.e. the beam current is overcompensated.

Fig. 9 shows the radial dependence of the degree of current neutralisation (I_e/I_i) for different points in time after the onset of the proton current.

It should be emphasized, that these are the results of first test measurements and that their interpretation has not been finished as yet.

It is interesting to note, that these measurements do not only yield the current density of the beam electrons, but also allow conclusions concerning the energy distribution of these electrons. This information can be obtained through differentiation of the dependence of the collector current on the repeller electrode bias voltage. Knowledge of the energy distribution and of the current density of the electrons furthermore allows to determine the electron density and therefore to conclude on the degree of space charge neutralisation.[5]

6. BEAM COMPOSITION

The ion beam mass spectrum has been measured at St. Petersburg State University with a time of flight diagnostic. To achieve a better time resolution the configuration of the diode was altered in such a way, that the anode discharge circuit was decoupled from the voltage applied to the diode gap. This modification allowed to use a small acceleration voltage U_a without changing the physical processes of the plasma generation. A preliminary result of the mass spectrum measurements performed for $U_a = 400$ V is shown in Fig. 10, which was obtained after conditioning of new polyethylene plugs by several shots under residual gas pressure. It is clearly seen that protons represent the predominant beam component. After several hundreds of shots heavier components appear, presumably originating from degradation of the PE plug surface properties and formation of metal films, provoked by evaporation of the needle electrodes. A self cleaning effect of the discharge units has been observed for high discharge currents. A detailed presentation of the time of flight experiments will be reported elsewhere [6].

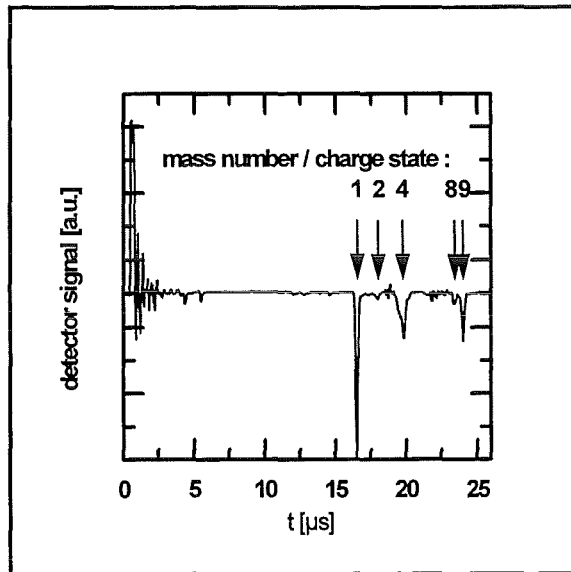


Fig. 10 Mass spectrum of the proton beam.

7. CONCLUSIONS

The mechanical and electrical optimization campaign carried out on the PROFA diode in 1995 has resulted in a significant improvement in facility performance. The parallel use of different diagnostic tools (like e.g. three electrode collector with repeller electrode and thermistor arrays) for the measurement of proton beam parameters has led to largely consistent results. The most prominent results found in recent experiments are the following:

¹ It should be mentioned, that these measurements were made prior to the hardware and electrical optimization campaign on PROFA, which explains the still relatively low current densities in Fig.8.

1. The homogeneity of ignition of the spark units, embedded into the anode discharge electrode is satisfactory. A comparison of long exposure photographs of the operating diode with voltage drop measurements over the anode resistors gives consistent results.
2. A maximum diode current of $\approx 100\text{A}$ was achieved when the anode grid is allowed to adopt the plasma floating potential. The projected maximum diode current for PROFA was 150A . ($100\text{mA}/\text{cm}^2$ for an anode surface of 1500cm^2).
3. The diode current is 5% of the discharge current establishing the anode plasma.
4. The peak ion current densities recorded to date are:
 - at the emitting surface $>0.1\text{A}/\text{cm}^2$ (near beam axis),
 - in the ballistic focus plane $1\text{A}/\text{cm}^2$ (without magnetic field),
 - in the target plane $5\text{A}/\text{cm}^2$ (more recently up to $13\text{A}/\text{cm}^2$).
5. The maximum achievable pulse length for low discharge currents is $40\ \mu\text{s}$, limited by the capability of the high voltage pulse generator. For higher currents, the pulse length decreases significantly.
6. The maximum beam divergence measured without magnetic field is rather high: $\approx 150\ \text{mrad}$ for the total beam current. Evidently, a significant part of this value is caused by residual beam space charge.

Present activities concentrate on improvements of the anode plasma homogeneity, on the identification of the mechanisms leading to premature diode breakdown in the high current operating regime, on the application of different methods for the improvement of the beam space charge neutralisation and on investigations concerning the origin of the relatively large beam divergence.

8. LITERATURE

1. V. Engelko, H. Giese, S. Schalk, Ch. Schultheiß, and H. Würz, in *Physics of Intense Light Ion Beams and Production of High Energy Density in Matter*, edited by H.-J. Bluhm (FZKA 5590), 64 (1995).
2. V. Engelko, H. Giese, S. Schalk, Ch. Schultheiss, H. Wuerz 'Pulse intense proton beam facility for for ITER disruption simulations', Proc. Beams '94, San Diego 1994
3. V. Engelko et al, 'Generation and Focusing of an Intense Long Pulse Proton Beam', IEEE Int. Conf. on Plasma Science ICOPS'95, Madison, Wisconsin, USA, June 5-8, 1995, Book of Abstracts, p. 289.
4. V. Engelko, V. Kuznetsov, G. Vjazmenova, H. Wuerz 'Compression of intense proton beams', Proc. Beams '94, San Diego 1994
5. V. Engelko, H. Giese, and S. Schalk, 'Measurement of extend of intense ion beam charge neutralization', Proceedings of the 11th International Conference on High Power Particle Beams, Prague, 1996 (to be published).
6. V. Engelko, H. Giese, M. Mischin, S. Schalk, and O.Y. Tsibin, 'Investigation of the composition of an ion beam produced using a multi arc ion source', Proceedings of the 11th International Conference on High Power Particle Beams, Prague, 1996 (to be published).

Plasma radiation in ITER tokamak hard disruption events*

B. Bazylev¹, F. Kappler, I. Landman², G. Piazza, H. Würz

permanent addresses: 1 Lykov Institute of Heat and Mass Transfer, Minsk, Belarus;
2 Troitsk Institute for Innovation and Fusion Research,
142092 Troitsk, Russia

Abstract

Physical properties of non-LTE carbon plasma shields were studied at the plasma gun facility 2MK-200 CUSP at Troitsk under conditions simulating hard disruptions and ELMs. The experimental data are used for validation of the theoretical modeling of the plasma surface interaction. Such important features of the carbon plasma shield as temperature and density distribution and its evolution are reproduced quite well. The conversion efficiency of the energy of the plasma stream into total radiation and soft x-ray line radiation from highly ionized evaporated target material is also reproduced. *

1. Introduction

The plasma shield formed in front of a target at the early stage of a plasma stream target event protects the target from further excessive heat load. This plasma shield effect though widely known was not systematically studied up to now. A rather general discussion is given in [1] and a few rather qualitative experimental results have been obtained so far [2 - 4]. Plasma shield formation and quantification of damage of targets under pulsed heat loads requires modeling of the interaction of intense plasma streams with targets. For this purpose the two codes FOREV-1 a one dimensional radiation magnetohydrodynamics (MHD) code and FOREV-2 a two-dimensional radiation MHD code both in planar geometry are developed [5]. Moreover the two-dimensional radiation transport code TWORAD, based on the first order discrete ordinate method (2D S_N) was developed also for planar geometry for calculation of directed spectral radiation leakage fluxes [6] and for quantification of damage to side walls due to intense lateral leakage radiation from the plasma shield [7].

In parallel with the development of codes, code validation is undertaken. Emphasis is put on the comparison of calculated and measured physical properties of the plasma shield. At the plasma gun facility 2MK-200 CUSP at TRINITI Troitsk [8,9], experiments were performed with plasma stream power densities typically around 10MW/cm² simulating hard disruptions and ELMs of the ITER tokamak. Properties and dynamics of the plasma shield have been studied by means of laser interferometry, Thomson scattering, optical spectroscopy in the visible and soft x-ray (SXR) wavelength range and

* This work was performed in the frame of the EUROPEAN Fusion Technology Program on Plasma Disruption Simulation and is part of the joint EU-RF ITER task T226.b on Disruption Erosion.

by radiation calorimetry. This paper only covers the work on code validation with respect to experimental results. Work on numerical simulation of disruption erosion performed in 1995 is described elsewhere [7, 10]. Results on energy transport in a non-homogeneous non-LTE plasma using a self consistent approach for the radiation transport are discussed in [11].

2. Facility and diagnostics

2.1 Facility description

The 2MK-200 facility (schematically shown in Fig. 1) is an open magnetic trap [12] with two CUSPs at either end. Its central solenoid has a length of 1.5 m. Two pulsed plasma guns inject deuterium plasma into the trap from opposite sides through the CUSPs. Collision of the counter-streaming plasma causes thermalisation of the directed energy of the plasma stream and produces a homogeneous unmagnetized high β plasma. The plasma finally escapes from the trap by diffusion across the magnetic field lines in the skin layer and is guided into the CUSP slit along open magnetic field lines.

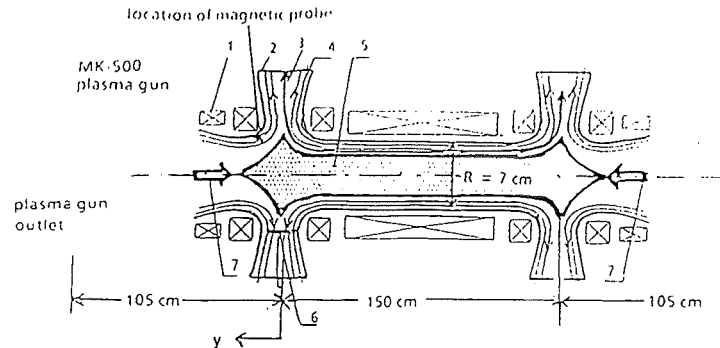


Fig. 1 Experimental facility 2MK-200

1 magnetic coils, 2 vacuum chamber, 3 plasma stream escaping the trap, 4 magnetic field lines, 5 trap plasma with $\beta \approx 1$, 6 target position in the CUSP ring slit at $R_0 = 18$ cm, 7 plasma stream from plasma gun

plasma parameters

<p>trap</p> <p>plasma energy ≤ 50 kJ</p> <p>temperature $T_e + T_i \leq 0.9$ keV</p> <p>density $n_e \leq 2 \times 10^{16}$ cm$^{-3}$</p> <p>$\beta \approx 1$</p> <p>confinement time $t \leq 35$ μs</p>	<p>center of CUSP slit at $R = 18$ cm</p> <p>$W_0 \leq 200$ J/cm2</p> <p>$T_e + T_i \leq 0.8$ keV</p> <p>$n_e \leq 10^{16}$ cm$^{-3}$</p> <p>$\beta \approx 0.25$</p> <p>pulse duration = 20 μs</p> <p>magnetic field $B_i = 2.5$ T</p>
---	---

layer and is guided into the CUSP slit along open magnetic field lines.

2.2 SXR spectroscopy and radiative calorimetry

A transmission grating spectrometer (TGS) spectrometer was used [13] for detection of SXR radiation from the plasma shield emitted in perpendicular direction. The diagnostical scheme for time integrated measurements is shown in Fig. 2. Three slits (collimator, image and grating slit) allow a spatial resolution of 2.5 mm perpendicular to the target and a total viewing length of 7 cm. The width of the viewing zone across the slit (y-direction) is 2 mm.

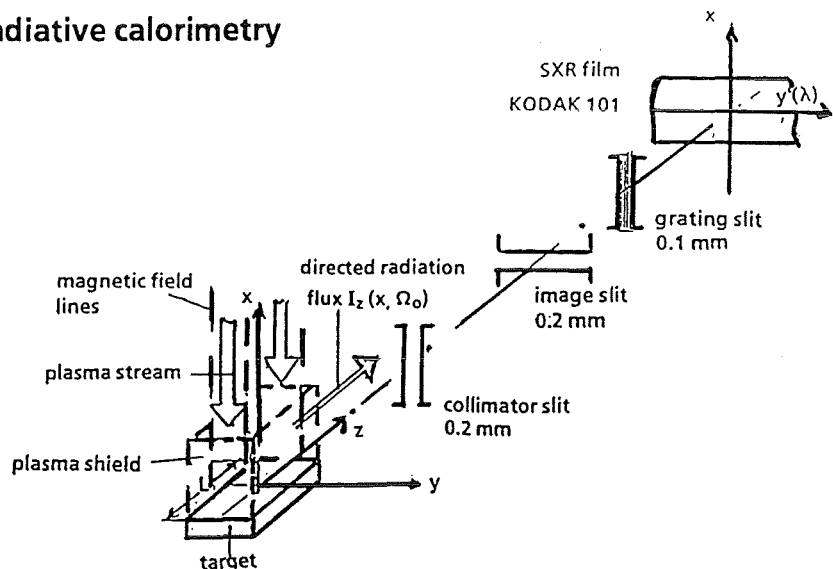


Fig. 2 Transmission grating spectrometer (TGS) for time integrated measurement of the directed leakage radiation flux $I_2(x, \Omega_0)$. Length of plasma shield $L = 5$ cm.

Gratings with 5000 lines/mm and 2000 lines/mm are used. The spectral resolution achieved is 13.3 $\text{\AA}/\text{mm}$ and 40 $\text{\AA}/\text{mm}$. For recording of the spectra a Kodak 101 film is used. Film densities were evaluated by using a computerized microscope with video camera [14]. For the film sensitivities no single curve is available for the whole wave-

length range from 10 Å up to 1500 Å. The published data [15, 16] were used and interpolated to cover the required wavelength range.

Perpendicular total radiation fluxes from the plasma shield have been measured with a radiation calorimeter. The system adjusted to the position $R = 18$ cm has a spatial resolution in the direction perpendicular to the target surface (x-direction) of 5 mm. The calorimeter consists of a thermobattery with 1000 thermocouples mounted on a plate of size 25 x 25 mm². An aluminum oxide film of thickness of 300 μm is used to absorb the plasma radiation. Calibration of the system was performed for wavelengths larger than 2480 Å and shorter than 120 Å. In the VUV region the absorption coefficient κ of the coating is assumed to be about 85 %.

2.3 Evaluation of directed radiation fluxes

Assuming isotropy of the leakage radiation flux $I_z(x, \Omega_0)$ the radiative energy flux W_{rad} emitted from all 4 surfaces of the plasma shield is calculated according to

$$W_{rad} = \frac{2}{L} \left(1 + \frac{d}{L} \right) \int dx \int I_z(x, \Omega_0) \Omega d\Omega = \frac{2\pi}{L} \left(1 + \frac{d}{L} \right) \int I_z(x) dx \quad (1)$$

with L the length of the plasma shield in the viewing direction (z direction, $L = 5$ cm), d the half width of the plasma shield in the perpendicular direction (y-direction across the slit ≈ 1 cm), x the distance from the target, $I_z(x, \Omega_0)$ the directed lateral radiation flux.

The efficiency $\varepsilon = W_{rad}/W_0$ with which the energy of the incoming plasma stream W_0 is converted into radiation in the plasma shield is obtained as

$$\varepsilon = \frac{2\pi(L+d) \int I_z(x) dx}{W_0 L^2 d} \quad (2)$$

3. Experimental results

Fig. 3a shows a time integrated soft x-ray spectrum measured at a distance of 20 mm from the target. In the wavelength region below 300 Å line radiation from CV ions is observed. The intense lines at 40.3 and 35 Å are K_α and K_β lines corresponding to the transitions $1s^2 - 1s2p$ and $1s^2 - 1s3p$ from the first and second excited level of the CV ion (He like) to the ground state. In the wavelength region 130 - 300 Å radiation from transitions between excited levels of the CV ions may occur. However presently it can't be excluded that impurities contribute to the detected radiation.

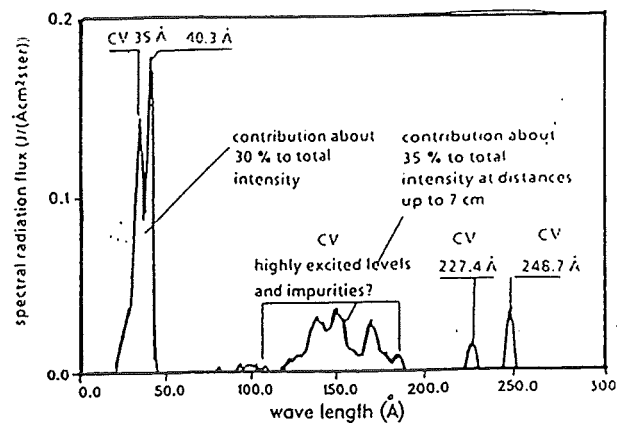


Fig. 3a Soft x-ray spectrum from carbon plasma shield of length of 5 cm at a distance of 20 mm from target.

Fig. 3b shows the total perpendicular leakage radiation flux obtained from radiation calorimetry and the SXR leakage radiation flux from the two CV resonance lines at 40.3 Å and 35 Å. At distances larger than 3 cm from the target the radiation is only due to SXR radiation. Its intensity becomes constant and amounts up to 2 (J/(cm²ster)). Approaching the target the total radiation intensity increases due to increasing contributions from the visible wavelength region. From radiation calorimetry the directed flux integrated over the extension of the plasma shield in x-direction (7 cm) and normalized to a lateral length of 1 cm was obtained to be 4.4 J/cm² for one surface. Applying eq. (1) the total angular integrated lateral radiation flux W_{rad} from all 4 sides of the plasma shield is estimated to be 33 J/cm². Thus up to 20 % of the incoming energy is converted into radiation in the plasma shield.

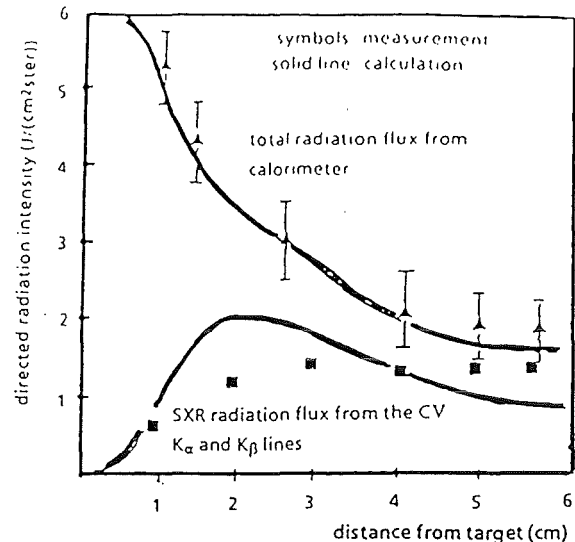


Fig. 3b Measured and calculated perpendicular SXR and total radiation fluxes for a carbon plasma shield of length of 5 cm for the 2MK-200 CUSP facility.

4. Modelling of disruptive plasma surface interaction with FOREV-1

4.1 Power density of the plasma stream

There are two plasma streams arriving at the target. The first one is due to direct impact of plasma from the gun. Typical ion impact velocities are 4×10^7 cm/s and the peak densities are around 1.5×10^{15} cm⁻³ [12]. The temperature of the Maxwellian distributed electrons in this head plasma stream is 160 eV. The time evolution is described by a triangular function with full width at half maximum of 1.5 μs. The second plasma stream is due to thermalized plasma from the trap. For estimation of the power density and its time evolution a simplified theoretical model of the trap was used. The parameters n_e , T_e and T_i of the trap plasma are obtained from the balance equations for the energy content of the ions and electrons of the trap plasma and for the particle density of the quasineutral deuterium plasma. It is assumed that ions and electrons escape through holes in the confining magnetic field as Maxwellian distributed particles.

Calculated electron and ion temperatures in the trap plasma are shown in Fig. 4a together with experimental values obtained from measurements of neutron yields (T_i) and Thomson scattering (T_e). The stored plasma energy in the trap was used as parameter to fit the calculated energy density to the experimental value of about 200 J/cm². The thus obtained value of the energy stored in the trap was 40 kJ. The electron temperature in the slit is about half of the value in the trap. This indicates that the electron tempe-

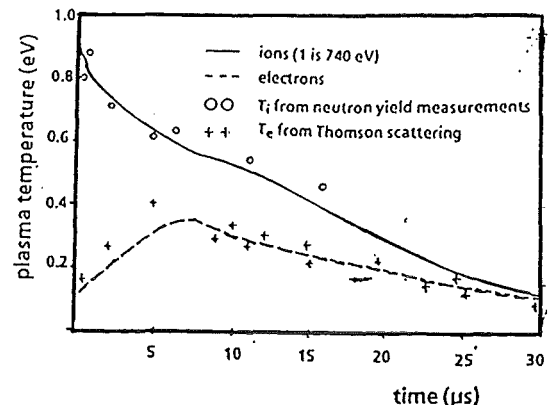


Fig. 4a Comparison of calculated and measured evolution of plasma temperature in the trap.

perature in the trap decreases in the outer skin layer due to across magnetic field diffusion. The power densities of plasma ions and electrons in the slit center are shown in Fig. 4b together with the early peak after 1.5 μ s caused by the head plasma. Due to the thermalization process in the trap the electrons gain energy and despite the electric potential which rejects electrons the heat load as carried by the electrons is about a factor of 4 larger than for the ions.

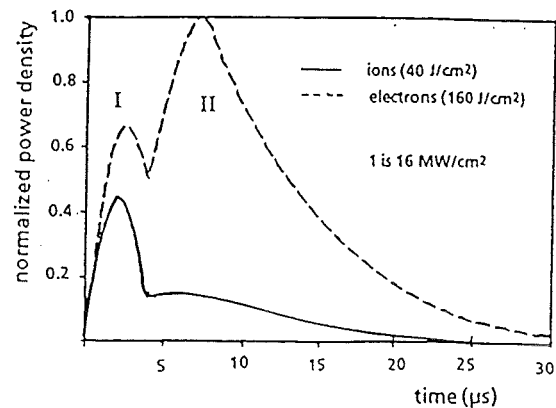


Fig. 4b Evolution of the power density of the plasma stream in the center of the CUSP slit.

Part I due to head plasma from plasma gun
Part II due to magnetized plasma from the trap

4.2 Details on modelling

The modelling was done with the radiation magnetohydrodynamics (MHD) code at FOREV-1 in 1D geometry [5]. The situation

the 2MK-200 facility requires a special modeling. The hot part of the plasma shield expanding towards the trap (see Fig. 1) is continuously dumped into the trap and is continuously reproduced by heating by the impinging plasma stream. To describe this situation it was assumed that once the plasma shield is formed the plasma mass expanding beyond 10 cm is removed and the plasma stream deposits its energy continuously at that distance into the plasma shield. For the impinging plasma stream time dependent power densities and temperatures for ions and electrons as shown in Figs. 4a and b were used. The ions were assumed to be monoenergetic whereas the electrons are Maxwellian distributed.

The width at half maximum of the plasma stream across the CUSP slit of the 2MK-200 facility (y-direction in Fig. 1) is about 11 mm and the target length along constant power density of the impinging plasma stream is 5 cm. This requires to take into account plasma mass losses through the side surfaces (lateral) and if the plasma shield is optically thin also lateral radiation losses. The mass losses are due to loss of unmagnetized vapor and due to across magnetic field diffusion of target plasma adjacent to the target where the temperature in the plasma shield and thus the magnetic confinement is low. For modelling of the mass losses it is assumed that the vaporized material expands isotropically till at higher plasma temperatures it becomes confined in the magnetic field.

In this case the lateral mass losses can be described by a simplified model in which a cylindrical component is introduced into the $\text{div } \vec{v}$ terms as

$$\frac{\partial v}{\partial x} = \frac{1}{r} \frac{\partial r v}{\partial r} = \frac{\partial v}{\partial r} + \frac{v}{r} = \frac{\partial v}{\partial x} + \frac{v}{r_0 + x} \quad (3)$$

with v the expansion velocity, x the distance from the target and r_0 a starting radius.

Adiabatic cooling of the plasma due to the mass losses is taken into account. In the balance equations the following terms are added:

$$\begin{aligned}
\text{density: } \quad & \frac{dn}{dt} + \frac{nv}{r_o + x} \theta(T_o - T_e) = 0 \\
& \frac{3}{2} \frac{dT_e}{dt} + T_e \frac{v}{r_o + x} \theta(T_o - T_e) = 0 \quad (4)
\end{aligned}$$

with $\theta(\zeta) = \begin{cases} 0 & \text{at } \zeta < 0 \\ 1 & \text{at } \zeta > 0 \end{cases}$ with $T_e \approx 5$ eV what means that for plasma temperatures > 5 eV the plasma is magnetically confined

Lateral losses of radiative energy may result in a redistribution of the forward and reverse radiative energy fluxes calculated in 1D geometry. In a 1D calculation lateral radiation losses can only be calculated in a simplified way. $I_z(x)$ is estimated according to

$$I_z(x) = n L \sum_{\sigma} \int \frac{I_{\omega}^{\sigma}(x)}{h_{\omega}} d\omega \quad (5)$$

with L length of the plasma shield in z direction ($L = 5$ cm), h_{ω} a characteristic length for photon losses of energy $\hbar\omega$, and I_{ω}^{σ} the spectral radiation flux in direction σ .

h_{ω} is given as

$$h_{\omega} = L \left(\frac{2}{\sqrt{3}} + \kappa_{\omega} L \right) \quad (6)$$

with $\kappa_{\omega} L$ the optical thickness of the plasma shield (κ_{ω} the absorption coefficient)

For optically thin plasma $h_{\omega} = 1/\sqrt{3}/2 L$ with $\sqrt{3}/2 = \cos 60^\circ$ and 60° the mean angle. h_{ω} increases for optically thick plasma. The forward and reverse fluxes I_{ω} are calculated from

$$\frac{1}{2} \frac{dI_{\omega}^{\sigma}}{dx} = \eta_{\omega} - \kappa_{\omega} I_{\omega}^{\sigma} - \frac{1}{h_{\omega}} I_{\omega}^{\sigma} \quad (7)$$

with κ_{ω} the multigroup Planck opacities for absorption and $\eta_{\omega} = \beta_{\omega} I_{\omega}^p$ the plasma emissivity with β_{ω} the multigroup Planck opacity for emission and I_{ω}^p the Planck spectrum.

4.3 Results for carbon

FOREV-1 modeling results are shown in Fig. 5 for carbon. For describing the optical properties of the carbon plasma shield 512 group non-LTE Planck opacities were used. More details are described in [5]. Curve 1 shows the time evolution of the power density of the free plasma stream, curve 2 the time evolution of the heat flux at the target due to the impinging plasma stream, curve 3 the heat flux into the bulk graphite target due to thermal heat conduction, curve 4 the radiative heat flux to the target, curve 5 the lateral radiation flux, integrated over the extension of the plasma shield in

x-direction and normalized to a length of 1 cm and curve 6 the target heat load due to electron heat conduction.

Evaporation starts after 0.45 μ s. Formation of the plasmashield needs less than 1 μ s. Afterwards the plasma shield starts to radiate. Both radiation fluxes to the target and lateral carry up to about 10 % of the incoming energy. The total radiation intensity (curves 4 and 5) follows closely the time evolution of the power density. The lateral leakage radiation is rather high resulting in an effective redistribution of the forward and reverse radiation fluxes. The target heat load is dominated by radiation. A considerable fraction of the energy of the plasma stream is going into ionization (internal energy) and thermal energy of the plasma shield. The calculated erosion is 0.05 μ m in comparison with the measured value of 0.25 μ m.

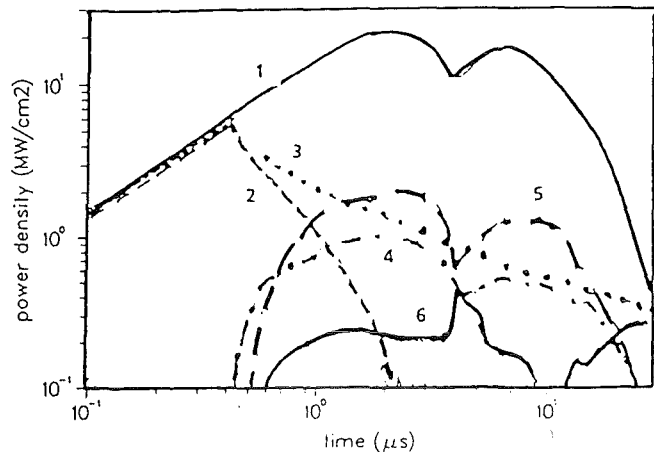


Fig. 5 Results from FOREV-1 calculations. Lateral mass and radiation losses are taken into account.

- 1 power density of the plasma stream
- 2 heat load at the target
- 3 heat flux into the bulk target
- 4 radiation flux onto the target
- 5 integrated lateral radiation flux $\int I_z(x) dx$ for a plasma shield of length of 1 cm
- 6 heat load at the target due to electron heat conduction

4.4 Comparison with experimental results

Fig. 6 shows a comparison of calculated and measured profiles of plasma temperature and density at 10 μ s. There is a rather good agreement between the calculated results and the results from Thomson scattering. Due to the high plasma temperature and the rather low density the plasma shield remains confined in the magnetic field and expands along the field lines. Lateral movement of plasma was not observed [17].

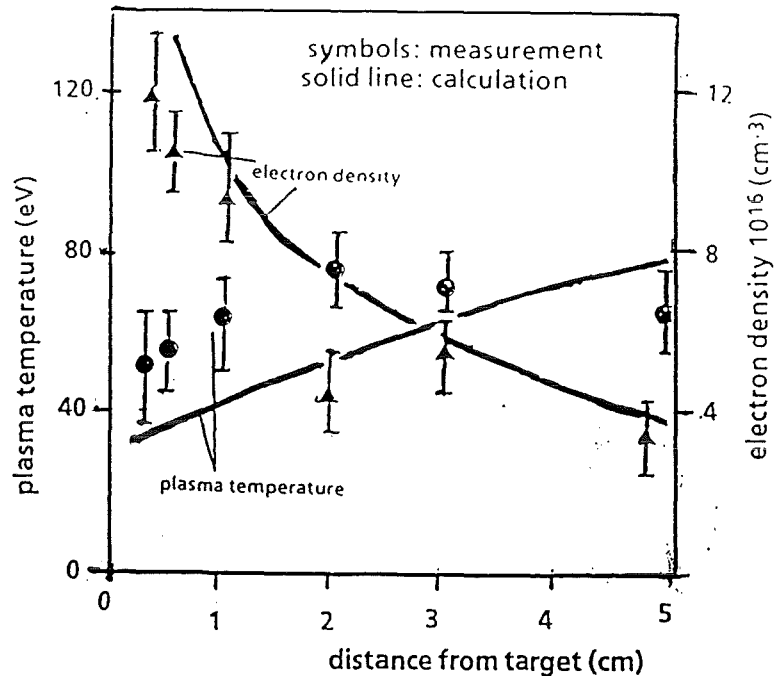


Fig. 6. Calculated and measured profiles of plasma temperature and electron density in the carbon plasma shield at 10 μ s for the 2MK-200 CUSP facility.

5. 2D radiation transport

The radiation flux in optically not thick plasmas of finite width which additionally have temperature and density gradients is non-isotropic. Moreover a comparison of measured and calculated directed leakage radiation fluxes requires 2D radiation

transport calculations. Therefore the code TWORAD based on the first order discrete ordinate method was developed [6].

5.1 The method

The radiative transfer equation in 2D cartesian coordinates is written as

$$\left(\mu \frac{\partial I_\omega}{\partial x} + \sqrt{1 - \mu^2} \frac{\partial I_\omega}{\partial y} \right) = \eta_\omega - \kappa_\omega I_\omega \quad (8)$$

with I_ω the 2D spectral radiation flux and $\mu = \cos\phi$ with ϕ the azimuthal angle. For the meaning of the other parameters see eq. (7).

The x and y components of the radiative flux are given as

$$\begin{aligned} S_x &= \frac{1}{2} \int_0^{2\pi} \cos\phi I_\omega d\phi \\ S_y &= \frac{1}{2} \int_0^{2\pi} \sin\phi I_\omega d\phi \end{aligned} \quad (9)$$

From eq. (8) the finite difference equations for the spectral radiation flux $I_{i,j}^{k,m}$ at the knots i,j of the mesh are obtained with m the quadrant number and k the angle number in the quadrant. The x and y components of the forward and reverse radiation flux are calculated according to

$$\begin{aligned} S_{x,i,j}^+ &= \sum_k \mu_1^k I_{i,j}^{k,1} A_k + \sum_k \mu_4^k I_{i,j}^{k,4} A_k \\ S_{x,i,j}^- &= \sum_k \mu_2^k I_{i,j}^{k,2} A_k + \sum_k \mu_3^k I_{i,j}^{k,3} A_k \\ S_{y,i,j}^+ &= \sum_k \zeta_1^k I_{i,j}^{k,1} A_k + \sum_k \zeta_2^k I_{i,j}^{k,2} A_k \\ S_{y,i,j}^- &= \sum_k \zeta_3^k I_{i,j}^{k,3} A_k + \sum_k \zeta_4^k I_{i,j}^{k,4} A_k \end{aligned} \quad (10)$$

with A_k the weights for the Gaussian numerical integration. To be consistent with Fig. 2 the lateral direction now will be denoted with z instead of y .

5.2 Comparison with experimental results

Directed spectral leakage radiation fluxes were calculated with TWORAD. Time dependent plasma density and temperature profiles in x-direction as obtained from FOREV-1 were used. In z-direction constant density and temperatures along the length of the target of 5 cm was assumed. The TWORAD calculations were performed for 16 directions per quadrant, 64 meshes in x-direction and 40 meshes in z-direction were used. The same 512 frequency group non-LTE Planck opacities for emission

and absorption were used as for FOREV-1. With TWORAD calculated perpendicular spectral radiation leakage fluxes are shown in Fig. 7 at 10 μ s where according to Fig. 5 the power density of the plasma stream and the lateral radiation flux reach their maximum values. The K_{α} resonance line from CV dominates closer to the target and contributes about 50 % to the total intensity. With increasing distances the CVI resonance line dominates. This line being close to the CV line can't be resolved in the measurements. In the calculation line radiation in the photon energy range 50 - 100 eV from transitions between highly excited levels of CV remains rather small. Measured and calculated radiation fluxes are shown in Fig. 3b. The calculated perpendicular total and SXR radiation fluxes are in good agreement with the measured values.

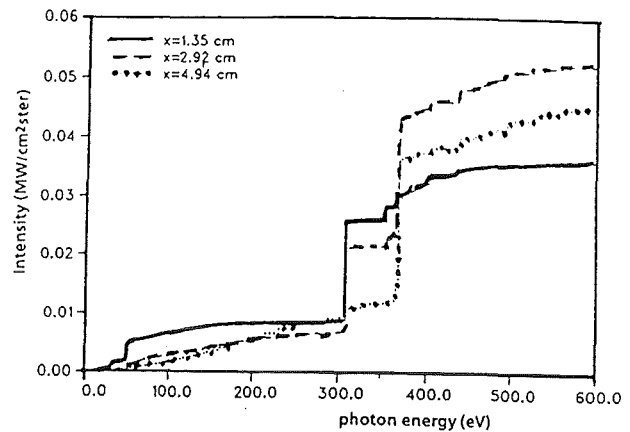


Fig. 7 Integrated perpendicular leakage radiation flux from a carbon plasma shield at 3 different distances from the target at 10 μ s.

6. Conclusions

The non-LTE carbon plasma shield converts up to 20 % of the energy of the impinging plasma stream into SXR radiation. 1D modelling with FOREV-1 reproduced all important features of the plasma shield such as the high temperature of the plasma corona and its evolution and the plasma density and its evolution. In the calculated spectral radiation flux line radiation from CV and CVI ions contributes about 80 % to the radiation intensity and the contribution from transitions between highly excited levels of CV remains rather small.

The disruption simulation experiments differ from the tokamak situation in several points: 1) the impact energy of the plasma stream is considerably less than for ITER, thus the energy deposition into the target and the plasma shield occurs in a rather shallow region. 2) the MHD behavior is different. The significance of lateral losses of plasma mass has to be evaluated. 3) the high intensity of lateral radiation from the plasma shield results in erosion at side walls not hit directly by the disruptive plasma stream. The MHD behavior of the resulting rather complex plasma shield has to be modelled.

For ITER tokamak hard disruptions and ELMs the main features of the plasma shield as described above remain valid as long as the power density is in the 10 MW/cm² range [7]. These features are rapid evaporation of divertor material and its immediate ionization, formation of a protective two zone plasma shield for low Z materials and a rather high conversion efficiency of the energy of the plasma stream into soft x-ray line radiation in the plasma shield. Thus hard disruptions and ELMs at ITER are accompanied by SXR flashes originating from line and recombination radiation of evaporated highly ionized divertor material. Of concern in the ITER tokamak disruption scenario is the lateral movement of plasma mass, becoming still more pronounced in case of divertor targets tilted in the poloidal plane. Moreover the interaction of the ener-

getic tail of the Maxwellian distributed plasma electrons with the target has to be investigated in detail. Electrons deposit their energy into the solid target and thus could cause rather large explosive like erosion [18, 19]. Their role in tokamak typical disruptions still has to be evaluated. The high lateral radiation fluxes cause evaporation at the side walls of the ITER divertor slot thus requiring 2D methods with 2½D MHD models for predicting the MHD behaviour of the plasma shield [10].

Acknowledgement

The authors would like to thank Vladimir Tolkach from Lykov Institute of Heat and Mass Transfer Minsk for making available atomic data bases and optical data including plasma emissivities with escaping factor correction for beryllium and carbon. Thanks also to Dima Toporkov, Valeri Safronov and Anatoli Zhitlukhin from Trinita Troitsk for making available their experimental results obtained at the 2MK-200 CUSP facility. The support of H. Guth from FZK Karlsruhe in evaluating the SXR sensitive films is also acknowledged.

7. References

- [1] A. Sestero, Nucl. Fusion Vol 35, No. 8, 1995.
- [2] V. Engelko et al., J. Nucl. Mater 220 - 222, 1995, p. 1071.
- [3] A.A. Drozdov et al., Plasma Devices and Operations, 1995, Vol. 4, p. 53.
- [4] J. Bradley et al., ICOPS 95, June 5 - 8, 1995, Madison Wisconsin, USA, paper 4EP17.
- [5] F. Kappler et al., Annual report 1994, FZKA-5590, June 1995.
- [6] B. Bazylev, The 2D S_N radiation transport code. TWORAD, to be published as FZKA report.
- [7] B. Bazylev et al., 22nd EPS Conf on Controlled Fusion and Plasma Physics Bournemouth 3 - 7 July 1995.
- [8] N.I. Arkhipov et al., Fusion Technology 1994, Vol. 1, p. 395; Proc. 18th SOFT August 22 - 26, 1994, Karlsruhe.
- [9] H. Würz et al., J. Nucl. Mater. 220 - 222, 1995, p. 1066.
- [10] H. Würz et al., ICFRM-7, Spt. 25 - 29, 1995 Obninsk, to be published in J. Nucl Mater.
- [11] H. Würz et al., ICOPS 1995 June 5 - 8, 1995. Madison Wisconsin, USA paper 1A03.
- [12] N.I. Arkhipov et al., Proc. 12 Internat. Conf. on Plasma Physics and Controlled Nucl. Fusion Research, France, Nice, 1988, Vol. 2p. 683.
- [13] P.D. Rockett et al., J. of Nucl. Mater. 220 - 222 (1995), p. 785.
- [14] H. Guth, private communication
- [15] K. Eidmann et al., Laser and Particle Beams 4, p. 521, 1986.
- [16] W. Schwanda, K. Eidmann, Calibration of KODAK101 x-ray film, Appl. Optics., Vol. 31, p. 554 (1994).
- [17] N.I. Arkhipov et al., Fusion Technology 1992, Vol 1, p. 171, 1993.
- [18] A.V. Burdakov et al., J. Nucl. Mat. 212 - 215, 1994, p. 1345.
- [19] V. Engelko et al., ICFRM-7 Sept. 25 - 29, 1995, Obninsk, paper 27009.

MODIFICATION OF MATERIAL SURFACES BY THE PULSED ELECTRON BEAM FACILITY „GESA“

G. Müller, G. Schumacher, D. Strauß
Forschungszentrum Karlsruhe GmbH, Institut für Neutronenphysik und Reaktortechnik,
Postfach 3640, D-76021 Karlsruhe, (Germany)

V. Engelko, A. Andreev, V. Kavaljov
D.V. Efremov Institute, 189631 St. Peterburg (Russia)

Abstract

Pulsed heat treatment is a modern and ecologically sound technique of surface modification. The special feature of pulsed heat treatment is the possibility of applying high heating and cooling rates. Fast cooling rates (as much as 10^7 K/s) of the heated layer cause a change in its physical properties; metastable phases with amorphous and nanocrystalline structures are formed. For investigation of the modifications of material properties by pulsed electron beams a new powerful electron beam facility GESA was developed and manufactured [1]. It produces an electron beam with a kinetic energy of 50 - 150 keV, a max. beam current of 500 A, a beam diameter of 6 - 10 cm and a pulse duration of 5 - 40 μ s. All marked beam parameters (energy, current density, pulse duration) are controlled.

The paper presents the results of investigation focused on the transformation of the microstructure, alloy formation and high temperature corrosion behavior of the Superalloy MCrAlY treated by an electron beam. Further the improvement of tribological properties by pulsed heat treatment of tappets used in car engines, consisting of a 16MnCr5 steel, are described.

1 INTRODUCTION

The possibility of applying high heating and cooling rates to material surfaces is the special feature of pulsed heat treatment. Fast cooling rates (as much as 10^7 K/s) of the heated layer cause a change in its physical properties (change of microstructure, improved wear and corrosion resistance, and increased microhardness) [2,3].

Proper adjustment of the energy supplied in the pulsed mode is crucial for successful surface treatment to generate the desired modifications. The decisive parameters are the energy of the electrons, the current density and the pulse duration. It is necessary that these three parameters can be set ad lib and independent of each other.

The GESA facility produces an electron beam with a kinetic energy of 50 - 150 keV; maximum beam current of 500 A;

beam diameter 6 - 10 cm and pulse duration of 5 - 40 μ s. All beam parameters mentioned (energy, current density, pulse duration) are controllable.

The influence of the pulsed electron beam treatment performed by the GESA facility on the micro-structure, alloy formation and high temperature oxidation behaviour of the Superalloy MCrAlY was investigated. MCrAlY type coatings are widely used for oxidation protection on gas turbine blades at high temperature ($>900^\circ\text{C}$), with M being Ni and/or Co [4]. An improvement of the corrosion resistance of these coatings would allow higher combustion temperatures leading to enhanced efficiency of gas turbines and increased life time.

Hardening of car engine tappets consisting of 16MnCr5 steel has also been investigated with the goal to improve the tribological properties.

2 RESULTS AND DISCUSSION

2.1 CONTROLLED MELT AND RESOLIDIFICATION OF HIGH TEMPERATURE SUPER-ALLOY MCrAlY

The specimens consisting of Inconel 738 were coated by low pressure plasma sprayed (LPPS) MCrAlY with 35% Co, 28% Ni, 20,5% Cr, 16% Al and 0,5%Y. The coating thickness was 200 μm which is one order of magnitude higher than the electron range used in the experiments. Therefore only the MCrAlY-coating is involved in the pulsed heat treatment.

The beam parameters are the following: electron energy $E=120$ keV, current density $j=8$ A/cm² and pulse duration $\tau=30$ μs .

By solving numerically the heat equation using the energy deposition profile and thermal properties of MCrAlY at given parameters, the maximum cooling rate and resolidification velocity were obtained to be $2,5 \cdot 10^6$ K/s and 0,3 m/s.

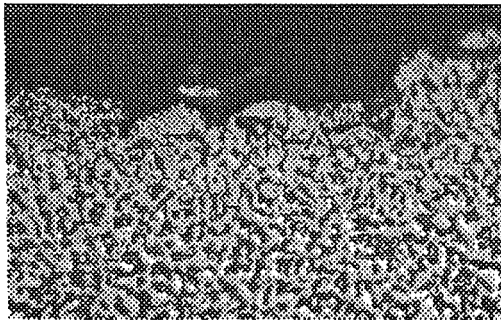


Fig. 1: MCrAlY as Plasma Sprayed



Fig.2: MCrAlY after Electron Beam Treatment

After treatment the irradiated zone was examined metallographically by SEM. Fig. 1 and Fig. 2 show the micrographs of

cross section before and after irradiation. After electron beam treatment a glassy surface layer with a thickness of approximately 20 μm can be observed. The original two phase structure changed into a single phase structure in the melting zone. This modified layer was not affected by etching, while the two-phase structure shows deep corrosion traces. Further the surface roughness induced by the LPPS process is reduced significantly. The hardness of the single phase layer increased from 440 HV to 1200 HV.

2.2 HIGH TEMPERATURE OXIDATION TEST AT 1000°C IN AIR

The specimens for investigation of high temperature corrosion behaviour were treated under isothermal conditions at 1000°C up to 9600 hours in air. During the experiment the specimens were frequently examined metallurgically by SEM to monitor the formation of the Al₂O₃- and Cr₂O₃-oxide layer. This layer acts as a barrier against oxidation in the high temperature region.

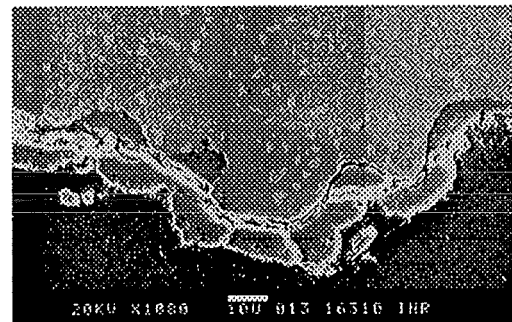


Fig. 3: Untreated Specimen after 6500 h

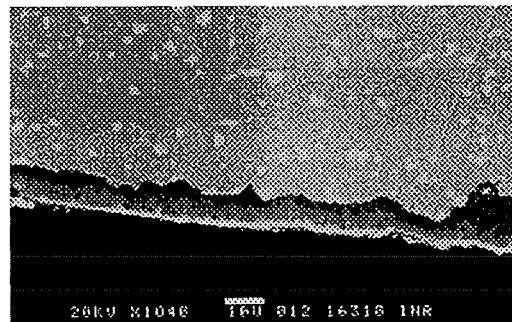


Fig. 4: Treated Specimen after 9600 h

In the untreated specimen after 6500 h exposure the oxide layer is traversed by mi-

cro-fissures. This leads to spallation of parts of the oxide layer, that must be built up again by Al out of the MCrAlY (Fig 3.). The periodical occurrence of this oxide loss is responsible for the limited life time of the protective coating.

In contrast, the treated specimen shows a homogeneous dense Al₂O₃ layer on the top of the melting zone even after 9600 h oxidation test (Fig. 4). The homogeneous single phase surface structure suppresses micro-stresses and the so initiated crack formation.

2.3 PULSED HEAT TREATMENT OF TAPPETS

Tappets serve as the intermediate component between camshaft and valve of a car engine (Fig. 5) and consist of a carburized 16MnCr5 steel. The material loss by friction does not allow a precise function during the engines life time. The experimental goal is the improvement of tribological behaviour by modifying the tappet's surface using pulsed electron beams.

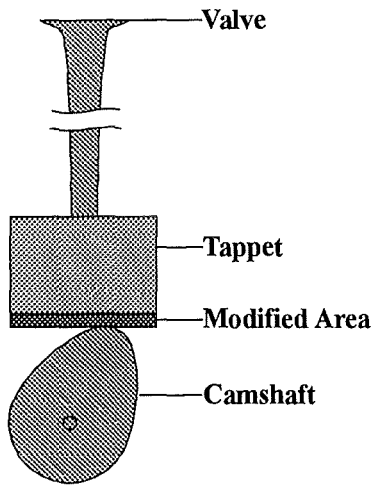


Fig. 5: Tappet, Camshaft and Valve

The beam parameters are E=100 keV, j=6 A/cm² and τ=25 μs.

In Fig. 6 the materials hardness with and without electron beam treatment is shown as a function of the depth in the specimens cross section. The hardness (Vickers, 25 p) within the melting zone in-

creases from 1200 HV to 1300 HV. At the interface to the bulk material the hardness declines and approximates the untreated tappets values.

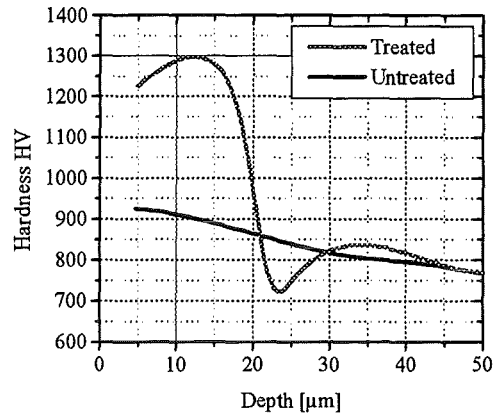


Fig. 6: Hardness of Treated and Untreated Tappet

In SEM studies grain sizes of about 300 nm were found in the melting zone. The reason for the decline of hardness under the untreated tappets value between 20 and 25 μm could be a tempering effect that leads to a fine bainitic structure. Investigations of this effect are in progress.

To compare the wear resistance of treated and untreated surfaces a car engine test was performed. The rippled surface formed during the treatment through boiling required polishing before installing the tappet. The material loss during 18 runs (2h per run) at different revolutions were measured in situ by the radioactive tracer method (RTM) [5]. Tab. 1 shows an increase of the tappets wear resistance by a factor of 4,3. Even the non-treated camshaft lost less material in combination with a modified tappet by a factor 2,3.

	Treated Tappet	Untreated Tappet	Ratio
Tappet	0,87 mg	3,79 mg	4,3
Camshaft	0,88 mg	2,04 mg	2,3

Tab. 1: Total Wear of Treated and Untreated Tappets after the Test Runs of the Engine

3 CONCLUSIONS

Pulsed electron beam treatment has proved a powerful tool for surface property improvement; in particular for the enhancement of wear and corrosion resistance.

1. Treated test specimens exhibit the formation of homogeneous surface layers with an increase in hardness between 40% and a factor of three.

2. The high temperature corrosion resistance of the Superalloy MCrAlY can be improved by electron beam treatment. The stable protective oxide layer suppresses material loss by spallation as observed on the untreated coating.

3. The wear resistance of tappets can be significantly (x4,3) increased by pulsed electron beam treatment as shown by an RTM test. Even its friction partner, the camshaft, shows a reduced material loss by a factor of 2,3.

4 REFERENCES

- [1] G. Müller, G. Schumacher, D. Strauß, V. Engelko, A. Andreev, O. Kamarov and K. Shigalichin, BEAMS 96, in press.
- [2] V. Engelko, A. Lazarenko and O. Pechersky, BEAMS 92, Washington, D.C., May 25-29, 1992, Vol. III, pp. 1935-1941.
- [3] Yu.F. Ivanov, I.S. Kashinskaya, S.V. Lykov, A.B. Markov, E.M. Oks and V.P. Rothstein, BEAMS 94, San Diego, CA, June 20-24, 1994, Vol. II, pp. 857-860.
- [4] R.J. Hecht, G.W. Goward and R.C. Elam, US Patent 3 928 026 1975.
- [5] P. Fehsenfeld, A. Kleinrahm, E. Bollmann, KfK-Nachr. Jahrg. 18 4/86, pp. 224-234

Process and Device for Electrodynamical Fragmentation of Solids - FRANKA

W. Edinger*, V. Neubert, C. Schultheiss, R. Strässner*, H. Wieczorek, Forschungszentrum Karlsruhe, Postfach 3640, Karlsruhe, FRG

* Ingenieurbüro D.T.I. , Karlsruhe

Abstract: Solids in a non-conducting liquid are subjected to electric discharges with a pulse duration of 200 ns at 250 kV voltage and a peak current of 6 kA. In this parameter field the discharge runs through dielectric solids and avoids paths through the liquid. The advantage is the generation of shockwaves in the solids and a correspondingly effective fragmentation. In the case of minerals a break-up occurs at the natural grain boundaries. The operation of a pilot plant (FRANKA) is described as well as the spectra of possible applications in the fields of recycling and break-up of precious materials.

1. Introduction

The generation of shockwaves by means of electrodynamic methods is a technique, which came up in the fifties and is actually the subject of many investigations [1]. In most cases capacitors are the storage of electric energy in the order of some kilojoule. By means of a spark gap the electric energy is switched to an electrode pair in a liquid (in most cases water) and a discharge through the water takes place, which generates a shockwave of amplitudes in the order with that of explosives. Fig.1 shows the scheme of such a device.

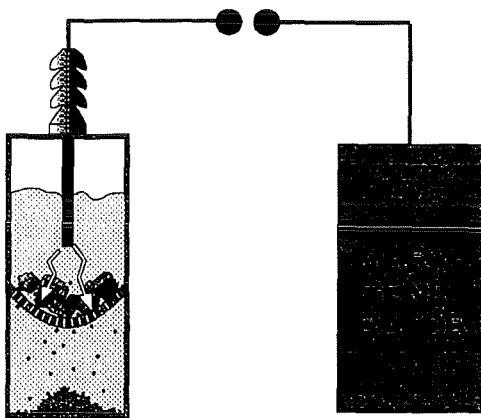


Fig.1: Scheme of a high voltage pulsed power driven discharge device with electrodes in a liquid medium. High amplitude shockwaves destroy material.

Parameters of a high voltage pulse generator used in this field can be varied in a wide range. Most of the generators are simple capacitor banks of a capacitance of some microfarads, which are charged up to 20 to 50 kV. The power devel-

oped during a micro-second lasting discharge in water is sufficient for crushing material in the very vicinity of the discharge column (see fig.1).

Detailed investigations of the discharge behavior in a liquid in presence of dielectric material are shown in fig.2. In most cases the impedance design of the pulse generators is such, that the electrical pulse length is in the order of microseconds. As can be seen in fig.2 (left side) in this case the discharges exclusively run along a path through the water between the electrodes (or other liquids, exceptions are high insulating transformer oils). However, if the pulse length of the generator decreases below 500 ns a transition in the discharge behavior becomes visible. The discharge now tends to run through the dielectric material, if this material is in the nearer vicinity (see fig.2, right side). This mode of operation is the subject of this paper.

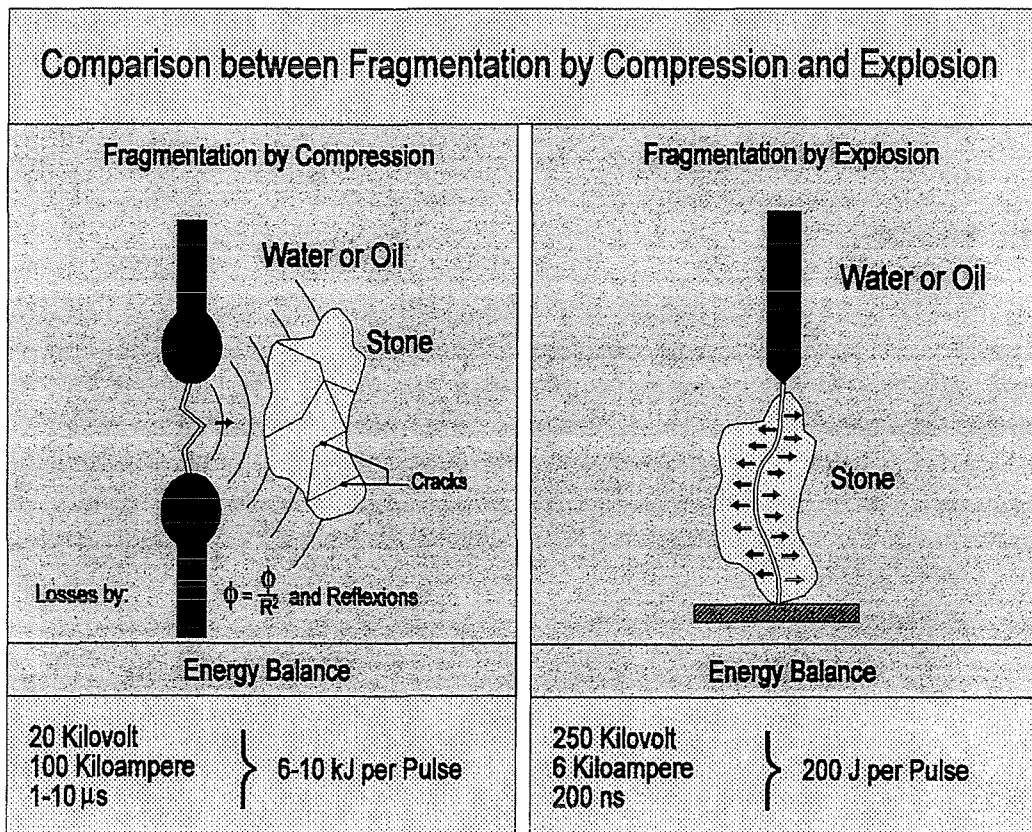


Fig.2: Comparison between the two modes of operation of electrodynamic fragmentation. The advantage of the explosion mode, i.e. the discharge runs directly through the material, is the 10 times lower energy consumption then in the case of compression mode. The latter one suffers on the dissipation of energy by the distance law and reflections of the shock wave during the invasion into the material.

The transition behavior of the discharge is the concern of fig.3. Different substances, like water, dielectric material and gases are exposed to high voltage pulses of different ramp times (see fig.3 upper part) and the break-down behavior is measured [2]. In the lower part of fig. 3 the results of the measurements are shown. There is an overall tendency of increased high voltage strength of the substances with steeper pulses. However, if a gas is present between the

electrodes, a discharge will run through it, since the levels of a breakdown curves of gases are fairly low. Even in the case, where a dielectric blocks the direct way between the electrodes the discharge takes a detour path over the dielectric surface and never penetrates. In this frame discharges in gas have to be excluded, since shockwaves are coupled fairly inefficiently into a gas, not able to crush material. In absence of a gas the ramp time decides, whether a discharge takes a way through water or through a dielectric.

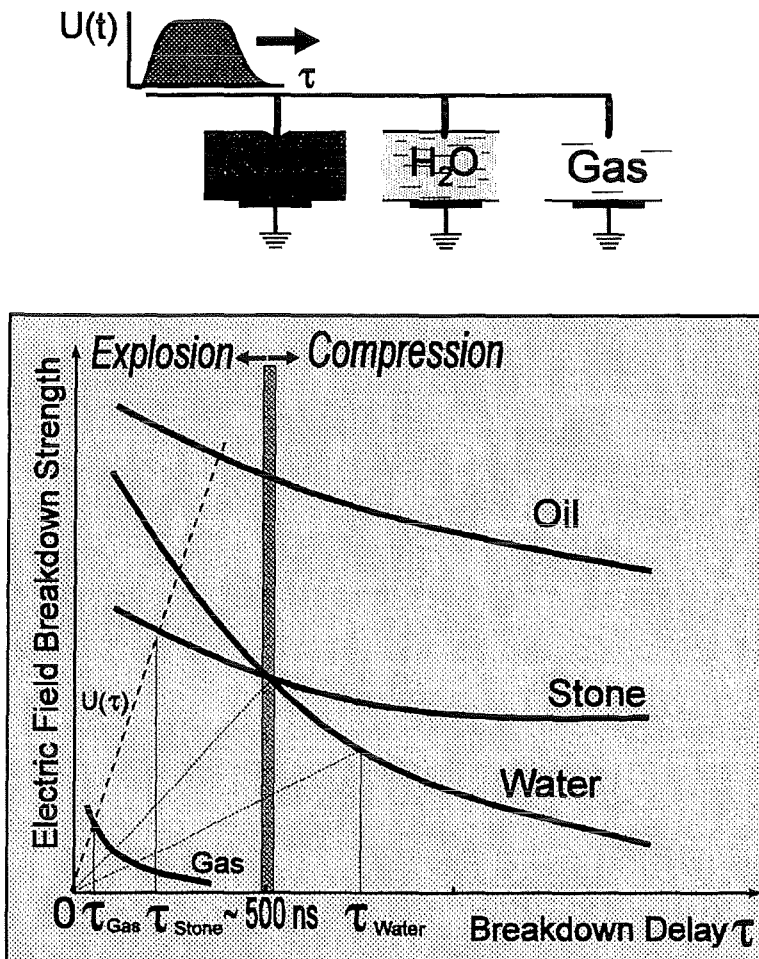


Fig.3: Breakdown behavior in liquids, dielectrics and gases as a function of the ramp-time of the high voltage pulse. The shorter the pulses are (measure τ), the more the breakdown voltage increases for all materials. In absence of gas and for ramp times τ below 500 ns, in presence of water as the liquid the discharge prefers a path through dielectrics (e.g. „stone“).

If transformer oil is used, even for long pulses the discharge occurs unproblematically in dielectrics. In most cases contaminations with oil are not desired, therefore applications and processes based on oil as liquid medium are not considered here.

At a ramp time of about 500 ns discharges run through water as well as through dielectrics (see. fig 3), i.e. explosion- and compression processes as described in fig.2 are in balance. For reliable discharges mainly in dielectrics a pulse time is chosen below 500 ns. In reality the discharge path jumps from the electrodes through the water (high ohmic) to a dielectric (low ohmic), from there

through the water to another dielectric and so on, depending on fragment- size and distribution around the electrodes.

The mechanism of crushing material in the long pulse case is compression. Two loss processes are combined with compression, where the shock energy is carried from outside to the material (see again fig.2). First: the amplitude of the discharge generated shockwave decays quadratically with the propagation distance. Second: the density jump at the border line from water to material implies reflections of the shock waves. If R is a measure for the reflections and T a measure for the transition, then:

$$\frac{R}{T} = \frac{(w-1)^2}{4w} \quad w = \frac{\rho_{H_2O} c_{H_2O}}{\rho_M c_M},$$

where ρ are the densities and c the corresponding speeds of sound.

In the case of ordinary stone ($\rho=3$), 2/3rd of the shockwaves become reflected at the border line. In average both loss processes reduce the shockwave intensity on the way from the discharge channel into the material by a factor of roughly 10.

In contrast to the compression case described above, discharges with pulse lengths below 500 ns run directly through the material, generate shockwaves inside the material with maximum amplitude. 2/3rd of the shockwaves are reflected backward into the material at the borderline to the water, so that most of the acoustic energy dissipates in the material and fragments it in an explosion manner. Therefore this process is called „fragmentation by explosion“.

The energy consumption in the compression mode is about 10 kJ/pulse whereas the explosion mode needs below 1 kJ/pulse. Since the high voltage strength increases rapidly with shorter electric pulses (see fig.2), the output voltage of the electric generator has to be increased strongly in comparison with capacitor banks. Therefore Marx generators are used, where a number of n capacitors are charged parallel and then switched in series. The output voltage there is $n \cdot U$; U is the charging voltage.

2. Pilot plant for fragmentation - FRANKA

At the Forschungszentrum Karlsruhe a pilot plant for fragmentation is installed (FRANKA, stands for **F**ragmentierungs**A**nlage **K**arlsruhe). The set-up is similar to the scheme in fig.1, consisting of a Marx generator and a vessel for fragmentation.

The Marx generator is a suitable tool for producing the high voltage pulses with correspondingly short pulse durations. The generator has five stages, i.e.: five capacitors are charged to 50 kV parallel and then switched in series by air gaps to an output voltage of 250 kV.

The main operation parameters are:

• Output voltage Marx generator:	250 kV
• Output current (maximum):	6 kA
• Pulse length (nominal until breakdown):	200 ns
• Charging voltage:	50 kV
• Repetition rate:	5 Hz
• Energy per pulse:	200 J
• Power consumption:	7.5 kW
• Electric efficiency:	10 %
• Max. field strength of max. 2 cm gap length	10^7 V/m
• Fragmentation (milling) power:	1 to/d

The low electrical efficiency in the order of 10 % results mainly on the high inductive construction of the Marx generator and electrode feeds. The oscillation frequency of the electric circuit (generator plus feed) is below 1 MHz, whereas the flash lasts only 100 ns. A new, low impedance Marx generator is in design; the use of a demineralized water filled pulse forming line to produce pulses in the 100 ns order are in discussion.

The fragmentation vessel has a volume of 15 l and can accommodate approximately 3 kg of fragmentation material per batch. The bottom of the vessel is a screen made from stainless steel. A container below the screen seals the whole device. The screen is used for classification of the solid; fragmentation, consequently, can be conducted until all the particles produced pass through the screen. The container below collects the fragmented material.

The high voltage carrying electrode penetrates into the polythene vessel. It is made from carbon steel, which withstands thermal- and shock induced stress satisfactory. The electrode (diameter 10 mm) is insulated except for the bottom end of approximately 4 cm. The electrode penetrates into the vessel to a distance of 20 mm from the screen. The other pole is the screen, which is grounded.

Wear measurements show that the loss of electrode material (both electrode and screen) is approximately 6 μ g iron per pulse in form of small iron particles. These particles can be trapped easily by a magnet. The parallel switching of the capacitors in the Marx generator is done by air switches (ball electrodes). Since the maximum current is below 10 kA the evaporation effects are still low.

The appearance of free radicals coming from the collapse of gas bubbles behind the shockwave front is a well studied process [3]. Free radicals are responsible for a strong wear (electrodes, vessel) in devices operating in the compression mode. The reason is the high amplitude of the shock waves. In the explosion mode this effect is moderate, since the input energy is reduced by a factor of 10. Measurements show, that in the FRANKA device the radicals are responsible for the built up of ozone, hydrogen peroxide and organic acids. The latter

one come from reactions between the polythene vessel and radicals. Chlorine in water as well as salt react with radicals to chloroform [4].

3. Fragmentation mechanism

As already shown in the figures 2 and 3 for a special set of parameters (see chap.2) the discharge runs through dielectrics. In a dielectric the current follows a path, where the conductivity is relatively high. In a crystalline conglomerate (e.g. „stone“) the current streams mainly along grain boundaries between the crystals, avoiding a path directly through the electrically non-conducting crystals. Thus electric energy is deposited at the boundaries and develops a discharge channel, filled with low density hot plasma. The channel is built up by a fast displacement of the material in perpendicular direction with respect to the channel axis. To stimulate a sufficient strong shock wave the energy deposited per centimeter has to be 40 - 80 Joule.

In contrast to conventional milling, this type of electrodynamic fragmentation first of all destroys crystalline conglomerates. If the treatment is continued then even crystals become destroyed. The process is self milling by mutual impaction of the crystals accelerated by shock waves generated in water discharges. In comparison with the decay of conglomerates, the destruction of crystals itself is a more slow going process, of course depending on the physical properties of the crystals and finally on the mill goal.

The electrodynamic fragmentation in the explosion mode allows the break up of heterogeneous material selectively. If stone contains metallic (gold) or conducting- or semiconducting material, as it is in many cases for minerals, the high electric field in the order of 10^7 V/m induces electric polarisations and field enhancements at these places. The consequence is the built up of current paths along these places in the heterogeneous material and a selective break up.

Other conglomerates, respectively compound materials like mineral-metal, mineral-polymer and polymer-metal tend to decay fastly into clean material, ready for separation.

4. Review on applications

Experiences in the fragmentation of different kind of materials and processing methods are listed up in the following:

- Opening-up of precious materials in mining, like gold, gems, minerals etc..
- Fragmentation of granite or similar materials into its constituent parts.
- Fragmentation of hard material like Alumina, Siliconcarbide, Boronnitride etc..
- Fragmentation of pure silicon metal on a low contamination level.
- Recycling of concrete, respectively steel reinforced concrete into steel, gravel (undestroyed grain) sand and cement.
- Spallation of contaminated concrete surfaces.

- Recycling of composite structures, like spark plugs, electro mechanical devices like razor, mixer, televisions etc..
- Preparation of stable suspensions.
- Destruction of cellular tissue (protein, starch).
- Sterilization of water/waste water.

5. Outlook

Electrodynamic fragmentation becomes more and more a serious alternative to mechanical processes, as they are performed in mills, jaw breakers, crushers and so on. The philosophy in a mechanical separation process of heterogeneous material is to break the material to such a degree, that most of the small particles produced are clean, respectively freed from other constituent material. The milling goal in many processes is 100 μm and below (!). Under this condition most of the crystals become destroyed; the milling process consumes extra energy. It should be also mentioned that 95 % of the milling energy get lost in frictional heat. In the light of these facts selective electrodynamical fragmentation seems to be the better way. However, groups working in this field, use a variety of parameter sets, i.e. voltage, current and pulse length, in their electrodynamical fragmentation devices. In many cases the specific energy consumption shows no advantage in comparison with mechanical devices. In addition most groups use powerful capacitor banks, where not only the material becomes destroyed but also switches, electrodes and the water vessel. Therefore the parameter set presented in this paper (see chap. 2) allows to direct the electric energy straight into the material; electrodes and vessel underlie a relatively low wear. The electric efficiency in terms of specific energy is optimum, however relatively high losses still come up with the Marx generator for producing the high voltage pulse. Therefore in future developments some emphasis has to be focused to increase the electric efficiency of the pulse generators.

References:

- [1] G. Linke, Chemie-Ing.-Techn. 40. Jahrg., Heft 3 1969
- [2] B.V. Semkin, A.F. Usov, V.I. Kurets, „The Principles of Electric Impuls Destruction of Materials“, Russian Academy of Sciences, Kola Science Centre, Editor N. P. Tuzov, p. 9, 1995 (in Russian)
- [3] The effect is called cavitation, which is responsible for the wear at ship propellers. For detailed information see: Kernforschungszentrum Karlsruhe. S. Suslik, „ Die chemische Wirkung von Ultraschall“, Spektrum der Wissenschaft, April 1989
- [4] J. Schwendinger, Diplomarbeit, Forschungszentrum Karlsruhe, 1995



ELBA Deposition of Glass Layers on Hydrocarbon Foils

M. Konijnenberg, G. Krafft, G. Schmitt, C. Schultheiss, M. Söhner, Forschungszentrum Karlsruhe GmbH, Institut für Neutronenforschung und Reaktortechnik, Postfach 3640, D-76021 Karlsruhe

Abstract: *Deposition of thin borosilicate- or window glass-films on hydrocarbon foils by means of pulsed electron beam ablation (ELBA) is a new technique for producing packaging foils with a barrier layer against gas diffusion. In contrast with borosilicate glass the barrier effect of window glass coated foils appear with a time delay of about 20 days.*

1. Introduction

Foils of hydrocarbon (HC) are used for packaging in many fields since they are cheap, easy to handle and not detrimental to health. The disadvantage for the use in food industry is the low barrier against diffusion of gases like oxygen and water vapor [1]. One famous exception are aluminum coated HC-foils, which show nearly no permeability for all gases. The thickness of the layer in this case is only 30 nm. These foils are widely used to pack aroma-sensitive food like coffee etc.. However transparency is demanded in many cases. Therefore compound foils are on the market, which consist of layers of polyethylene (PE) and polyamide (PA). PE forms a barrier for water vapor and PA reduces oxygen diffusion [1].

In comparison to simple PE-foils, the barrier effect of compound foils is enhanced by a factor of 2 to 3 depending on the thickness of the foils which ranges up to 150 μm and the PA/PE thickness ratio. The material consumption, as well as the use of expensive PA in the foil are responsible for a restricted use in the field of sensitive foods.

New types of coating systems, where inorganic transparent material like Al_2O_3 or SiO_2 are evaporated by dc-operating electron guns, are actually under development. Such systems waste energy and demand big efforts for cooling, since the melting- and evaporation temperatures of the above mentioned metal oxides are fairly high [2]. Other systems are based on CVD (Chemical Vapor Deposition). The enhanced costs in this procedure result from the use of metal-organic chemical compounds [3].

A promising deposition system for metal oxides, or mixtures of them, is the pulsed UV-laser, which evaporates target material fairly stoichiometrically by means of ablation [4]. In the case of ablation the thermal load of the HC-foil during deposition is low. It is determined mainly by the heat of condensation of the ablated target material and by light emitted from the ablation plasma. How-

ever the capital costs of a multiple-laser-system for large area deposition, the reliability and the energy consumption resulting from the low electric efficiency of only some percents are serious obstacles for an industrial application up to now.

The subject of this paper is the application of pulsed self-pinched electron beams instead of lasers to ablate metal oxides like glass etc. The electron source is called Channel Spark (CS, s. fig.1) - a development of Forschungszentrum Karlsruhe (FZK) [5]. Deposition systems on the basis of CS are called ELBA. In contrast to UV-lasers the main advantages of CS-systems are their simplicity and their high efficiency in converting electric energy in beam energy of about 50 %.

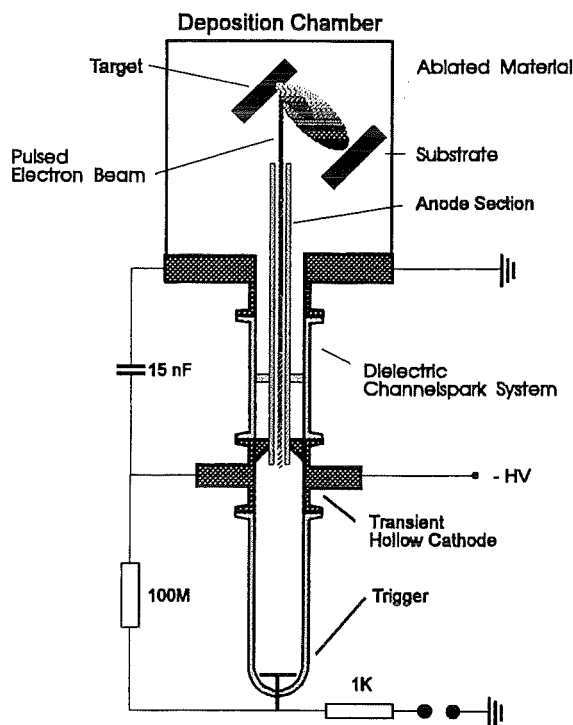


Fig.1: Scheme of a Channel Spark (CS) system with deposition chamber. The CS-source consists of a small capacitor bank, which is charged by a 20 kV HV-source. By switching of an air gap (at the bottom of the figure) the trigger is activated. Plasma in the hollow cathode generates an electron current in the order of kA's. The electron beam formed escapes during 100-200 ns via a dielectric channel into the anodic deposition chamber. A residual background gas filling of 1 Pa compensates the repelling space charge forces of the electrons and forms a self pinched beam, which is able to propagate in the chamber area some centimeters until it hits the target. The maximum electron energy is 15 keV. The repetition rate up to now is several 10 Hz (systems with several 100 Hz are under development).

2. Glass coated HC-foils

Since fibers of glass with a diameter on the order of some micrometers are known to be extremely elastic, glass was chosen as the barrier material. The thickness of a layer of 100 nm is expected to follow all curvatures of the foil even if it is folded.

Two kinds of glasses are under investigation, namely borosilicate- and normal window glass. The deposition system used consists of five CS-sources in a mutual distance of 6 cm. The distance between the glass-targets and the HC-foil is about 8 cm. With this device large area test foils could be produced (20 cm x 10 cm).

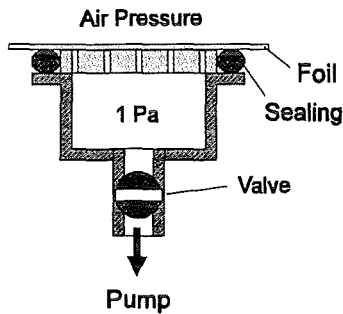


Fig.2: Device for measuring the barrier effect of foils against diffusion of air. One side of a small recipient is sealed with a test foil. Test parameter is the pressure increase versus time with closed valve.

The growth of the layer in normal position is up to 1 nm/shot, depending on the operation pressure (which influences the efficiency of the CS-sources and therefore the amount of ablated material). Normally layers on foils were prepared with 100 to 200 shots, which means 100 to 200 nm layers. These foils were checked afterwards for their barrier effect against air penetration. The testing device is shown in fig.2.

In principle a small-volume recipient is pumped down to vacuum. One side of the recipient is sealed by the foil to be tested. In the first pumping phase recipient and foil become out-gassed. In the second phase the valve is closed and the increase of pressure versus time is measured [6]. The measurements were carried out for two kinds of coated HC-foils, namely polyethylene (PE) and polypropylene (PP). In order to compare the barrier effect of these foils with compound foils (PA/PE), these are included in the measurements.

Fig.3 shows the measurements for 100 μm -PE-foils non-coated (PE 100) and coated with a relatively thick borosilicate layer (PE 100 (2000); 2000 weak ablation shots, which corresponds to a layer thickness of about 1 μm). For comparison reasons the barrier effect of two different compound foils with comparable thickness are included (PA/PE 150, PAPE 20/70). As can be seen easily in the case of a non-coated PE-foil, air passes rather fast through the foil. In a borosilicate glass coated foil the diffusion has slowed down by a factor of 2.5. The coated foil shows a better performance than the best compound foil (PA/PE 150 μm).

The results of window glass coated polypropylene (PP)-foils deviate from those of borosilicate glass coated. The initial barrier effect, shortly after the deposi-

tion, is poor (10 %-effect). However after 10 days the barrier effect has increased by a factor of 2; after 30 days by a factor of nearly 4. Thus, 35 μm -PP-foils with such layers have a factor of 2 better barrier effect then the thickest compound foil (PA/PE 150 μm). This measurement is shown in fig.4.

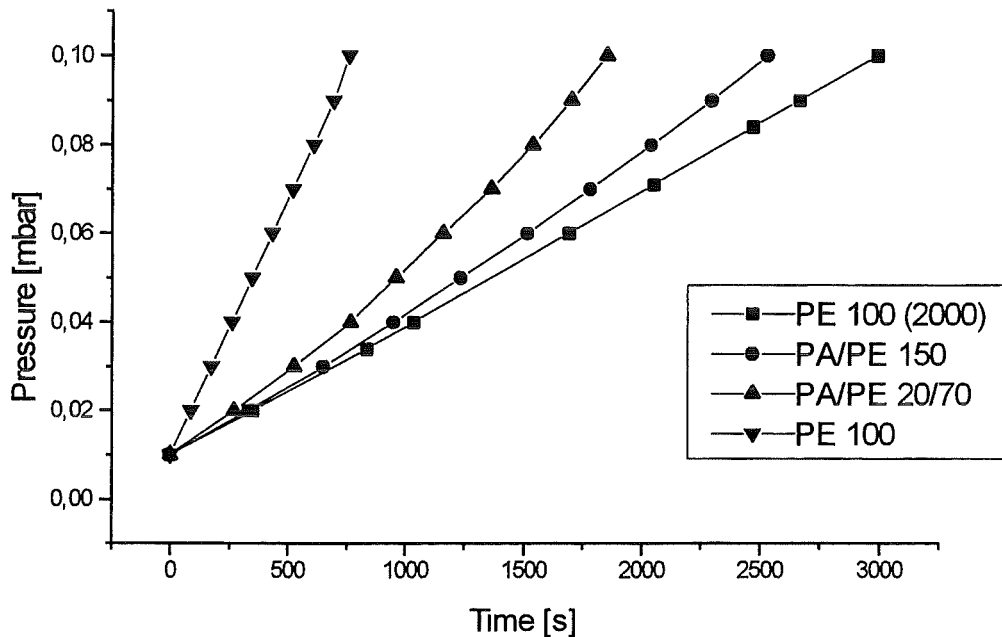


Fig.3: Measurement of barrier effect of PE-foil, non-coated (PE 100) and coated with a borosilicate glass layer (PE 100(2000)) in comparison with similarly thick compound foils (PA/PE 150; PA/PE 20/70) of similar thickness

Up to now the reason for this behavior is unknown. Chemical reactions between the constituents of window glass and the hydrocarbon foil can be assumed. It is known that ablated metal oxides undergo an oxygen loss [7] and are therefore chemically reactive. The difference between the two glasses is the appearance of sodium and calcium in window glass, which in this interpretation (one, or both) are responsible for this time dependent effect.

Borosilicate coated foils do not show an improvement of performance with time. It is even vice versa: the stress on the foil in the testing device (air pressure on the one side, vacuum on the other side) leads to a slow-going elastic strain of the foil into the holes of the support (see fig.2), destroys the coating in these places successively (cracks) and therefore reduces the performance as time passes.

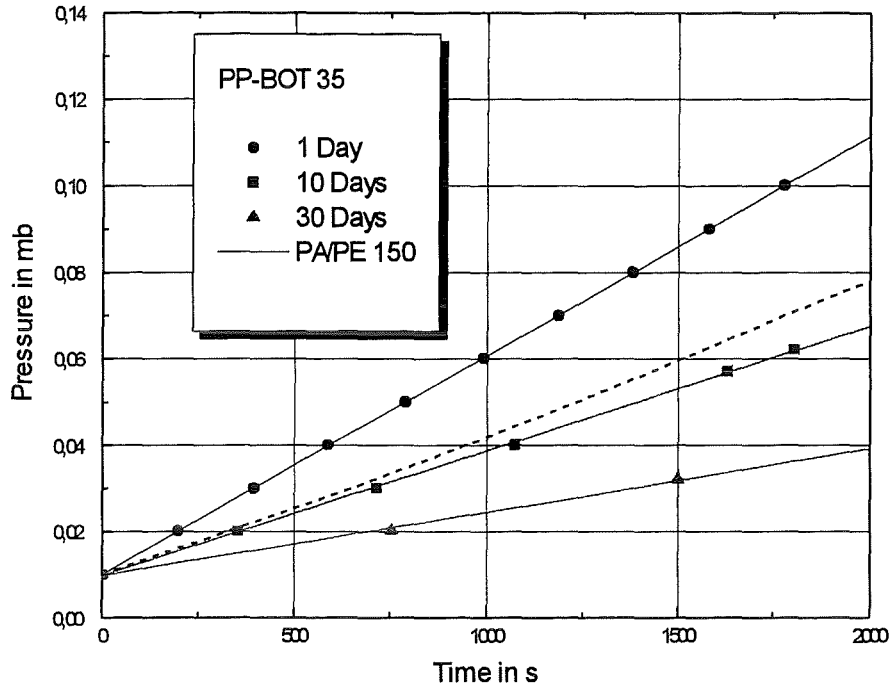


Fig.4: Time dependent increase of the barrier effect of a window glass coated 35 μm PP-foil. In comparison with the best compound foil PA/PE 150 μm , the air diffusion is reduced after 30 days by a factor of 2.

3. Pilot-Rollcoater

At present a pilot-rollcoater is under construction - in cooperation with an industrial company - to coat PP-foils with a width of 60 cm continuously (see fig.6). The foil speed will be 10 cm/s. Two CS-arrays of 13 CS-sources each are arranged below the cooled coating roll (see fig.5). In a first stage the repetition rate of the CS-systems is 50 to 100 Hz. In a next step larger devices and repetition rates of several 100 Hz, foil speeds of several meters per second are achievable.

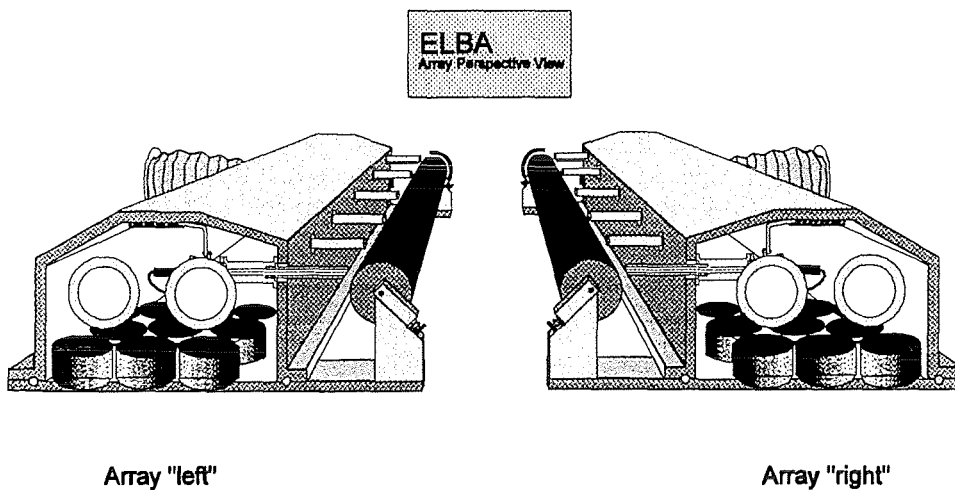


Fig.5: Perspective view of the two CS-arrays with 13 CS-systems (channels, capacitors) each, which direct their beams onto cylindric, rotating glass targets (black). The main stream of the glass vapor escapes vertical upwards.

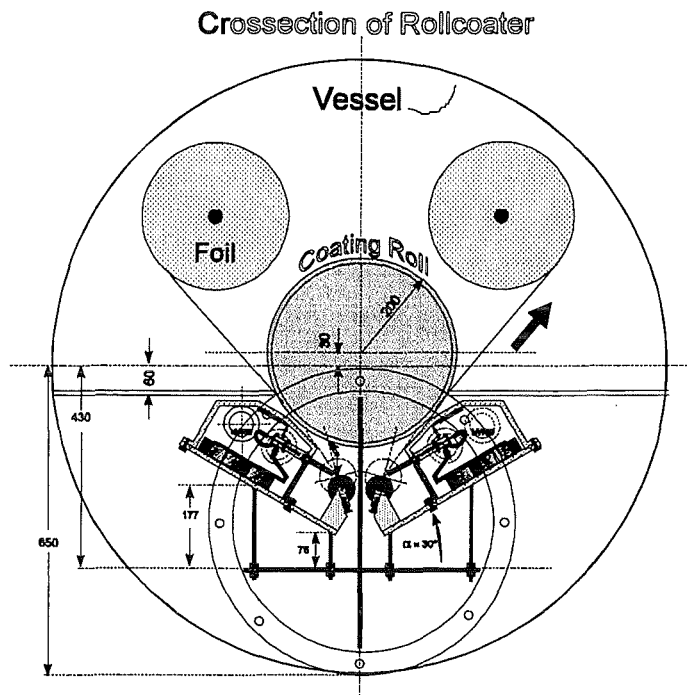


Fig.6: Crossection of a rollcoater to deposit a thin glass layer on PP-foils. Shown are the two CS-arrays of 13 CS-sources each(see fig.5) below the coating roll. The upper sphere of the roll coater shows the simplified mimicry of the foil feed (to the coating roll) and the storage of the coated foil.

4. Outlook

Ablation techniques allow the deposition of various materials to any material surfaces, as it is demonstrated in this paper with thin-film glass on HC-foils to gain a barrier effect against diffusion of gases. However the collection of tools to generate ablation is small- it consists mainly of the short-pulse UV-laser. The high capital costs and the energy consumption of UV-lasers are the main obstacles for a wide spread of this technique in industry. The appearance of pulsed, self-pinched electron beams, produced in CS-systems, is a new promising and economically attractive device for the industrial productions of coatings.

Reverences:

- [1] Bodo Carlowitz, *Kunststofftabellen*, 3. Auflage 1986, Hansa Verlag
- [2] *Spektrum der Wissenschaften*, Mai 1996
- [3] M. Vogt, R. Hauptmann, *Surface and Coatings Technology* 74-75 (1995) 676-681
- [4] E. K. Storm et al., *Phys. Rev. Lett.*, vol. 40, numb 24 (1978)
- [5] G. Müller, M. Konijnenberg, G. Krafft, C. Schultheiss, *Science and Technology of Thin Films*, World Scientific Publishing Co. PTE.LTD (1995) and *Interner Bericht, Forschungszentrum Karlsruhe* 50U159.OP02B
- [6] A construction aparent to DIN 53380, 1969 (German Industrial Standard)
- [7] See for example: H. C. Linker et al., *Appl. Phys. Lett.* 52,1098 (1988)

Production and compaction of nano-crystalline metal oxides by pulsed power techniques

R. Böhme, G. Schumacher, A. Weisenburger, INR

An electrical discharge can be applied for melting and evaporating any kind of conducting wire. This "exploding wire technique" was formerly used for fuses, the generation of aerosols and shock wave investigations. If explosions of metal wire are carried out in oxidizing atmosphere the reaction products are oxide particles with diameters in the nanometer range which can be used for manufacturing advanced ceramics. For the compaction of such fine powders to sinterable greens dynamic methods are of advantage. A device has been developed for this purpose. The Lorentz forces created in a conductor by a pulsed magnetic field are used for the dynamic densification of simply shaped samples.

1. Introduction

The discharge of a capacitor may be used to melt or evaporate the load. The physical phenomena connected with a short and powerful discharge through a piece of metal wire were intensively studied in the sixties /1/. "Exploding wires" were also applied for the generation of aerosols, for the investigation of materials properties at high temperatures and for shock wave investigations. The final products of such an explosion depend on the electrical parameters of the discharge and on the surrounding atmosphere. Thus, in an oxidizing atmosphere metal oxide particles with diameters in the range of a few to 100 nm can be created. Such particles are nowadays of considerable interest for the production of advanced ceramics with unusual properties, like plastic deformation at half melting temperature /2/. The temperature required for sintering powders with this particle size to solid ceramic bodies is also considerably lower than the melting temperature. For the large scale production of oxide powder needed for manufacturing advanced ceramics a new exploding wire device was developed and brought into operation.

Forces acting between nanocrystalline particles cause their agglomeration but also hinder a densification of the powders by conventional methods. Considerable compaction can be achieved by application of a dynamic pressure pulse. Such pressure pulses can be created by detonation of explosives, and also by Lorentz forces of a pulsed magnetic field acting on a conducting medium. The last method is applied in a device developed for manufacturing small green samples. In order to prevent considerable grain growth during sintering of these samples - the final step in the process of making nanostructured ceramics - rapid heating with mm-wave radiation is under investigation.

2. Production of nano-crystalline metal oxides by the exploding wire technique

A device for the explosion of metal wires by means of an electric discharge was developed in the frame of a common research program with the Russian Institute of Electrophysics in Ekaterinburg. The device was installed at FZK and used for the production of Al_2O_3 , ZrO_2 and TiO_2 (Fig. 1).

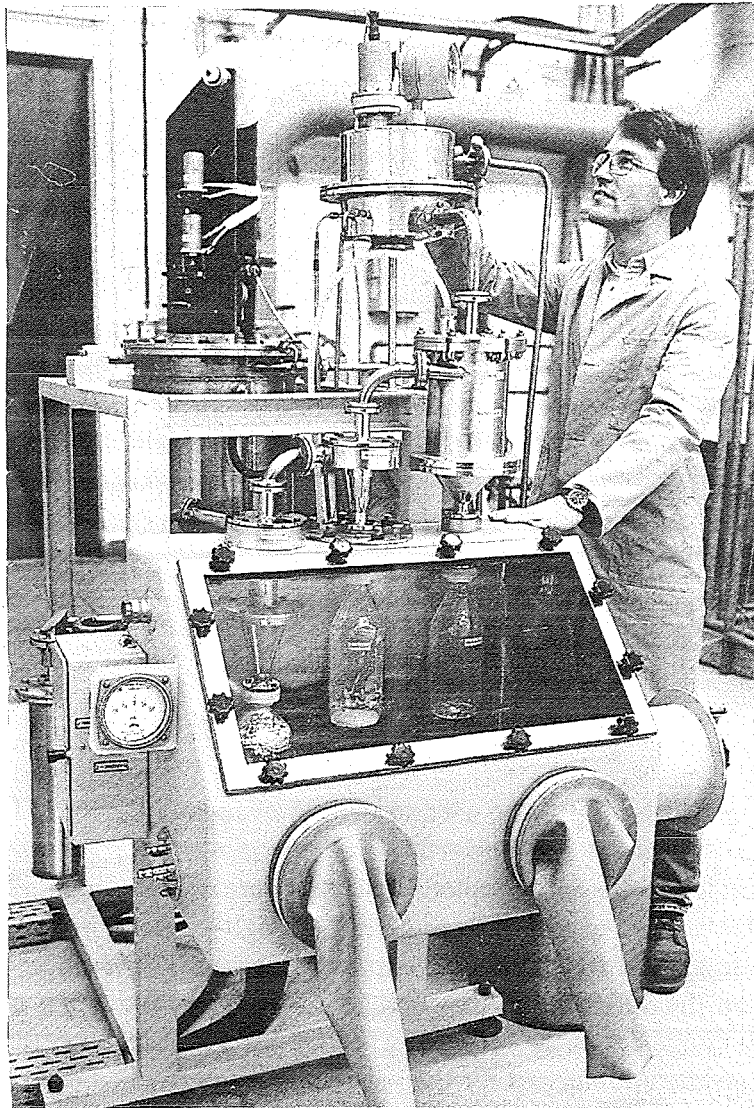


Figure 1: Device for the production of nanocrystalline oxide powder by the exploding wire technique

About 4 kJ of energy are stored in a capacitor bank and used for the explosion of 227 mm of metal wire of 0.8 mm diameter. Up to one explosion per second can take place. The reaction chamber is filled with a mixture of oxygen and nitrogen. During the explosion and succeeding oxidation process metal oxide particles with a wide size distribution are formed and carried away by a purging gas stream. The particles are removed from the gas stream in several successive separation units. Very heavy particles are collected in a simple trap. Then the gas stream passes two cyclones for the separation of particles with diameters in the range of 100 nm. The finest fraction is collected in an electric filter. The maximum productivity of the device is 1 kg of oxide per hour. About one third of the oxide powder consists of particles with diameters < 80 nm. The separation of these particles from the rest is at the moment not satisfactory. Better methods of classification of the powder particles are under investigation. The specific surface of the powder separated by the existing cyclones and electric filter was determined by gas absorption (BET method). It depends on the production parameters, like energy input per pulse and flow rate of the circulating gas [3]. At present the specific surface of the finest fraction collected in the electric filter is 35 to 57 m^2/g .

3. Compaction of nano-crystalline oxide powder by a pulsed magnetic field

For the production of greens from the nano-crystalline powder produced in the exploding wire device a compaction device was developed in cooperation with the Institute of Electrophysics in Ekaterinburg. It was installed and operated at FZK. The device consists of a vacuum apparatus for degassing the powder in a suitable mold at temperatures up to 400°C. After thorough degassing the powder is dynamically compacted by Lorentz forces created by an electric discharge of up to 28 kJ stored in a capacitor bank into an inductor. The forces are either transmitted to a piston compressing disk-shaped samples or to a conducting sleeve surrounding a cylindrical sample. A scheme of the apparatus for the compaction of platelets is shown in Fig. 2.

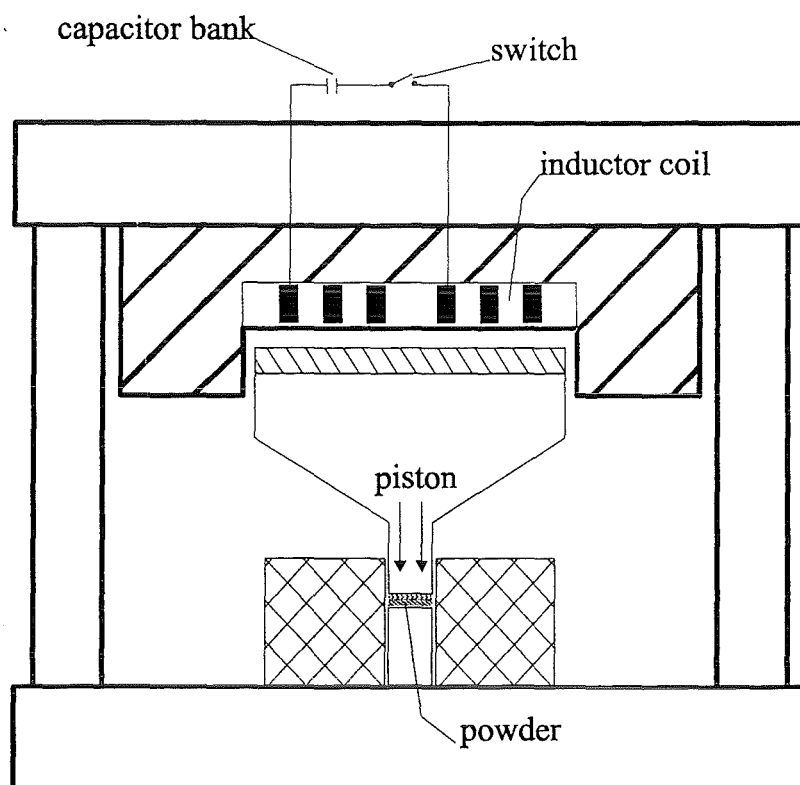


Figure 2: Scheme of the pulsed magnetic compaction apparatus

So far, samples of 4 and 15 mm diameter and 1 to 3 mm thickness were pressed. With pressure pulses lasting about 200 μ s and amplitudes up to 3 GPa crack-free greens with densities of 65 to 85 % of the theoretical density were made. Also, hollow cylinders of ca. 20 mm length, 12 mm outer diameter and a few millimeters wall thickness were manufactured. The production process is still cumbersome and not yet suited for industrial applications. The fine structure and the phase of the nano-crystalline raw material is maintained /4/. A scanning electron microscope picture taken at a fracture surface of a disk is shown in Fig. 3.

The ultimate goal is the production of nano-structured ceramics by sintering the greens. Conventional sintering is strongly connected with grain growth. Therefore, several samples made of Al_2O_3 were quickly heated by mm-waves emitted from the gyrotron of ITP /5/. At heating rates between 80 and 100 K/s sintering started at 1150°C. During the heating process a complete transformation of the Al_2O_3 from γ - to α -phase took place. By scanning electron microscopy a grain size of the sintered samples of about 100 nm was observed.

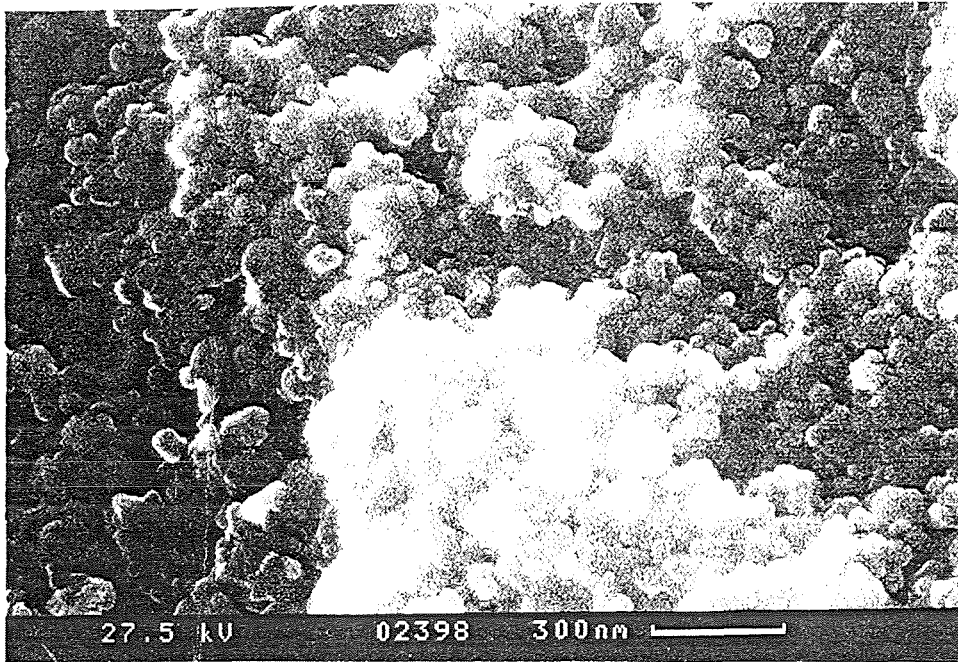


Figure 3: Structure at the fracture surface of a green made from ZrO_2 (SEM-picture taken by K. Spieler, INE)

4. Summary

It has been demonstrated that pulsed power techniques can be used to produce and to compact nanocrystalline metal oxide powders. An exploding wire device permits the production of powder in the kg-range. Simply shaped greens can be made by dynamic compaction of the powder using forces generated by a magnetic pulse. Both methods require further development: the powder produced has to be separated in narrower size fractions and the productivity of the compaction device has to be increased.

5. References

/1/ W.G. Chase and H.K. Moore, Ed.: "Exploding Wires", Vols. 1-4, Plenum Press, New York (1959, 1962, 1964, 1968)

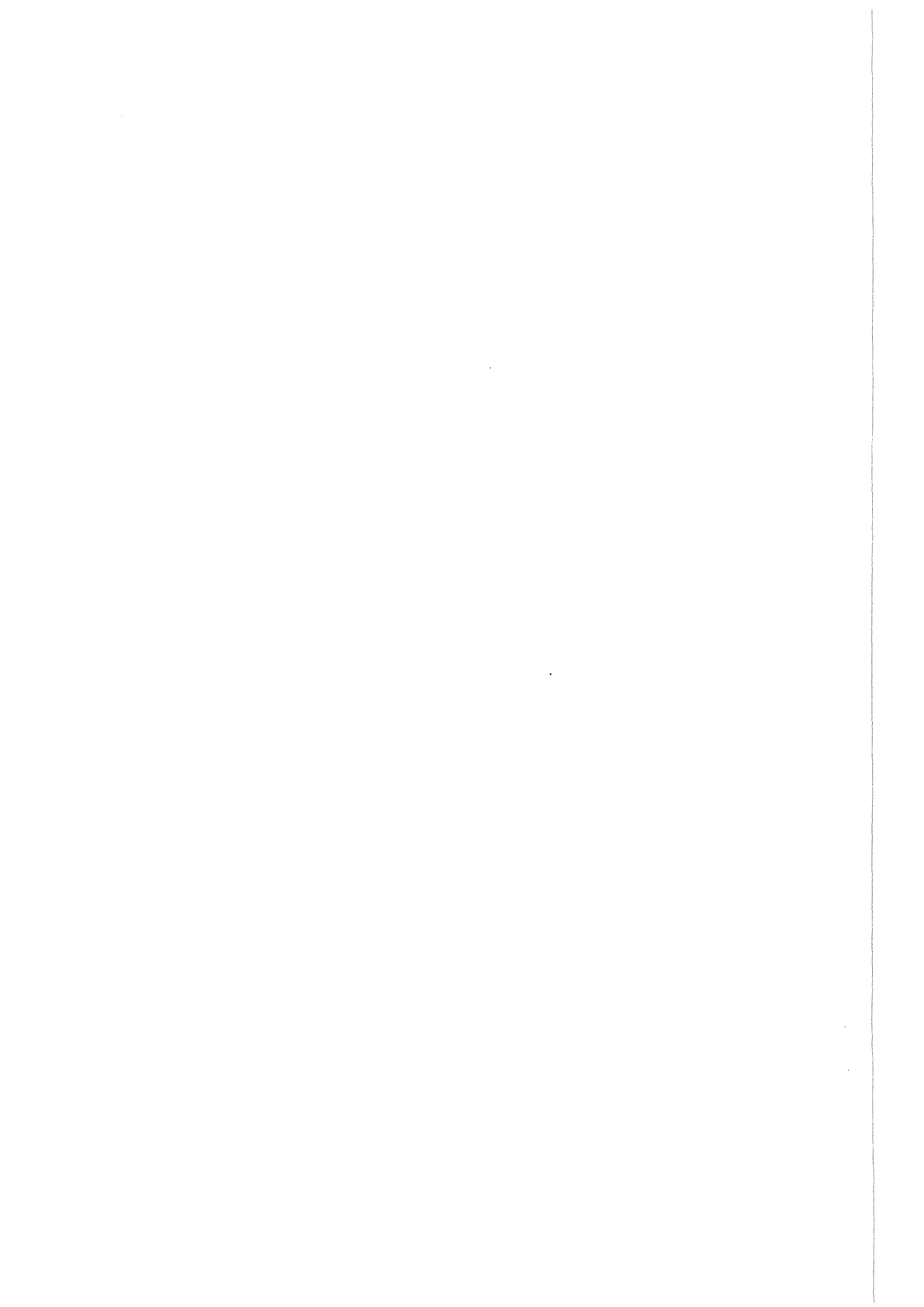
/2/ H. Gleiter, *Nanostructured Materials* 1 (1992), pp. 1-19

/3/ I.V. Beketov, Y.A. Kotov, A.M. Murzakaev, O.M. Samatov, V. Volkov, R. Böhme, G. Schumacher: "Synthesis of nanometer-sized powders of alumina and titania using the electrical explosion of wires", *Proc. Fourth Euro Ceramics, Riccione, October 2-6, 1995, Vol. 1*, pp. 77-82

/4/ V.V. Ivanov, S. Pararin, A. Vikhrev, R. Böhme, G. Schumacher: "Densification of ceramic nano-sized powders by pulsed magnetic technique", *Proc. Fourth Euro Ceramics, Riccione, October 2-6, 1995, Vol. 2*, pp. 169-176

/5/ G. Link, V. Ivanov, S. Pararin, V. Khrustov, R. Böhme, G. Müller, G. Schumacher, M. Thumm, A. Weisenburger: "A comparison of mm-wave sintering and fast conventional sintering of nanocrystalline Al_2O_3 ", *MRS spring meeting, San Francisco, April 8-12, 1996*

VI Publications



VI Publications

Journals:

- H. Laqua, H. Bluhm, L. Buth, P. Hoppé
"Properties of the nonequilibrium plasma from a pulsed sliding discharge in a hydrogen gas layer desorbed from a metal hydride film",
J. of Appl. Phys., 77 (1995) p. 5545 - 52.
- R. Schneider, C.-D. Munz
"Approximation of two-fluid plasma flow with explicit upwind schemes",
Int. J. Num. Modelling 8 (1995) 399.
- A.L. Ni, B. Goel
"Stability of a deflagration front in compressible media",
Zeitschrift für angewandte Mathematik und Physik, 46 (1995) 328 - 38.
- H. Würz, N.I. Arkhipov, V. P. Bakhtin, I. Konkashbaev, I. Landman, V.M. Safronov,
D.A. Toporkov, A.M. Zhitlukhin
"Experimental simulation and numerical modelling of vapor shield formation and divertor material erosion for ITER typical plasma disruptions",
Journal of Nuclear Materials, 220 - 222 (1995), 1066 - 70.
- K. Baumung, H. Bluhm, P. Hoppé, H.-U. Karow, D. Rusch, O. Stoltz, J. Singer,
G.I. Kanel, A.V. Utkin, S.V. Razorenov, V.E. Fortov
"Hypervelocity launching and impact experiments on the Karlsruhe light ion facility KALIF",
International Journal of Impact Engineering, 17 (1995), 37 - 46.
- C. Schultheiß
"Science and technology of thin film"
World Scientific Publ., Singapore, 1995.

Conference Contributions

- V. Engelko, R. Kurunov, I. Landman, B. Ljublin, L. Smirnov, H. Würz
"Test of divertor materials under simulated plasma disruption conditions at the SOM electron beam facility",
Prof. of the 11th Conf. on Plasma Surface Interaction (PSI), Mito, J, May 23 - 27, 1994
Journal of Nuclear Materials, 220 - 222 (1995), 1071 - 75

- B. Basylev, I. Landman, H. Würz
 "Numerical modeling of plasma flow target interaction for prediction of divertor behavior under ITER typical disruption conditions",
 Jaffrin, E. [Hersg.]
 21th EPS Conf. on Controlled Fusion and Plasma Physics, Montpellier, F, June 27 - July 1, 1995; Contributed Papers, Part II Europhysics Conference Abstracts, 18B (1994), 742 - 45.
 Conf. on Physics and Technology of Plasma, Minsk, GUS, September 13 - 15, 1994.
- I. Landman, H. Würz
 "Vapor shield formation and erosion of divertor plates during ITER Tokamak plasma disruptions",
 Herschbach, K., [Editor]
 Fusion Technology 1994: Proc. of the 18th Symp. Karlsruhe, August 22 - 26, Vol. 1, 335 - 38
 Amsterdam [u.a.]: Elsevier, 1995.
- H. Bluhm, P. Hoppé, H. Bachmann, W. Bauer, K. Baumung, L. Buth, H. Laqua, A. Ludmirski, D. Rusch, O. Stoltz, S. Yoo
 "Stability and operating characteristics of the applied B proton extraction diode on KALIF",
 Beams 94: Proc. of the 10th Internat. Conf. on High-Power Particle Beams, San Diego, Calif., June 20 - 24, 1994
 Springfield, Va.: NTIS, 1995, 77 - 82.
- N.I. Arkhipov, V.P. Bakhtin, V.M. Safronov, D.A. Toporkov, S.G. Vasening, H. Würz, A.M. Zhitlukhin
 "Plasma material interaction under simulated disruption conditions",
 Herschbach, K. [Editor]
 Fusion Technology 1994: Proc. of the 18th Symp., Karlsruhe, August 22 - 26, 1994, Vol. 1, 463 - 66.
- K. Baumung, H. Bluhm, P. Hoppé, H.-U. Karow, D. Rusch, O. Stoltz, J. Singer, G.I. Kanel, A.V. Utkin, S.V. Razorenov
 "Hydrodynamic beam-target interaction experiments on the Karlsruhe Light Ion Facility KALIF",
 Beams 94: Proc. of the 10th Internat. Conf. on High-Power Particle Beams, San Diego, Calif., June 20 - 24, 1994
 Springfield, Va.: NTIS, 1995, 211 - 14.

- W.H. Bauer, W. Höbel, E. Stein, A. Ludmirsky, T. Westermann
 "A contribution to the magnetic focusing in an applied B-extractor ion diode by a laser pulse driven solenoid",
 Beams 94: Proc. of the 10th Internat. Conf. on High-Power Particle Beams, San Diego, Calif., June 20 - 24, 1994
 Springfield, Va.: NTIS, 1995, 83 - 86.
- G. Piazza, B. Goel, W. Höbel, H. Würz, I. Landman
 "The magnetic vapor shield effect at divertor plates during plasma disruptions",
 Herschbach, K. [Editor]
 Fusion Technology 1994: Proc. of the 18th Symp., Karlsruhe, August 22 - 26, 1994, Vol. 1, 319 - 22.
- B.A. Knyazev, P.I. Melnikov, H. Bluhm
 "Catalytic resonance ionization - a novel universal technique for the formation of a two-component anode-plasma",
 Beams 94: Proc. of the 10th Internat. Conf. on High-Power Particle Beams, San Diego, Calif., June 20 - 24, 1994
 Springfield, Va.: NTIS, 1995, 451 - 54.
- H. Bluhm, P. Hoppé, H. Bachmann, W. Bauer, K. Baumung, L. Buth, H. Laqua,
 A. Ludmirsky, D. Rusch, O. Stoltz, S. Yoo
 "Recent progress in ion diode development at KfK",
 Coutant, J. [Editor]
 Prof. of the IAEA Technical Committee Meeting on Drivers for Inertial Confinement Fusion, Paris, F., November 14 - 18, 1994
 Paris: Commissariat a l'Energie Atomique 1995, 305 - 06.
- G.I. Kanel, S.V. Razorenov, A.V. Utkin, K. Baumung, H.-U. Karow, V. Licht
 "Spallations near the ultimate strength of solids",
 Schmidt, S.C. [Editor]
 High-Pressure Science and Technology: 1993
 Proc. of the Joint Internat. Assoc. for Research and Advancement of High Pressure Science and Technology and American Physical Society Topical Group on Shock Compression of Condensed Matter Conf., Colorado Springs, Colo., June 28 - July 2, 1993
 New York, N.Y.: Americal Inst. of Physics, 1994, 1043 - 46 (AIP Conference Proceedings, 309, Pt. 2).
- G.I. Kanel, A.V. Utkin, K. Baumung, H.-U. Karow, D. Rusch
 "Dynamics of the high-power ion beam interaction with targets",
 Beams 94: Proc. of the 10th Internat. Conf. on High-Power Particle Beams, San Diego, Calif., June 20 - 24, 1994
 Springfield, Va.: NTIS, 1995, 236 - 39

V.S. Koidan, V.T. Astrelin, A.V. Burdakov, V.V. Filippov, S.V. Lebedev, K.I. Mekler, P.I. Melnikov, V.V. Postupaev, A.F. Rovenskikh, M.A. Sheheglov, K.V. Tsigutkin, S.G. Voropaev, H. Würz

"E-beam heated plasma as a tool for ITER disruption simulation",
Beams 94: Proc. of the 10th Internat. Conf. on High-Power Particle Beams, San Diego, Calif., June 20 - 24, 1994
Springfield, Va.: NTIS, 1995, 240 - 43

V. Engelko, C. Schultheiß

"Model of the vacuum diode with adsorbate anode operation",
Beams 94: Proc. of the 10th Internat. Conf. on High-Power Particle Beams, San Diego, Calif., June 20 - 24, 1994
Springfield, Va.: NTIS, 1995, 491 - 94

V. Engelko, V. Kuznezov, G. Vjazmenova, H. Würz

"Compression of intense proton beams",
Beams 94: Proc. of the 10th Internat. Conf. on High-Power Particle Beams, San Diego, Calif., June 20 - 24, 1994
Springfield, Va.: NTIS, 1995, 691 - 94

A. Ludmirsky, K. Baumung, H. Bluhm, L. Buth, B. Goel, G. Meisel, D. Rusch, O. Stoltz, J.J. MacFarlane, P. Wang

"Calculations for K_{α} -spectroscopy of hot dense plasmas produced by the KALIF ion beam",
Beams 94: Proc. of the 10th Internat. Conf. on High-Power Particle Beams, San Diego, Calif., June 20 - 24, 1994
Springfield, Va.: NTIS, 1995, 723 - 26

V. Engelko, C. Schultheiß, H. Würz, S. Schalk, H. Giese

"Pulsed intense proton beam facility for ITER disruptions simulation"
Beams 94: Proc. of the 10th Internat. Conf. on High-Power Particle Beams, San Diego, Calif., June 20 - 24, 1994
Springfield, Va.: NTIS, 1995, 785 - 88

O.Y. Vorobiev, B. Goel

"Application of intense ion beams for investigation of matter properties under high pressures and temperatures"
Beams 94: Proc. of the 10th Internat. Conf. on High-Power Particle Beams, San Diego, Calif., June 20 - 24, 1994
Springfield, Va.: NTIS, 1995, 825 - 28

G. Müller, C. Schultheiß

"Deposition by means of pulsed electron beam ablation"
Beams 94: Proc. of the 10th Internat. Conf. on High-Power Particle Beams, San Diego, Calif., June 20 - 24, 1994
Springfield, Va.: NTIS, 1995, 833 - 36

K. Baumung, H.-U. Karow, V. Licht, D. Rusch, J. Singer, O. Stoltz, H. Bachmann, W. Bauer, H. Bluhm, L. Buth, B. Goel, M.F. Goez, H. Gutz, P. Hoppé, H. Lotz, C.D. Munz, G.I. Kanel, A.L. Ni, A. Shutov, O.Yu. Vorobjev

"Hydrodynamic target experiments with proton beams at KALIF"

Paisley, D.L. [Editor]

Selected Papers on Scientific and Engineering High-Speed Photography. Technology, Systems and Applications, Bellingham, Was.: SPIE Optical Engineering Press, 1995, 555 - 64 (SPIE Milestone Series: 109).

I.V. Beketov, Y.A. Kotov, A.M. Murzakaev, O.M. Samatov, V. Volkov, R. Böhme, G. Schumacher

"Synthesis of nanometer-sized powders of alumina and titania using the electrical explosion of wires",

Galassi, C. [Editor]

4th Euro-Ceramics: Proc. of the 4th European Ceramic Society Conf., Riccione, I, October 2 - 6, 1995

Vol. 1: Basic Science - Developments in Processing of Advanced Ceramics Part I, Faenza. Gruppo Editoriale Faenza Editrice, 1995, 77 - 82

V. Ivanov, S. Paranin, A. Vikhrev, R. Böhme, G. Schumacher

"Densification of ceramic nanometer-sized powders by pulsed magnetic technique"

Galassi, C. [Editor]

4th Euro-Ceramics: Proc. of the 4th European Ceramic Society Conf., Riccione, I, October 2 - 6, 1995

Vol. 1: Basic Science - Developments in Processing of Advanced Ceramics Part I, Faenza. Gruppo Editoriale Faenza Editrice, 1995, 169 - 76

Y.A. Kotov, I.V. Beketov, T.I. Demina, A.M. Murzakaev, O.M. Samatov, G. Schumacher, R. Böhme

"Characteristics of ZrO₂ nanopowders produced by electrical explosion of wires"

European Aerosol Conf., Helsinki, SF, September 18 - 22, 1995

Journal of Aerosol Science, 26 (1995) Suppl. 1, 905 - 906.

Reports

H. Bluhm

"Die Erzeugung gepulster Megaampere-Ionenströme für die Materie- und Trägheitsfusionsforschung"

Wissenschaftliche Berichte, FZKA-5528 (März 1995)

Habilitation, Universität Karlsruhe 1995

E. Halter, M. Krauss, C.D. Munz, R. Schneider, E. Stein, U. Voss, T. Westermann

"A concept for the numerical solution of the Maxwell-Vlasov system"

Wissenschaftliche Berichte, FZKA-5654 (Oktober 1995)